Wrocław University of Technology
Centre of Advanced Materials and Nanotechnology

Materials Science
Poland

Conference
Intermolecular and Magnetic Interactions in Matter
Nałęczów 8–10 September 2005

Guest Editors
Jan M. Olchowik, Wojciech Sadowski, Nikos Guskos

Vol. 24 • No. 4 • 2006

Oficyna Wydawnicza Politechniki Wrocławskiej

Materials Science is an interdisciplinary journal devoted to experimental and theoretical research into the synthesis, structure, properties and applications of materials.

Among the materials of interest are:

- glasses and ceramics
- sol-gel materials
- photoactive materials (including materials for nonlinear optics)
- laser materials
- photonic crystals
- semiconductor micro- and nanostructures
- piezo-, pyro- and ferroelectric materials
- high-T_c superconductors
- magnetic materials
- molecular materials (including polymers) for use in electronics and photonics
- novel solid phases
- other novel and unconventional materials

The broad spectrum of the areas of interest reflects the interdisciplinary nature of materials research. Papers covering the modelling of materials, their synthesis and characterisation, physicochemical aspects of their fabrication, properties and applications are welcome. In addition to regular papers, the journal features issues containing conference papers, as well as special issues on key topics in materials science.

Materials Science is published under the auspices of the Centre of Advanced Materials and Nanotechnology of the Wrocław University of Technology, in collaboration with the Institute of Low Temperatures and Structural Research of the Polish Academy of Sciences and the Wrocław University of Economics.

All accepted papers are placed on the Web page of the journal and are available at the address:
http://MaterialsScience.pwr.wroc.pl

Materials Science is abstracted/indexed in: Chemical Abstracts; Materials Science Citation Index; Science Citation Index Expanded.

The Journal is supported by the State Committee for Scientific Research

Editorial Office

Tomasz Fałat
Karol Langner

Printed in Poland

Drukarnia Oficyny Wydawniczej Politechniki Wrocławskiej
Zam. nr 1060/2006.

CONTENTS

Preface

This issue of the *Materials Science-Poland* contains a selection of papers presented during the 8th International Conference on Intermolecular and Magnetic Interactions in Matter held in Nałęczów (Poland) between 8 and 10 September 2005. The conference was organized by the Institute of Physics of Lublin University of Technology in cooperation with the Institute of Physics of Szczecin University of Technology, the Faculty of Physics and Mathematics of Gdańsk University of Technology, the Department of Physics of University of Athens (Greece) and the Polish Society for Crystal Growth.

The scope of the conference covered theoretical and experimental aspects of various intermolecular and magnetic interactions in strongly arranged and disordered matter. This included the following topics:

- crystal field, dipole–dipole, exchange interactions,
- crystallization and dissolution processes,
- phase transitions,
- low-dimensional structures and related phenomena,
- nanocrystalline materials and nanocomposites,
- synthesis and characterization of thin films,
- superconductors, magnetic and organometallic materials
- nonlinear interactions in materials,

The conference was a successor of seven previous meetings, organized by various Polish technical universities with the intention to bring together experimentalists and theoreticians representing various disciplines dealing with the intermolecular and magnetic interactions in the matter. A wide range of topics presented at the conference reflects research carried out in physical and chemical institutes affiliated to Polish technical universities as well as other national and foreign scientific institutions dealing with similar topics.

The conference was organized with the assistance given by the financial support of the Polish Committee for Scientific Research and the Lublin University of Technology.

Jan M. Olchowik
Chairman

Materials Science-Poland, Vol. 24, No. 4, 2006

Carbon encapsulated iron nanowires

R. RAMIREZ[1*], M. WEISSMANN[2], G. GARCIA[1], M. KIWI[1]

[1]Facultad de Física, Pontificia Universidad Católica de Chile, Casilla 306, Santiago 7820436, Chile

[2]Departamento de Física, Comisión Nacional de Energia Atómica,
Avda. Libertador 8250 (1429) Buenos Aires, Argentina

A study of the structural and magnetic properties of carbon encapsulated iron nanowires is presented. The influence of carbon presence on iron magnetic ordering by means of an *ab initio* computer simulation has been studied. For wires tightly encapsulated, i.e. with large ratio of wires and nanotubes radii, the presence of carbon strongly alters Fe magnetic configuration of free standing wires, in some cases yielding antiferromagnetic ordering. The energy differences between ferromagnetic and antiferromagnetic phases are small enough to allow their coexistence in a nanowire, which is in agreement with the experimental evidence of exchange-bias in such systems.

Key words: *nanowires; nanotubes; magnetism; ab-initio; exchange bias*

1. Introduction

Carbon nanotubes are promising candidates for a variety of applications due to their uncommon and versatile electrical and mechanical properties which recently generated an active area of research [1]. Possible technological applications include, among others, nanotransistors [2, 3], spin-polarized electron sources [4], hydrogen storage [5, 6], flat display panels [7] and magnetic inks. Transition metal (TM) filled nanotubes are expected to have a strong impact on magnetic recording devices since dramatic improvement in memory density could be achieved in quantized magnetic disks, taking advantage of small sizes and magnetic anisotropy of the nanowires. Moreover, experimental works on iron filled nanotubes with shifted hysteresis loops suggest the presence of γ-Fe–α-Fe interfaces, and the existence of the exchange bias phenomenon [8, 9]. Theoretical works on TM-filled nanotubes deal with a small number of iron atoms inside a carbon nanotube [10, 11].

*Corresponding author, e-mail: rramirez@pauli.fis.puc.cl

We present the results of the investigation of structural and magnetic properties of iron nanowires encapsulated by single wall, zigzag type, carbon nanotubes of several diameters. For the iron nanowires, we adopted two different diameters; the smaller unit cell consists of two triangular Fe layers of six atoms each, resembling a part of the hcp structure. For wires of larger diameter, we increase the number of Fe atoms per layer from six to twelve.

2. Simple model

We start with the mentioning of the results of a simpler model presented previously [12]. Here a nanowire with six Fe atoms per layer is surrounded by a rather small number of carbon atoms arranged as six symmetrical lines parallel to the axis of the wire, as shown in Fig. 1. It is not a real nanotube-encapsulated iron nanowire but it may be considered as a first order approximation, suitable for a fast DFT study on the carbon influence on the magnetic behaviour of a nanowire. The system has the diameter of 6 Å.

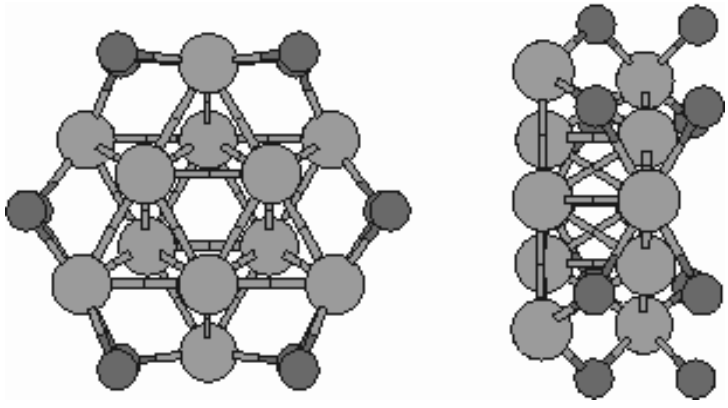

Fig. 1. Unit cell of 6 Fe atoms per layer surrounded by six lines of carbon viewed perpendicular (left) and parallel to the tube axis. The distance between the carbon layers is 2.03 Å and the C–C distance in the same layer is 3.5 Å. The Fe–C distance is taken equal to 2.03 Å, similar to that found in cementite. The AFM phase is energetically favourable for this system, lower than the FM phase energy by 0.014 eV/atom. The energy gain due to encapsulation was estimated as 3.77 eV/atom for the FM and 3.87 for the AFM phase. The magnetic moments present lower values at $2.0\mu_B$ (peripheral Fe), $1.8\mu_B$ (interior Fe) and $-0.1\mu_B$ (C)

Since in the bulk the fcc structure has the same number of nearest neighbours as the hcp one, we expect similar results for both structures. The Wien2k code [13] has been used in the calculation which is an implementation of the FPLAPW (full potential linear augmented plane aves) method. It uses the exchange and correlation given by Perdew, Burke and Ernzerhoff [19, 20]. The GGA (generalized gradient approximation) was chosen because it gives good results for the bulk bcc Fe lattice parameter

and cohesive energy. The number of plane waves used, given by the parameter RKM = 7, corresponds to the energy cut-off of 206 eV. The calculation is scalar relativistic and includes local orbitals for the 3p states of Fe. Muffin tin spheres radii are 2 a.u. for Fe and 1.8 a.u. for C. A calculation of bulk bcc Fe with these parameters yields the nearest-neighbour distance of 2.48 Å and the magnetic moment of $2.25\mu_B$. For fcc Fe, the nn distance is the same, but the optimal magnetic structure is antiferromagnetic (AFM), with a local magnetic moment of $1.4\mu_B$. In the case of the hcp structure we also obtain an AFM phase, but the energy per atom is 0.01 eV lower than for the fcc. This information is used in the construction of the nanowire unit cell.

For a free standing nanowire, the cohesive energy of such artificial unit cell of 6 atoms per layer is 4.78 eV/atom, surprisingly close to the 6.16 eV/atom for bcc bulk. ferromagnetic (FM) order is favoured over AFM by 0.1 eV/atom. Notice that for bulk fcc or hcp structures, the opposite result is obtained, since with the same Fe–Fe distance the AFM structure has the lowest energy. In the AFM arrangement, the magnetic moments alternate on a single layer with values of 1.1 and $2.9\mu_B$, while for the FM structure the values are $3.0\mu_B$ for the peripheral and $2.5\mu_B$ for the interior atoms. There is a large polarization at the Fermi level since the DOS for the majority iron spin is rather small.

The unit cell of the encapsulated wire is built by adding a layer of six carbon atoms which form a hexagon situated half way between the Fe layers as shown in Fig. 1.

3. Small-diameter nanowires

Now we present the results for nanowires encapsulated in real carbon nanotubes. We considered nanowires of six and twelve Fe atoms per layer, arranged in structures similar to those described in the preceding section. The six-atom per layer wires were introduced in zigzag nanotubes of the (9,0) and (11,0) type. The former case is certainly an extreme situation where the system is in a non-stable repulsive configuration. It was studied, however, as a test case for a very strong interaction between carbon and a wire. The 12-atoms per layer wires will be discussed in the next section. We performed *ab-initio* spin polarized geometry optimization of the structure by means of the SIESTA code within the framework of DFT [14, 15], using a basis set of strictly-localized numerical pseudoatomic orbitals, as implemented in the SIESTA code [16–18] within the generalized gradient approximation (GGA-PBE). The exchange-correlation energy was calculated as parameterized by Perdew, Burke and Ernzerhof [19, 20]. Norm-conserving pseudopotentials [21] in their non-local form were used to describe the electron-ion interactions, including non-linear core corrections [22]. In the SIESTA calculation, we have used a double-zeta basis set including polarization functions (DZP) [17]. Convergence tests have demonstrated that this basis yields reliable results in a variety of cases including covalent, ionic and metallic systems. In fact, tests by Junquera et al. [23] show that the results of DZP calculations are comparable to well converged plane-wave results.

We start with perfect structures as shown in Fig. 2. Notice a large distortion suffered by the wire and the nanotube upon relaxation. The wire maintains the FM phase and there is very little charge transfer from the iron atoms to the carbons. The peripheral Fe atoms show a larger magnetic moment than the inner ones, while the opposite situation occurs for more tightly encapsulated wires. The results are shown in Table 1.

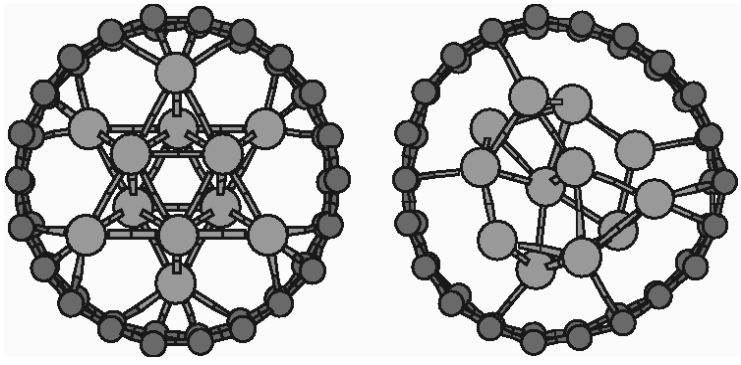

Fig. 2. Unit cell of six Fe atoms per layer encapsulated in a (11,0) nanotube viewed perpendicular to the tube axis. Both the unrelaxed (left) and relaxed configurations (right)are illustrated

Table 1. Magnetic moments per atom μ_{at}, in Bohr magnetons (μ_B), and charge transfer $\Delta\rho$ from Fe to C atoms in a.u. for relaxed nanowires of 6 or 12 Fe atoms per layer encapsulated in a (n,0) carbon nanotube (CNT). The last two rows refer to free standing iron wires with 6 and 12 atoms per layer, respectively

Nanowire	μ_{at}		$\Delta\rho$		Order
	Peripheral	Interior	Peripheral	Interior	
(9,0)-6 Fe	0.40	1.87	0.05	0.02	FM
(11,0)-6 Fe	2.6	2.36	0.046	–0.052	FM
(13,0)-12 Fe	–1.16	2.07	0.058	0.0	–
(15,0)-12 Fe	2.62	2.62	0.0	0.0	FM
6 Fe	3.20	2.65	–	–	FM
12 Fe	2.34	1.96	–	–	FM

4. Larger diameter nanowires

In this section, we present the results for nanowires with 12 Fe atoms per layer encapsulated in a (13,0) and in a (15,0) nanotube. We have performed an optimization of the geometry of the structure by means a DFT spin polarized calculation with the SIESTA code within the generalized gradient approximation (GGA-PBE). We started with perfect structures shown in Figs. 3(a) and (c).

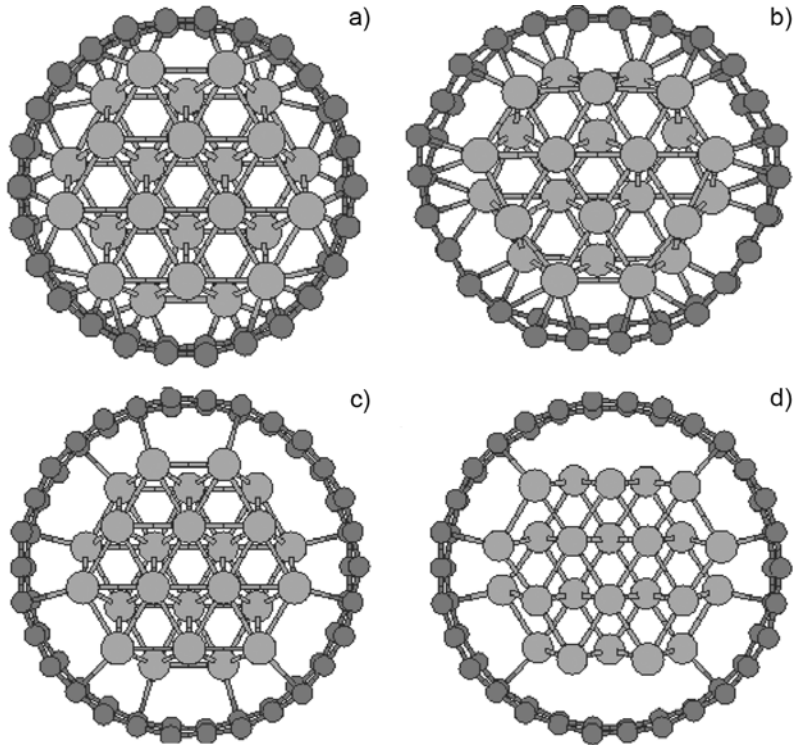

Fig. 3. Unit cell of 12 Fe atoms per layer encapsulated in a (13,0) nanotube (a, b) and in a (15,0) nanotube (c, d) viewed perpendicular to the tube axis. The unrelaxed configurations are shown on the left and relaxed configurations on the right

For the (13,0) nanotube, the optimized geometry of the wire appears slightly distorted when compared with the initial ones (Figs. 3a, b). The average diameter of the nanotube increases from 10.28 Å to 10.81 Å but the width of the wire shrinks from 7.57 Å to 7.29 Å. The distance between Fe layers stretches from 2.023 Å to 2.138 Å. The average magnetic moment for the innermost iron atoms is $2.07\mu_B$, while for the outermost atoms it is $-1.16\mu_B$. The average magnetic moment of the carbon atoms is less than $0.1\mu_B$. These values are summarized in Table 1.

After relaxation, the nanowire inside the (15,0) nanotube changes its structure into a bcc configuration. The initial diameter of 7.57 Å stretches to 8.5 Å after relaxation. The nanotube also increases its diameter to about 12.2 Å.

The isocurves of the charge density distribution are shown in Figs. 4 and 5, where the darker lines represent net spin up charge, and the lighter ones – net spin down charge. In a more tightly encapsulated nanowire (13,0), the charge densities of the outermost iron atoms have opposite polarizations to the inner ones. Notice that in this case there is a charge transfer from Fe to C atoms (see Table 1). The (15,0) nanotube is quite different since all the iron atoms are polarized in the same direction, with almost the same charge, and there is a negligible charge transfer.

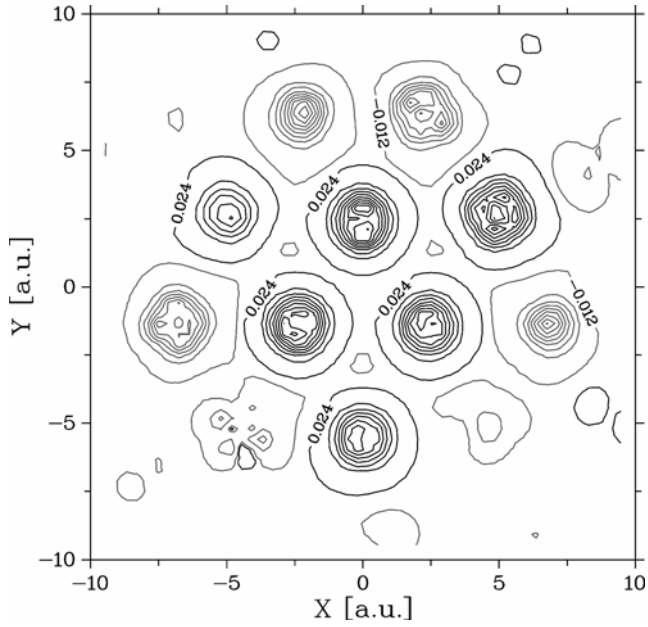

Fig. 4. Isocurves of the difference between the spin up and the spin down charge densities for a 12 Fe atom per layer wire encapsulated in a (13,0) carbon nanotube. The darker lines represent a net spin up and the lighter ones a net spin down charge

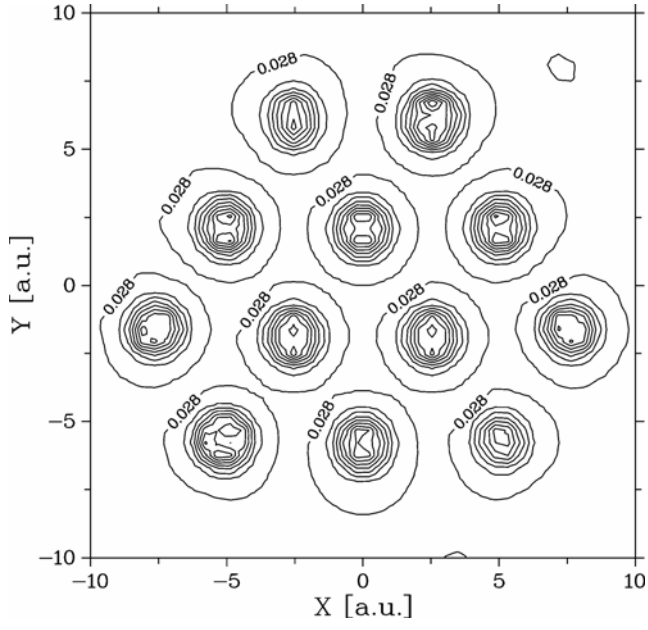

Fig. 5. Isocurves of the difference between the spin up and the spin down charge densities for a 12 Fe atoms per layer wire encapsulated in a (15,0) carbon nanotube. All the Fe atoms show a net spin up charge

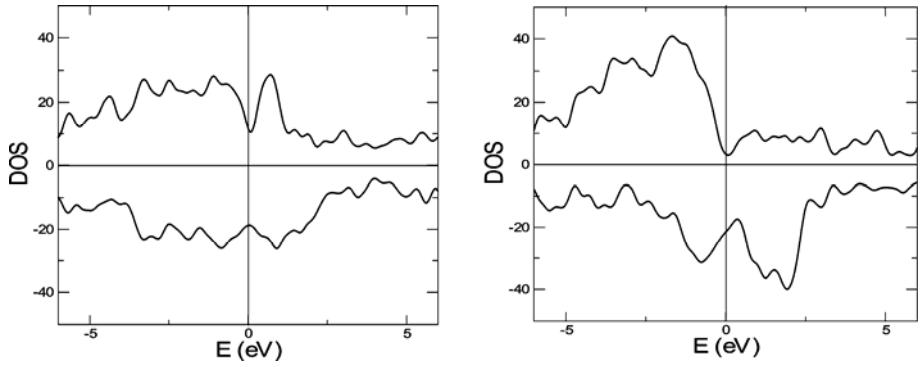

Fig. 6. Densities of states of wires with 12 Fe atoms encapsulated in a (13,0) nanotube (left) and in a (15,0) nanotube (right) for the majority and the minority bands. Notice a large difference in the DOS at the Fermi level for the wire in the (15,0) nanotube

The average magnetic moment of the innermost iron atoms of a (13,0) nanotube is $2.07\mu_B$, while for the outermost atoms it is $-1.16\mu_B$. The average magnetic moment of carbon atoms is less than $0.1\mu_B$. For the (15,0) nanotube all the iron atoms have similar magnetic moments of $2.62\mu_B$. The densities of states for these structures, for the majority and the minority band, are shown in Fig. 6. The density of states at the Fermi level for the (15,0) nanotube greatly differs for the spin up and the spin down bands. This could be interesting in a possible application of these systems in electron spin injection.

5. Conclusions

We have studied several configurations of iron nanowires inside a carbon nanotube structure. Within a very simple static model, we found that the energy difference between the FM and the AFM phases is very small, and therefore we conclude that they could coexist in an encapsulated nanowire, a fact that could explain the observation of exchange-bias in these systems [8, 9].

The spin polarization of an iron atom in an encapsulated wire depends on the number of neighbouring carbon atoms and the Fe–C distance. We also found that iron magnetic configuration in a carbon encapsulated nanowire strongly depends on the ratio of the diameters of the nanotube and the wire. If this ratio is large, the iron spin polarization of the peripheral iron atoms decreases, and in some cases the whole structure tends to an AFM configuration. On the other hand, if this ratio is small, the charge transfer from Fe to C is small. In this case, however, the densities of states at the Fermi level greatly differ between spin up and spin down bands. This fact could be of interest in a possible use of these systems in spin injection. We also observe that for large ratios of the diameters of the nanotube and the wire, the layers of the wires prefer the [110] bcc structure.

References

[1] MONTHIEOUX M., Carbon, 40 (2002), 1809.
[2] ESFARJANI K., FARAJIAN A.A., EBRAHIMI F., KAWAZOE Y., Eur. Phys. J. D, 16 (2001), 353.
[3] TSUKAGOSHI K., YAGI I., AOYAGI Y., Appl. Phys. Lett., 85 (2004), 1021.
[4] HAO S., ZHUO G., WU J., DUAN W., GU B.L., Phys. Rev. B, 69 (2004), 113403.
[5] DILLON A.C., Nature, 386 (1997), 377.
[6] LIU C., FAN Y.Y., LIU M., CONG H.T., CHENG H.M., DRESSELHAUS M.S., Science, 286 (1999), 1127.
[7] HEER W.A., CHATELAIN A., UGARTE D., Science, 270 (1996), 1179.
[8] KIWI M., J. Magn. Magn. Mat., 234 (2001), 584.
[9] PRADOS C., CRESPO P., GONZALEZ J.M., HERNANDO A., MARCO J.F., GANCEDO R., GROBERT N., TERRONES M., WALTON R.M., KROTO H.K., Phys. Rev. B, 65 (2002), 113405.
[10] FAGAN S.B., MOTA R., DA SILVA A.J.R., FAZZIO A., Phys. Rev. B, 67 (2003), 205414.
[11] YANG C.K., ZHAO J., LU J.P., Phys. Rev. Lett., 90 (2003), 257203.
[12] WEISSMANN M., GARCIA G., KIWI M., RAMIREZ R., Phys. Rev. B, 70 (2004), 201401.
[13] BLAHA P., SCHWARZ K., MADSEN G.K.H., KVASNICKA D., LUITZ J., *An Augmented Plane Wave + Local Orbitals Programs for Calculating Crytal Properties*, Karlheinz Schwarz, Techn. Universität Wien, Austria, 2001.
[14] HOHENBERG P., KOHN W., Phys. Rev. B, 136 (1964), 834.
[15] KOHN W., Rev. Mod. Phys., 71 (1999), 1253.
[16] ORDEJON P., ARTACHO E., SOLER J.M., Phys. Rev. B, 53 (1996), R10441.
[17] SOLER J.M., ARTACHO E., GALE J.D., GARCIA A., JUNQUERA J., ORDEJON P., SANCHEZ-PORTAL D., J. Phys.: Condens. Matter, 14 (2002), 2745.
[18] SANCHEZ J.M., MICHAELIAN M.R.B.K., GARZON I.L., ORDEJON P., SANCHEZ-PORTAL D., ARTACHO E., Phys.Rev. B, 61 (2000), 5771.
[19] PERDEW J.P., BURKE K., ERNZERHOFF M., Phys. Rev. Lett., 77 (1996), 3865.
[20] PERDEW J.P., BURKE K., ERNZERHOFF M., J. Chem. Phys., 105 (1996), 9982.
[21] TROULLIER N., MARTINS J.L., Phys. Rev. B, 43 (1991), 1993.
[22] LOUIE S.G., FROYEN S., COHEN M.L., Phys. Rev. B, 26 (1982), 1738.
[23] JUNQUERA J., PAZ O., SANCHEZ-PORTAL D., ARTACHO E., Phys. Rev. B, 64 (2001), 235111.

Received 8 September 2005
Revised 11 November 2005

Materials Science-Poland, Vol. 24, No. 4, 2006

Interface effects on the NLO properties of guest–host materials

M. MAKOWSKA-JANUSIK[1*], A.-H. KASSIBA[2], G. FAILLEAU[2], J. BOUCLÉ[2]

[1]Institute of Physics, Jan Długosz University, al. Armii Krajowej 13/15, 42-201 Częstochowa, Poland

[2]Laboratoire de Physique de l'Etat Condensé – UMR CNRS 6087,
Institut de Recherche en Ingénierie Moléculaire et Matériaux Fonctionnels, FR CNRS 2575,
Université du Maine, 72085 Le Mans Cedex 9, France

Electro-optical properties of silicon carbide (SiC) nano-sized clusters embedded into three different polymeric matrices, i.e., poly(methyl methacrylate, poly-N-vinylcarbazole and polycarbonate were investigated. Electric properties of SiC were calculated using time-dependent DFT methods considering an isolated cluster and environmental effects. The concept of the polymeric influence on optical properties of chromophores was executed by the local electric field approach. Electric field created by charge distribution of the surrounding polymer was calculated using guest–host structures obtained by the molecular dynamics simulations. Optical properties of SiC situated in polymeric environments differ from those of free clusters. It is seen more significantly for the hyperpolarizability than for the polarizability. The spatial distribution of SiC in the matrix depends on the kind of polymer and gives an important influence on the obtained local electric field value. The Si–C distances do not change with variation of the polymeric matrix. The geometry of 3C–SiC is very stable and does not change during MD simulations performed at 300 K.

Key words: *composite material*; *guest–host material*; *nonlinear optics*; *electro-optics*; *SiC*

1. Introduction

In the recent decades, increasing interest has been paid to nonlinear optics (NLO) in hybrid nanomaterials due to a possibility of incorporation of semiconducting nanograins as chromophores in a polymeric medium [1–3]. The importance of semiconductor nanocrystals consists in exhibition of size-dependent electronic and optical properties, significantly different from those of the corresponding bulk-like lattice [4]. The strategy to develop efficient NLO composite materials requires appropriate matrices in

* Corresponding author, e-mail: m.makowska@ajd.czest.pl

order to enhance the physical responses. Furthermore, the polymeric matrix should assure the photo-transparency, mechanical hardness and thermal stability. On the other side, the electrostatic influence coming from a host polymer and the intermolecular forces can affect external structure of guest grains and change electric molecular properties. Moreover, it is necessary to investigate experimentally difficult environmental effects (polymer–nanograin) on the optical properties of the nanocomposites. For this purpose, molecular simulations are powerful methods to evaluate the guest–host interaction and to separate their individual contributions to the overall NLO response. Macroscopic susceptibility of a guest–host system is determined by microscopic polarizabilities and hyperpolarizabilities of the constituents and their distribution. In the frame of the local field theory, linear and nonlinear macroscopic susceptibilities are related to molecular properties by local field factors. The local field approach may be taken into account to analyse the nature of the molecular environment of nanograins and to calculate macroscopic electro-optical (EO) properties of composite materials.

In the present work, silicone carbide (SiC) nanograins were chosen as inorganic chromophores because composite materials consisting of the SiC nanocrystallites embedded within the photopolymer olygoetheracryalte matrices were proposed as promising NLO materials [5]. From the wide variety of SiC polymorphic structures, the 3C–SiC nanograins were studied and the influence of organic host matrices on their optical properties was examined. Poly(methyl methacrylate) (PMMA), poly-N-vinylcarbazole (PVK) and polycarbonate (PC) were chosen as hosts due to their good optical and thermomechanical properties. The results presented in the paper include only theoretical investigations of polymeric influence on NLO properties of SiC chromophores.

The guest–host systems were built using molecular dynamic (MD) simulations method and the full atomistic modelling of the composite materials was achieved. The first order nonlinear optical hyperpolarizabilities $\beta(-\omega; 0, \omega)$ for the SiC nanograins were calculated using the density functional theory (DFT) methods. The structures of modelled systems were used to analyse environmental effects of polymeric matrices on the optical properties of the SiC chromophores. The macroscopic susceptibilities of the considered systems were computed using the local field theory and the obtained results have been compared with the experimental data [1, 2]. In the present work, we tried to simulate the physical process to assess the impact of main structural fragments on the electronic properties of the composite materials using time-dependent DFT (TDDFT) simulations together with the method of MD. Additionally, it was found that polymer environment reconstructs the surface of the SiC nanograin, contributing critically to the NLO properties of these hybrid materials.

The physical insight into the interface effects obtained by numerical methods was the goal of the presented paper and as a support for the theoretical models, we considered the Pockels effect demonstrated experimentally in SiC-based hybrid materials.

2. Molecular dynamic simulations

Three host–guest systems were simulated, namely SiC/PMMA, SiC/PC and SiC/PVK structures. Three equivalent starting structures, for each system, were generated using Hyper-Chem program package [6]. A unit cell of each investigated system consisted of one chain of PMMA 90-mer with molecular weight 9012.58 amu, one PC 50-mer chain (12716.21 amu), one PVK 50-mer chain (9664,45 amu), respectively and one SiC cluster. The structures of the polymers are presented in Fig. 1.

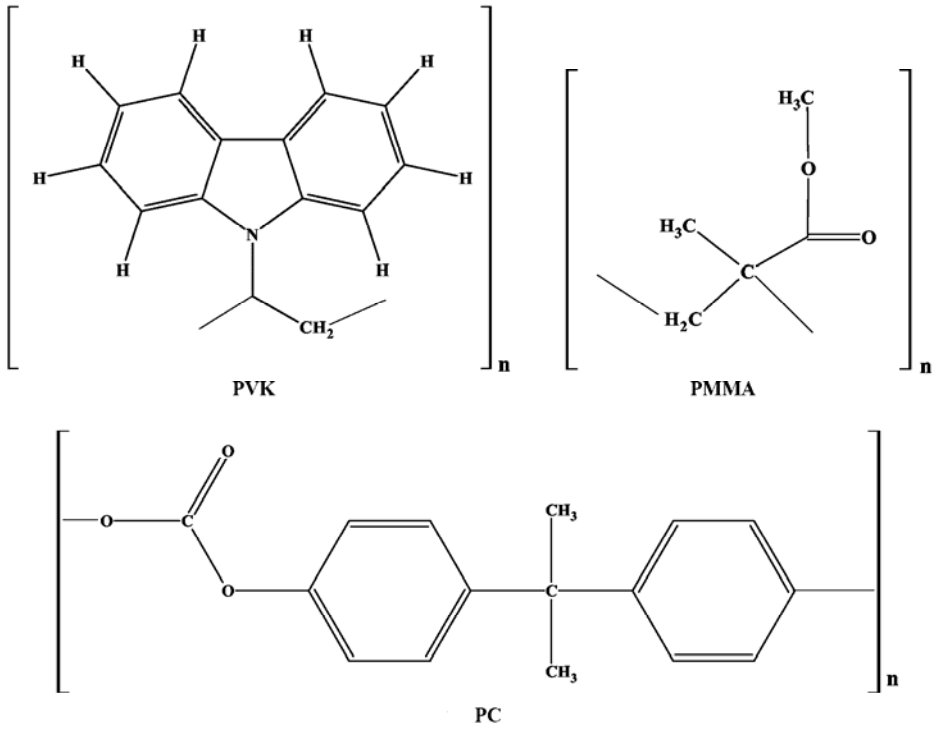

Fig. 1. Formulae of the PVK, PMMA and PC structural units

The SiC cluster (the mass of 4330.48 amu), was built with the cubic crystalline arrangement consisting of 108 SiC pairs. Every simulated unit cell of investigated structures was cubic with the edge length of 27.10 Å, 29.99 Å, 28.34 Å for the SiC/PMMA, SiC/PC and SiC/PVK systems, respectively. The density of each system was 1.20 g/cm^3 and corresponded to the solid state densities of considered matrices. The mass fractions of SiC embedded into the polymeric environment were 48.05 wt. % for PMMA/SiC, 34.05 wt. % for PC/SiC and 44.81 wt. % for PVK/SiC systems.

MD simulations were performed using the GROMACS software [7]. A leap-frog algorithm was used to integrate Newton's equations of motion [8]. The potential en-

ergy was computed as a summation of the contributions of bonded terms and non-bonded interactions such as the Lennard–Jones 12–6 and Coulomb potentials. Bonded interactions are based on a fixed list of atoms and non-bonded ones on a dynamic list. The atomic charges of the system constituents were obtained using DFT calculations described below. The pair list was updated after every step of MD run. To make the neighbour list, the grid search algorithm was used with the cut-off parameter equal to 1.3 nm. Bond interactions were represented by harmonic potentials, while angle and dihedral distortions were modelled by a simple cosine function. The potential function of the modelled system is described via the all-atom consistent valence force field (CVFF) [9]. The parameters of SiC_4 and CSi_4 tetrahedral bonding potentials are given in [10]. The CVFF force field has been successfully used to model a wide variety of biophysical, crystal and guest–host systems [11–13].

At first, geometry of each investigated system was optimized using energy minimization employing the steepest descent method with a convergence criterion of 10 $kcal \cdot mol^{-1} \cdot Å^{-1}$. All MD simulations were conducted at constant number of particles, volume and temperature (NVT ensemble) by applying periodic boundary conditions. Each investigated system was first evaluated during 2 ns at 300 K, using the time step of 1 fs to allow sufficient equilibration of the system. These data were not used in a subsequent analysis. The stability of the total energy was reached after about 1.5 ns of MD run. Then, the simulations were ran again at 300 K, with the time step of 1 fs and the coordinates were stored every 1000 steps. Equilibration of temperature to the desired value of 300 K was carried out in increments of 2 K using the Nose–Hoover thermostat [14]. A cut-off of 1.3 nm was used for the van der Waals interaction. The particle mesh Ewald (PME) summation [15] was employed for the electrostatic long-range interactions. The cut-off distance for the integrating coordination numbers was larger than the nearest-neighbour distance of a perfect 3C–SiC crystal structure.

3. Quantum-chemical computation

Optical properties of the SiC nanograins were calculated in the finite-cluster and local field modification approaches using geometries of isolated 3C–SiC structure of 216 atoms. Quantum-chemical computations reported in this paper were performed using the Amsterdam Density Functional (ADF) package [16] implementing Slater-type basis sets. All calculations were performed with the standard double ζ basis sets available in ADF, described in the references. The polarizability α and first hyperpolarizability β were calculated using ADF-RESPONSE module [17] within the frame of time-dependent DFT (TDDFT) theory. The local density approximation (LDA) for the potential and kernel was used, which compose the local Slater exchange functional [18] and the uniform electron gas local correlation functional due to Vosko, Wilk, and Nusair (VWN) [19]. All the clusters were rotated to align maximal ground state dipole moment along the Z-axis.

In the frame of the local field theory, linear and nonlinear macroscopic susceptibilities are related to molecular properties by the local field factors. In the discrete local field theory, the local fields are computed considering the molecular environment rigorously. The intensity of the created electric field depends on the arrangement of the polarized molecules around the point of interest, in our case in the centre of mass (COM) of the SiC cluster. Using the results of MD simulations, the guest–host structures were considered to calculate the electrostatic interaction between the polymer and SiC cluster. The local electric field was calculated for each system in the COM of SiC, for each snapshot of the MD simulations via the boundary condition and then averaged. The influence of the next neighbour cells was taken into account up to the difference ΔF between two calculated electric fields less than 10^{-3} GV/m. The calculated electric fields for all considered systems are collected in Table 1. In order to calculate electrostatic intermolecular interactions, the data from the last 0.5 ns of MD run were considered. The obtained electric fields were applied to predict the linear and nonlinear response of investigated composites as it was developed for the poled guest–host polymer systems [20].

Table 1. Average local fields (F) on COM of SiC in PMMA, PVK and PC matrix

System	F_x [GV/m]	F_y [GV/m]	F_z [GV/m]	F [GV/m]
PMMA/SiC	–0.34	–0.68	0.99	1.28
PVK/SiC	–0.18	–0.81	–0.93	1.25
PC/SiC	5.16	–4.44	11.98	13.78

4. Results and discussion

The MD resulting structure of SiC cluster can be characterized by its radial distribution function (RDF). The highest, considered distance between investigated groups is equal to the half of the unit cell length. The atomic RDFs of Si and C atoms at the end of MD simulations are presented in Fig. 2. The maximum of presented RDFs, for each investigated polymeric matrix, is located at 0.189 nm, corresponding to the nearest-neighbour distance in 3C–SiC structure. This peak describes Si–C bonds, and is related to a C–Si–C configuration. In the SiC solid crystal, the atoms are located in well-defined lattice-site equilibrium positions, around which they perform vibrations with relatively small amplitudes of motion with slight variation of interatomic distances. The second peak of the curves is centred at the distance of 0.378 nm, which is related to Si–C farthest neighbour distance. Computed RDFs of Si–C distances do not change with the variation of the polymeric matrix. Thus one can conclude that the geometry of 3C–SiC is very stable and average distances between Si and C atoms do not change during MD simulations performed at 300 K, which is very far from the

melting point of SiC. Internal Si–C structure of the investigated clusters is their intrinsic property and does not change under influence of considered polymeric matrices.

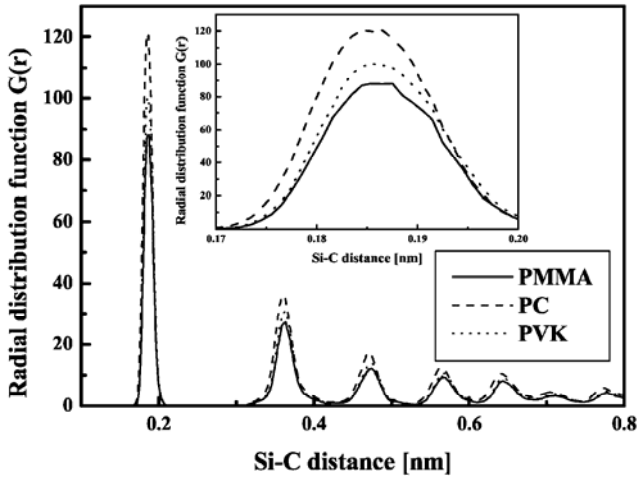

Fig. 2. Atomic radial distribution function $G(r)$ between the Si and C atoms of the 3C–SiC clusters embedded into PMMA, PVK and PC polymeric matrix

The principal goal of the investigation was not to simulate the structure of SiC but rather to determine their polymeric environment. Spatial distribution of the SiC clusters in polymeric matrix was investigated basing on intermolecular RDFs which were calculated between last Si-C surface atoms of SiC structure and determined groups of considered polymers. For the PMMA the COM of four groups were used, namely: methyl group bonded to the backbone carbon atom, methyl group bonded to COO, COO group and CH_2. The RDFs between SiC nanograin and PC polymer were calculated for the COM of four polymeric groups: both of two benzene rings, C-$(CH_3)_2$ group and C=O group. For the PVK also four groups were chosen, namely: COM of both of two benzene rings, COM of CH_2 group and the N atom. In order to show spatial distribution of the SiC nanograin in polymeric environment, only the nearest distances between the cluster and polymeric groups are drawn (Fig. 3). The presented RDF of the SiC–PMMA distance has been calculated for the methyl group bonded to COO. It is the nearest polymeric group to the SiC cluster with the distance equal to 0.4 nm. For the PC and PVK, as the RDF describing the nearest SiC–matrix distances, benzene rings and the carbazole group were taken, respectively. The SiC cluster situated in the PC matrix is located closer to the polymer than it was found for PMMA, the calculated distance being equal to 0.34 nm. A similar distance was found between the SiC cluster and PVK. The first RDF peak related to the SiC–PVK distance is very broad, which means that nanograins located closer to the polymer chain than 0.34 nm may be found. One can conclude that a free space around SiC cluster in the PVK matrix is the lowest as compared to PMMA and PC. All observed RDFs are typical of amorphous structures. No long-range order exists for considered systems but one can

see that the PC polymeric matrix with SiC nanoclusters is more ordered than the two other investigated systems. A free space around SiC clusters incorporated into PMMA matrix is the largest among all investigated matrices and has the same value as it was calculated for variety of organic chromophores [11].

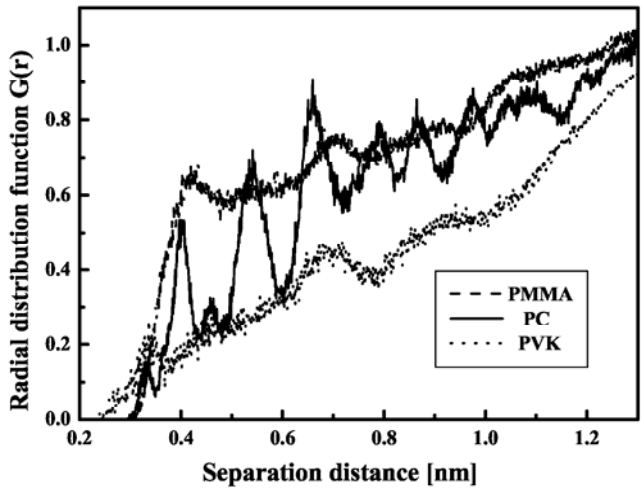

Fig. 3. The function of intermolecular radial distribution for the last Si–C surface atoms of SiC nanograins and the polymer chains

Rotation of the SiC nanorgains in PMMA is relatively easy as compared to the other systems. On the other hand, a free rotation motion of SiC is allowed in PMMA matrix, hence the relaxation of the aligned nanograins should be easy and fast.

Table 2. Molecular electric dipole moments μ, HOMO-LUMO energy splitting $\Delta E_{\text{HOMO-LUMO}}$, polarizability α and hyperpolarizability β of the SiC cluster calculated in vacuum and in a polymeric environment (λ = 633 nm; 1 au = 0.16487×10^{-40} $C^2\cdot m^2\cdot J^{-1}$ for α and 0.32066×10^{-52} $C^3\cdot m^3\cdot J^{-2}$ for β)

Molecule	μ [D]	$\Delta E_{\text{HOMO-LUMO}}$ [eV]	α_{av} [a.u.]	$\beta_{vec}(\omega;0,\omega)$ [a.u.]
SiC	5.86	3.40	2069.2	743.6
SiC in PMMA	17.54	3.30	2071.1	1951.5
SiC in PVK	9.19	3.26	2069.4	897.4
SiC in PC	69.82	1.31	2098.3	235400.0

In Table 2, electric properties of the isolated SiC clusters calculated by DFT method are presented. The obtained energy splitting $\Delta E_{\text{HOMO-LUMO}}$ value for the SiC isolated grain is in agreement with the work of Reboredo et al. [21] and is blue-shifted as compared to the bulk 3C–SiC because of small cluster size. The $\Delta E_{\text{HOMO-LUMO}}$ and μ values calculated for the SiC clusters located in polymeric matrix demonstrate that the environmental effect narrows the energy gap of the SiC clusters and increases the static dipole moment. The most important change was found for the SiC embedded into PC

matrix due to a high local electric field created by the polymer in the COM of the investigated cluster (see Table 1). Generally, each considered polymer matrix delocalizes charge density of the semiconducting cluster. One can conclude that all investigated polymers should be appropriate to use them like matrices keeping the SiC clusters.

Polarizabilities α and hyperpolarizabilities β related to the electrooptical effect of the SiC clusters were calculated using the Hartree-Fock and time-dependent DFT approaches at $\lambda = 0.633$ μm. The calculations are performed for the isolated molecule as well as for those embedded into polymeric matrix. Environmental effects are taken into account via the local field theory using the point-dipole approach and the obtained results are compared with the experimental data published earlier [1, 2]. The obtained polarizabilities α and hyperpolarizabilities $\beta(\omega;0,\omega)$ are presented in Table 2. Even taking into account the differences observed for the local field calculations, considering investigated systems (see Table 1), the environmental effect related to the linear optical properties can be neglected for all matrices. The average value α_{av} calculated in the respective local field is about 1% higher as compared with the polarizability calculated for the isolated molecule in any polymeric environment. One can see the tendency for the calculated local field to be parallel to the molecular dipole moment direction. The absolute field values obtained for the PMMA and PVK matrices are much lower than those calculated for the molecular crystals [22] but comparable with previously investigated other guest–PMMA systems [20]. The intermolecular SiC–PC interactions are many times higher than for the PMMA and PVK matrices.

The environmental effect is more distinct for the NLO properties that for the linear ones. All considered matrices increase the $\beta(\omega;0,\omega)$ value of the 3C–SiC clusters. The observed effect is the most distinct for SiC-PC system because of high local field in COM of cluster. The effect of the local field on the liner polarizability is negligible for all investigated systems but should be considered calculating NLO properties. In Figure 4, the experimentally obtained effective EO parameters r_e are presented for the 3C–SiC nano-sized grains embedded in polymeric matrices of various kinds (bars). The set-up used in the experiment is described in details in previous works [1, 2]. EO coefficients are obtained for the poled guest–host systems. These results are compared to the hiperpolarizability $\beta(\omega;0,\omega)$ related to the EO effect, computed within the local field approach. In practice, this comparison is not straightforward. The r_e parameter depends not only on the effective hiperpolarizability $\beta(\omega;0,\omega)$ of considered molecule but also on the unit cell volume, density of active molecules and the order parameters of the system. We compare only the tendency of changes of both investigated properties. One can conclude that the theoretically obtained data are in a good agreement with the experimental results. A very high value of the $\beta(\omega;0,\omega)$ obtained for the SiC–PC system can be practically decreased by the relatively difficult orientation of the SiC nanograins because of low free space around the chromophores. The order parameters obtained for the SiC–PVK system will probably decrease the EO molecular output signal.

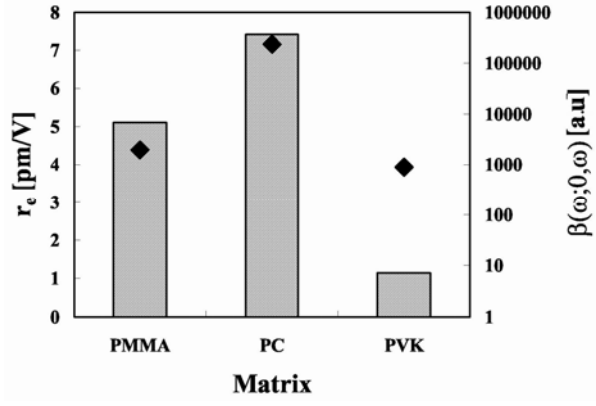

Fig. 4. Linear effective EO parameters r_e experimentally obtained for various kinds of polymeric matrices (bars) and hiperpolarizability $\beta(\omega;0,\omega)$ calculated via the local field theory (diamonds)

The EO properties of the considered systems can be confirmed by more detailed MD simulations of the electrically polled systems, however, the calculations of the macroscopic optical properties should be supplemented with the Lorentz field factor calculations. This approach can be combined with the permanent field effect on the surface-perturbed molecular response. It will be the subject of future work.

5. Conclusions

The EO properties of the composite materials were investigated by the MD study of the SiC–polymer structure. We attempted to describe the factors affecting microscopic molecular NLO properties of the SiC clusters embedded in PMMA, PVK and PC matrices.

The distance between SiC clusters and the polymer depends on the kind of polymer. By the study of the SiC–PMMA system and comparing the obtained results to the previously reported data one can conclude that the location of the chromophore in PMMA matrix is an intrinsic property of the polymer used and is not affected by the organic or inorganic dopants. Free space around SiC cluster in PVK matrix is the lowest as compared to the PMMA and PC. The alignment of the SiC nonograins in PVK is more difficult than in PC or PMMA matrix. Concerning the free space around 3C–SiC the SiC–PMMA system is not stable because of easy back relaxation of the chromophores. The Si–C distances do not change via the variation of the polymeric matrix. The geometry of 3C–SiC is very stable and does not change during MD simulations performed at 300 K.

The optical properties of the SiC clusters were calculated via the local field approach. The environmental effect on the molecular polarizability is not significant and may be neglected during the quantum-chemical calculations. The local field effect is

much more pronounced for the NLO properties of SiC and may not be omitted. The tendency of the $\beta(\omega;0,\omega)$ changes via the variety of polymeric matrices by the simple local field approach can be reproduced. All considered polymeric matrices increase the NLO properties of SiC nanosized crystals.

References

[1] BOUCLÉ J., KASSIBA A., KITYK I.V., HERLIN-BOIME N., SANETRA J., MAKOWSKA-JANUSIK M., REYNAUD C., Solid State Phenom., 94 (2003), 115.

[2] BOUCLÉ J., KASSIBA A., EMERY J., KITYK I.V., MAKOWSKA-JANUSIK M., SANETRA J., HERLIN-BOIME N., MAYNE M., Phys. Lett. A, 302 (2002), 196.

[3] KITYK I.V., MERVINSKII R.I., KASPERCZYK J., JOSSI S., Mater. Lett., 27 (1996), 233.

[4] MEWS A., KADAVANICH A.V., BANIN U., ALIVISATOS A.P., Phys. Rev. B, 53 (1996), 13242.

[5] KITYK I.V., MAKOWSKA-JANUSIK M., KASSIBA A., PLUCIŃSKI K.J., Optical Mater., 13 (2000), 449.

[6] *HyperChem® Computational Chemistry*, Publication HC50-00-03-00 October 1996, Hypercube, Inc.

[7] BERENDSEN H.J.C., VAN DER SPOEL D., VAN DRUNEN R., Comput. Phys. Comm., 91 (1995), 43; LINDAHL E., HESS B., VAN DER SPOEL D., J. Mol. Model., 7 (2001), 306; VAN DER SPOEL D., VAN BUUREN A.R., APOL E., TIELEMAN P.J., SIJBERS A.L.T.M., HESS B., FEENSTRA K.A., LINDAHL E., VAN DRUNEN R., BERENDSEN H.J.C., *GROMACS-User Manual*, Dept. Biophys. Chem., University of Groningen, the Netherlands, 2002.

[8] HOCKNEY R.W., GOEL S.P., J. Comp. Phys., 14 (1974), 148.

[9] HAGLER A. T., HULER E., LIFTON S., J. Am. Chem. Soc., 96 (1974), 5319; KITSON D.H., HAGLER A.T., Biochemistry, 27 (1988), 5246; DAUBER-OSGUTHORPE P., ROBERTS V.A., OSGUTHORPE D.J., WOLFF J., GENEST M., HAGLER A.T., Proteins: Struct. Funct. Genet., 4 (1988), 31.

[10] MIRGORODSKY A.P., SMIRNOV M.B., ABDELMOUNÎM E., MERLE T., QUINTARD P.E., Phys. Rev. B, 52 (1995), 3993.

[11] MAKOWSKA-JANUSIK M., REIS H., PAPADOPOULOS M.G., ECONOMOU I.G., ZACHAROPOULOS N., J. Phys. Chem. B, 108 (2004), 588.

[12] KIM W.-K., HAYDEN L. M. J. Chem. Phys., 111 (1999), 5212; LAU K.F., ALPER H.E., THACHER T.S., STOUCH T.R., J. Phys. Chem., 98 (1994), 8785.

[13] MA B., LII J. H., CHEN K., ALLINGER N.L., J. Am. Chem. Soc., 119 (1997), 2570.

[14] NOSE S., Mol. Phys., 52 (1984), 255; HOOVER W.G., Phys. Rev. A, 31 (1985), 1695.

[15] ESSMAN U., PERERA L., BERKOWITZ M. L., DARDEN T., LEE H., PEDERSEN L. G., J. Chem. Phys., 103 (1995), 8577; DARDEN T., YORK D., PEDERSEN L., J. Chem. Phys., 98 (1993), 10089.

[16] *Amsterdam Density Functional*; ADF2002.03 Ed.; Vrije Universiteit, Department of Theoretical Chemistry, Amsterdam, 2002; BAERENDS E.J., ELLIS D.E., ROS P., Chem. Phys., 2 (1973), 41; VELDE G.T., BICKELHAUPT F.M., BAERENDS E.J., GUERRA C.F., VAN GISBERGEN S.J.A., SNIJDERS J.G., ZIEGLER T.J., Comput. Chem., 22 (2001), 931.

[17] VAN GISBERGEN S.J.A., SNIJDERS J.G., BAERENDS E.J., Comput. Phys. Commun., 118 (1999), 119.

[18] SLATER J.C., Phys. Rev., 81 (1951), 385.

[19] VOSKO S.J., WILK L., NUSAIR M., Can. J. Phys., 58 (1980), 1200.

[20] REIS H., MAKOWSKA-JANUSIK M., PAPADOPOULOS M.G., J. Phys. Chem. B, 108 (2004), 8931.

[21] REBOREDO F.A., PIZZAGALLI L., GALLI G., Nano Letters, 4 (2004), 801.

[22] REIS H., PAPADOPOULOS M.G., MUNN R.W., J. Chem. Phys., 109 (1998), 6828.

Received 8 September 2005
Revised 4 November 2005

Materials Science-Poland, Vol. 24, No. 4, 2006

ESR study of spin dynamics in $(Er_{0.5}Y_{0.5})_2Cu_2O_5$ solid solutions

J. TYPEK[1*], N. GUSKOS[1, 2]

[1]Institute of Physics, Szczecin University of Technology, al. Piastów 17, 70-310 Szczecin, Poland

[2]Solid State Physics Section, Department of Physics, University of Athens, Panepistimiopolis, 15 784 Zografos, Athens, Greece

Powder samples of $(Er_{0.5}Y_{0.5})_2Cu_2O_5$ have been synthesized by a solid state reaction method. Electron spin resonance (ESR) measurements have been carried out on a Bruker E 500 X-band spectrometer in the 4–300 K temperature range. A single, almost Lorentzian-shaped resonance line has been recorded for the whole investigated temperature range and its ESR parameters (integrated intensity, linewidth and resonance field) displayed a strong temperature dependence. The integrated intensity of the resonance line showed a pronounced maximum in low-temperature range and vanished at the transition to the antiferromagnetic ordering at T_N = 11 K. The temperature at which the ESR integrated intensity reaches its maximum is different for the heating and cooling runs. Below 40 K, on approach to T_N, the linewidth exhibited a divergent behaviour due to the onset of three-dimensional magnetic order. At higher temperatures (about 220 K), variations in ESR magnetic susceptibility suggest the presence of dynamical processes in copper–oxygen chains leading to the formation of copper dimers. The observed changes of the ESR parameters are interpreted in terms of 2D magnetism of the copper–oxygen system in the $(Er_{0.5}Y_{0.5})_2Cu_2O_5$ solid solution.

Key words: *ESR; spin chains; copper complex*

1. Introduction

$(Er_{0.5}Y_{0.5})_2Cu_2O_5$ belongs to the family of $R_2Cu_2O_5$ compounds (R = rare earth ion smaller than Gd ion, i.e., Tb, Dy, Ho, Yb, Er, Tm, Yb, Lu, as well as Y, Sc, In) with the orthorhombic $Pna2_1$ space group symmetry [1–3]. The most characteristic feature of $R_2Cu_2O_5$ crystallographic structure is the presence of zigzag copper chains along the *a*-axis. A distorted square planar arrangement of four oxygen atoms around copper atom exists, with a fifth oxygen making a sort of pyramid. These copper–oxygen pyramids are joined at the common edges forming Cu_2O_8 dimers. The dimers, through

* Corresponding author; e-mail: typjan@ps.pl

the bridging oxygen, form an infinite zigzag Cu_2O_5 copper–oxygen chains. Furthermore, each copper ion is coupled to four other Cu ions along the *b*-axis forming *ab*-pseudoplanes. The rare earth ions are octahedrally coordinated and resulting distorted RO_6 octahedra are linked in a three-dimensional network occupying the space between copper–oxygen planes [3].

All $R_2Cu_2O_5$ compounds order antiferromagnetically at low temperatures, ranging from 11 K (Dy) to 30 K (In), and most of them exhibit metamagnetic behaviour below the Neel temperature [4]. The magnetic properties of $Y_2Cu_2O_5$ have been studied extensively [4–10]. Above 120 K, the magnetic susceptibility of this compound is well described by the Curie–Weiss law with a positive Curie temperature of $\theta = 38.5$ K, indicating a considerable contribution of ferromagnetic interaction [4]. At $T_N = 11.5$ K, a sharp maximum in the susceptibility gives a strong indication of an antiferromagnetic ordering. In the antiferromagnetic state two jumps in the $M(H)$ magnetization curve (with the external field H applied along *b*-axis) are observed, corresponding to two metamagnetic transitions [10]. The magnetic properties of $Er_2Cu_2O_5$ have been investigated previously [4, 5, 11–15]. The susceptibility follows the Curie–Weiss law exactly down to the transition temperature of $T_N = 27$ K, with a negative value of the Curie–Weiss temperature of $\Theta = -4$ K (antiferromagnetic interaction) [4]. The magnetic structure in an ordered state of $R_2Cu_2O_5$ could be viewed as consisting of ferromagnetic CuO layers parallel to the *ab*-plane coupled antiferromagnetically with the copper magnetic moments aligned along the *b*-axis. These copper pseudolayers are bracketed by two Er layers having their magnetic moment antiparallel to copper magnetic moments. This indicates that the superexchange Er^{3+}–Cu^{2+} is antiferromagnetic [13]. Despite a large experimental material gathered from magnetic susceptibility and neutron diffraction measurements, the nature of magnetic interactions in the $R_2Cu_2O_5$ family is still incomplete.

$(R_xR'_{1-x})_2Cu_2O_5$ solid solutions could be prepared by the solid state reaction technique. XRD, thermogravimetry and ESR at room temperatures have been used to study $(Er_xY_{1-x})_2Cu_2O_5$, $(Dy_xY_{1-x})_2Cu_2O_5$, and $(TbxY_{1-x})_2Cu_2O_5$ solid solutions [15–17]. Only the signal from copper(II) ions has been recorded by conventional X-band ESR spectroscopy. It was found that the relative ESR signal intensity varies with the magnetic rare earth ion concentration index x according to a simple power law function.

The aim of this work was to extend previously reported room-temperature ESR study of $(Er_{0.5}Y_{0.5})_2Cu_2O_5$ to the whole temperature range available (4–300 K) in order to gain insight into the dynamics of copper spin system. Special attention was paid to the behaviour of copper spin chains present in the $(Er_{0.5}Y_{0.5})_2Cu_2O_5$ structure in a low -temperature range, close to the transition to the antiferromagnetic phase.

2. Experimental

Ceramic sample of $(ErY)_2Cu_2O_5$ has been prepared by heating an appropriate stoichiometric amounts of metal oxides in air and was described elsewhere [15].

X-ray characterization showed that the sample is single phase with the following orthorhombic lattice parameters: a = 1.0878 nm, b = 0.3477 nm, c = 1.2446 nm. No significant traces of copper tetramers in this sample have been observed by ESR spectroscopy.

ESR variable temperature experiments were performed with a Bruker E 500 spectrometer operating at X-band microwave frequency equipped with TE102 cavity with 100 kHz field modulation. The investigated sample was in a form of loose powder and during the measurements it was placed in a quartz tube. The sample was cooled by flowing He gas and the temperature was controlled within about 1% by using a digital temperature controller. In this paper, the resonance magnetic field B_{res} is defined as the field where the applied magnetic field derivative of the resonance absorption line becomes zero. The effective g-value, g_{eff}, was also be used, defined by the relation $h\nu = g_{eff}\mu_B B_{res}$, where μ_B is the Bohr magneton, and ν the microwave frequency. Decomposition of the observed ESR spectrum on constituent components has been done using the SIMPOW computer program.

3. Results and discussion

ESR spectra of $(ErY)_2Cu_2O_5$ at selected temperatures in high and low-temperature ranges are presented in Figs. 1 and 2, respectively. At a specific temperature, the spectrum consists of a single, almost symmetrical, Lorentzian-shape line, whose ESR amplitude increases as the temperature is decreased. Also the linewidth broadens with temperature decrease, especially very quickly in the low-temperature range. At the lowest investigated temperatures, the ESR line is very broad, intense and asymmetrical. It was also noticed that the behaviour of the spectra depends on the thermal history of the sample, in particular whether the spectrum was recorded during cooling or heating runs. The spectra, although very broad and asymmetrical, were observed down to the temperature of the appearance of an antiferromagnetic state for this sample, i.e. 11 K. Comparing this value with the published results for $Y_2Cu_2O_5$ (T_N = 11.5 K) and for $Er_2Cu_2O_5$ (T_N = 27 K) it could be deduced that the ESR signal originated only from the copper ions located in the vicinity of non-magnetic Y^{3+} ions, and not from copper ions close to the magnetic Er^{3+} ions. This is consistent with the conclusion made previously that the presence of a magnetic ion effectively switches out the copper ions in its vicinity from taking part in formation of the ESR signal [15–17]. A closer inspection of the obtained ESR spectra suggests discussion of the temperature dependence of the ESR parameters separately in the low- (T < 50 K), intermediate- (50 < T < 175 K) and high- (T >175 K) temperature ranges.

In the low-temperature range, critical behaviour of the ESR parameters (linewidth, g-factor, integrated intensity) due to approaching to the antiferromagnetic phase tran-

sition, is expected. Figure 3 presents the temperature dependence of the effective peak-to-peak linewidth, ΔB_{eff} below 50 K.

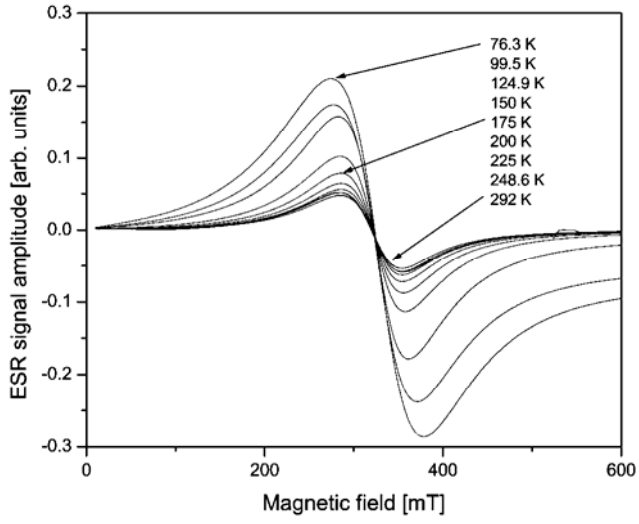

Fig. 1. ESR spectra of $(ErY)_2Cu_2O_5$ at selected temperatures in the high-temperature range ($T > 60$ K)

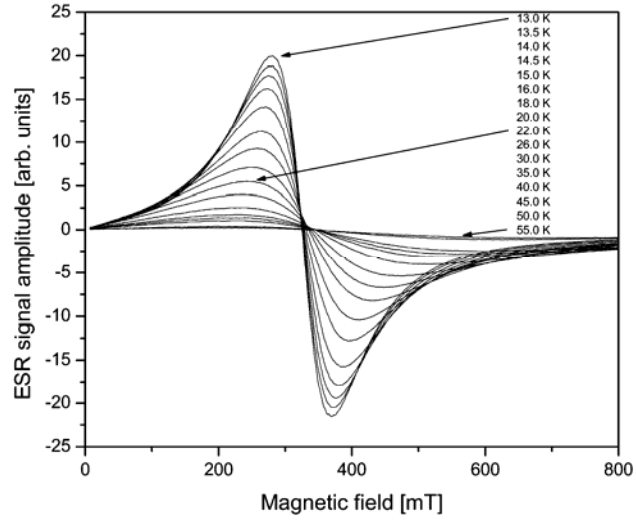

Fig. 2. ESR spectra of $(ErY)_2Cu_2O_5$ at selected temperatures in the low-temperature range (T<60 K)

A sharp increase in the linewidth with decreasing temperature is indicative of co-operative character of the magnetic ordering and can be explained by magnetic fluctuations in the vicinity of the transition temperature. It is reasonable to analyse this dependence in terms of the reduced temperature $(T - T_N)/T_N$, where T_N is the Neel

temperature at which the sample undergoes a long-range antiferromagnetic ordering. As the linewidth is expected to follow a power law dependence on reduced temperature, the experimental results have been fitted (Fig. 3) with the function

$$\Delta B_{\text{eff}} = \Delta B_0 + A\left(\frac{T - T_N}{T_N}\right)^{-p} \tag{1}$$

where ΔB_0 and A are temperature independent constants, and p is the critical exponent for the linewidth.

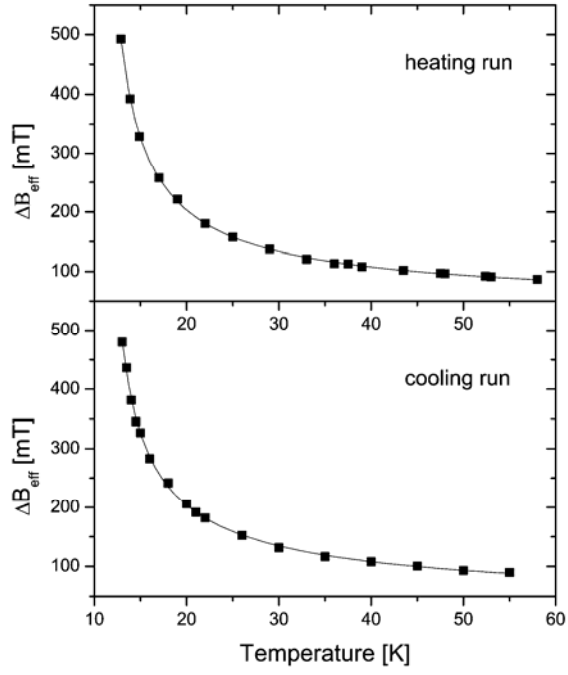

Fig. 3. Temperature dependences of the effective linewidth, ΔB_{eff}, in the low-temperature range for the cooling and heating runs. Experimental points (full squares) have been fitted with Eq. (1) (solid line)

Equation (1) describes a critical line broadening during the antiferromagnetic ordering in many 3D and non-ideal low-dimensional magnetic compounds. As the ESR spectrum of $(Er_{0.5}Y_{0.5})_2Cu_2O_5$ at a specific temperature suggested dependence on whether the measurement was done during the cooling or heating run, the fitting was done separately for these runs. The least-squares fitting gave the following values in Eq. 1: ΔB_0 = 26(15) mT, A = 162(10) mT, T_N = 10.7(4) K, and p = 0.68(9) for the cooling run; ΔB_0 = 39(5) mT, A = 158(2) mT, T_N = 10.2(2) K, and p = 0.78(4) for the heating run. Although different values were obtained for the Neel temperature and the critical exponent, the difference might be apparent resulting from the uncertainties

only. The calculated value of $p \approx 0.74$ reflects the low-dimensional character of the ESR line when it is compared with the critical behaviour of ΔB in typical 1D antiferromagnets, such as $CuCl_2 \cdot 2\,NC_5H_5$ ($p = 0.5$), $Sr_2V_3O_9$ ($p = 1$), or in the 3D case, such as GdB_6 ($p = 1.5$) [18]. Furthermore, it was shown that in the low-dimensional spin systems an essential broadening can occur in a rather broad temperature range of about $1.5T_N < T < 10T_N$.

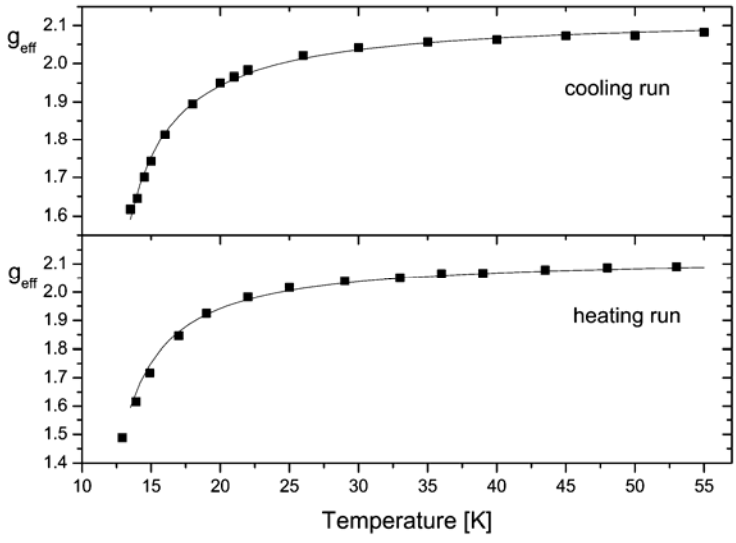

Fig. 4. Temperature dependences of the effective g-factor, g_{eff}, in the low-temperature range, for the cooling and heating runs. Experimental points (full squares) have been fitted with the function (2) (solid line)

Figure 4 presents temperature dependences of the effective g-factor, g_{eff}, below 50 K for cooling and heating runs. Because the resonance line shifts to a higher magnetic field with decreasing temperature, the the g-factor shifts to lower values, implying a rapid evolution of a short-range antiferromagnetic order. This negative deviation in g-value is predicted for a system dominated by spin symmetric exchange, when the magnetic field is applied parallel to the chain direction [19]. Many studies of the copper spin systems devoted to the thermal behaviour of the g-factor have found the shift that was proportional to reciprocal temperature, e.g. in single crystals of the copper salt of l-alanine amino acid $Cu[NH_2CHCH_3CO_2]_2$ [20]. The observed shift was explained by the polarization of the spin system induced by the external magnetic field when the temperature is lowered. Thus the thermal behaviour of g_{eff} in $(Er_{0.5}Y_{0.5})_2Cu_2O_5$ has been simulated with the following function

$$g(T) = g_0 - c\left(\frac{T - T_N}{T_N}\right)^{-q} \tag{2}$$

where g_0 and c are temperature-independent parameters, T_N is the Neel temperature, and q the critical exponent for the g-factor. The least-squares fitting produced satisfactory results and the following values of the parameters in Eq. (2) were obtained; for the heating run: $g_0 = 2.12(2)$, $c = 0.20(5)$, $T_N = 9.5(1.4)$ K, $q = 1.1(3)$; for the cooling run: $g_0 = 2.13(1)$, $c = 0.18(1)$, $T_N = 10.2(1.4)$ K, $q = 1.01(6)$. Also in this case both sets of parameters seem to be the same within experimental errors. The most important result of this fitting is that the value of the critical exponent for the g-factor is equal to unity, i.e., the factor is inversely proportional to temperature.

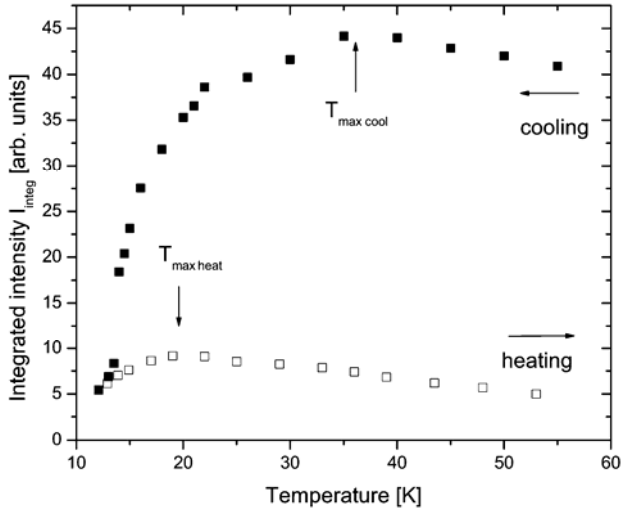

Fig. 5. Temperature dependences of the integrated intensity, I_{integ}, during the cooling (full squares) and heating (empty squares) runs in the low-temperature range

Another important ESR parameter is the integrated intensity, I_{integ}, defined as the area under the ESR absorption curve. In the paramagnetic regime, I_{integ} is proportional to the static susceptibility of spins participating in the resonance. Figure 5 presents the temperature dependences of I_{integ} in the low-temperature range for the cooling and heating runs. Clear maxima of I_{integ} is to be observed for both runs but at significantly different temperatures. During the cooling run, the maximum is reached at 36 K, while during the heating run much smaller values of I_{integ} are observed and the maximum is seen at 19 K. The appearance of maxima of the integrated intensity (and thus spin susceptibility) at temperatures different from T_N is a clear manifestation of a low-dimensional magnetic system. An empirical criterion for determination of the magnetic dimensionality is offered by the ratio T_N/T_{max}, where T_{max} is the temperature of the maximum susceptibility [21]. For 1D magnetic systems, $T_N/T_{max} < 0.1$, for 2D systems $0.25 < T_N/T_{max} < 0.5$, and $T_N/T_{max} > 0.9$ for 3D magnets. Applying this criterion to our spin system, it could be concluded that $(Er_{0.5}Y_{0.5})_2Cu_2O_5$ is a 2D magnetic system.

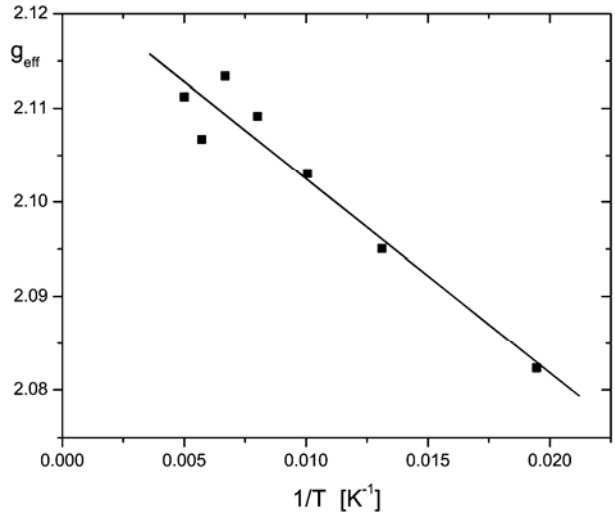

Fig. 6. Temperature dependence of the effective g-factor, g_{eff}, in the intermediate temperature range. The data are plotted as a function of inverse temperature to show the linear behaviour

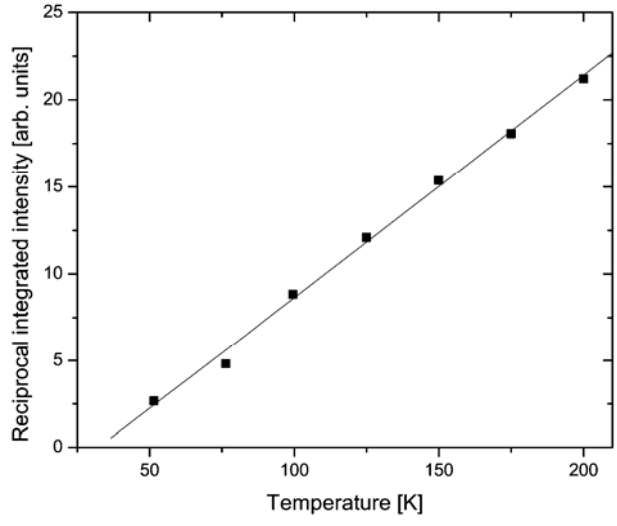

Fig. 7. Temperature dependence of the reciprocal integrated intensity in the intermediate temperature range

In the intermediate temperature range the (50 K < T < 200 K), the effective linewidth and g-factor follow the same temperature dependences as in the low-temperature range, i.e. Eqs. (1) and (2), respectively. Figure 6 demonstrates this for the temperature behaviour of the g-factor. There is a clear linear dependence between T^{-1} and g_{eff} also in this temperature range. The integrated intensity follows the Curie–Weiss law, $I_{integ} = C/(T - \Theta)$, where C and Θ are the Curie constant and Curie–Weiss

temperature, respectively. Least-squares fitting of the experimental data gave $\Theta = 32(2)$ K (Fig. 7). The positive sign of the Curie–Weiss temperature is an evidence for ferromagnetic interactions between copper paramagnetic centres.

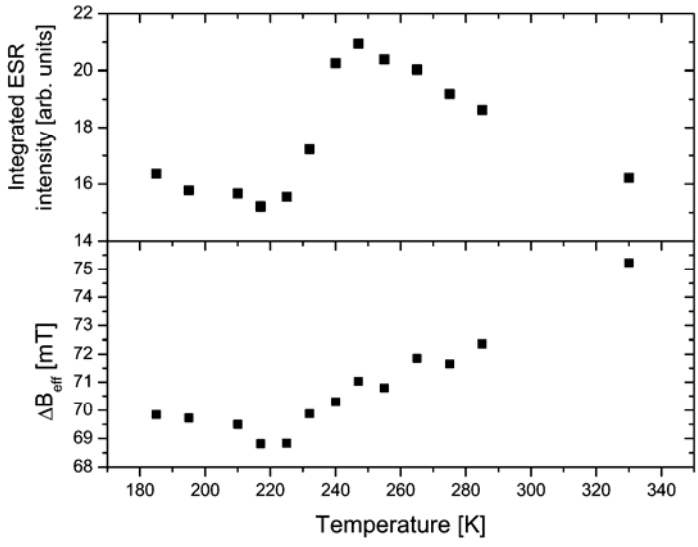

Fig. 8. Temperature dependence of the integrated intensity (upper panel) and effective linewidth (lower panel) in the high-temperature range

In the high-temperature range, an unexpected behaviour of the integrated intensity and linewidth is observed (Fig. 8). On the background of steady decrease of the integrated intensity extending from the intermediate temperature range, a rather abrupt increase above 220 K is seen (Fig. 8, upper panel). At the same temperature, the linewidth reverses its trend of decreasing with the temperature and begins to increase (Fig. 8, lower panel). I_{integ} reaches a local maximum at 245 K and continues to decline upon a further temperature increase. This local peak in thermal dependence of the integrated intensity could be connected with the presence of a small number of isolated copper dimers forming –Cu–Cu–O–Cu–Cu–O– spin chains. At high enough temperatures, $T > 400$ K, the spins are expected to behave as $S = 1/2$. When the short-range order develops in this compound as a result of decreasing T, a pair of two spins which antiferromagnetically couple is expected to behave as a spin with $S = 0$. The number of the pairs (each pair could be regarded as a singlet dimer) increases with decreasing T, what is producing decreases of the integrated intensity, as most dimers fall into nonmagnetic $S = 0$ ground state.

Below 220 K the dimers are not recorded by the ESR spectrometer. The increase of observed linewidth above the same temperature may be the result of existence of an additional relaxation channel (through dimer subsystem) in high temperatures.

ESR of powder samples provides only limited information about the investigated specimens due the availability of only averaged magnetic characteristics. Computer

simulation programs might help to resolve the observed powder spectrum into its anisotropic g_i-factors and ΔB_i components. We have used the SIMPOW program and were able to make the decomposition of spectra recorded at temperatures higher than 25 K. For lower temperatures, the spectra of $(Er_{0.5}Y_{0.5})_2Cu_2O_5$ were too anisotropic, probably due to the admixture of non-diagonal terms in dynamic susceptibility [22]. The result of decomposition is presented in Fig. 9. The upper panel presents temperature dependences of three ΔB_i linewidths, while the middle and lower panels – three g_i-factors. The middle panel displays the same g_i-factors, but on reduced scales to present small variations, not visible in the lower panel. As could be easily noticed, already at temperature as high as 175 K, the g_i-factors start to differ, although drastic differences are observed only below 30 K. Thus one can conclude that the local internal field, produced by local order of copper spins, develops at temperatures much higher than T_N. It is interesting to note the behaviour of g_i-factors close to T_N: the shift of g_x-factor, from the high-temperature value of 2.1 to low-temperature 1.6, is roughly twice as large as the shift of g_z to higher values (from 2.1 to 2.4).

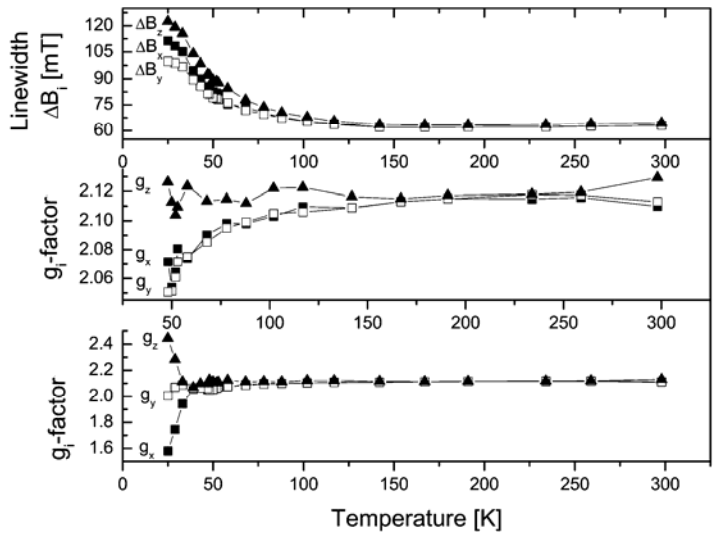

Fig. 9. Temperature dependences of three linewidths ΔB_i (upper panel) and g_i-factors (middle and lower panels) of the decomposed ESR spectrum. The middle panel presents only part of the lower panel graph, but in reduced g-factor scales

The theory of thermal shifts of g-factors in low-dimensional magnetic systems has been presented in Ref. 21. For an infinite 1D spin chain the fractional shift $\partial g(T)$ is

$$\partial g(T) = -\frac{C_1}{T}\left(1 - 3\cos^2\theta\right) \tag{3}$$

where θ is the angle between the applied field and the chain axis, C_1 is a constant depending on lattice parameters. The maximum shift is for $\theta = 0°$. It is reduced to a half

and changes its sign for $\theta = 90°$, while it vanishes for 'the magic angle' $\theta = 54.75°$. For a 2D square planar lattice one obtains

$$\partial g(T) = \frac{C_2}{T}\left(1 - 3\cos^2\theta\right) \tag{4}$$

where θ is the angle between the applied field B and the normal to the spin layer. A positive shift is expected whenever B is within the layer ($\theta = 90°$), doubling this value and changing sign for B along the normal to the layer. For 3D simple cubic lattice, no shifts are expected. Comparison of the shifts of the experimental g-factor in $(Er_{0.5}Y_{0.5})_2Cu_2O_5$ with theoretical predictions clearly indicates on the 2D magnetic case. Thus g_x plays a role of g-factor perpendicular the Cu ab-pseudoplanes, that is along c-axis.

4. Conclusions

ESR signals follow the magnetic activity of only the copper subsystems in $(Er_{0.5}Y_{0.5})_2Cu_2O_5$ solid solution. The transition to the antiferromagnetic state at $T_N = 11$ K is accompanied by a critical behaviour of the ESR parameters. Local ordering of magnetic spins starts already at 175 K. Part of copper ions are involved in dimer formation with the $S = 0$ ground state unobserved by the ESR method. In general, there is a strong spectroscopic evidence for the 2D magnetism in the investigated compound. Extension of the this type of study to other $(R'_xY_{1-x})_2Cu_2O_5$ solid solutions might clarify the remaining problems.

References

[1] BERGERHOFF G., KASPER H., Acta Crystallogr., B 24 (1968), 388.
[2] FREUD H.R., MULLER-BUSCHBAUM H., Z. Naturforsch., B 32 (1977), 609.
[3] GARCIA-MUNOZ J.L., RODRIQUEZ-CARVAJAL J., J. Solid State Chem., 86 (1990), 310.
[4] TROĆ R., KLAMUT J., BUKOWSKI Z., HORYŃ R., STĘPIEŃ-DAMM J., Physica B, 154 (1989), 189.
[5] KAZEI Z.A., KOLMAKOVA N.P., LEVITAN R.Z., MILL B.V., MOSHCHALKOV V.V., ORLOV V.N., SNEGIREV V.V., ZOUBKOVA JA., J. Magn. Magn. Mater., 86 (1990), 124.
[6] GARCIA-MUÑOZ J.L., RODRIGUEZ-CARVAJAL J., OBRADORS X., VALLET-REGI M., GONZALEZ CALBET J., GARCIA E., Phys. Lett., A 149 (1990), 319.
[7] HORYŃ R., KLAMUT J., WOŁCYRZ M., WOJAKOWSKI A., ZALESKI A.J., Physica B, 205 (1995), 51.
[8] BARAN M., LEVITIN R.Z., MILL B.V., SZYMCZAK R., Zh. Eksp. Teor. Fiz., 109 (1996), 961.
[9] SZYMCZAK R., SZYMCZAK H., BARAN M., LEVITIN R.Z., MILL B.V., J. Magn. Magn. Mater., 157–158 (1996), 667.
[10] MATSUOKA Y., NISHIMURA Y., MITSUDO S, NOJIRI H., KOMATSU H., MOTOKAWA M., KAKURAI K., NAKAJIMA K., KARASAWA Y., NIIMURA N., J. Magn. Magn. Mater., 177–181 (1998), 729.
[11] ZOUBKOVA YA., KAZEI Z.A., LEVITIN R.Z., MILL B.V., MOSHCHALKOV V.V., SNEIGIREV V.V., Pisma Zh. Exp. Teor. Fiz., 49 (1989), 524.

[12] PLAKHTII V.P., BONNE M., GOLOSOVSKI I.V., MILL B.V., RUDO E., FEDOROVA E.I., Pisma Zh. Exp. Teor. Fiz., 51 (1990), 637.
[13] GARCIA-MUÑOZ J.L., RODRIGUEZ-CARVAJAL J., OBRADORS X., VALLET-REGI M., GONZALEZ-CALBET J., PARRAS M., Phys. Rev. B, 44 (1991), 4716.
[14] SZYMCZAK R., SZYMCZAK H., BARAN M., LEVITIN R.Z., MILL B.V., J. Magn. Magn. Mater., 157–158 (1996), 667.
[15] TYPEK J., KOSTRZEWA J., SZYMCZYK A., GUSKOS N., Mol. Phys. Rep., 39 (2004) 233.
[16] TYPEK J., BUCHOWSKI D., GUSKOS N., SZYMCZYK A., WABIA M., Rad. Eff. Def. Solids, 158 (2003) 105.
[17] TYPEK J., KOSTRZEWA J., GUSKOS N., Mater. Sci.-Poland, 23 (2005), 929.
[18] IVANISHIN V.A., YUSHANKHAI V., SICHELSCHMIDT J., ZAKHAROV D.V., KAUL E.E., GEIBEL C., Phys. Rev. B, 68 (2003), 064404.
[19] NAGATA K., TAZUKE Y., J. Phys. Soc. Jpn., 32 (1972), 337.
[20] CALVO R., PASSEGGI M.C.G., Phys. Rev. B, 44 (1991), 5111.
[21] JACOBS I.S., BRAY J.W., HART H.R., INTERRANTE L.V., KASPAR J.S., WATKINS G.D., PROBER D.E., BONNER J.C., Phys. Rev. B, 14 (1976), 3036.
[22] BENNER H., BRODEHL M., SEITZ H., WIESE J., J. Phys. C: Solid State Phys., 16 (1983), 6011.

Received 9 September 2005
Revised 23 November 2005

Materials Science-Poland, Vol. 24, No. 4, 2006

Effect of crossed flux on flux pinning in YBCO superconductor

A. AMIRABADIZADEH[1*], S. K. HASANAIN[2]

[1] Department of Physics, Faculty of Science, University of Birjand, Birjand, Iran

[2] Department of Physics, Quaid-Azam-University, Islamabad, Pakistan

We have conducted magnetization experiments on melt-texture grown YBCO superconductor at 77 K. The magnetic anisotropy and its effects on flux pinning and remanence have been investigated using two pickup coil measuring systems. The remanence along the *c*-axis decreases as the field in the *ab*-plane increases, and the crossed flux magnetization curves merge with the uncrossed one. The decrease of the remanence and flux pinning along the *ab*-plane are discussed in terms of rotation and expulsion of flux, and the possibility of flux cutting.

Key words: *superconductivity; anisotropy of magnetization; flux pinning*

1. Introduction

High-T_c superconductors (HTS) represent an interesting group of substances for both theoretical and experimental investigations. Anisotropy is perhaps the most interesting aspect of the HTS. The layered crystal structure of HTS produces anisotropy in many of their physical properties, such as electrical resistivity, critical magnetic field and magnetization [1–3].

The magnetic properties of the Cu-O layered superconducting compounds are known to reflect the pronounced crystallographic asymmetry. As observed in $Y_1Ba_2Cu_3O_{7-x}$ crystals, not only are the lower and upper critical fields much larger and smaller, respectively, for external fields applied parallel rather than perpendicular to the *c*-axis, but the vortex pinning is also anisotropic, being stronger by far for the vortex line along *c*-axis [4].

The purpose of this study is to observe the effects of crossed remnant flux on the magnetization and hysteresis in a transverse direction using bulk-textured high-T_c material. The study carried out at 77 K, the temperature higher than that in Refs. [4]

* Corresponding author, e-mail: ahmadamirabadi@yahoo.com

and [5]. Thus we may expect drastic differences in the behaviour of crossed flux, due to the weakening of flux pinning and smaller elastic moduli of the vortex lattice at elevated temperatures [6, 7]. Using two coil arrangement, we monitor the changes in both the longitudinal ($M \parallel H$) components as the field is varied, and compare the hysteresis loops in the crossed and uncrossed conditions.

2. Experimental

The experiments were performed on a family of melt-textured-grown $Y_1Ba_2Cu_3O_{7-x}$ samples. The sample was prepared by the standard method [8] of very slow cooling (not faster than 2 $K \cdot h^{-1}$) through the paratactic temperature, after a partial melting at 1100 °C, for about 30–40 min. After oxygen annealing at 600 °C for 48 h, the sample was cut out in a suitable size, typically $1 \times 4 \times 4$ mm^3. The texturing was checked by SEM and XRD. Large, clear grain growth was visible. The sample had a zero-resistance temperature close to 89 K and a sharp diamagnetic transition between 90 and 89 K. All dc magnetization measurements were made at 77 K using a commercial vibrating sample magnometer (VSM). While the longitudinal moment (M_x) was measured with the commercially obtained set of pickup coils, the transverse moment (M_y) was measured with a self-wound set of coils, designed according to Ref. [9]. Each component was measured using a separate lock-in amplifier. The sample vibration was along the z direction, while the field applied along the x direction. By rotating the sample around the z-axis, the c or ab direction can be made parallel to the applied field. The rotational head of the VSM allowed a 1° resolution of orientation. The sample was field cooled at a particular angle Φ with respect to the c-axis in field cooling condition (FC) and also the sample was cooled down at zero field (ZF). The details of the experimental procedure are brought in Chap. 3 for better understanding.

3. Results and discussion

The following chapter is divided into two parts. Section 3.1 describes basic anisotropy effects characterizing the sample, Section 3.2 discusses the effect of a crossed remnant flux on hysteresis curves.

3.1. Anisotropy effects of the sample

The magnetization of HTS is well known to be anisotropic. The effect of this anisotropy can be observed in melt textured sample with well defined directionality of the grains. To quantify the anisotropy, we define the anisotropy ratio as $M^c_{\mathrm{rem}}/M^{ab}_{\mathrm{rem}}$, where M^c_{rem} is the value of remnant magnetization for a field applied (and later re-

moved) along the *c*-axis and M_{rem}^{ab} is the remnant magnetization for the field along the *ab*-plane. The procedure of determining this ratio was as follows. First, the sample was cooled down to 77 K in zero field (ZF) conditions, then the external field along the *c*-axis was raised to about 4 kOe and then cycled to zero and the remnant magnetization (i.e., the magnetization which is present when $H \to 0$) along this axis was measured. The same procedure was repeated for the *ab*-plane. ure 1 shows the $M(H)$ loops along these respective directions, where curve (a) refers to the *c*-axis and curve (b) to the *ab*-plane. To obtain the anisotropy ratio we divided the value of M_{rem}^{c} at the point A by the value of M_{rem}^{ab} at the point B when $H = 0$. We obtain the anisotropy ratio of about 3.6, while a number close to 4 is reported by Song et al. [10]. The value of 3.6 indicates that our sample is characterized by a high anisotropy of structure and magnetization M_{rem}.

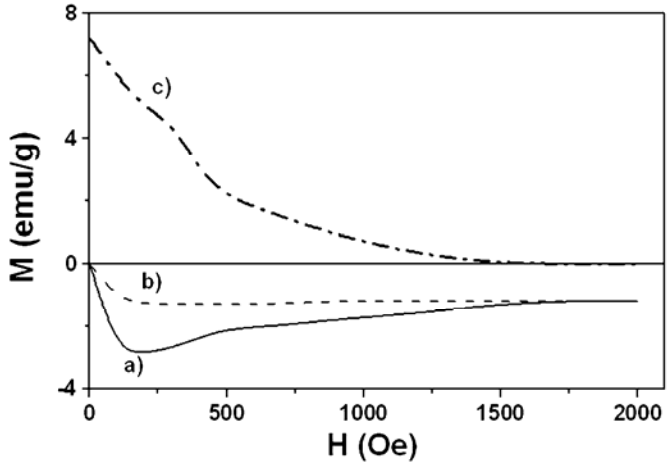

Fig. 1. M(H) loops of $YBa_2Cu_3O_{7-x}$ at T = 77 K in zero field cooling condition: a) along *c*-axis, b) along *ab*-plane

Flux trapping can also show anisotropy of the sample. In order to study the effect of anisotropy on flux trapping, we carried out the following experiment. The sample was cooled down to a low temperature (77 K) in an FC condition for field applied parallel to the *c*-axis ($\Phi = 0$) and for field applied perpendicular to the *c*-axis (parallel to *ab*-plane), $\Phi = 90°$. Then the field was turned off and M_{rem} was recorded. In Figure 2, we have plotted M_{rem}^{c} ($\Phi = 0$) and M_{rem}^{ab} ($\Phi = 90°$) at 77 K as a function of the applied cooling field.

We see that M_{rem}^{c} and M_{rem}^{ab} increase with the increasing magnetic field until the saturation level is reached. This occurs at the field H_c^{sat} of about 400 Oe for $\Phi = 0$ and H_{ab}^{sat} 200 Oe for $\Phi = 90°$, i.e. the remanence for $H \parallel c$ attains the maximum value at the field higher than for $H \perp c$. This has been reported by Song et al. [10] on the

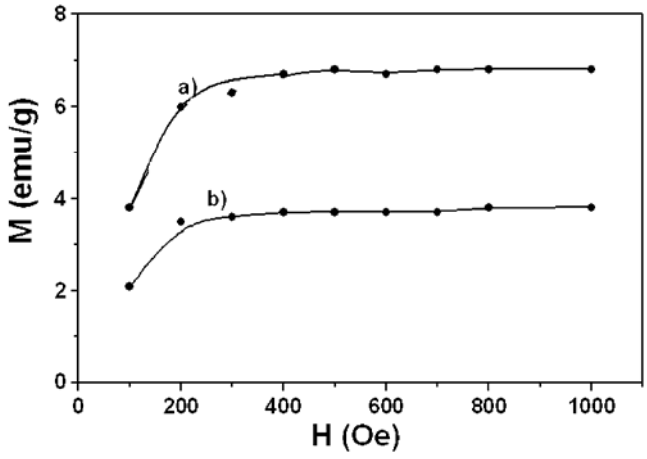

Fig. 2. Remnant moment against cooling field H_{FC} for the field along: a) the *c*-axis (M^{c}_{rem}), b) along the *ab*-plane (M^{ab}_{rem})

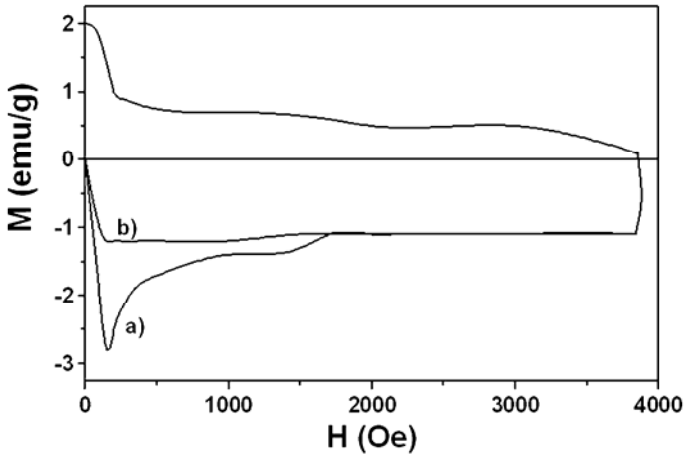

Fig. 3. *M*(*H*) loops along the *ab*-plane: a) single flux state, b) two flux state for $\Phi = 0$, $H_{FC} = 1$ kOe and $T = 77$ K (see the text for details)

single crystal sample. We can explain this behaviour as follows. Figure 2 clearly shows the anisotropy of flux trapping and the difference between the pinning strengths in the two different directions. Note that M_c saturates at 6.8 emu/g and M_{ab} at 3.5 emu/g, i.e. $M_c^{\mathrm{sat}}/M_{ab}^{\mathrm{sat}} = 1.9$. This behaviour has been attributed to the anisotropic nature of H_{c1} (lower critical field). The point of deviation from linearity of *M*(*H*) loop, H_{c1} is almost 80 Oe for *H* parallel to the *c*-axis and is approximately 35 Oe for *H* perpendicular to the *c*-axis (parallel to the *ab*-plane) [10]. Thus $H^{c}_{c1}/H^{ab}_{c1} = 2.3$. At the same time we note that the ratio of saturation field for remnant magnetizations ($H_c^{\mathrm{sat}}/H_{ab}^{\mathrm{sat}}$) is equal to 2.

3.2. Crossed flux conditions

We show first the effect of the crossed flux on the magnetization loops. The procedure for making these experiments was as follows. The sample was cooled down to low temperature in the field H_{FC} = 1 KOe along the *c*-axis, then the field was turned off, the sample was rotated by θ = 90° and the $M(H)$ loop was taken along the *ab*-plane (Fig. 3b). Figure 3a shows the corresponding $M(H)$ loop taken without crossed flux (i.e., the sample cooled down to low temperature in a zero field and then the field cycled along the *ab*-plane without remnant flux along the *c*-axis). It is apparent that the magnetization in the *ab*-plane shows a higher flux penetration in Fig. 3b. M_{ab} at the cusp is less than half the value for the curve in Fig. 3b. The initial slope of the loop (b) is also significantly lower than of loop (a), depicting the case of flux entry in the former case. For low fields (H < 1.5 kOe), the total width of loop (b) is less than the width at corresponding field values in the single flux loop (a). It is quite evident that in the crossed flux mode large amount of the flux penetration reduces the shielding currents (leading to lower diamagnetic signal). Furthermore, the flatness of the curve after the cusp indicates that higher initial flux penetration leads to slowing down of subsequent flux entry as the field along the *ab*-direction is increased. The points of merger of the curves (a) and (b) are found to depend on the cooling field, e.g. for a lower field H_{FC} = 400 Oe the curves merge at about 800 Oe, while for H_{FC} = 200 Oe they merge at about 600 Oe (not shown here). Clearly, the higher the cooling field and the remanence along the *c*-axis, the greater the persistence of the effect on the *ab*-plane moment.

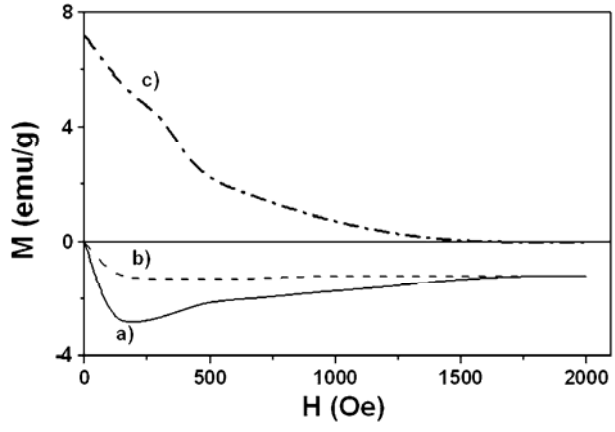

Fig. 4. Simultaneous measurement of two components (M_x and M_y) vs. applied field: a) M_x (single flux state) along the *x*-direction (*ab*-plane), b) M_x (two flux condition) along the *x*-direction (*ab*-plane), c) M_y (two flux condition) along the *y*-direction (*c*-axis), H_{FC} = 1 kOe and T = 77 K

Similarly we recorded $M(H)$ loops for the Φ = 90° case, i.e. the hysteresis of the *c*-axis moment in the presence of remnant flux along the *ab*-plane. The effects in this

case are much weaker, as expected for a much smaller remanence of the *ab*-plane moment, particularly after turning on the field along the *c*-axis.

A question related to the above experiments remains unanswered: what happens to the remnant flux when we turn on the transverse field. In order find the answer, we carried out other set of experiments. The procedure was identical to that of the previous one: after rotating the sample, the $M_x(H)$ loops as well as the variation of the remnant moment on Y-coil were recorded in this experiment, M_x corresponds to the moment along the applied field direction while M_y is the remanence now rotated perpendicular to the *x*-direction. Figure 4 shows this variation when the field is applied along the *ab*-plane at a very slow rate. We can see that the remanences along the *c*-axis decrease with increasing H and become zero at about the merge point of two $M(H)$ loops along the *x*-direction. Thus it is clear ($\Phi = 0$ case) that the differences in the loops persist as long as $M_y \neq 0$, and that the application of H (along the *x*-direction) decreases M_{rem} continuously. The data however does not clarify what is the cause of decreasing of M_{rem}. This is addressed in the next section.

4. Conclusion

We have shown that in the higher temperature region in which we have worked, the effect of the crossed flux is to reduce shielding currents and enhance depinning effects. This is in contrast to the data of Park et al. [4] where the *c*-axis remanence stabilized the *ab*-plane flux. There are two possible causes for such effects:

1. Mutual repulsion between vortices called *depinning torque* acts on one magnetization M_1 trying to align it along the field due to the other one. In this rotation (caused by the torque), the vortices M_1 may get deppined and be expelled leading to lowering of remanence as observed.

2. The other process, so-called the flux cutting process, takes place when flux families at some mutual angles are made to traverse each other. This results in cutting of a part of one vortex and joining up with a part of the other one. The cut vortices are freed, being able to be expelled and depinned. In our case this may also be a significant source of reduction of pinning, due to a crossed flux.

The results of our experiments at this stage cannot unambiguously indicate which of the two effects is active or predominant. To identify the process unambiguously, a careful examination of temperature and field dependences of the effects is required, or a helical field setup should be used.

References

[1] CRABTREE G.W., LIU J.Z., UMEZAWA A., KWOK W.K., SAWERES G H., MALTK S.K., VEAL B.W., LAM D J., BRODSKY M.B., DO J.W., Phys. Rev. B., 36 (1987), 4021.

[2] DAEMEN L.L., CAMPELL L.J., Phys. Rev. Lett., 70 (1993), 29448.

[3] DINGER T.R., WORTHINGTON T.K., GALLAGHER W.J., SANDSTROM R.L., Phys. Rev. Lett., 58 (1987), 2687.

[4] PARK S.J., KOUVEL J.S., Phys. Rev. B., 48 (1993), 2687.
[5] PARK S.J., KOUVEL J.S., RADOUSKY H.B., LIN J.Z., Phys. Rev. B., 48 (1993), 133998.
[6] BRANDT E.H., Int. J. Mod. Phys. B., 5 (1991), 751.
[7] ULLAMAIER H., *Irreversible properties of type II superconductors*, Springer-Verlag, Berlin, 1975.
[8] SALAMA K., SELVAMANICKAM V., GAO L., SUN K., Appl. Phys. Lett., 54 (1989), 2354.
[9] MALLINSON J., J. Appl. Phys., 37 (1966), 2514.
[10] SONG Y., CHARLS B., HELELEY E., MISRA A., GAINES R., Phys. Lett. A., 173 (1993), 489.

Received 9 September 2005
Revised 3 November 2005

Materials Science-Poland, Vol. 24, No. 4, 2006

Computer simulation of Poisson's ratio of soft polydisperse discs at zero temperature

J. NAROJCZYK, K. W. WOJCIECHOWSKI*

Institute of Molecular Physics, Polish Academy of Sciences,
ul. M. Smoluchowskiego 17, 60-179 Poznań, Poland

A simple algorithm is proposed to study structural and elastic properties of matter in the presence of structural disorder at zero temperature. The algorithm is used to determine the properties of the polydisperse soft disc system. It is shown that Poisson's ratio of the system essentially depends on the size polydispersity parameter; larger polydispersity implies larger Poisson's ratio. In the presence of any size polydispersity, Poisson's ratio increases also when the interactions between the particles tend to the hard potential.

Key words: *Poisson's ratio; polydispersity; elastic constant; inverse-power potential; soft matter*

1. Introduction

It is expected that future "intelligent materials" will combine various unusual properties, e.g. unusual electromagnetic properties with unusual elastic properties. Although the elasticity has been the field of human investigation since the ancient times, many problems interesting from both the point of view of basic research and possible applications remain unsolved. One of such problems is the influence of various forms of disorder on the microscopic level on the elastic properties of matter.

In the present note, we concentrate on studies of one of the forms of disorder – the size polydispersity. The question we pose is: How the elastic properties of a system are modified when instead of consistingd of identical particles it is formed of particles having some distribution of sizes? Polydisperse systems have recently been intensively studied because of their role in various fields of science and technology [1, 2]. In contrast to the phase diagram and structure, however, their elastic properties remain an open field.

*Corresponding author, e-mail: kww@man.poznan.pl

The subject of our study is a two-dimensional polydisperse model system at zero temperature. The simulations done here were meant to provide additional data to the work described in [3] in which the investigations were carried out at positive temperatures. We concentrate on studies of Poisson's ratio [4] directly describing the deformation of materials under loading/unloading stress. The latter subject is related to increasing interest in so-called auxetic materials, i.e. systems showing negative Poisson's ratio [5–9]. Studies of influence of various mechanisms on Poisson's ratio can help in searching for or manufacturing real materials of this unusual property.

The paper in organized as follows. In Sec. 2, the studied model is described. In section 3, some theoretical background is reminded. In section 4, the chosen method of simulations is sketched. In section 5, the results are presented. Conclusions are drawn in section 6.

2. The system studied

The system under study, shown in Fig. 1 and further referred to as the polydisperse soft disc system, consists of soft particles which interact only with their nearest neighbours through the interaction potential of the form

$$u_{ij}(r_{ij}) = \left(\frac{d_i + d_j}{2r_{ij}} \right)^n \tag{1}$$

where d_i and d_j are the diameters of the interacting particles. The values of the diameters were generated [10] according to the Gauss distribution function with the fixed size polydispersity parameter δ, defined as

$$\delta = \frac{\left(\langle d^2 \rangle - \langle d \rangle^2 \right)^{1/2}}{\langle d \rangle} \tag{2}$$

It can be seen in Figure 1, that the soft discs form a nearly hexagonal lattice for which the elastic properties are isotropic for small deformations [4]. It is worth to stress that when the exponent n tends to infinity, the above system tends to the static (i.e., zero temperature), polydisperse, hard disc system, studied in [3] at positive temperatures.

Our aim was to determine the dependence of the elastic constants and Poisson's ratio of a given structure on the amount of disorder introduced into the system; the disorder was quantified by the parameter δ. The data which will be shown below were obtained by computer simulation. Although the polydisperse soft disc system is very simple, it includes two main features of various real systems: repulsive forces at high densities and a certain distribution of sizes of the interacting bodies. Hence, one can

expect that it will supply some (qualitative, at least) information on the behaviour of more complex, real systems.

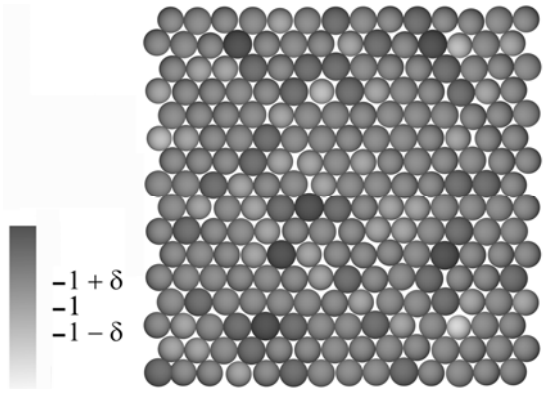

Fig. 1. Typical configuration of the studied system for $N = 224$ particles; δ is the polydispersity parameter. Discs of different sizes are represented by different intensities of greyness

3. Theoretical analysis

As the studied system is isotropic in terms of its elastic properties, it can be described by only two elastic constants [4]: the bulk modulus, B, and the shear modulus, μ. The elastic constants B and μ characterize the resistance of material against the changes of the volume and the shape, respectively. Both mentioned values must be positive in the range of the mechanical stability of the system.

The free energy of the deformed two-dimensional (2D) crystal exhibiting a 6-fold symmetry axis can be written as a function of the strain tensor components and the elastic constants [4]:

$$F = -p\left(\varepsilon_{xx} + \varepsilon_{yy}\right) + 2\lambda_{\xi\eta\xi\eta}\left(\varepsilon_{xx} + \varepsilon_{yy}\right)^2 + \lambda_{\xi\xi\eta\eta}\left[\left(\varepsilon_{xx} - \varepsilon_{yy}\right)^2 + 4\varepsilon_{xy}^2\right] \tag{3}$$

The values of the elastic constants and pressure can be obtained by differentiation of the free energy with respect to the strain tensor components, see e.g. [11]:

$$\begin{aligned} \left.\frac{\partial F}{\partial \varepsilon_{xx}}\right|_{\varepsilon=0} &= p \\ \left.\frac{\partial^2 F}{\partial \varepsilon_{xx}^2}\right|_{\varepsilon=0} &= 4\lambda_{\xi\eta\xi\eta} + 2\lambda_{\xi\xi\eta\eta} \\ \left.\frac{\partial^2 F}{\partial \varepsilon_{xx}\partial \varepsilon_{yy}}\right|_{\varepsilon=o} &= 4\lambda_{\xi\eta\xi\eta} - 2\lambda_{\xi\xi\eta\eta} \end{aligned} \tag{4}$$

The bulk modulus, B, and the shear modulus, μ, can be easily related [12] to the quantities used in Eq. (3):

$$B = 4\lambda_{\xi\eta\xi\eta}, \qquad \mu = 2\lambda_{\xi\xi\eta\eta} - p \tag{5}$$

Poisson's ratio ν for an isotropic 2D system can be expressed by the elastic moduli as follows [12]:

$$\nu = \frac{B - \mu}{B + \mu} \tag{6}$$

In the case of the discs of equal diameters ($\delta = 0$), one can obtain analytical formulae for the elastic constants:

$$p_0 = n\sqrt{3}a^{-n-2}, \qquad B_0 = \left(\frac{n}{2} + 1\right)p_0, \qquad \mu_0 = \left(\frac{n}{4} - \frac{1}{2}\right)p_0, \qquad \nu_0 = \frac{n+6}{3n+2} \tag{7}$$

where n is the power of the potential and a is the distance between the centres of particles.

4. The method of simulation

The elastic properties with respect to the degree of polydispersity [3] were studied. For each of more than 1000 different structures the reference state of minimal energy was found. Then the deformation and the "measurement" took place.

Simulations were based on the algorithm searching for a configuration of minimum energy for a given shape of the system. The model was enclosed in periodic boundary conditions. Its total energy was a sum of the interactions of the form (1) between the nearest-neighbouring particles (i.e., those whose Dirichlet polygons have a common side). In search for the minimum energy states, the program conducted a series of translational moves of particles; only those decreasing the energy of the system were accepted. The particles were moved in the direction of the total force acting on them by an arbitrary vector $d\mathbf{r}_i$. After acceptance/rejection of each move, the vector was modified with respect to the change of the total energy of the system: if the move led to increase/decrease of the energy $d\mathbf{r}_i$ was decreased/increased, respectively. The particles were moved one-by-one in the order they were placed in the lattice. Enumeration of the particles was arbitrary and was checked to have no influence on the application of the algorithm and its results. To avoid trapping the system into a local minimum, some "'shaking" (random changes of the particle positions) was introduced. Each particle was randomly displaced by a vector $d\mathbf{r}_{\mathrm{rand}}$ of a random length and orientation, generated within a defined range of values. The program moved all the particles of the system as long as the system energy was no longer changing within the given accuracy.

After calculating the energy of the system at equilibrium (equal to its free energy at zero temperature) the shape of the system was deformed by strains for which the minimum energy configurations of particles were searched for. Then a numerical differentiation of the energy with respect to the deformations was used to determine the

values of elastic constants B and μ from which Poisson's ratio of the system was obtained. The precise description of the algorithm will be given elsewhere.

5. Results

The figures presented below summarize the results of simulation. It can be seen that for large values of the exponent n, the elastic properties of the system strongly depend on its polydispersity.

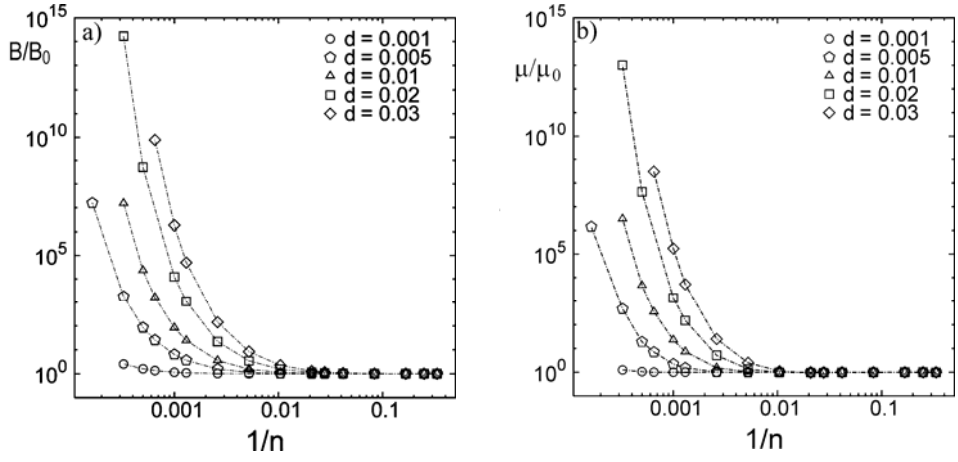

Fig. 2. The dependence of: a) the bulk modulus B, b) the shear modulus μ, on the inverse of the exponent n. The dotted lines are presented to guide the eye

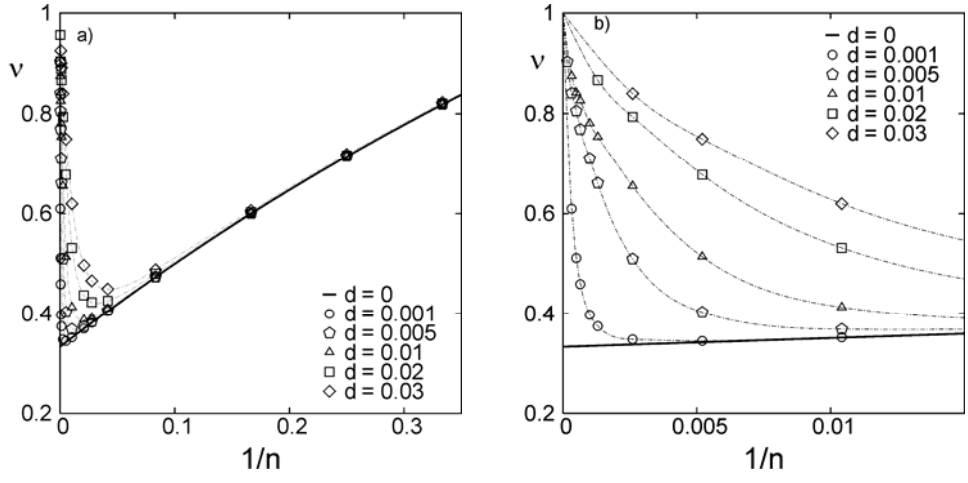

Fig. 3. The value of Poisson's ratio against the inverse of the exponent n for two-dimensional soft discs with different values of the polydispersity parameter: a) $n \geq 3$, b) $n \geq 96$. The thick solid line shows the exact result for $\delta = 0$, see Eq. (7). The dotted lines are presented to guide the eye

In particular, it can be seen in Fig. 2 that when $n \to \infty$, both B and μ grow rapidly with respect to the values obtained for the systems composed of identical particles. By increasing the polydispersity of the system, its Poisson's ratio grows with respect to the periodic system of discs with identical diameters (Fig. 3). When $n \to \infty$, then for any non-zero polydispersity, Poisson's ratio tends to its maximum value possible for a two-dimensional isotropic system equal 1. The elastic properties of the polydisperse soft disc system at zero temperature are in very good agreement with the Monte Carlo simulations of this system at positive temperatures, when the temperature tends to zero [13].

6. Conclusions

A simple and efficient algorithm to study static structures of polydisperse soft particles has been proposed. It was shown that the static disorder studied (the lack of periodicity of the particle positions caused by unequal sizes of the particles) has an essential influence on the value of Poisson's ratio. Typically, for positive values of the polydispersity parameter, the bulk modulus B, the shear modulus μ, and Poisson's ratio v, increase with increasing n when potentials become strongly repulsive, i.e. when the exponent n is large, which corresponds to the hard particle limit. These quantities increase also with increasing polydispersity parameter δ, in the same limit of large values of n.

The results obtained in this work show an excellent agreement with recent results obtained by the Monte Carlo simulations of the soft polydisperse discs at the low temperature limit [3], which, in turn, agree very well with the results obtained for hard polydisperse discs [13] in the limit of high temperatures and large n. This confirms the hypothesis that the elastic properties of hard-body systems can be obtained by studying soft-body systems and taking the $n \to \infty$ limit. We plan to apply the method to three-dimensional systems of isotropic and anisotropic particles recently studied at positive temperatures. We expect that studies of very simple models, as the one described in the present paper, will help in understanding and predicting behaviour of real systems. It is interesting to check to what extent such simple models approximate the properties of some real systems like those described in [14].

Acknowledgements

This work was supported by the Polish Committee for Scientific Research (grant No. 4T11F01023) and by the Center of Excellence for Magnetic and Molecular Materials for Future Electronics within the European Commission contract No. G5MA-CT-2002-04049. The simulations were performed at the Poznań Supercomputing and Networking Centre.

References

[1] SOLLICH P.J., J. Phys.: Condens. Matter, 14 (2002), R79.
[2] XU H., BAUS M.J., J. Chem. Phys., 118 (2003), 5045.

[3] TRETIAKOV K.V., WOJCIECHOWSKI K.W., Phys. Status Sol. B, 242 (2005), 730.
[4] LANDAU L.D., LIFSHITS E.M., *Theory of Elasticity*, Pergamon Press, London, 1986.
[5] LAKES R.S., Science, 235 (1987), 1038; ibid 238 (1987), 551 .
[6] WOJCIECHOWSKI K.W., Phys. Lett., A 137 (1989), 60.
[7] EVANS K.E., ALDERSON A., Adv. Mater., 12 (2000), 617.
[8] WOJCIECHOWSKI K.W., *Monte Carlo simulations of model particles forming phases of negative Poisson's ratio*, [in:] *Properties and Applications of Nanocrystalline Alloys from Amorphous Precursors*, B.Idzikowski, P. Svec, M. Miglierini (Eds.), Kluwer, Dordrecht, 2005, 241–252.
[9] WOJCIECHOWSKI K.W., ALDERSON K.L., BRAŃKA A.C., ALDERSON K.L., Phys. Status Sol., B 242 (2005), 497; http://www.ifmpan.poznan.pl/zp10/auxet2/main.html.
[10] PRESS W.H., TEUKOLSKY S.A., VETTERLING T.W., FLANNERY B.P., *Numerical Recipes in FORTRAN*, 2nd Ed., Cambridge University Press, Cambridge, 1992.
[11] WOJCIECHOWSKI K.W., TRETIAKOV K.V., KOWALIK M., Phys. Rev. E, 67 (2003), 0361211.
[12] WOJCIECHOWSKI K.W., J. Phys. A: Math. Gen., 36 (2003), 11765.
[13] TRETIAKOV K. V., WOJCIECHOWSKI K. W., Phys. Rev. E, unpublished.
[14] VAN BLAADEREN A., MRS Bulletin, 29, (2004), 85.

Received 15 September 2005
Revised 30 November 2005

Materials Science-Poland, Vol. 24, No. 4, 2006

Sb-contained thin films Structural and electric properties

V. I. BILOZERTSEVA[1], H. M. KHLYAP[2*], P. S. SHKUMBATYUK[2], N. L. DYAKONENKO[1], S. S. KRIVONOS[1]

[1]National Technical University Kharkiv Polytechnical Institute, 21 Frunze str., Kharkiv 61002, Ukraine

[2]University of Technology, 56 Erwin-Schroedinger str., D-67663 Kaiserslautern, Germany
State Pedagogical University, 24 Franko str., 82100, Drohobych, Ukraine

First results of experimental study of the structure of Sb_2Se_3 and $NaSbSe_2$ thin films by means of transmission electron microscopy and electron diffraction methods are reported. Structural and morphological peculiarities of crystal growth in films are discussed. Some electrical properties, in particular, current–voltage characteristics in metal–semiconductor (MS) structures: In/Sb_2Se_3 and In/$NaSbSe_2$, are presented.

Key words*: chalcogenide semiconductor; thin film; structure; current–voltage characteristics*

1. Introduction

Investigations of multicomponent semiconductor compounds allow one to expand possibilities of their practical applications in modern microelectronics and photonics [1–5]. In amorphous films of multicomponent chalcogenides containing alkali metals, physical and chemical properties of prospective active elements may be varied in a wide range of functional characteristics. Bulk $NaSbSe_2$ has been reported [3] as a perspective photoelectric semiconductor material (T_{melt} = 1013 K). The compound is formed by the equimolar ratio of Na_2Se and Sb_2Se_3 in the in ternary Na–Sb–Se system [4]. $NaSbSe_2$ crystallizes in a NaCl-like cubic lattice with the lattice constant a = 5.96 Å. Sb_2Se_3 crystallizes in the orthorombic system, with the following lattice parameters: a = 11.6 Å, b = 11.7 Å, c = 3.97 Å. Amorphous thin films of semiconductor chalcogenides have principally new perspectives for applications as aggressive gas environment and electric field sensors [1]. Sb-contained semiconductor materials seem to be attractive not only for structural studies (the question is still open), but also as a subject

*Corresponding author, e-mail: hkhlyap@yahoo.com

of electric investigations. Their electrical properties were not studied until recently. Electrical characteristics of the semiconductor materials p-Sb_2Se_3 (the gap E_g = 1.16 eV) and p-$NaSbSe_2$ (E_g = 1.36 eV) have not been investigated. We should note that there are practically no references concerning the electrical behaviour of these materials. The paper reports on structural characteristics of the films and for the first time on the electric field-induced characteristics of metal–semiconductor (MS) structures In/Sb_2Se_3 and In/$NaSbSe_2$.

2. Experimental

Sb_2Se_3 thin films were grown by thermal evaporation from a quasi-closed system. As was shown earlier [2], this technique gives a good possibility to obtain films of chalcogenides with the compositions corresponding to those of the initial material. The films were condensed at 10^{-3} Pa on glass substrates, at various temperatures of substrates: T_s = 300 K and T_s = 400 K with the rates of deposition from 0.1 to 0.5 nm/s. The thickness of the films was estimated to be 40–80 nm. The nanostructure of the films was studied by methods of electronography and transmission electron microscopy. Cluster-like and whisker-like structure of the films was revealed (Fig. 1).

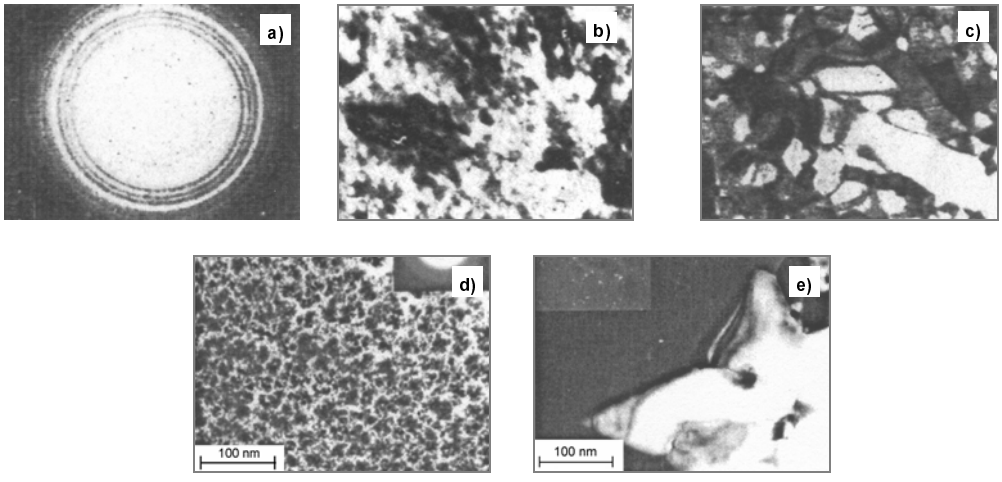

Fig. 1. TEM images of SB_2Se_3 films deposited onto (001) NaCl substrates, T_s = 293 K [3]: microdiffraction pattern (a), after vacuum annealing during 15 h at 493 K (b), and at 593 K (c); the film grown on the glass substrate under T_s = 500 K, crystalline nano-whiskers are observed (d); the micrograph of $NaSbSe_2$ film deposited onto glass substrate, T_s = 400 K. The rectangles in Figs. d) and e) show microdiffraction patterns illustrating the amorphous structure of the films under study

The properties of the films under external electric fields are completely unknown. To investigate the electric field-induced characteristics of the compounds, one should fabricate metallic contacts working as quasi-ohmic ones or as active elements, i.e., barrier-like structure; in the active mode, charge carriers flow through such a contact

due to the monopolar injection from the metal [7]. As we have mentioned above, there is no information about properties of the barrier (i.e., formation, height, width etc.). We have studied some structural and electric field-induced properties of $NaSbSe_2$ thin films prepared by the pulse laser deposition (PLD) technology [6]. Here we report similar investigations of the samples obtained by the thermal evaporation technique. In order to make electrical experiments In contacts of ~2.0–3.5 mm^2 area were deposited on the films for non-destructive current–voltage studies. Electric measurements were carried out at the room temperature under electric fields up to $5 \cdot 10^4$ $V \cdot m^{-1}$.

3. Results

Figure 2 shows experimental current-voltage characteristics (IVC) obtained for Sb_2Se_3 films deposited on both cold and hot substrates.

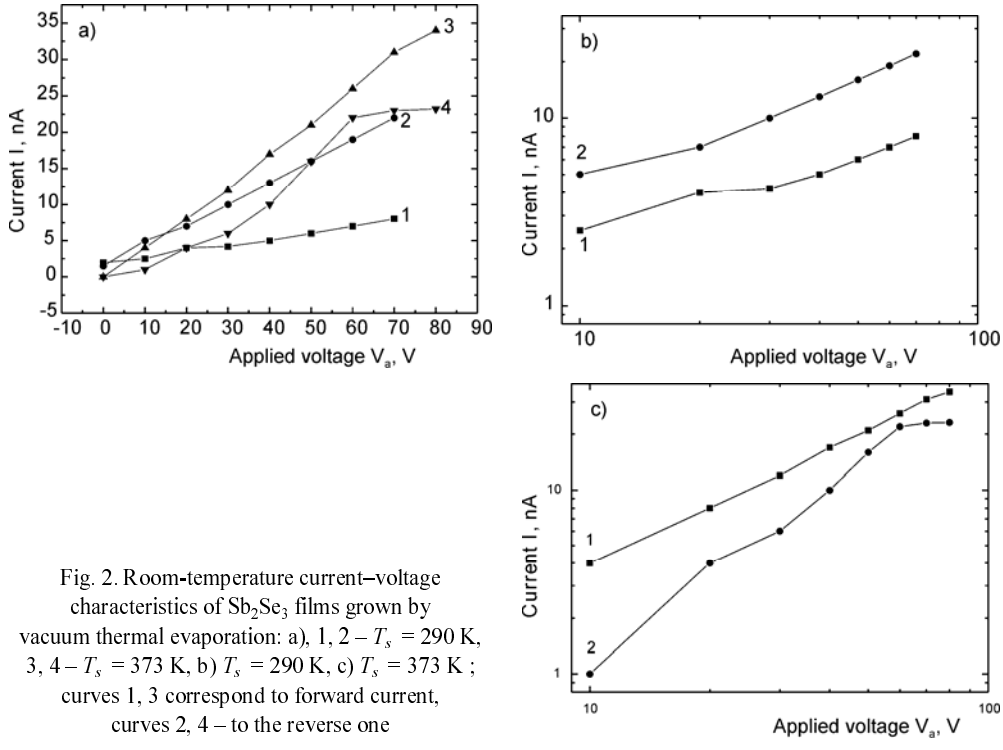

Fig. 2. Room-temperature current–voltage characteristics of Sb_2Se_3 films grown by vacuum thermal evaporation: a), 1, 2 – T_s = 290 K, 3, 4 – T_s = 373 K, b) T_s = 290 K, c) T_s = 373 K ; curves 1, 3 correspond to forward current, curves 2, 4 – to the reverse one

Qualitatively, the "cold" IVC (Fig. 2b) can be described as follows:

$$I \propto V_a^m \tag{1}$$

where V_a stands for the applied voltage and m = 0.6–0.8.

Unlike this case, "hot" samples (i.e., grown at T_s = 400 K) exhibited diode-like characteristics (Fig. 2c):

$$I_{f1} \propto V_a^m, \qquad I_{f2} \propto \exp\left(\frac{eV_a}{nk_BT}\right) \tag{2}$$

where I_{f1}, I_{f2} are currents corresponding to the forward sections of the experimental IVC, m = 3.5, n = 1.04. The reverse current is:

$$I_r \propto V_a^m \tag{3}$$

where $m \approx 0.9$.

Experimental data for $NaSbSe_2$ films are plotted in the Fig. 3a–c.

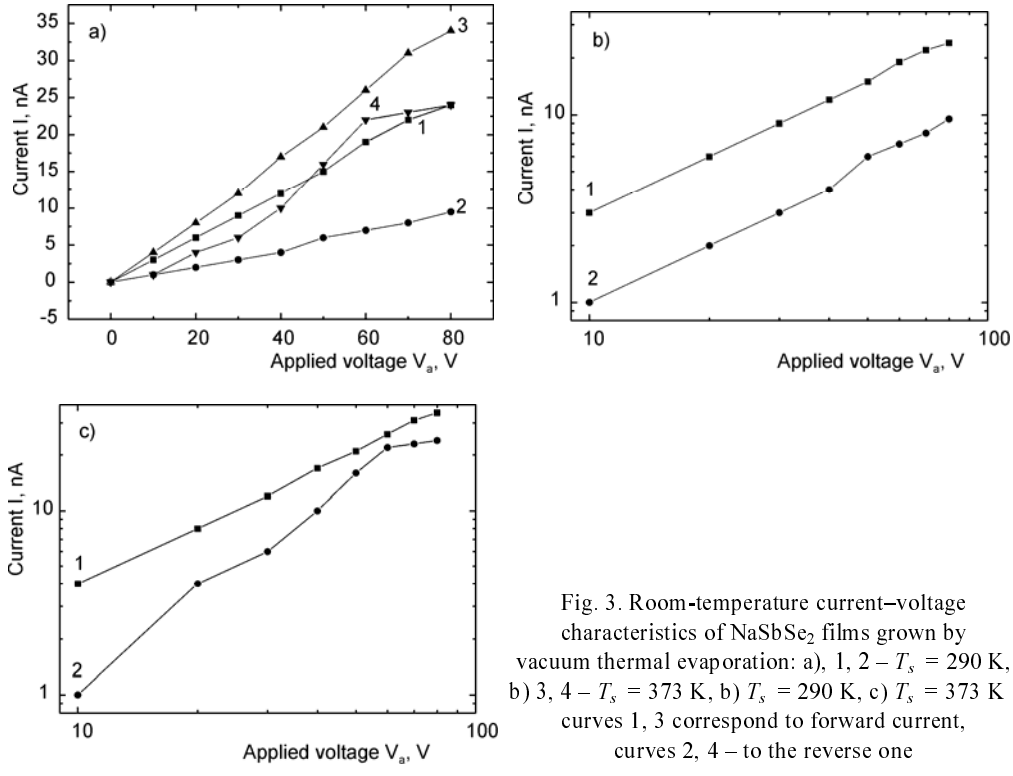

Fig. 3. Room-temperature current–voltage characteristics of $NaSbSe_2$ films grown by vacuum thermal evaporation: a), 1, 2 – T_s = 290 K, b) 3, 4 – T_s = 373 K, b) T_s = 290 K, c) T_s = 373 K ; curves 1, 3 correspond to forward current, curves 2, 4 – to the reverse one

Figure 4 illustrates experimental and calculated IVC of the $NaSbSe_2$ film. As is shown, the forward and reverse sections are alike and are well described by the velocity saturation mode:

$$J \sim \frac{2\varepsilon_0\varepsilon_s v_{sat} V_a}{L^2} \tag{4}$$

In this expression, v_{sat} stands for the carrier saturation velocity, experimentally determined by so-called threshold voltage on the forward section of the IVC, L is the thickness of the film, ε_0 is the permittivity of free space, and ε_s is the relative electric permittivity.

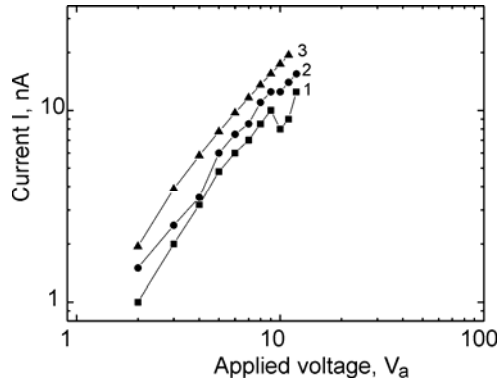

Fig. 4. Room-temperature experimental (1, 2) and calculated (3) current-voltage characteristics of $NaSbSe_2$ films deposited onto the "cold" substrate

Sb_2Se_3 films deposited onto the "hot" substrate demonstrate IVC typical of metal –semiconductor structures [7]. Unlike these layers, the films grown on the "cold" substrates, as well as $NaSbSe_2$ layers exhibit IVC which are characteristic of structures metal–amorphous semiconductor [8].

4. Conclusions

The growth conditions and the surface structure as well as electric field-induced characteristics of semiconductor Sb-contained thin films were investigated. The structural research performed by means of tunneling electron microscopy demonstrated a crystalline whisker-like surface relief of the Sb_2Se_3 films. Such a surface is observed only for the films grown by the pulsed laser deposition technology.

The experimental data obtained under study of the electric field-induced characteristics (room-temperature current-voltage functions) enabled us to estimate charge transfer mechanisms in the films under applied electric field (the power law-like dependences are observed) and made it possible to simulate numerically electrical behavior of the investigated films.

References

[1] BILOZERTSEVA V.I., BASAKUTSA V.A., PANCHENKO L.N., Cryst. Res. Technol., 34 (1999), 677.
[2] BILOZERTSEVA V.I., BASAKUTSA V.A., GAPOCHENKO S.D., LEMESHEVSKAYA YE.T., MUSSIL V.V., Proceedings SPIE 5024 (2003), 84.
[3] BASAKUTSA V.A., ZOZULYA L.P., LUZHNAYA N.P., GNIDASH N.I., Inorg. Mater. (Russia), 12 (1976), 1533.
[4] BASAKUTSA V.A., LASAREV V.B., GNIDASH N.I., PODJCHAJA E.N, TRIPELL A.F., Inorg. Mater. (Russia) 23 (1988), 1255.

[5] LASAREV V.B., BERUL S.L., SALOV A.V., *Ternary Semiconductor Compound in systems A^{I}-B^{V}-C^{VI}*, Nauka, Moscow, 1982.
[6] KHLYAP H., BILOZERTSEVA V., OVCHARENKO S., DYAKONENKO N., Thin Solid Films, 453–454 (2004), 154.
[7] SZE S. M., *Physics of Semiconductor Devices*, Wiley, New York, 1981.
[8] VISHNYAKOV N. V., VIKHROV S.P., MISHUSTIN V.G., APACHEV A.P., UTOCHKIN I.G., POPOV A.A., Semiconductors (Russia), 39 (2005), 1189.

Received 9 September 2005
Revised 3 November 2005

Materials Science-Poland, Vol. 24, No. 4, 2006

Formation of soft material in terms of a coupled matter migration-and-relaxation picture: a synchronous mode

A. GADOMSKI[1*], M. DRESSLER[2], I. SANTAMARÍA-HOLEK[3], J. M. RUBÍ[4]

[1]Institute of Mathematics and Physics,
University of Technology and Life Sciences, 85-796 Bydgoszcz, Poland

[2]Institute of Food Science and Nutrition, Eidgenosische Technische Hochschule,
CH-8092 Zurich, Switzerland

[3]Facultad de Ciencias, Universidad Nacional Autonoma de Mexico,
Circuito Exterior de Ciudad Universitaria, 04510, D. F., Mexico

[4]Departament de Física Fonamental, Universitat de Barcelona, E-08028 Barcelona, Spain

This study is devoted to draw a mesoscopic nonequilibrium thermodynamics (mnet)-based description of the model soft material, such as that made of clusters of amphiphilic molecules or biopolymer surfactants. The description offered also enters the region of nonlinear viscoelastic behaviour of soft-matter agglomerates, both in a fluctuation-driven (quantitatively, being realized in an synchronous mode) and some flow-driven (mostly, qualitatively) regime. A special emphasis is placed on a novel concept, termed the emergent (power-law) behaviour, which tries to effectively combine data available about specific soft-matter (complex) systems that under variety of physicochemical conditions often manifest a certain interesting mesoscopic properties.

Key words: *model soft material; viscoelasticity; matter agglomeration; fluctuations; emergent behaviour*

1. Introduction

Soft matter consists of materials whose constituents have a mesoscopic size (typically, 10^3–10^5 nm) for which k_BT is the relevant energy scale, whence the softness at ambient conditions as a main landmark. Examples of soft-matter systems include polymers, colloidal suspensions, liquid crystals, foams, gels, membranes, biological and granular matter of all types, etc. Soft matter comprises a variety of states perhaps best distinguished by being dominated by thermal energies at room temperature, with quantum aspects generally of secondary importance.

*Corresponding author, e-mail: agad@atr.bydgoszcz.pl

The realization that soft matter contains innumerable examples of generalized elasticity, symmetry breaking, and many fluctuating degrees of freedom has re-opened classical fields of physics such as fluids (now frequently referred to as rheology [1], with non-Newtonian and structured-media aspects) and elasticity (membranes, filaments, and anisotropic networks are all important and common aspects) for new theoretical and experimental investigations. For both generalities and subtleties on soft matter, and the physics one may play on it, let us encourage a reader to consult Ref. [2], in which two major features of any soft-matter (complex-fluid) system have been emphasized, namely, its complexity and viscoelasticity. For a more recent review, in which weak connectivity and entropic interactions as the major features, distinguishing polyatomic (macromolecular) soft-matter systems from their non-polyatomic (small-molecule) counterparts, have been underlined, see [3].

As has been argued very recently, complexity might be a key feature of such systems, though still elusive and poorly defined, being responsible for their *emergent behaviour*, which eventually leads to a multitude of dynamic mesostructures, appearing while their parametric zone is appropriately scanned (cf. [4]) for reviewing the subject. Emergent behaviour is usually attributed to a physical system about which one may firmly say that its higher-level properties are not readily predictable from a detailed knowledge of its lower-level properties, such as those coming from the material subunits (atoms; molecules) alone. In a very real sense [4], emergence represents a democracy of physical scale: no size or time scale is more fundamental than any other. For some theoretical physicists such an assertion may imply: the renormalization-group, and in particular, self-similarity ideas are somehow hidden behind such a claim.

In this study, we would like to focus on one specific example of what one may, after seeing the argumentation developed in the paper, call the emergence in complex late-stage (model) matter agglomeration. The emergence discussed in our matter-agglomeration example relies on detection and exploration of power laws that, being scale-free, by definition do not distinguish any physical scale the properties of which they are pretending to describe. In the presented model, we claim that the complexity arose from a coupling of two basic modes of the slowly evolving model soft-matter system: a certain growing mode with some mechanical-relaxation one, presumed, however, that a (mechanical) stress field is generated within the material agglomerate also under its late-stage growth. Some examples of such systems, in particular biomolecular and colloidal assemblages, have been contained in [5].

The paper is structured as follows. In the next section, we have made a quick tour toward the model soft-matter agglomeration at a mesoscopic level, paying special attention to its basic notions and some landmark features (Fig. 1) which have not been reported. In Section 3, we have looked at volume fluctuations in an agglomerate under two different phase-state conditions, attributed to densely as well as loosely packed matter assemblages, abbreviated by CP and LP matter agglomerations, respectively, concentrating mainly on the so-called synchronous (coupling) mode [5], also trying to answer the question: When late-stage matter agglomeration demands its mechanical

response? In Section 4, we have elaborated the CP and LP packing states even more, and looked more carefully at the soft agglomerate in its *liquidus* and *solidus* phase -state limits. The closing address, presented in sec. 5, will summarize what we have found.

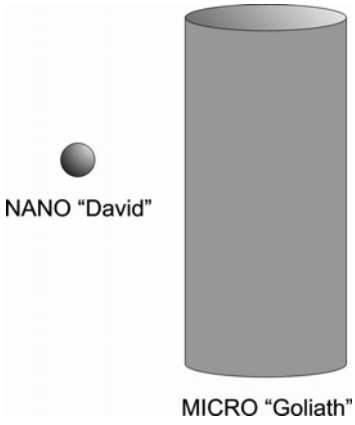

Fig. 1. How to differentiate between matter nano- (10^{-9} m) and micro-agglomerations (10^{-6} m), i.e. those occurring within the length scale of interest expressed by the present paper? The answer, coming from mnet, would be: For instance, and amongst many things, by letting the materials-science researcher know which local curvatures [1], either only the spontaneous or twice the mean (sphere), or even that of Gaussian type (cylinder) modify the surface tension conditions of any soft-matter agglomerate (for some example, see [6], and especially, ref. [22] therein)

2. Quick tour toward model soft-matter agglomeration at a mesoscopic level

There is a consequent and unambiguous method of deriving the main kinetic equation for the overall model matter agglomeration being applicable to soft-matter agglomeration. The method is called mesoscopic nonequilibrium thermodynamics, mnet [7, 8]. It starts with the Gibbs equation which defines the variations of entropy [9, 10]

$$\delta S = -\frac{1}{T}\int \mu(v,t)\delta f \, dv \tag{1}$$

where $f \equiv f(v,t)$ (see below), T is the temperature, and $\mu(v,t)$ is the chemical potential in a v-space, i.e. in the (hyper)volume space of the material agglomerate. The potential $\mu(v,t)$ is given by (here, $\mu \equiv \mu(v,t)$ is taken for brevity)

$$\mu = k_B T \ln(af) \tag{2}$$

where a is the activity coefficient, k_B is the Boltzmann constant, and $k_B T$ stands for the thermal energy. Next, a is given in terms of a thermodynamic potential, denoted by $\Phi \equiv \Phi(v)$. Thus, a reads now [8, 10]

$$a = \exp\left(\Phi / k_B T\right) \tag{3}$$

Providing the temporal derivative in Eq. (1) and after partially integrating it over both sides (assuming additionally that $J \equiv J(v,t)$ vanishes at the ends of the phase space), one gets the entropy production, σ_E

$$\sigma_E = -\frac{1}{T} J \frac{\partial \mu}{\partial v} \tag{4}$$

from which we may easily get the expression for the matter flux

$$J = -\frac{1}{T} L(v) \frac{\partial \mu}{\partial v} \tag{5}$$

Here, we have assumed that the process is local in v. One could also consider, if necessary, a non-local case by [5, 8, 10]

$$J(v) = -\frac{1}{T} \int dv' L(v,v') \frac{\partial \mu}{\partial v'}$$

Combining Eqs. (5), (2) and (3) one gets

$$J = -\frac{1}{Tf} L(v) \left[k_B T \frac{\partial f}{\partial v} + f \frac{d\Phi}{dv} \right] \tag{6}$$

Now, let us define the mobility $b(v)$ as

$$b(v) = \frac{1}{Tf} L(v) = \frac{D}{k_B T} v^{\alpha}$$

where D is a constant [5], and α reads

$$\alpha = 1 - \frac{1}{d} \tag{7}$$

where d is the spatial dimension in which the described agglomeration occurs. The derived flux J is given by

$$J = -Dv^{\alpha} \frac{\partial}{\partial v} f - b(v) f \frac{d}{dv} \Phi \tag{8}$$

The obtained expression looks quite general, probably in spite of the power-law form (cluster–volume correlations) assumed in the Onsager coefficient $L(v)$ [9]. At this stage of presentation, let us anticipate this form by stating explicitly

$$D(v) = Dv^{\alpha} = k_B T b(v) \tag{9}$$

which also implies $b(v) \propto v^{\alpha}$. It means that both kinetic coefficients, namely that of diffusion as well as the one attributed to the drift term in Eq. (8), which for its own is

a kind of generalized Fick's law, are power-dependent on v. The term v^{α} represents the magnitude of the surface of a cluster (the contact area for an agglomeration event to take place), with the molecular cluster *per se* as the basic constituent of the agglomerate at the mesoscopic (molecular cluster-based) level of description [5].

After deriving the flux (8) in its explicit form, we have to apply it to a local continuity equation:

$$\frac{\partial}{\partial t} f(v,t) + \frac{\partial}{\partial v} J(v,t) = 0 \tag{10}$$

where v is the volume of a molecular cluster (a stochastic variable), $f(v,t)$ is the distribution function of the clusters at time t (having a meaning of the number density [11]), that means, $f(v,t)dv$ is a relative number of clusters of a size taken from the narrow volume interval $[v, v + dv]$. This way, we may arrive at a Fokker–Planck–Kolmogorov (FPK)-type equation that governs the agglomeration dynamics [5, 10, 11].

It is instructive to transform the local partial differential equation (PDE) formulation of the matter agglomeration into its possibly simple functional representation, abbreviated for further use by F-representation [12]. For doing it, let us state the matter flux, (8), in the following form

$$J(v,t) = -(B(v)\frac{\delta F(f)}{\delta f(v,t)} + \beta D(v)\frac{\partial}{\partial v}\frac{\delta F(f)}{\delta f(v,t)}) \tag{11}$$

where $B(v) = b(v)d\Phi(v)/dv$, and $\beta = 1/(k_B T)$ is the so-called inverse thermal energy. Here $\delta F(f)/\delta f(v,t)$ stands for the functional derivative, and the free-energy functional $F(f)$ is as follows:

$$F(f) = \frac{1}{2} f(v,t) \int K(v - v') f(v',t) dv dv' \tag{12}$$

If one takes the kernel K, $\mathrm{K}(v - v') = \delta(v - v')$ (applying the delta Dirac distribution $\delta(v - v')$), i.e. when the "instantaneous" inter-cluster interaction is switched on, one provides

$$F(f) = \frac{1}{2}\left(f(v,t)\right)^2 \tag{13}$$

which because of the power 2 in the equality obtained, suggests unambiguously the pairwise (binary) interactions between clusters, as is, for example, assumed in van der Waals (real) gases between the gas molecules within the framework of a mean-field description. In general, it is accepted for Lennard–Jones potential-driven systems, the class of which is quite broad. Notice, that in such a simple case just described, the energy functional $F(f)$ can be set to be zero in both ends of the phase space $v \in [0,\infty]$ because the standard and physically justified boundary conditions (bcs) to be obeyed,

are: $f(v = 0,t) = f(v = \infty,t) = 0$ [11]. They are consistent with the natural mnet bcs that require the matter flux must vanish in both ends mentioned, too. This, in turn, is very consistent with the well-known Kramers' picture of the stochastic process with a single activation barrier (see [8], and refs. therein). Such a picture is typically offered in terms of the FPK dynamics but may also be proposed in terms of the free -energy functional representation, which is actually the case presented here.

Now, the chemical potential reads

$$\mu = \frac{1}{2}\beta \ln \frac{F(f)}{F_{eq}(f)} \tag{14}$$

i.e., it is recovered in a Boltzmann-type (logarithmic) form, whereby

$$F_{eq}(f) = \frac{1}{2} f_{eq}^2 \tag{15}$$

where $f_{eq} = \exp(-\beta\Phi)$, well within the accuracy of a constant pre-factor [5]. Note that a pairwise interaction between clusters is still present when looking at Eq. (15). Moreover, note that if $K(v - v') \neq \delta(v - v')$ were chosen, one would likely be able to model more complex interactions between clusters, which is usually of very interest to biological systems, such as protein aggregations under various physicochemical contexts [4]. The activity of the agglomerating system reads $a = \exp(\beta\Phi)$, this way reproducing the form of Eq. (3), where finally $f_{eq} = 1/a$ is required.

Both above kinetic-thermodynamic descriptions of the soft-matter agglomeration, the PDE-based of FPK type as well as that of F-functional representation, with the free-energy non-monotonous landscape staying behind it, enable one to proceed further toward getting its fluctuation-influenced characteristics as well as to differentiate between their principal forms, being matter-packing dependent (CP and LP), and depending mostly upon the fluctuation-influenced behaviour as well as upon a certain temperature-caused change of connectivity between clusters of which the material agglomarate is being made [5, 10]. Some d-dimensional considerations, where typically $d = 1, 2, 3$ [5], complete the overall comprehensive picture of various soft-matter clusterings.

3. Volume fluctuations under two different phase-state conditions. When late-stage matter agglomeration demands its mechanical response?

Herein, we would like to describe the matter agglomeration in a viscoelastic matrix. Our description rests on the observation that it is realized by more or less vigorous volume fluctuations of the clusters constituting the agglomerate. Though the flow of matter, in contrast to the following section, is not provided by means of the velocity gradient (Newton's law), resulting in a drift, nevertheless, the drift term is present

in the current, see Eq. (8), thus it is generically present in the system. Moreover, the driving force of the process as a whole, which is typically the free energy decrease (also, the CP agglomeration is specifically driven by capillary forces), superimposes a directional matter flow on the matter-agglomerating Potts-type system under study [11]. The direction, however, cannot be globally viewed as, say, a line in the space, but one may think of a natural course of the process; locally, one might, of course, identify some geometrical directions. The origin of more vigorous volume fluctuations, quantified by the reduced variance given below, can primarily be attributed to some thermal excitement of the soft-matter system. This is because the system is entropic, which by the way stands for the main assumption of our mnet-involving formalism. A certain inflow or outflow of thermal energy submitted to the system, may simply cause either a disconnectivity or connectivity of the clusters, thus changing the overall inter-cluster space amongst them. A second physical set-up to which the volume fluctuations can be assigned is the interaction map within the emerging agglomerate. This interaction map is related to the degrees of freedom the system exhibits, or explores, rather. They, in turn, can be estimated somehow by realizing that they are "better viewed" in higher dimensional spaces, in the sense, that a $d = 3$ space has usually more degrees of freedom than its two-dimensional counterpart can have.

As has been suggested above, the fluctuations $\sigma^2(t)$ can be different in different systems. In our case, if the LP agglomerations of loosely packed clusters emerge in the course of time t, they are evaluated to obey a power law, namely

$$\sigma^2_{LP}(t) \propto t^{1/(d+1)} \tag{16}$$

whereas the CP-counterpart is related to the above by

$$\sigma^2_{CP}(t) \propto \sigma^2_{LP}(t)^d \tag{17}$$

i.e., they proceed in a much more vigorous way, mostly because of the CP agglomerates being denser than the LP flocks [5]; note, that $\sigma^2(t)$ are defined by the reduced variance in a standard way

$$\sigma^2(t) = \frac{< v^2(t) > - < v^1(t) >^2}{< v^1(t) >^2} \tag{18}$$

where, in turn, the central moments take on a standard form, namely

$$< v^n(t) >= \int_0^\infty v^n f(v,t) dv$$

For the LP agglomeration in the long-time limit one obtains [5]

$$< v^n(t) > \propto t^{[(n-1)+\alpha]/(2-\alpha)}, \qquad n = 0,\ 1,\ 2 \tag{19}$$

whereas (under the same late-stage conditions) for CP agglomerations one appreciates another power law [5]

$$< v^n(t) > \propto t^{(n-1)/(2-\alpha)}, \qquad n = 0,\ 1,\ 2 \tag{20}$$

From the above it is then seen that our fluctuation-driven agglomeration, being a stochastic process [10], is mostly governed by power laws. Thus, and so described, it appears to be a scale-free process, since the algebraic relation such as $\omega(x) \propto x^{\varepsilon}$ is preserved under any arbitrary scale x change, such as $x \to \lambda x$ for any real and nonzero scaling factor λ, and for an arbitrary power-type function ω, with exponent ε, which can be, for example, σ^2 defined above. This can be viewed as a signature of the announced (see Introduction) emergent behaviour of the matter-agglomerating system.

Next, if such an eruption of power laws is naturally present in the system (see present as well as preceding section), let us proceed further along these lines. Namely, bearing in mind that we pretend to model agglomeration in a viscoelastic milieu, let us propose a coupling of the late-stage growing mode to some mechanical relaxation one [5]. If such a coupling existed, we would prefer to call it a synchronous mode of the late-stage (meaning: typically, very slow) agglomeration. This mode emerges when the LP agglomeration is switched on for the first time, typically by adequately increasing T. It can be represented by the approximate formula:

$$\sigma_{QY} \approx \sigma^{-1} \tag{21}$$

thus imposing that the quasi-yield stress σ_{QY}, emerging in the agglomerate is almost entirely due to the matter fluctuations in the system. In other words, the fluctuations in soft-matter system may also cause a small plastic effect, especially in the nanometre scale. For further argumentation accompanying the conjecture (21), one is encouraged to look into [5]. From the most general point of view, we opt for Eq. (21) since it supports very much the celebrated emergent behaviour [13], called by some researchers the middle may, i.e. the way of appreciation for mesoscopic matter organization, which is, by the way, well-described by mnet formalism proposed by the present study. A few other examples of mesoscopic systems successfully studied by mnet one can find in [14–16]. They mostly emphasize the so-called slow relaxation (ageing) effect, and possible variations of temperature with time, $T(t)$, often observed in colloidal as well as some granular, i.e. rheologically nontrivial [1] systems. It inevitably leads to an interesting temporal behaviour of the kinetic coefficients, e.g. those involved in Eq. (8). This can be of special interest for the LP agglomeration for which only one kinetic coefficient is of importance, since the drift term in Eq. (8) can be washed out. This is $D(v)$ that can be "renormalized" to some $D(v,t)$ either in a phenomenological [17] or in some more systematic, and therefore advised, way to follow. In particular, in [18] the presence of memory effects in FPK non-Markovian dynamics has been treated by means of mnet-involving formalism, where the corresponding Onsager coefficients [9] were found in terms of generalized regression laws that incorporate moments of the probability distribution higher than the second one.

The above conjecture, Eq. (21), yields slower than exponential, herein algebraic temporal behaviour

$$\sigma_{QY}(t) \propto t^{-1/(a(d+1))}, \qquad t >> 1 \tag{22}$$

It is assumed that $1/a$ is a system-dependent constant, typically close to one half, i.e. to the characteristic Hall–Petch exponent [19], see below. The constant characterizes somehow quantitatively the strengthening mechanism of the material output viz. soft-matter object. Moreover, it is worth realizing that Eq. (21) offers an inter-connecting relationship between a "macroscopic" quantity, here σ_{QY}, and its clearly microscopic *alter ego*, namely σ^2, which is undoubtedly in the spirit of the Onsager's regression hypothesis, though a more precise argumentation must certainly follow such an assertion [9].

Following this idea, now we will outline a quasi-phenomenological argumentation which shows that the viscoelastic milieu is responsible for memory effects similar to those shown, for example, in Eqs. (20) and (22). In this approximation, the manifestation of the viscoelastic and, in general, non-Newtonian effects (which will be analyzed in detail in the following section) can be characterized through the time dependence of the kinetic coefficient $D(v,t)$, which may, in general, be expressed through the relation

$$D(v,t) = \beta^{-1}\mu(t)b_0 v^{\alpha} \tag{23}$$

where $\mu(t)$, to be not confused with that of Eq. (7), has the dimension of inverse of time and b_0 accounts for the correct dimension in the resulting FPK equation

$$\frac{\partial}{\partial t} f(v,t) = \frac{\partial}{\partial v}\left[\beta^{-1}\mu(t)b_0 v^{\alpha} \frac{\partial}{\partial v} f \right] \tag{24}$$

which was obtained by assuming $T >> T_{th}$, where T_{th} stands for a temperature value above which the LP agglomeration occurs [5], and by substituting Eq. (8) for (10) after using (9). Notice that $D(v,t)$ is precisely the corresponding Onsager coefficient entering the linear law (8); for a specific form of $D(v,t)$, characteristic of a biopolymer CP agglomeration of spherulitic type, taking place in some fluctuating environment, one is encouraged to see [17]. To sketch how the power-law behaviour of the moments of $f(v,t)$ arise according with this model, let us consider a simple case in which the solution of Eq. (24) can be splitted into the product $f(v,t) = g(t)h(v)$. Avoiding the details of the calculations (see, e.g., [20]), a little thought shows that, even in the simple case, the behaviour of the time dependent part $g(t)$ is determined by the properties of the viscoelastic milieu as follows

$$\frac{d}{dt}\ln g(t) = -c_0\mu(t) \tag{25}$$

where c_0 is a constant arising from the variable separation. At the late-stage of growing, characterized by the slow relaxation of the system, the dissipation rate of the system depends, in general, on the "age" of the system and can be well described in the form of

$$\mu(t) \propto \frac{\xi}{t_0}\left(\frac{t_0}{t}\right)^{\delta+1}$$

where ξ is a constant and the exponent δ characterizes mean viscoelastic properties of the medium, and may depend, in general, on the size of the molecular clusters. Here, t_0 is the initial time measured. This dependence of $\mu(t)$ can, in principle, be calculated by analyzing the elastic properties of the background medium as a continuum; see, for example, Ref. [21], where this idea has been implemented to describe anomalous transport in an intracellular medium. Applying this relation to Eq. (25), one obtains that

$$g(t) \propto \mathrm{e}^{\xi c_0/\delta (t_0/t)^{\delta}}$$

i.e. it is here in the form of a stretched exponential. This relation, valid for a sufficiently wide range of times, can, for very long times $t >> t_0$, be expressed in a more convenient form by expanding the exponential up to first order in its argument, thus providing

$$g(t) \propto \frac{\xi c_0}{\delta}\left(\frac{t_0}{t}\right)^{\delta} + O\left(t^{-2\delta}\right) \tag{26}$$

This relation is directly related with the relaxation of the moments of the distribution as, for example, the reduced variance $\sigma(t)$, see above. In particular, for this function one obtains, without taking into account constants arising from averaging over the volume space, the relation $\sigma(t) \approx g(t)^{-1} - 1$, which can finally be expressed as

$$\sigma(t) \propto \frac{\delta}{\xi c_0}\left(\frac{t}{t_0}\right)^{\delta} \tag{27}$$

From this point of view, it is plausible to assume that during the slow stage of the dynamics of the system, there appears a coupling between the relaxation of the elastic stresses $\sigma_{QY}(t)$ and that related with the volume fluctuations, benchmarking both the CP and LP matter agglomeration, characterized by $\sigma(t)$. This coupling takes place because the viscoelastic properties of the medium have the same characteristic time scale $\mu(t)$. Thus, in similar but slightly different form as in Ref. [5], stress relaxation can be described through the following equation [22]:

$$\frac{d\sigma_{QY}(t)}{dt} + \mu(t)\sigma_{QY} = 0$$

for another soft-matter scenario drawn, therein for describing the hydration kinetics of relaxing model lipid membranes. This equation can be obtained from the mnet-formalism by following a method similar to that followed in [14, 15]. Notice that by

integrating this equation and taking the long time approximation consistent with that to obtain Eq. (26), one arrives at the expression

$$\sigma_{QY}(t) \propto \left(\frac{t_0}{t}\right)^{\delta} \tag{28}$$

The last equation seems to give a solid basis for the before mentioned conjecture given in (21).

4. Soft agglomerate in its *liquidus* and *solidus* as well as intermediate phase-state limits

To get a more comprehensive picture of the soft-matter agglomeration, let us explore it further taking into account its non-Newtonian character, again well described by the Ostwald–de Waele laws of power type, interconnecting the shear stress with the shear rate [23]. From the below stated it will be seen that the agglomeration under flow, both of CP and LP type, somehow interpolates between two phase-state limits, accordingly to LP and CP agglomerations to be named: *liquidus* and *solidus* limits. Note that the mostly nonlinear viscoelastic properties of the agglomerating system are pronounced here even more.

The nonlinear flow curve of CP and LP agglomerates of deformable droplets, rigid particles, and flexible polymer chains dispersed in a viscous medium exhibit a typical power-law behaviour, i. e. the shear viscosity, $\eta = \sigma_h/\dot{\gamma}$, is a non-linear function of shear rate $\dot{\gamma}$, where σ_h is the shear stress measured in a homogeneous shear flow $\dot{\gamma}$.

The non-linear flow curve of the agglomerating system is expected to have three regimes being characterized by different shapes $\eta(\dot{\gamma})$. The low shear rate regime with a Newtonian plateau for the LP agglomerates and an infinite shear viscosity for the CP agglomerates, an intermediate regime, and a high shear rate regime. In what follows the three regimes will be explained and interpreted from a physical point of view: In the low shear rate regime the structural forces (e.g. Brownian forces) are stronger than the orienting forces due to the externally imposed flow. Consequently, we do not observe flow-induced structural changes and the shear viscosity is constant, η_0. The infinite shear viscosity of the CP agglomerates is due to the constant yield stress, τ_0. This means that the CP agglomerates behave as a rigid body under application of a small shear force and thus the CP agglomerates do not flow.

According to the Hall–Petch relation the yield stress τ_0 is given as

$$\tau_0 = K_2 d^{-1/2} + K_1 \tag{29}$$

where K_1 and K_2 are material-dependent constants and d, to be not confused with that of Eq. (7), is proportional to the average radius of the clusters (grains). Note that the

average radius d is taken as a scalar parameter and thus also the Hall–Petch relation does not account for anisotropic stresses. (In the same vein, the stresses arising during the late-stage matter agglomeration, when no special "macroscopic" matter flow is detected, are involved as zero-rank tensors in the description offered [5].) Moreover, note that the above equation is mostly expected to hold only for CP agglomerates which exhibit a yield behaviour. For LP agglomerates, the stress tensor is isotropic with its trace corresponding to three times the hydrostatic pressure. It would be interesting to adopt the theoretical framework used in [1] to derive a set of dynamic equations for a complex material with yield stress which takes into account anisotropic material behaviour in shear and elongational deformation.

In the intermediate shear rate regime of the non-linear flow curve, the hydrodynamic (or viscous) forces are of the same order of magnitude as the structural (e.g. Brownian) forces. Now one observes an orientation and deformation of the LP agglomerates which correlates with a decrease of the shear viscosity. For the CP agglomerates the flow stresses exceed the yield stress τ_0 and the material begins to flow. Also for the CP agglomerates one can observe a deformation and orientation of the microstructure which leads to a decrease of the shear viscosity. The reason for the decrease of the shear viscosity is that the microstructural components orient in flow thus lowering their flow resistance. This is seen as a decrease of the shear viscosity.

In the high shear rate regime, it is possible to observe a second Newtonian plateau and a shear thickening regime, i.e. a small increase of the shear viscosity for the CP as well as the LP agglomerates. The microstructural interpretation of this behaviour is the formation of aggregates in a high shear flow which increase the flow resistance and which correlates with the increase of the shear viscosity.

The qualitative behaviour described above is the most important non-Newtonian flow behaviour of CP and LP agglomerates [24]. Note that the decrease of the Newtonian viscosity in the intermediate shear rate regime can be several orders of magnitude which is very important for the processing of these fluids in chemical or food industries. However, the shear thinning behaviour displayed in a figure in [24], in general, correlates with other non-Newtonian effects such as normal stresses due to elastic material behaviour. These non-Newtonian effects are normal stresses in homogeneous shear flows. Physically this means, e.g., that in order to maintain steady shear flow in a non-Newtonian liquid one needs not only a shear stress, σ_h, but also normal stresses, e.g. acting perpendicular to the confining plates of the liquids. Further non-Newtonian effects can be observed in time-dependent shearing flows, e.g. in start-up or cessation of steady shearing flow. In such flows, one observes a transient behaviour of the flow stresses (i.e., shear stresses and normal stress differences).

As for some crude analogies between fluctuation-driven and flow-driven matter agglomeration, one may classify them both as activated processes, underlying to some extent the mentioned Kramers' picture, where the energy barrier is permanently surmounted. In both cases, i.e. in the random walk theory [5, 10, 11] as well as in the Ostwald–de Waele dynamic relations for the flow [23], qualitatively the same power-

law (ultimately, also temporal) behaviour may appear: Normal diffusion (random walk) would be equivalent to Newtonian behaviour of the system, whereas the non-Newtonian behaviour would correspond to the anomalous diffusion (random walk), being either subdiffusion (slow or damped motion) or superdiffusion (vigorous or turbulent motion). This way, the analogy is completed, at least from the qualitative viewpoint.

5. Closing address

Let us start with a motto which itself characterizes well the basic motivation of our study. This motto reads: It is not enough to break up matter into its most fundamental pieces, and then to reassemble them, just to gain some, even poor, understanding about the output (matter) assemblage, see Sec. 1. According to it, we are of the opinion that the offered mnet-based description is a good tool [5, 6, 10, 14, 15, 18] for dealing with complex matter agglomerations, because for many important purposes, studying and comprehending matter organizations is sufficient just at the mesoscopic (molecular-cluster) based level of description.

For example, in protein aggregation and crystal growth ([4] and refs. therein), efforts of many researchers have been distributed over controlling really important details of the process. As a consequence, this led to (almost) full understanding of some specific (say, selected for special purpose) protein aggregations, postponing, unfortunately, to some, sometimes quite large extent, principia of matter organization, and trying to replace them by computer simulations [25]. It is a necessary way, of course, but it should be complemented by some investigations on the principia that have to go in parallel with those detailed studies. In particular, in authors' very individual (and specific) opinion there is a need to enlighten unambiguously how the speed of the crystal, being attempted to maintain by an experimenter at a constant value, which is the most stable hydrodynamic mode of the process, will influence the obtained structural output of the non-Kossel type, emerging from such an entropic environment [16].

When advocating for the mnet-based modelling, one is obliged to answer quite a basic question: What do we loose and what do we gain while doing so? Certainly, we cannot take control over most of the microscopic quantities of any agglomeration that we are dealing with – this is without question. But we may still have, just in a parametric manner, quite many of them, see [16]. Moreover, we are capable of looking into key microscopic details, thus ascertaining quite univocally, when for example the local curvatures of the end product, modifying significantly the surface-tension conditions, see Fig. 1, may really change the overall system behaviour [16]. This even enables one to first differentiate between nano- and micro-agglomerations of soft-matter (see [5, 25], and refs. therein).

What do we gain by applying mnet? Above all, a quite simple (but by no means exhaustive!) insight into the above underscored principia of matter organization [10] just in an entropic environment; also, a tractable description, preferentially in terms of

the FPK framework, or as freshly included in Sec. 2, by means of the energy-functional method. The limitations of applying mnet have been explicitly stated for the first time in [8], though many studies along these lines appeared before, giving the final address ([7], and refs. therein).

A careful reader will also notice that high appreciation is given here to almost omnipresent power laws that arise from the proposed modelling. This is, for sure, very consistent with the emergent (ageing-dependent) behaviour assigned in last years to soft-matter systems [3, 4, 13]. The question is, however: How far may such idealization go?

Concluding this section, let us mention that, in contrast with the material presented in our previous study [5], we did not include any considerations on d-dimensional as well as on chaotic behaviour of the model soft-matter system. They are really interesting per se. For example, the picture drawn under chaotic vs. regular matter-organization regime is consistently defined by the type of definition of Sinai–Kolmogorov (fractal) entropy which corresponds directly to the aggregation rate in the space of Euclidean dimension d. (Some signatures of the Farey's three in the d-dimensional construction of the model can also be announced [26], according to the below mentioned Bethe-lattice landmarks, characteristic of model gelation.) This rate, in turn, is uniquely defined based on the volume fluctuation σ^2 derived in Sect. 3.

To sum up, and according to what has been obtained in [5], we can list even more: (i) an algebraic decay in time of the internal stresses propagating along the inter-cluster spaces (depletion zones) of lower viscosity has to be underscored as an interesting phenomenon revealed; (ii) a gelling-type effect with microstructural constraints, due to the critical relaxation exponent of the process, that bears a Flory–Stockmayer-type, though d-dependent, mean-field approximation to gelling systems, clearly of the form of the critical percolation probability, such as $p(d) = 1/(q(d) - 1)$, where $q(d)$ $2(d + 1) + 1$, is possible to obtain by the present mnet model; (iii) an interesting behaviour, pertaining to a way of developing the two basic dynamic constituents of the process, i.e. late-time matter migration and mechanical relaxation [5], namely, that the rates of both of them obey the mean-harmonicity rule in dimension d, resembling partially the case of transient coagulation in aerosols and/or hydrosols [27], such as biopolymers dispersed in water solution, interpenetrating between the so-called free-molecule and continuum levels of matter microstructural organization, can bee seen; the synchronous mode, because of the emergent behaviour, might resemble to some reasonable extent a *SOC* (self-organized criticality) phenomenon [28], which goes in the space d in a common mean-harmonic [5] and continuum-percolative [11] way, showing up similarity relations both in cluster-size space and time domains [29].

Acknowledgement

A. G. and M.D. would like to take the opportunity of thanking very much the ESF Programme – Stochastic Dynamics: Fundamentals and Applications (STOCHDYN) for a support. A.G. would also like to

mention 2P03B 03225 (2003-2006) under which part of this work has been done, as well as to appreciate many helpful discussions and constructive advices of Prof. Marek Cieplak, I.F. P.A.N., Warsaw.

References

[1] DRESSLER M., EDWARDS B.J., Rheol. Acta, 43 (2004), 257.
[2] DE GENNES P.G., *Nobel Prize Lecture on Soft Matter*, College de France, Paris, 1991.
[3] WITTEN T.A., Rev. Mod. Phys., 71 (1999), S367.
[4] COX D.L., PINES D., MRS Bulletin, 30 (2005), 425.
[5] GADOMSKI A., RUBÍ J.M., ŁUCZKA J., AUSLOOS M., Chem. Phys., 310 (2005), 153.
[6] GADOMSKI A., SIÓDMIAK J., SANTAMARÍA-HOLEK I., RUBÍ J.M., AUSLOOS M., Acta Phys. Pol. B, 36 (2005), 1001.
[7] REGUERA D., RUBÍ J.M., PÉREZ–MADRID A., J. Chem. Phys., 109 (1998), 5987.
[8] VILAR J.M.G., RUBÍ J.M., Proc. Natl. Acad. Sci. USA, 98 (2001), 11081.
[9] ONSAGER L., Phys. Rev., 37 (1931), 405.
[10] RUBÍ J.M., GADOMSKI A., Physica A, 326 (2003), 333.
[11] GADOMSKI A., Physica A, 274 (1999), 325.
[12] GIACOMIN G., LEBOWITZ J.L., MARRA R., Nonlinearity, 13 (2000), 2143.
[13] LAUGHLIN R.B., PINES D., SCHMALIAN J., STOJKOVIC B.P., WOLYNES P., Proc. Natl. Acad. Sci. USA, 97 (2000), 32.
[14] SANTAMARÍA-HOLEK I., PÉREZ–MADRID A., RUBÍ J.M., J. Chem. Phys., 120 (2004), 2818.
[15] RUBÍ J.M., SANTAMARÍA-HOLEK I., PÉREZ–MADRID A., J. Phys. C: Cond. Matter., 16 (2004), S2047.
[16] FRANZ S., VIRASORO M.A., J. Phys. A: Math. Gen., 33 (2000), 861.
[17] GADOMSKI A., Chem. Phys. Lett., 258 (1996), 6.
[18] SANTAMARÍA-HOLEK I., RUBÍ J.M., Physica A, 326 (2003), 384.
[19] FRIEDMAN L.H., CHRZAN D.C., Phys. Rev. Lett., 81 (1998), 2715.
[20] NIEMIEC M., GADOMSKI A., ŁUCZKA J., Acta Phys. Pol. B, 32 (2001), 1513.
[21] LAU A.W.C., HOFFMANN B.D., DAVIES A., CROCKER J.C., LUBENSKY T.C., Phys. Rev. Lett., 91 (2003), 198101.
[22] GADOMSKI A., J. Phys. II (France), 6 (1996), 1537.
[23] PRZYGOCKI W., WŁOCHOWICZ A., *Polymer Physics*, WN PWN, Warsaw, 2001, in Polish.
[24] WEIPERT D., TSCHEUSCHNER H.-D., WINDHAB E., *Rheologie der Lebensmittel*, Behr's Verlag 1993, Hamburg, in German, p. 585.
[25] THIRUMALAI D., KLIMOV D.K., DIMA R.I., Curr. Opin. Struc. Biol., 13 (2003), 146.
[26] SCHUSTER H.-G., *Deterministic Chaos. An Introduction*, VCH, Weinheim, 1988.
[27] TALUKDAR S.S., SWIHART M.T., J. Aerosol Sci., 35 (2004), 889.
[28] BAK P., TANG C., WIESENFELD K., Phys. Rev. Lett., 59 (1987), 381.
[29] GALINA H., LECHOWICZ J.B., Macromol. Symp., 174 (2001), 307.

Received 8 September 2005
Revised 9 November 2005

Materials Science-Poland, Vol. 24, No. 4, 2006

100 years of work function

S. HAŁAS*

Institute of Physics, Maria Curie-Skłodowska University, 20-031 Lublin, Poland

This paper traces early inquires on the nature of the work function (*WF*). Much attention was paid to the papers published by Einstein (1905), Richardson (1901), Jentzsch (1908), Debye (1910), Schottky (1914) and Langmuir (1916). Those authors assumed that the image force, introduced already by Thomson for macroscopic bodies, may be the main reason for the barrier at the metal surface. The formula derived by Schottky (1914) is still used for calculation of the lowering of the surface barrier in presence of an external electric field. In further development of surface physics, however, much emphasis was paid to the role of a dipole layer. However, at the end of 20th century the idea of the image potential as the main contribution to *WF* was restored by Brodie (1995) and subsequently improved by Halas and Durakiewicz (1998). In these theories a distance *d* from which the image force can be integrated is found from the uncertainty principle and from the length of spontaneous metallic plasma polarization, respectively. The last approach has appeared to be very useful in calculation of *WF* of conducting compounds and ionization potentials of metallic clusters.

Key words: *cluster; cold emission; ionization potential; photoeffect; surface ionization; thermionic emission; work function*

1. Introduction

The term "work function" (*WF*) was coined about 1923 for the work expressed in eV which is necessary to get electron out of metal. Prior to that time it was defined as *the work necessary to get electron out of metal*, or *work done when electron escapes from a metal*. Over the last 100 years this fundamental property of a surface has been examined nearly for all elements and for many conducting compounds or alloys. It is related to the ionization energy of atoms, but it is less strictly defined than ionization energy because it strongly depends on the presence of impurities at surface and *WF* appears to be face-dependent, if single crystals are investigated. Table 1 contains *WF* for polycrystalline elements along with ionization energies and the values of electron affinity (which is discussed in Sect. 4). This paper contains a brief review of the *WF* significance in understanding various phenomena and the nature of *WF* itself.

*Corresponding author, e-mail: halas@tytan.umcs.lublin.pl

Table 1. The periodic table of elements*

$_{1}$H 13.598 0.7542																	$_{2}$He 24.58 –0.22
$_{3}$Li 5.39 2.9 0.6182	$_{4}$Be 9.32 4.98 –0.19											$_{5}$B 8.30 4.45 0.227	$_{6}$C 11.26 5.0 1.2629	$_{7}$N 14.54 –0.07	$_{8}$O 13.61 1.462	$_{9}$F 17.42 3.399	$_{10}$Ne 21.56 –0.3
$_{11}$Na 5.14 2.75 0.5479	$_{12}$Mg 7.64 3.66 –0.22											$_{13}$Al 5.98 4.28 0.442	$_{14}$Si 8.15 4.85 1.385	$_{15}$P 10.55 0.7464	$_{16}$S 10.36 2.077	$_{17}$Cl 13.01 3.615	$_{18}$Ar 15.76 –0.36
$_{19}$K 4.34 2.30 0.5015	$_{20}$Ca 6.11 2.87 0.0215	$_{21}$Sc 6.56 3.4 0.189	$_{22}$Ti 6.83 4.33 0.080	$_{23}$V 6.74 4.3 0.526	$_{24}$Cr 6.76 4.5 0.667	$_{25}$Mn 7.43 4.1 <0.005	$_{26}$Fe 7.90 4.5 0.164	$_{27}$Co 7.86 5.0 0.662	$_{28}$Ni 7.63 5.15 1.157	$_{29}$Cu 7.72 4.51 1.228	$_{30}$Zn 9.39 4.33 0.093	$_{31}$Ga 6.00 4.15 0.31	$_{32}$Ge 7.89 5.0 1.23	$_{33}$As 9.81 4.77 0.81	$_{34}$Se 9.75 5.9 2.0208	$_{35}$Br 11.84 3.364	$_{36}$Kr 14.00 <0
$_{37}$Rb 4.18 2.16 0.4859	$_{38}$Sr 5.69 2.59 0.11	$_{39}$Y 6.38 3.1 0.308	$_{40}$Zr 6.95 4.05 0.427	$_{41}$Nb 6.88 4.3 0.894	$_{42}$Mo 7.18 4.6 0.747	$_{43}$Tc 7.28 4.9 0.55	$_{44}$Ru 7.36 4.71 1.05	$_{45}$Rh 7.46 4.98 1.138	$_{46}$Pd 8.343 5.12 0.558	$_{47}$Ag 7.57 4.26 1.303	$_{48}$Cd 8.99 4.22 0.260	$_{49}$In 5.78 4.12 0.30	$_{50}$Sn 7.34 4.42 1.15	$_{51}$Sb 8.64 4.55 1.07	$_{52}$Te 9.01 4.95 1.9708	$_{53}$I 10.45 3.059	$_{54}$Xe 12.13 <0
$_{55}$Cs 3.893 2.14 0.4716	$_{56}$Ba 5.21 2.7 0.17	$_{57}$La 5.57 2.96 0.518	$_{72}$Hf 7.00 3.9 ≥0.1	$_{73}$Ta 7.89 4.25 0.323	$_{74}$W 7.98 4.55 0.816	$_{75}$Re 7.87 4.87 0.12	$_{76}$Os 8.70 4.83 1.12	$_{77}$Ir 9.0 5.27 1.566	$_{78}$Pt 8.96 5.65 2.128	$_{79}$Au 9.22 5.1 2.309	$_{80}$Hg 10.43 4.49 0.186	$_{81}$Tl 6.11 3.84 0.3	$_{82}$Pb 7.41 4.25 0.364	$_{83}$Bi 7.29 4.22 0.946	$_{84}$Po 8.43 5.0 1.9	$_{85}$At 9.64 2.8	$_{86}$Rn 10.74 <0
$_{87}$Fr 3.98 2.1	$_{88}$Ra 5.28 2.8 0.17	$_{89}$Ac 5.17 3.2															

$_{58}$Ce 5.466 2.97 0.518	$_{59}$Pr 5.42 2.96 ≥0.1	$_{60}$Nd 5.49 3.2 ≥0.05	$_{61}$Pm 5.54 3.1	$_{62}$Sm 5.6 2.85 ≥0.05	$_{63}$Eu 5.67 2.5 ≥0.05	$_{64}$Gd 6.14 3.17 ≥0.1	$_{65}$Tb 5.85 3.15 ≥0.1	$_{66}$Dy 5.93 3.25 0.15	$_{67}$Ho 6.02 3.22 <0.005	$_{68}$Er 6.10 3.25 <0.005	$_{69}$Tm 6.18 3.1 0.035	$_{90}$Yb 6.25 3.0 0.010	
$_{90}$Th 6.08 3.4 >0.05	$_{91}$Pa 5.89 3.7 >0.05	$_{92}$U 6.05 3.63 >0.05	$_{93}$Np 6.19 3.9	$_{94}$Pu 6.06 3.6 ≥0.05	$_{95}$Am 6.00 3.7	$_{96}$Cm 6.02 3.9	$_{97}$Bk 6.23 3.8	$_{98}$Cf 6.30 4.0	$_{99}$Es 6.42 3.3	$_{100}$Fm	$_{101}$Md	$_{102}$No	

*The numbers under the symbols of elements are the ionization energies (upper rows), work functions (middle rows) and electron affinities (lower rows), given in eV/atom.

2. Einstein's heuristic paper

In 1895 Heinrich Hertz observed that ultraviolet light from the sparks of the generator of the radio waves he had recently discovered, falling on the negative electrode of his radio wave detector, induced the flow of electricity in the gap between the electrodes. He discovered the photoelectric effect. Lenard made improved measurements and he demonstrated by determination of their charge-to-mass ratio that the ejected particles are identical with the electrons.

In 1905, 26 year old Albert Einstein wrote within a few months five papers which changed the foundations of physics and our understanding of the Universe. The first paper of this series, written in May 1905, Einstein calls in a letter to his friend Conrad Habicht *very revolutionary* [1]. The paper deals with radiation and the energy properties of light. It was the objective of his paper to fill the gap, which existed at the beginning of XX century, between wave theory of light and statistical description of gas molecules. He considered Planck's quanta as particles of energy:

$$E = \frac{R}{N}\beta\nu \tag{1}$$

Equation (1) is equivalent to $E = h\nu$ introduced later by Millikan, since $R/N = k$ is the Boltzmann constant, and β is the second radiation constant in the Planck formula for the energy density of black-body radiation:

$$\rho_\nu = \frac{\alpha\nu^3}{\mathrm{e}^{\beta\nu/T} - 1} \tag{2}$$

Therefore $\beta\nu/T = h\nu/kT$ from which it follows that $h = k\beta$ or $h = (R/N)\beta$.

After the derivation of entropy of radiation, Einstein subsequently considered the following three phenomena in which light was transformed and converted to energy of various forms: (i) photoluminescence, (ii) photoeffect, and (iii) gas ionization by ultraviolet light.

In (i), he derives the Stokes rule on the basis of energy conservation to light quanta:

$$\frac{R}{N}\beta\nu_2 \le \frac{R}{N}\beta\nu_1 \tag{3}$$

where ν_1 is the frequency of primary beam and ν_2 is the frequency of the light to which the primary beam is converted. The Stokes rule, i.e. $\nu_2 \le \nu_1$ follows directly from Eq. (3).

The photoeffect was already investigated experimentally by Lenard in 1902 [2]. Einstein considers this effect as generation of electrons from a cathode by its irradiation by light quanta. He assumed that *on every electron leaving a solid has to be done a characteristic work P, therefore the kinetic energy of such electron is*

$$\frac{R}{N}\beta\nu - P \tag{4}$$

In this statement we recognize both the definition of electronic work function and the conservation energy principle. Using Lenard's experimental data, Einstein estimated P value for Zn as 4.3 eV. Later on the Einstein's photoelectric equation (4) for maximum energy of emitted electron was rewritten to the following form [3]:

$$\frac{1}{2}mv^2 = h\nu - P \tag{5}$$

From this equation Millikan determined the Planck constant, h, with much greater accuracy than it was possible to calculate it from the Planck radiation law (Table 2).

Table 2. The evolution of Planck constant

Author	h [J·s]
Einstein (1905)	$6.74\cdot10^{-34}$
Millikan (1914)	$6.58\cdot10^{-34}$
Today	$6.626\cdot10^{-34}$

In (iii), Einstein considers the action of ultraviolet light on gas molecules, and introduces *the work for ionization of one mole of a gas, J* and writes the following condition for the frequency of light:

$$R\beta\nu \geq J \tag{6}$$

Then using Lenard's maximum wavelength of light which is capable to ionize the air he estimated an average ionization energy of air molecule as ca. 10 eV, which is in fairly good agreement with determined by mass spectrometry the appearance potential of O_2^+, (12.3±0.3) V [4] which is the lowest among the air constituents.

In summary of Einstein revolutionary article on the quantum nature of light, let us emphasize that the introduced quanta can be converted to other quanta and can do real work. He defined *works* which later on were called as *work function* and *ionization energy*.

3. *WF* in thermionic emission

Somewhat earlier than Einstein's consideration of the photoeffect, the work function was defined by Richardson in his paper *On negative radiation from hot platinum* [5]. The thermionic emission was studied by various researchers in the last decade of 19th century, but Richardson first published in 1901 a quantitative interpretation of this phenomenon as the release of free-electron gas (*corpuscles*) existing in any con-

ducting material. Starting from the Maxwell–Boltzmann distribution of electron velocity, he found the following law for the saturation current density (j_s) which can be measured at sufficiently high potential of anode vs. hot cathode (120 V in his experiments):

$$j_s = ne\sqrt{\frac{kT}{2\pi m}}\mathrm{e}^{-\Phi/kT} \tag{7}$$

where Φ is defined by himself as *the work done by a corpuscle in passing through the surface layer*, T is the absolute temperature, k is Boltzmann constant (in his paper it was denoted as *R being the gas constant for a single corpuscle*), n is the total number of corpuscles per unit volume and m is its mass.

From his law, by plotting $\ln j_s$ vs. $1/T$, Richardson could determine both Φ and n for platinum: Φ = 4.1 eV and $n = (1.0–2.0)\cdot 10^{21}$ cm^{-3}. He used, after Thomson, $6.0\cdot 10^{-16}$ C for the elementary charge, and $1.204\cdot 10^{-11}$ cgs units for the m/k ratio.

Richardson interprets Φ/e as *the discontinuity in the potential at the surface of the metal*. Though from his paper follows the electric nature of *WF*, neither he nor Einstein did explain the origin of the postulated electric barrier which appears at the metal surface.

Richardson's law was derived about three decades later using the Fermi–Dirac distribution, see eg. textbook by Max Born [6]:

$$j_s = \frac{4\pi emk^2}{h^3}T^2\mathrm{e}^{-\Phi/kT} \tag{8}$$

where the universal constant $4\pi emk^2/h^3$ = 120 A·cm^{-2}·K^{-1} is expressed in terms of defined above physical constants e, m, k and h (Planck constant) which appear in the Fermi–Dirac distribution.

An entirely different derivation of the equations for electron emission from metals was published by Dushman in 1923 [7]. He considered electron emission from a metal as thermodynamically equivalent to the evaporation of atoms from a monoatomic solid. He derived identical temperature dependence as Eq. (8) but with the constant

$$\frac{2\pi emk^2}{h^3} = 60\ \mathrm{A}\cdot\mathrm{cm}^{-2}\cdot\mathrm{K}^{-2} \tag{9}$$

which differs by the factor two, because Dushman could not consider the statistical weight of the spin of free electrons (Uhlenbeck and Goudsmit derived the electron spin in 1926). The values reported in Dushman's paper for the thermionic emission constant varied from 60.2 to 38.4 A·cm^{-2}·K^{-1}. Later studies by numerous researches yield highly scattered results, but for pure metals with high melting point the emission constant is about 60 A·cm^{-2}·K^{-1}, which does not mean that only about 50% of the surface emits electrons if we consider that *WF* is variable (patchy) in the atomic scale.

4. Other phenomena

Simultaneously with the early investigations of the photoeffect and thermionic emission, the following phenomena were studied experimentally and considered theoretically, in which *WF* plays a great role. Below we briefly discuss these phenomena.

When electrons are emitted from incandescent metals there is an *absorption of thermal energy*, the absorbed power P is related to Φ as follows:

$$Pe = j\Phi \tag{10}$$

where j is the emission current, Φ is the work function and e is elementary charge. Note that Φ/e is the height of electric barrier at metal surface. From the heat absorption accompanying electron emission, Richardson and Cooke determined Φ values for several metals, which agree fairly well with those obtained from the Richardson law. Equation (7) was supplemented by Richardson with a small term of the average kinetic energy of emitted electrons which is $2kT$ and not $3/2kT$, hence

$$Pe = j(\Phi + 2kT) \tag{10a}$$

Davisson and Germer derived $\Phi = 4.52$ eV for tungsten from their calorimetric determinations using Eq. (10a), whereas their direct measurement of the emission as a function of temperature yields 4.48 eV [8].

The contact potential difference between a pair of metals, e.g. copper and zinc, was studied by Lord Kelvin in 1898 in the paper entitled *Contact electricity of metals* [9]. However the origin of the contact electricity was finally understood a decade later due to a great effort of Richardson, Debye and Langmuir. Making this long story as short as possible, I will recall a sharp distinction between potential difference and electromotive force (EMF) made by Langmuir in his seminal paper [10]: *The potential difference is equal to dW/de, i.e. work per unit charge when the charge becomes infinitesimal. In contrast, the EMF is defined as W/e, where W is the work done when an electron (charge e) moves from one place to another. Thus EMF is that which tends to cause current (actual electrons and ions) to flow*.

Langmuir shows that at the surface of a metal EMF = Φ/e (tending to make electrons flow into the metal), but there is no potential difference between metal and a remote point in vacuum. However, at the contact of two metals there is a potential difference which appears equal to $(\Phi_1 - \Phi_2)/e$, but there is no EMF (at identical temperature of both metals). A little EMF is observed when one junction is maintained at different temperature than the other. This effect is a measure of the temperature coefficient of the potential difference.

It should be emphasized here that the accurate method devised by Lord Kelvin becomes later on a very important method of *WF* determination, in which the contact potential difference is measured between an investigated sample and an electrode with known Φ. This electrode is made in form of a tip, and this way of *WF* determination is known as Kelvin probe method. The method is very useful in surface science until today.

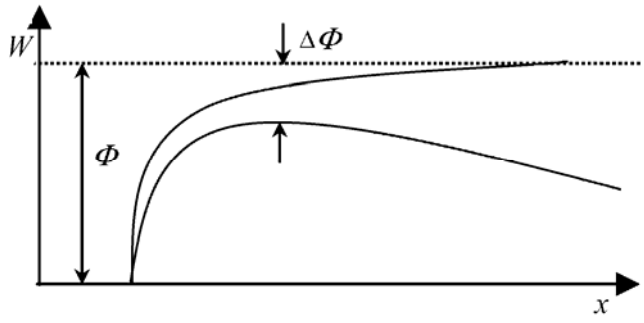

Fig. 1. Explanation of the Schottky effect

The *WF* is also connected with ionizing potentials of metal atoms but this relationship was poorly understood for a long time. This matter will be explained below in discussion of the ionization potential of metal clusters.

The Schottky effect is the effect of stronger electric fields applied to draw electrons emitted by hot cathodes and also by illuminated photocathodes. This effect of lowering the electric barrier at the surface was predicted theoretically by Schottky in 1923 [13]. He assumed that without external field an electron outside of a metal surface experiences the electrostatic image force, which was introduced previously by Thomson (i.e., Kelvin) for explanation of attraction of charged balls by a grounded metal plane. Considering the potential energy of an electron at distance x, we have

$$W_{\text{image}} = \int_x^\infty \frac{e^2}{4\pi\varepsilon_0 (2x)^2} dx = -\frac{e^2}{16\pi\varepsilon_0 x} \tag{11}$$

where ε_0 is the electric permittivity of free space. When a field strength E is applied the total potential energy near the surface is

$$W = \Phi - \frac{e^2}{16\pi\varepsilon_o x} - eEx \tag{12}$$

This function is plotted in Fig. 1. The maximum value of W is lowered by

$$\Delta\Phi = e\sqrt{\frac{eE}{4\pi\varepsilon_0}} \tag{13}$$

The Schottky formula was very well confirmed experimentally for moderately strong fields at which the barrier is very thick and no tunnelling of electrons occurs. In the case of thermionic emission, a test was made by Bruyne in 1928, and in the photoeffect case by Lawrence and Linford in 1930. These researchers have found *that outside the film of potassium on a thin layer of oxygen on tungsten the field followed closely the Schottky image law in the range* 1.5×10^{-6}–10^{-5} *cm from the surface* [14].

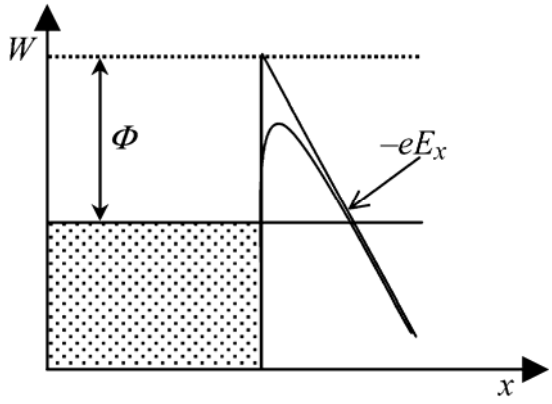

Fig. 2. A simplified plot of electron energy barrier at high electric fields E at the metal surface used by Fowler and Nordheim

Cold emission and STM. It was observed in the beginning of 20th century by a number of workers that electrons can be drawn from a cold cathode to which strong electric fields (~10^7 V·cm^{-1}) were applied. In 1928, Millikan and Lauritsen showed that the emission current density depends on the electric field according to the empirical formula

$$j = aE^2 \exp\left(-\frac{b}{E}\right) \tag{14}$$

where a and b are constants to be fitted for a particular material.

Electron emission under strong electric field at metal surface was theoretically described as the quantum-mechanical tunneling of electrons through a thin barrier by Fowler and Nordheim [11]. For the barrier shown in Fig. 2, they demonstrated that Eq. (14) holds with the following emission constants:

$$a = \frac{e}{2\pi h}\left(\frac{E_F}{\Phi}\right)^{1/2}\left(\Phi + E_F\right)^{-1}, \qquad b = \frac{8\pi\sqrt{2m}}{3h}\Phi^{3/2} \tag{15}$$

where E_F is the Fermi energy, Φ is work function, h is Planck constant, m is mass of electron. It is seen from Eq. (15) that WF is strongly related to the cold emission constants. Nowadays the formulae (14) and (15) are the basis of the scanning tunneling microscopy (STM). The tip of a STM may also be considered as the tool for WF examination in the atomic scale (cf. ref. [12]).

Surface ionization is a phenomenon of positive or negative ion emission from hot solid or liquid surfaces. The use of hot surfaces for ion production requires much lower temperatures than thermal ionization proceeding in the volume of a hot gas. The first observation of positive ion currents emitted from hot Pt were made by Richardson in 1906 and he noticed a similar exponential dependence vs. $1/T$ as in the case of

electron emission. In 1923, surface ionization of Cs atoms was investigated on heated tungsten wire by Kingdon and Langmuir [15].

In order to understand why hot surface with $WF = \Phi$ enhances the production of positive ions, consider the equivalent 3-step process: (i) evaporation of a neutral atom, (ii) its ionization in vacuum to ion and electron and (iii) return of this electron to the surface. The first step (i) requires little work in comparison to step (ii) where ionization energy EI, is needed. However in step (iii) the WF is returned to the surface. Hence practically only work equal to $EI - \Phi$ is needed in surface ionization, whilst as much as EI is needed in the thermal ionization in volume of a gas containing metal vapours. Conclusion: for high efficiency of positive ion emission one has to use a surface with high WF, eg. oxidized tungsten.

The case of negative ion emission, is equivalent to: (i) evaporation of a neutral atom, (ii) evaporation of electron and (iii) formation of negative ion, at which process the energy equal to the electron affinity (EA) is released. Assuming that EA is totally returned to the surface, we see that practically work $\Phi - EA$ is needed for negative ion formation. Hence for their efficient production one has to apply a low WF surface, eg. covered by Cs atoms or alkali earth oxides.

4. The nature of *WF*

Richardson in his pioneering study understood WF as the height of an electric barrier which keeps electrons within the metal volume. In 1912, he considered the existence of a double layer at a surface and the work against the attraction of its image in the conductor. Richardson explained why this work is not infinite, as in the ordinary electrostatics: This is *because the volume density of the electrification in the ultimate atoms of positive and negative electricity is finite* [16].

The earlier attempts to apply the Thomson formula for the potential energy of electron at distance x

$$W = -\frac{e^2}{16\pi\varepsilon_0 x} \tag{16}$$

can be found in papers by Jentzsch [17] and Debye [18], however these authors, similarly to Schottky [13], did not succeed in derivation of the potential energy at distances comparable to the size of atoms. This subject was considered in detail by Langmuir in 1916 [10], but he also could not find any method for calculation the critical distance x_0 from which the substitution to Eq. (16) leads to the proper value of WF. Instead he and also Dushman [7] calculated x_0 from known Φ and they found that x_0 runs from 1.58 Å (tungsten) to 3.19 Å (calcium). The intriguing question why work must be done against the image force in the region outside x_0 was attacked by Langmuir again in 1933. He concluded that in the region from metal interior to x_0 the forces acting on electrons are balanced by *electron pressure and the force due to po-*

tential gradient [19]. This explanation, however, did not lead him to a method of calculation of x_0 and *WF*. It should be noted that the formula for electron energy at a distance x proposed by Seitz [20]

$$W(x) = -\frac{e^2}{16\pi\varepsilon_o x + \frac{e^2}{\Phi}}, \qquad 0 \le x < \infty \tag{17}$$

and other similar formulae, which appeared later on, are useless in *WF* calculation because Φ has to be known for $W(x)$ calculation.

In 1936, Bardeen in his quantum-mechanical calculation first considered the exchange and correlation forces acting on electron close to the surface. Unfortunately, the quantum-mechanical calculation methods following Bardeen's idea did not lead to a formula for *WF* calculation.

With the advent of high speed computers sophisticated algorithms were developed to compute electronic properties of crystalline solid by solving the Schrödinger equation. These *ab-initio* methods succeeded in calculation of bulk electron energy distribution, but the surface properties were weakly predicted until early 70's of XX century. The most successful calculations of *WF* and surface energy for simple metals (Li, Na, K, Rb, Cs, Al, Pb, Zn and Mg) on the basis of uniform-positive-background model (latter called *jellium* model) were published by Lang and Kohn [21] in 1971. They obtained Φ values for simple metals which agree with experimental data within 5–10%. However, for noble metals the computed *WF* are 15–30% too low. It is important for understanding the nature of *WF* that they calculated

$$\Phi = \Delta\Phi - \overline{u} \tag{18}$$

where $\Delta\Phi$ is the change in electrostatic potential across the surface dipole layer created by the spilling out of electrons, and $\overline{u}$ is the chemical potential of the electrons in the bulk metal relative to the mean electrostatic potential there (Fig. 3). Equation (18) includes all many-body effects, in particular, the work against the image force.

The original *jellium* model, which totally ignored the discrete ionic structure, leads to a lack of mechanical equilibrium, hence it was "stabilized" by adding extra parameter to account properly the bulk metal properties, and the modified parameter accounting for atomic corrugation at the exposed crystal face. Good results with stabilized *jellium* model for simple metals were obtained recently by Kiejna [22].

Another important *ab-initio* study was published by Skriver and Rosengaard [23] in 1992. They implemented an efficient self-consistent Green's-function technique and calculated *WF* and surface energy for simple and transition metals. Their results for most of transition metals are, however, generally too high when compared with experiment, see comment by Durakiewicz et al. [24]. Moreover, the nature of electronic work function is lost in complex and approximate calculations.

An entirely different approach was proposed by Brodie [25] in 1995. He returned to the electrostatic image potential energy (see Eq. (11)) but the integration is done

from a minimum distance d at which the image force starts to act. This distance is incidentally equal to x_0 in early works, e.g. in Dushman and Langmuir papers. However Brodie derived a simple formula from the Heisenberg uncertainty principle.

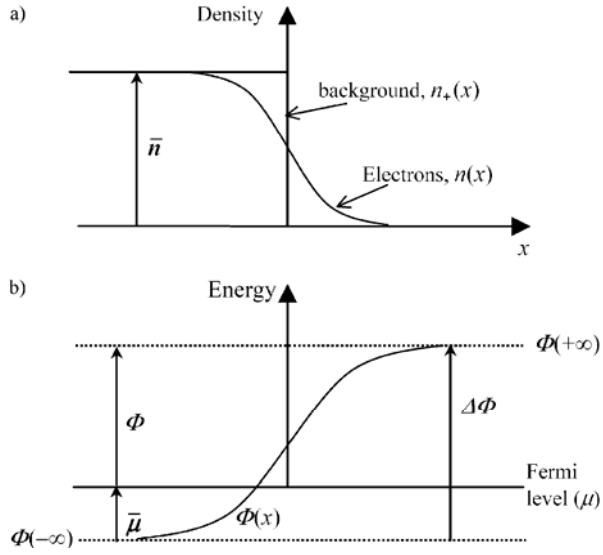

Fig. 3. Distribution of positive and negative charge densities in the jellium model (a) and plot of the potential energy of a free electron at the metal surface in jellium model (b)

He argues as follows: *There is a region bounded by a surface spaced d from the classical metal surface that an electron inside the metal can transverse by converting its kinetic energy to potential energy without doing any work. At d the kinetic energy of electron is zero and it is assumed that at this point the classical image force begins to act. The work function is then the energy that has to be given to an electron to take it from d where it has zero kinetic energy to a field-free region far enough away from the metal surface for the image force to be zero.* […] *Inside the metal, quantum theory is required to determine the highest kinetic energy an electron may have at 0 K as it approaches the classical metal surface (namely, the Fermi energy E_F). Beyond d, classical mechanics is adequate to determine the work function. Between the classical metal surface and the d surface, the momentum changes from $(2E_F/m^*)^{1/2}$ to zero, where m^* is the effective mass of the electron inside the metal as it approaches the surface. We identify the distance d with the Heisenberg uncertainty distance associated with this change in momentum, as appears to be required by continuous decoherence from quantum to classical states.*

Brodie's novel approach to *WF* calculation without use of the *ab-initio* methods was substantially improved by Halas and Durakiewicz [26], who applied the metallic plasma model for calculation of the *d* value. Their method become very effective not only in calculation *WF* of elements, but also for conducting compounds as hydrides [27], borides and alkali and alkaline earth metal oxides [28].

In order to introduce this method, let us recall the basic formulae from plasma physics such as these for the length of spontaneous polarization and the screening length. Necessary modifications of these formulae will be made to make them applicable to the plasma constituted of free electrons and ions in a metal lattice.

Locally, plasma can spontaneously polarize itself, which means that electrons are somewhat shifted against ions. The polarization requires energy which in the case of gaseous plasma is taken from thermal energy, i.e. average kinetic energy per degree of translational motion, (1/2)*kT*. In the case of free electrons such polarization can be produced mainly at the expense of Fermi kinetic energy E_F because even at melting point of a crystal, the thermal energy is small in comparison to E_F.

Hence, the polarization length in the case of metal may be calculated by replacing (1/2)*kT* by E_F in the classical formula of plasma physics, which leads to the following formula:

$$d = \sqrt{\frac{2\varepsilon_0 E_F}{ne^2}} \tag{19}$$

where ε_0 is the electric permittivity of free space, n is average density of free electrons in the metal lattice, and e is the elementary charge.

The work function is calculated from Eq. (11) in which x is substituted by d given by Eq. (19) being divided by the common scaling factor α. Before doing this, let us rewrite formula (11) in a more convenient form:

$$\Phi = \frac{\alpha}{2}\frac{e^2}{8\pi\varepsilon_0 a_0}\frac{a_0}{d} = \frac{\alpha Ry}{2\dfrac{d}{a_0}} \tag{20}$$

where a_0 is Bohr radius (0.52918 Å) and *Ry* is the atomic unit of energy (13.6058 eV). The d value is conveniently calculated using Eq. (19) in which free electron density n is replaced by density parameter r_s, defined as follows:

$$\frac{1}{n} = \frac{4}{3}\pi r_s^3 \tag{21}$$

Now, Eq. (19) can be rewritten in the following way:

$$d = \sqrt{\frac{2\varepsilon_0 EF}{e^2}\cdot\frac{4\pi r_s^3}{3}} = \sqrt{E_F\left(\frac{e^2}{8\pi\varepsilon_0 a_0}\right)^{-1}\frac{r_s^3}{3a_0}} = \frac{a_0}{\sqrt{3}}\left(\frac{E_F}{Ry}\right)^{1/2}\left(\frac{r_s}{a_0}\right)^{3/2} \tag{22}$$

When this formula is substituted to Eq. (21), one obtains:

$$\Phi = \frac{\alpha\sqrt{3}}{2}Ry\left(\frac{E_F}{Ry}\right)^{-1/2}\left(\frac{r_s}{a_0}\right)^{-3/2} \tag{23}$$

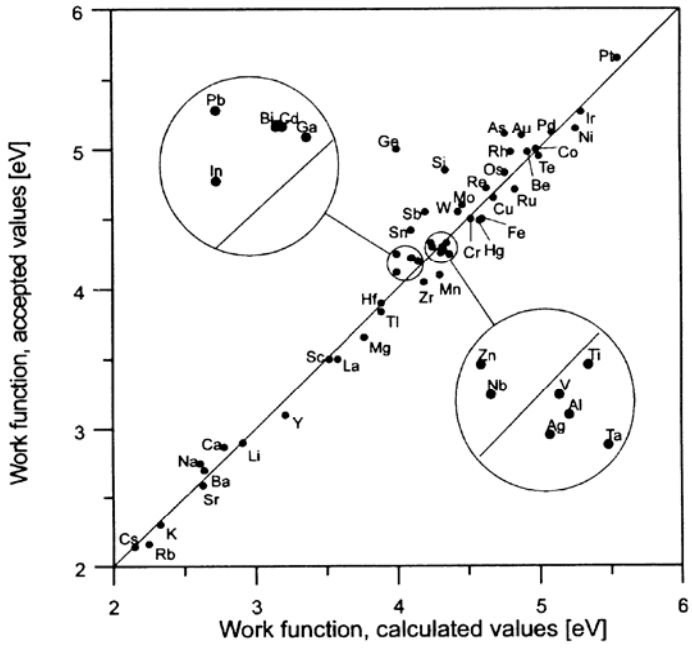

Fig. 4. Measured *WF* values vs. calculated by the metallic plasma model

For practical calculations, Eq. (23) may be rewritten in the following form:

$$\Phi = \frac{11.783\alpha}{\left(r_s[\text{a.u.}]\right)^{3/2}\left(E_F[Ry]\right)^{1/2}} = \frac{43.46\alpha}{\left(r_s[\text{a.u.}]\right)^{3/2}\left(E_F[\text{eV}]\right)^{1/2}} \quad [\text{eV}] \tag{24}$$

where r_s is expressed in units of the Bohr radius. One can see that work function is expressed by the density parameter r_s, and the Fermi energy E_f. The scaling factor α was assumed to be equal to unity for all elements except the alkali metals, Ca, Sr, Ba, Ra and Tl for which it was assumed to be equal 0.86. So far the α factor is treated as only an empirical constant which most likely may be derived theoretically. In Figure 4, measured *WF* values vs. those calculated by this method are shown.

6. Ionization potential (*IP*) and *WF*

The relation between *IP* and *WF* is conceptually very simple and it is shown in Fig. 5, where *a* represents a single atom of metal vapour with its barrier for a valence electron, while *b* represents a solid constituted from a few atoms. The ground state of the atom is split into a band of states which are filled to the maximum level, called the Fermi level. For no field in the space around the atom and the solid, the potential energy at infinity in both cases is the same and it may be assumed as zero. This simple

picture leads, however, to many-body calculation for a single atom but with a number of electrons and to yet more difficult calculation in the case of a solid. At the beginning of 21th century, there is no hope that a simple relationship between *IP* and *WF* will be found by the *ab-initio* methods.

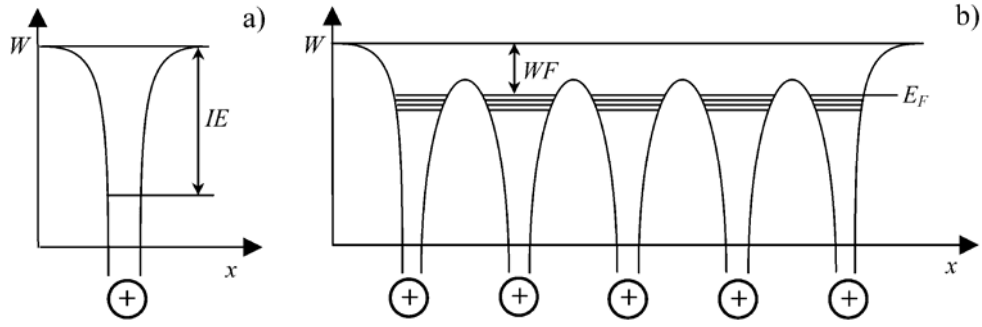

Fig. 5. Plot of potential energy of the valence electron as a function of distance from the positive ion core and its ground level (a), as well as plot of potential energy across a metal where the valence electrons occupy the conduction band up to the Fermi level E_F (b)

In order to solve this problem in a simplified way, consider a neutral spherical ball of a metal cluster consisting a large number N of atoms and then we will reduce $N \rightarrow 1$. Hence *IP* of the cluster will turn in to *IP* of single atom (of metal vapour). The *IP* of clusters were calculated for a long time very roughly without the metallic plasma model. Serious errors in derivation of the asymptotic formula (for cluster radius, $R >>$ atom radius, r) in the literature was corrected by the author of this paper [29]. The "exact" formula derived in the framework of the metallic plasma model for *IP* of a cluster is:

$$IP = \Phi\left[\left(1+\frac{x}{2}\right)^{-1} + 2x\frac{1+2x}{(1+x)^2}\right] \tag{25}$$

where Φ is the *WF* of a macroscopic piece of metal, $x = d/R$, d is the distance from which the image force starts to act (see the preceding section), and R is the cluster radius.

It follows from the image potential formula (11) that d may be expressed by Φ:

$$d = \frac{e^2}{16\pi\varepsilon_0\Phi} \tag{26}$$

Substituting Eq. (26) and $R = r$ into Eq. (25), we obtain the relationship between *IP* of a metal vapour and metal *WF*. Table 1 convinces us that $WF \approx 0.5IP$ which also follows from Eq. (25) applied to $N = 1$. Better agreement is obtained for transition metals if we consider that the number of free electrons per atom gradually increases

with N, when $N \rightarrow 1$. Therefore we should substitute into Eq. (26) not real *WF*, but modified Φ value for a reduced number z.

7. Conclusion

It seems that the semi-empirical approach in *WF* calculation, which was developed about 100 years after it was defined by Richardson and Einstein, provides a good basis for understanding the origin of *WF* and its relationship with *IP* of metallic clusters and atoms. So far the plasma model gives the best prediction of *WF* for metals and some important conducting compounds.

Acknowledgements

I thank most sincerely Professor Hans J. Lippolt from Heidelberg for his kind supply of hardly accessible literature from 19th and the beginning of 20th century. I am grateful to Dr. J. Szaran for his assistance in preparation of the manuscript and to Mr. M. Czarnacki for drawing figures. I appreciate the comments and corrections by professor A.E. Fallick from Scottish Universities Environmental Research Centre, by Dr. T. Durakiewicz from Los Alamos National Laboratories, and by an unknown reviewer.

References

[1] EINSTEIN A., Ann. Phys., 17 (1905), 132.
[2] LENARD P., Ann. Phys., 8 (1902), 150.
[3] MILLIKAN R.A., Phys. Rev., 7 (1916), 18.
[4] HAGSTRUM H.D., TATE J.T., Phys. Rev., 59 (1941), 354.
[5] RICHARDSON B.A., Proc. Camb. Phil. Soc., 11 (1901), 286.
[6] BORN M., *Atomic Physics*, 7th Edition, Blackie & Son, London, 1963.
[7] DUSHMAN S., Phys. Rev., 21 (1923), 623.
[8] DAVISSON C.J., GERMER L.H., Phys. Rev., 20 (1922), 300.
[9] LORD KELVIN, Phil. Mag., 46 (1898), 82.
[10] LANGMUIR I., Trans. Am. Electrochem. Soc., 29 (1916), 125.
[11] FOWLER R.H., NORDHEIM L., Proc. Roy. Soc. A, 119 (1928), 173.
[12] JIA J.F., INOUE K., HASEGAWA Y., YANG S.W., SAKURI T., Phys. Rev. B, 58 (1998), 1193.
[13] SCHOTTKY W., Physik. Zeitschr., 15 (1914), 872.
[14] LAWRENCE E.O., LINFORD L.B., Phys. Rev., 36 (1930), 482.
[15] KINGDON K.N., LANGMUIR I., Phys. Rev., 21 (1923), 380.
[16] RICHARDSON B.A., Phil. Mag., 23 (1912), 278.
[17] JENTZSCH F., Ann. Phys., 27 (1908), 129.
[18] DEBYE P., Ann. Phys., 33 (1910), 441.
[19] LANGMUIR I., Phys. Rev., 43 (1933), 224.
[20] SEITZ F., *The Modern Theory of Solids*, McGraw-Hill Book Co., New York, 1940.
[21] LANG W.D., KOHN W., Phys. Rev. B, 3 (1971), 1215.
[22] KIEJNA A., Prog. Surf. Sci., 61 (1999), 85.
[23] SKRIVER H.L., ROSENGAARD N.M., Phys. Rev. B, 46 (1992), 7157.
[24] DURAKIEWICZ T., HALAS S., ARKO A., JOYCE J.J., MOORE D.P., Phys. Rev. B, 64 (2001), 045101.
[25] BRODIE I., Phys. Rev. B, 51 (1995), 13660.
[26] HALAS S., DURAKIEWICZ T., J. Phys. C.: Condens. Matter, 10 (1998), 10815.

[27] HALAS S., DURAKIEWICZ T., Surf. Sci., 555 (2004), 43.
[28] HALAS S., DURAKIEWICZ T., Appl. Surf. Sci., 252 (2006) 6119.
[29] HALAS S., Chem. Phys. Lett., 370 (2003), 300.

Received 8 September 2005
Revised 2 November 2005

Table 1. The periodic table of elements*

$_{1}$H 13.598 0.7542																	$_{2}$He 24.58 –0.22
$_{3}$Li 5.39 2.9 0.6182	$_{4}$Be 9.32 4.98 –0.19											$_{5}$B 8.30 4.45 0.227	$_{6}$C 11.26 5.0 1.2629	$_{7}$N 14.54 –0.07	$_{8}$O 13.61 1.462	$_{9}$F 17.42 3.399	$_{10}$Ne 21.56 –0.3
$_{11}$Na 5.14 2.75 0.5479	$_{12}$Mg 7.64 3.66 –0.22											$_{13}$Al 5.98 4.28 0.442	$_{14}$Si 8.15 4.85 1.385	$_{15}$P 10.55 0.7464	$_{16}$S 10.36 2.077	$_{17}$Cl 13.01 3.615	$_{18}$Ar 15.76 –0.36
$_{19}$K 4.34 2.30 0.5015	$_{20}$Ca 6.11 2.87 0.0215	$_{21}$Sc 6.56 3.4 0.189	$_{22}$Ti 6.83 4.33 0.080	$_{23}$V 6.74 4.3 0.526	$_{24}$Cr 6.76 4.5 0.667	$_{25}$Mn 7.43 4.1 <0.005	$_{26}$Fe 7.90 4.5 0.164	$_{27}$Co 7.86 5.0 0.662	$_{28}$Ni 7.63 5.15 1.157	$_{29}$Cu 7.72 4.51 1.228	$_{30}$Zn 9.39 4.33 0.093	$_{31}$Ga 6.00 4.15 0.31	$_{32}$Ge 7.89 5.0 1.23	$_{33}$As 9.81 4.77 0.81	$_{34}$Se 9.75 5.9 2.0208	$_{35}$Br 11.84 3.364	$_{36}$Kr 14.00 <0
$_{37}$Rb 4.18 2.16 0.4859	$_{38}$Sr 5.69 2.59 0.11	$_{39}$Y 6.38 3.1 0.308	$_{40}$Zr 6.95 4.05 0.427	$_{41}$Nb 6.88 4.3 0.894	$_{42}$Mo 7.18 4.6 0.747	$_{43}$Tc 7.28 4.9 0.55	$_{44}$Ru 7.36 4.71 1.05	$_{45}$Rh 7.46 4.98 1.138	$_{46}$Pd 8.343 5.12 0.558	$_{47}$Ag 7.57 4.26 1.303	$_{48}$Cd 8.99 4.22 0.260	$_{49}$In 5.78 4.12 0.30	$_{50}$Sn 7.34 4.42 1.15	$_{51}$Sb 8.64 4.55 1.07	$_{52}$Te 9.01 4.95 1.9708	$_{53}$I 10.45 3.059	$_{54}$Xe 12.13 <0
$_{55}$Cs 3.893 2.14 0.4716	$_{56}$Ba 5.21 2.7 0.17	$_{57}$La 5.57 2.96 0.518	$_{72}$Hf 7.00 3.9 ≥0.1	$_{73}$Ta 7.89 4.25 0.323	$_{74}$W 7.98 4.55 0.816	$_{75}$Re 7.87 4.87 0.12	$_{76}$Os 8.70 4.83 1.12	$_{77}$Ir 9.0 5.27 1.566	$_{78}$Pt 8.96 5.65 2.128	$_{79}$Au 9.22 5.1 2.309	$_{80}$Hg 10.43 4.49 0.186	$_{81}$Tl 6.11 3.84 0.3	$_{82}$Pb 7.41 4.25 0.364	$_{83}$Bi 7.29 4.22 0.946	$_{84}$Po 8.43 5.0 1.9	$_{85}$At 9.64 2.8	$_{86}$Rn 10.74 <0
$_{87}$Fr 3.98 2.1	$_{88}$Ra 5.28 2.8 0.17	$_{89}$Ac 5.17 3.2															

$_{58}$Ce 5.466 2.97 0.518	$_{59}$Pr 5.42 2.96 ≥0.1	$_{60}$Nd 5.49 3.2 ≥0.05	$_{61}$Pm 5.54 3.1	$_{62}$Sm 5.6 2.85 ≥0.05	$_{63}$Eu 5.67 2.5 ≥0.05	$_{64}$Gd 6.14 3.17 ≥0.1	$_{65}$Tb 5.85 3.15 ≥0.1	$_{66}$Dy 5.93 3.25 0.15	$_{67}$Ho 6.02 3.22 <0.005	$_{68}$Er 6.10 3.25 <0.005	$_{69}$Tm 6.18 3.1 0.035	$_{90}$Yb 6.25 3.0 0.010	$_{71}$Lu 5.43 3.3 ≥0.1
$_{90}$Th 6.08 3.4 >0.05	$_{91}$Pa 5.89 3.7 >0.05	$_{92}$U 6.05 3.63 >0.05	$_{93}$Np 6.19 3.9	$_{94}$Pu 6.06 3.6 ≥0.05	$_{95}$Am 6.00 3.7	$_{96}$Cm 6.02 3.9	$_{97}$Bk 6.23 3.8	$_{98}$Cf 6.30 4.0	$_{99}$Es 6.42 3.3	$_{100}$Fm	$_{101}$Md	$_{102}$No	$_{103}$Lr

*The numbers under the symbols of elements are the ionization energies (upper rows), work functions (middle rows) and work functions (lower rows), given in eV/atom.

Materials Science-Poland, Vol. 24, No. 4, 2006

Analysis of the processes of silicon epitaxial lateral overgrowth in Ar ambient gas

I. JÓŹWIK*, J. M. OLCHOWIK

Institute of Physics, Lublin University of Technology, Nadbystrzycka 38, 20-618 Lublin, Poland

Liquid phase epitaxy (LPE) and, in particular, epitaxial lateral overgrowth (ELO) is an attractive method of thin film deposition, owing to the simplicity of its technology and a reduced growth temperature. In this paper, we present recent results of the ELO of silicon layers carried out by means of LPE using Ar as an ambient gas, without any addition of hydrogen, potentially explosive gas, which makes this deposition technique a very safe process. The aim of the this work focused on the silicon ELO growth on partially masked substrates was to determine optimal conditions of growth resulting in ELO layers of the maximum aspect ratio and minimum defect density. Data presented herein clearly show that the epitaxial layers characterized by the maximum value of the aspect ratio can be obtained by application of the 0.25 °C/min cooling rate. Noteworthy is the fact that in the same conditions the defect density achieves the minimum value of 1.07×10^4 cm^{-2}, which is the amount smaller by the factor of 10 than the defect density of Si substrates used (1.7×10^5 cm^{-2}). It confirms the ELO technique as a promising tool for the fabrication of low-defect density silicon layers of good morphology.

Key words: *liquid phase epitaxy; silicon thin films; crystal morphology*

1. Introduction

Attention of scientists has been focused in recent years on thin film materials technologies, as they seem to be promising alternatives to bulk silicon materials reducing the cost of photovoltaic (PV) modules production. Due to this fact, an increased activity has taken place using liquid phase epitaxy (LPE) and, in particular, epitaxial lateral overgrowth (ELO), to prepare silicon thin film materials for solar cells applications. LPE is an attractive method of the thin film deposition processes, owing to the simplicity of its technology and a reduced growth temperature (below the melting point of silicon).

ELO is a method of epitaxial growth on a partially masked substrate. Prior to the growth, the substrate is covered with a thin masking film of insulator and patterned by

*Corresponding author, e-mail: i.jozwik@pollub.pl

means of a standard photolithography technique forming a suitable set of silicon open windows on the sample area. Afterwards, the silicon epilayer is deposited on the surface of the masked substrate (Fig. 1). The growth of Si occurs selectively – it starts in the seeding windows and proceeds in two directions: normal to the surface, and also spreads over the parts of the insulating layer [1]. In favourable conditions, the adjacent stripes of Si tend to coalesce forming a continuous epilayer. One of the advantages of such an approach is that the thin masking film prevents the propagation of defects present in the Si substrate into the ELO layer, thus the ELO process is a promising tool in reducing defect density of epitaxial silicon layers.

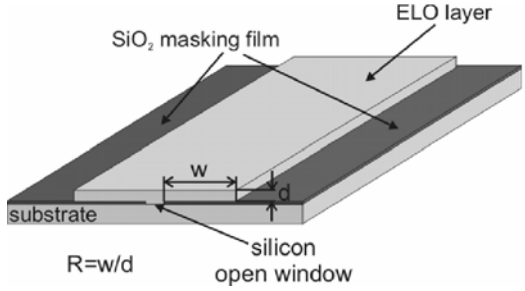

Fig 1. Schematic cross section of the ELO layer: the width *w* and thickness *d*, as well as the aspect ratio *R* of the ELO layer are defined herein

Generally, LPE is a promising technique in reducing the costs of the PV modules not only because of low-cost exploitation of the process but also because of the simplicity of the apparatus design. However, usually when it comes to the LPE process, a continuously flowing H_2 is used as a process gas, hence the safety level of the process decreases while there is a rise in the costs. A few attempts to avoid the H_2 application have been made, such as growth in a vacuum [2] or the use of Ar/H_2 mixture as ambient gas [3]. This paper reports on the results of the epitaxial lateral overgrowth of Si carried out by means of LPE using Ar as an ambient gas, without any additions of hydrogen. Elimination of a potentially explosive gas makes this technique a very safe process.

2. Experimental

The growth of Si epilayers was conducted by means of LPE with a horizontal sliding graphite boat system, with application of Ar pure gas. Si thin layers were grown on silicon substrates (111) oriented and partially masked with an SiO_2 film (0.1 μm thick) obtained by oxidization of Si wafers in dry O_2 for 1 hour at 1000 °C, and patterned by conventional photolithography technique, forming a suitable set of openings for seeding windows. Sample dimensions were 10×10 mm^2. As the result, a set of parallel lines of silicon seeding areas 50 μm wide with 100 μm SiO_2 spacing, oriented along $<0\,\bar{1}\,1>$ direction were formed.

We chose (111) oriented Si substrates as it is known [4] that the aspect ratio of Si films grown on (111) Si, defined as the width of the laterally overgrown Si to the thickness of Si film (see Fig. 1) is higher than in the case of (100) surface orientation, even though from the atomistic point of view the (100) surface offers more nucleation sites.

Prior to the growth, both substrate and the source Si were cleaned with organic solutions using acetone and trichloroethylene, then chemically etched in H_2SO_4:H_2O_2, 2:1 solution and dipped in 4% HF. To prepare the melt we used tin (5 *N*) as the solvent, which was etched in 36% HCl. In addition, small amounts (0.3 wt. % approx.) of Al (5 *N*) were incorporated into the growth solution, in order to remove native oxides formed on the silicon open window surfaces. After 1 hour of saturation at 920 °C, the growth was performed with various cooling rates: 0.25 °C/min, 0.5 °C/min, 1.0 °C/min with a fixed value of the supersaturation.

After the process of growth, the substrate with Si thin epilayers and the solution were disconnected, cooled to the room temperature and cleaned with aqua regia (HNO_3:HCl, 1:3) in order to remove any residual remains of the solution. The silicon thin layers grown on Si substrates masked with SiO_2 were examined using a scanning electron microscope (SEM).

3. Results and discussion

The experiments carried out, followed by the measurements of the width and thickness of the silicon ELO layers, resulted in the dependences of the parameters characterizing the ELO layers on the cooling rate at constant supersaturation. The values of particular parameters are the average values obtained after a series of experiments.

As shown in Fig. 2, the width of the ELO layer decreases with the increase of the cooling rate at constant supersaturation. This finding can be explained by consideration of the length of the growth period applied in each case. According to the data reported in previous works [5, 6], the value of width of the ELO layers depends on the time of growth at constant supersaturation, i.e. it increases in time until a plateau is achieved. At the first 2 hours of growth this dependence is approximately linear. Thus, as a high value of the cooling rate at a constant supersaturation means that the time of growth is shorter, it becomes clear why ELO layers obtained during the growth at lower values of cooling rates (here 0.25 °C/min) achieve higher values of width than in the case of 1.0 °C/min cooling rate, for example. In the cases investigated in this work, the difference between these two extreme widths reaches 20 μm, as the growth of ELO layer at 0.25 °C/min results in the widths equal 50 μm on average, while the width of ELO layer grown at 1.0 °C/min is ca. 30 μm.

A slightly different behaviour can be observed in the changes of the thickness of the ELO layers on the cooling rate. As the data show, the thickness of the ELO layer

is maximum reaching 38 μm when the 0.5°C/min cooling rate is applied during the growth, while the values in the two other cases are smaller by 3–5 μm, the differences being within the measurement error. That is why it is worthy to consider another parameter characterizing the ELO layers, i.e. the aspect ratio.

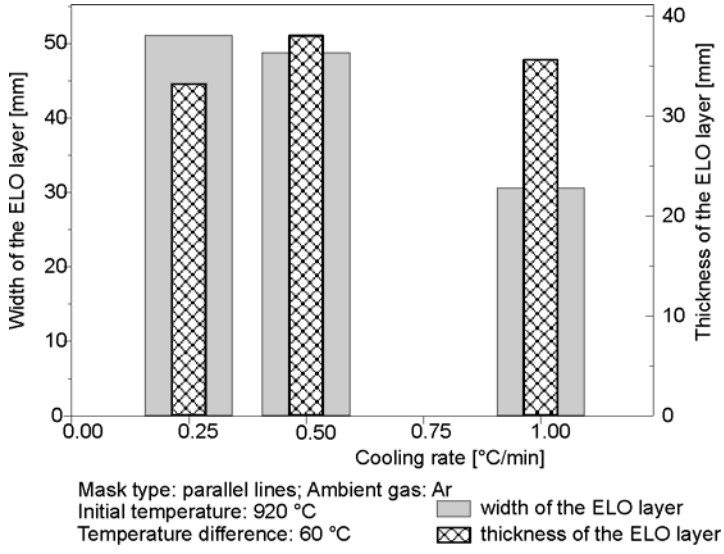

Fig. 2. Dependences of the width and thickness of the ELO layers on the cooling rate at a constant supersaturation

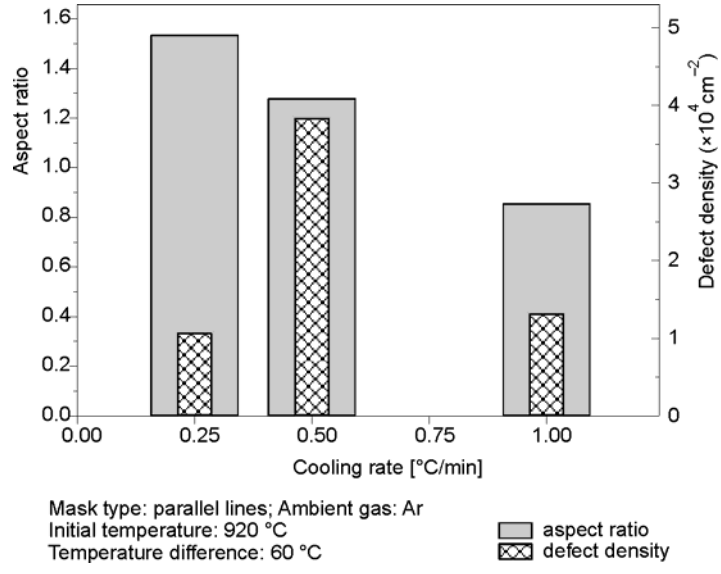

Fig. 3. Dependences of the aspect ratio and defect density on the cooling rate at a constant supersaturation

The dependences of the aspect ratio and of the defect density on the cooling rate at a constant supersaturation are presented in Fig. 3. The defect densities of silicon ELO layers as well as the Si substrates used were determined using the Secco etching method [7].

The aim of the this work, focused on the silicon ELO growth on partially masked substrates, was to determine the optimal conditions of growth resulting in the ELO layers of the maximum aspect ratio value and the minimum defect density. The data presented in Fig. 3 clearly show that the epitaxial layers grown in the conditions specified above, characterized by the maximum value of the aspect ratio can be obtained by application of the 0.25 °C/min cooling rate. Noteworthy is the fact that in the same conditions the defect density achieves the minimum value of 1.07×10^4 cm^{-2}, which is the amount smaller by one order of magnitude than the defect density of Si substrates used (1.7×10^5 cm^{-2}). It confirms the ELO technique as a promising tool for the fabrication of low-defect density silicon layers of good morphology.

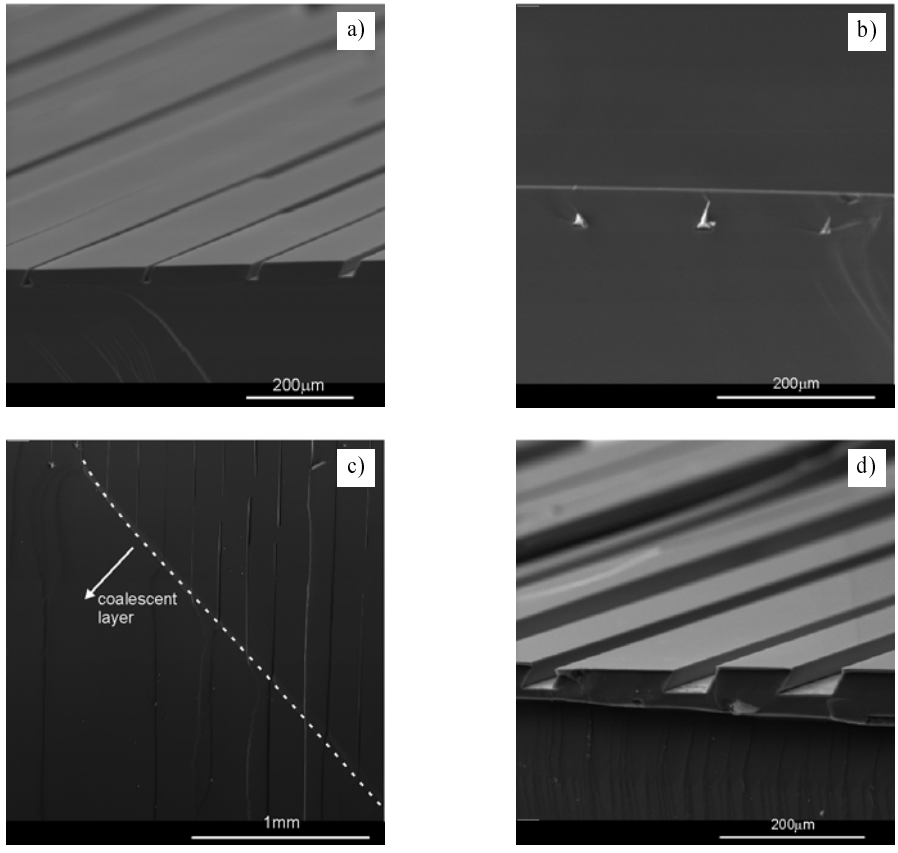

Fig. 4. The view of the epitaxial silicon layers grown with the application of various cooling rates: a) 0.25°C/min, b, c) 0.5°C/min and d) 1.0°C/min at constant supersaturation

The morphology of epitaxial layers is an important indicator of the crystal quality. It is essential to obtain planar, mirror-like surfaces, free of any surface imperfections or inclusions. The results of the investigations presented here show that the cooling rate is an important parameter influencing the layer morphology. Figure 4 presents the view of the epitaxially grown Si layers obtained in the experiments carried out under three different cooling rates.

The layers grown at 0.25 °C/min cooling rate are thinner than those obtained at 1.0 °C/min, but of the equal thickness of the neighbouring stripes (Fig. 4a), which is not observed in the epilayers grown at 1.0 °C/min cooling rate (Fig. 4d). The rise in the value of the cooling rate manifests itself also in the presence of tin inclusions observed in the epitaxial layers (Fig. 4b) which are the leftovers of the growth solution jammed between the adjoining stripes. These inclusions are distributed throughout the epitaxial layer and not just confined to the interface between epilayer and the substrate.

In some cases, the leftovers of the growth solution were present on the sample surface which served as a source of Si atoms being able to build in the crystal forming the upper parts of the ELO layer, leading to a continuous coalescent epilayer. The clear border line on the left-down of which the fully coalescent layer is visible can be seen in Fig. 4c.

4. Conclusions

The results of investigation presented here demonstrate that the ELO technique is a suitable method enabling one to obtain silicon thin layers without any use of H_2, with Ar as an ambient gas. The procedure reduces the costs simultaneously making the ELO a very safe process. The kinetics of growth as well as the morphology of the epitaxially overgrown layers have been studied. Data presented here show that the widths of the ELO layers strongly depend on the cooling rate at a constant supersaturation. A slightly different behaviour is observed in the case of the thickness of the epilayer, which stays at the same level in the range of the measurement error value. The results show that the epitaxial overgrowth resulting in the epilayers characterized by the maximum aspect ratio value and minimum defect density at the same time is possible. Epitaxial lateral overgrowth technique has been confirmed as a promising tool and suitable method for the fabrication of low-defect density silicon layers of good morphology.

References

[1] ZYTKIEWICZ Z.R., Thin Solid Films, 412 (2002), 64.
[2] SHI Z., YOUNG T.L., GREEN M.A., Mater. Lett., 12 (1991), 339.
[3] SHI Z., ZHANG W., ZHENG G.F., KURIANSKI J., GREEN M.A., BERGMANN R., J. Cryst. Growth, 151 (1995), 278.

[4] BERGMANN R., J. Cryst. Growth, 110 (1991), 823.
[5] JÓŹWIK I., KRAIEM J., OLCHOWIK J.M., FAVE A., SZYMCZUK D., ZDYB A., Mol. Phys. Rep., 39 (2004), 91.
[6] KRAIEM J., FAVE A., KAMINSKI A., LEMITI M., JÓŹWIK I., OLCHOWIK J.M., Proc. 19th European Photovoltaic Solar Energy Conference and Exhibition, Paris, France, 7–11 2004, 1 (2004), 1158.
[7] SECCO D'ARAGONA F., J. Electrochem. Soc., 119 (1972), 948.

Received 10 September 2005
Revised 21 November 2005

Materials Science-Poland, Vol. 24, No. 4, 2006

Surface free energy of zinc coating after finishing treatment

A. RUDAWSKA*, J. KUCZMASZEWSKI

Department of Production Engineering, Mechanical Engineering Faculty,
Lublin University of Technology, Nadbystrzycka 36, 20-618 Lublin

Protective properties of zinc coating increase with an additional coating such as: chromate, phosphate, paint and polymer coating. Besides, additional treatment of zinc coating serves decorative purposes as well. The paper presents the influence of additional coating of zinc coating on their adhesive properties which are especially helpful in processes where adhesion plays an essential role. These processes include among others: gluing, painting or varnishing. Adhesive properties are characterized by the value of surface free energy.

Key words: *surface free energy; adhesive properties*

1. Introduction

Surface free energy usually determines surface energetic state (adhesive properties) of construction materials. It is of great importance in such technologies as gluing, sealing, painting, printing, decorating, and in many others, where adhesion plays an important role.

The objects of tests and analyses are galvanic zinc-coated sheets after various finishing treatments applied in electrolytic zinc coating processes. The latter process is one of the future directions of development in electroplating. The aim is to produce in advance an additional coating on a covered coating. Electrolytic (galvanic) coatings are covered by organic layer (coating) through ion implantation, laser treatment or other methods to achieve significant improvement of electrolytic coating consumption properties or to obtain new coating properties. In many cases, additional treatment increases protective or decorative values. Very often additional treatments combine both these functions.

The finishing treatments such as chromate and phosphate coating, as well as special chemical treatment were analyzed. They were used to smoothen the coating (which requires etching in a bath of sulfuric acid and chromium trioxide).

*Corresponding author, e-mail: a.rudawska@pollub.pl

In terms of the adhesion theory, it is interesting whether the analyzed treatments have any important influence on the value of surface free energy, used as thermodynamic index of adhesive properties.

A comparison between polar and dispersion components of the surface free energy after finishing treatments is also interesting. It shows essential changes of polar component of surface free energy. These changes strongly influence a possibility of improving adhesive properties, in particular high-strength bonding join.

2. Theory

Surface free energy (γ_S) as one of the thermodynamic quantities describing equilibrium of atoms within the upper material layers, reflects specific unbalanced state of intermolecular interactions occurring at the surface phase between two media, being the characteristic feature of each material [1].

There are many methods to determine surface the free energy [1–5]. They are based on determination of dispersion and polar components according to the Berthelot hypothesis that the intermolecular interaction between molecules of two different materials is equal to geometric mean of the interactions between molecules.

In the paper, the surface free energy was determined by the Owens–Wendt method, one of the most popular methods to determine γ_S of solids. The polar and dispersion components of surface free energy were determined according to the following equations [4]:

$$\left(\gamma_s^d\right)^{0.5} = \frac{\gamma_d\left(\cos\Theta_d + 1\right) - \sqrt{\frac{\gamma_d}{\gamma_w}}\gamma_w\left(\cos\Theta_w + 1\right)}{2\left(\sqrt{\gamma_d{}^d} - \sqrt{\gamma_d{}^p\frac{\gamma_w{}^d}{\gamma_w{}^p}}\right)} \tag{1}$$

$$\left(\gamma_s{}^p\right)^{0.5} = \frac{\gamma_w\left(\cos\Theta_w + 1\right) - 2\sqrt{\gamma_s{}^d\gamma_w{}^d}}{2\sqrt{\gamma_w{}^p}} \tag{2}$$

where: γ_s^d – dispersion component of the surface free energy, γ_s^p – polar component of the surface free energy, γ_d – the surface free energy of diiodomethane, γ_d^d – dispersion component of the surface free energy of diiodomethane, γ_d^p – polar component of the surface free energy of diiodomethane, γ_w – the surface free energy of water, γ_w^d – dispersion component of the surface free energy of water, γ_w^p – polar component of the surface free energy water, Θ_d – contact angle of diiodomethane, Θ_w – contact angle of water.

3. Experimental

Zinc coatings are widely used for steel and cast iron corrosion protection. Zinc coated steel elements are relatively cheap, and in many cases this is the most effective corrosion protection [6, 7]. Zinc coatings are susceptible to darkening and spotting when touched. White rust appears on the surface during storage. That is why an additional treatment to protect zinc coatings surface is recommended [8]. Some finishing treatments are chromate coating, phosphate coating, painting, covering coatings of different resins, UV exposure and others [6, 8]. One of them is also a special chemical treatment in order to smoothen the coating (which requires etching in a bath of sulfuric acid and chromium trioxide). Another is adding a brightener to the galvanizing bath (glossy zinc coating).

Previously, the galvanizing (zinc coating) with glossing had more applications. Glossy zinc coatings, additionally coated by blue chromate coating can replace (in same applications) Cu–Ni–Cr decorative coatings, particularly when gloss life limitations and economical issues are important. Because of deficit and high cost of nickel (Ni), decorative zinc coatings are more and more popular in industry [6, 9].

Chromate treatment. In most cases, chromating is used to improve anticorrosive properties, in particular by increased electrochemical corrosion resistance [6, 8, 10, 11]. It requires creation of a thin passive layer. Corrosion resistance of a zinc coating can increase from 8 to 10 times after passivation in a proper bath [10]. Chromate coating (especially thicker) is characterized by some porosity. It creates a good ground coat under various kinds of paints, combining with ground and mechanical bonding, when penetrating in pores. Chromate ground protects zinc coating effectively in the caseof minor paints spalling. Chromate treatment is very often carried out directly after galvanizing. Protective properties of the chromate coating do not deteriorate in result of mechanical damage of the passive layer (e.g. scratches), due to so-called secondary passivation [8]. Chromate treatment can be applied together with brightening (glossing).

Phosphate treatment. Phosphate treatment can be carried out to seal and increase paint adhesion with zinc coating. It was proved that adhesion of non-metallic coatings to a pure zinc coating is less effective, than to zinc coating, which was chromated or phosphated [8].

Organic coatings. Coatings of different paints and resins are often used in addition to zinc coatings. These coatings are corrosion protective [12, 13]. It was proved that zinc coating's durability is 25–30% longer than the durability of coatings used separately. Steel protective system – zinc coating and paint coating is defined in literature as "Duplex" [7, 14, 15]. Protective period of Duplex system is longer than the sum of protective periods of these coatings used individually. A proper choice of paint coating is a fundamental problem in additional zinc coating protected by paint coating.

Recommendations for varnish products selection for painting zinc coatings and zinc coating treatments before covering paint coatings can be found in literature [15]. Hardenable polymers (polyester, melamine, acrylic, phenolic-formaldehyde and others) are very often used as organic coatings which cover zinc coatings. Better adhesion of the non-metallic coatings to zinc coatings which were phosphated or chromated, than to pure zinc coating can be noticed. Moreover, in the case of pure zinc coating there may appear corrosion products between this coating and the covering medium (especially if it is of acidic character). These corrosion products weaken the joint. That is why it is advantageous to use phosphate or chromate coatings which inhibit zinc corrosion and improve paint coating adhesion. Sometimes the semi-finished product (after zinc treatment and cooling) is covered by resin water emulsion, for example styrene-butadiene resin. Then the resin layer is formed on zinc surface. Its hardness is comparable with that of chromate coating hardness or even exceeds it.

Ultraviolet radiation exposure increases zinc coating protection as a result of special zinc variation coating. It has a higher durability and resistance than a typical variation [6, 8].

3.5. Testing materials

The research was carried out on the zinc galvanic (electrolytic) tests (sheets) subject to various technological operations. These operations create additional coatings on zinc coatings.

The following tests were used:

- the zinc galvanic sheets (about 1,00 sheet gauge) which were galvanized in cyanoalkaline bath, without any special chemical treatment, zinc coating thickness equal to about 10 μm/side,
- the zinc galvanic sheets (about 1,00 sheet gauge) which were galvanized in cyanoalkaline bath, with a special chemical treatment in order to smoothen the coating, zinc coating thickness equal to about 10 μm/side,
- the zinc galvanic sheets (about 1,00 sheet gauge), which were galvanized in cyanoalkaline bath, with chromate treatment, equal to about 10 μm/side zinc coating thickness,
- the zinc galvanic sheets (about 1,00 sheet gauge), which were galvanized in cyanoalkaline bath, with photosphate treatment, zinc coating thickness equal to about 10 μm/side.

3.6. Measurement method

Surface free energy value was determined using the Owens–Wendt method. The measurements of the contact angle Θ of testing materials were carried out to calculate the surface free energy. The method uses a direct measurement of the contact angle

formed between a droplet of a measuring liquid and the testing surface. Two reference liquids of specified values of both surface tension, polar and dispersion components of the surface free energy were employed: distilled water, which is strongly polar (its polar component is equal to 51 mJ/m^2 at the total free surface energy amounting to 72.8 mJ/m^2) was used as a dipolar liquid, and diiodomethane as an apolar one. The components of free surface energy for diiodomethane are respectively: polar – 2.4 mJ/m^2 and u-mode – 50.8 mJ/m^2 [1, 4].

The components γ_S^d and γ_S^p for tested materials can be calculated from the Eqs. (1) and (2).

4. Results

The obtained surface free energies of galvanic zinc coated sheets were presented in Table 1.

Table 1. Surface free energies and their components of galvanic zinc coated sheets

No.	Finishing treatment of galvanic zinc coated sheets	Surface free energy [mJ/m^2]		
		γ_S	γ_S^p	γ_S^d
1	Galvanizing in cyanoalkalline electrolyte	70.8	47.9	22.8
2	Galvanizing in cyanoalkalline electrolyte with special chemical treatment – coat smoothing	68	42.6	25.4
3	Galvanizing in cyanoalkalline electrolyte with chromate treatment (passivation)	41.7	8.6	33.1
4	Galvanizing in cyanoalkalline electrolyte with phosphatizing (passivation)	50.8	16.3	34.5

The highest surface free energy, among the tested samples, was obtained in the case of galvanizing in cyanoalkalline electrolyte (70.8 mJ/m^2), while the lowest – after chromate treatment (41.7 mJ/m^2). It can be noticed that the use of additional coating causes a significant reduction of the surface free energy in two cases (out of three tested). Moreover, the adhesion properties of chromate and phosphate coated surface deteriorates when compared to zinc coating surface without finishing treatment.

The relation between dispersion and polar parts of the surface free energy is also interesting. In the case of zinc coating without additional coating and with a special chemical treatment (in order to smoothen the coating) the polar component γ_S is almost twice larger than the dispersion component. For the zinc coating with chromate and photosphate passivation, the relation is opposite.

In the case of chromate treatment γ_S^p (8.6 mJ/m^2) is almost four times smaller than γ_S^d, the latter amounting to 33.1 mJ/m^2. After phosphatizing the polar component γ_S^p

is equal to 16.3 mJ/m^2 and the dispersion component value is 34.5 mJ/m^2. The former component is thus twice smaller.

The contribution of individual components to the surface free energy depend, among other things, on the kind of forces acting between atoms and molecules of the analyzed materials. The kind of forces depends mainly on the chemical structure of the material and external factors (e.g. temperature).

Dispersion forces are of a universal character and occur in all elements. This is why they always contribute to the surface free energy value. The polar component (including interaction derived orientation forces as well as inductive forces, for the sake of their character) can occur in specific conditions and its contribution may vary. Probably in the zinc coating (in particular in the zinc coating surface layer) polar interaction participate to a higher extent than in chromate or phosphate coatings. It is also possible that more polar molecules occur which are able to create polar forces.

It should also be noticed that the change of obtained values γ_S^p in function of finishing treatments procedure is considerably higher than the dispersion component γ_S. It is thus supposed that the polar component is more "sensitive" to the chemical composition of the material surface layer.

5. Summary

Based on the results reported in the paper, it can be noticed that the application of an additional finishing treatment of zinc coatings (which requires forming additional phosphate and chromate coatings) changes in the adhesive properties, as compared to zinc coatings without the additional treatment, decreasing their surface free energy value. In principle, our results contradict the published data stating that chromate and phosphate coating improve adhesion of, e.g. paint coating to zinc coating. Based on the obtained experimental results, a relation opposite to the published information was noticed for the samples and procedures employed in this work. Probably the reason was that the tested surface was oiled in order to protect it during transportation.

The changes of polar components of surface free energy are very interesting. After the finishing treatment, the value of this component is significantly reduced as compared to the value of galvanic zinc. Moreover, in the case of zinc coatings without finishing treatment and after a special chemical treatment (in order to smoothen the coating) the polar component value is twice larger than the dispersion component. As a result of other finishing treatments (chromating and photosphating), the polar component value is smaller: its value after photosphating is twice lower, and after chromating four times lower.

In the future, it could be extremely interesting to carry out more detailed analysis of the noticed differences between surface free energies and the data published in literature.

References

[1] ŻENKIEWICZ M., *Adhesion and Surface Layer Modification of Polymers*, WNT, Warsaw, 2000 (in Polish).
[2] LEE L.H., J. Adhesion Sci. Technol., 7 (1993), 538.
[3] DALET P., PAPON E., VILLENAVE J.-J., J. Adhesion Sci. Technol., 8 (1999), 857.
[4] JAŃCZUK B., BIAŁOPIOTROWICZ T., Polimery, 32 (1987), 269 (in Polish).
[5] CHIBOWSKI E., GONZALES-CABALLERO F., J. Adhesion Sci. Technol., 11 (1993),1195.
[6] LIPIŃSKA D., WEBER J., *Galvanizing*, [in:] *Electroplating Handbook*, WNT, Warsaw, 2002, 185.
[7] KRÓLIKOWSKI A., Corrosion Protection, 10 (2004), 258 (in Polish).
[8] KURSKI K., *Hot Galvanizing*, WNT, Warsaw, 1970 (in Polish).
[9] BURAKOWSKI T., Mechanic, 8–9 (1993), 309 (in Polish).
[10] WEBER J., Mechanical Inspection, 3–4 (1990), 18 (in Polish).
[11] REKŚĆ W., *Electroplating*, Publishing House of Technical University of Poznań, Poznań, 1992 (in Polish).
[12] ROCHE A.A., DOLE P., BOUZZIRI M., J. Adhesion Sci. Technol., 6 (1994), 587.
[13] VED M.V., SAKHNENKO N.D., NIKIFOROV K.V., J. Adhesion Sci. Technol., 2 (1998), 175.
[14] ANDZIAK J., KOBUS J., Corrosion Protection, 11 (2004), 276 (in Polish).
[15] ŚMIESZEK E., HAMELA D., Corrosion Protection, 11–12 (1989), 257 (in Polish).

Received 10 September 2005
Revised 4 November 2005

Materials Science-Poland, Vol. 24, No. 4, 2006

Effects of thermal treatment on magnetic properties of $Ni_2FeV_3O_{11-\delta}$ compound

N. GUSKOS[1, 2*], J. TYPEK[2], G. ŻOŁNIERKIEWICZ[2],
A. BŁOŃSKA-TABERO[3], S. LOS[4], W. KEMPIŃSKI[4]

[1]Solid State Section, Department of Physics, University of Athens,
Panepistimiopolis,15 784 Zografos, Athens, Greece

[2]Institute of Physics, Szczecin University of Technology, al. Piastów 17, 70-310 Szczecin, Poland

[3]Institute of Chemistry and Environmental Protection,
Szczecin University of Technology, al. Piastów 42, 71-065 Szczecin, Poland

[4]Institute of Molecular Physics, Polish Academy of Sciences,
Smoluchowskiego 17, 60-179 Poznań, Poland

$Ni_2FeV_3O_{11-\delta}$ samples have been synthesized by the solid-state reaction method using two different heat treatment processes (samples of the type A and B). The XRD measurements have shown the same diffraction patterns for both types of samples. The temperature dependences of the electron paramagnetic resonance (EPR) spectra have been recorded for the two types of thermal annealing processes of $Ni_2FeV_3O_{11-\delta}$. Strong differences have been observed in the EPR spectra of both types of $Ni_2FeV_3O_{11-\delta}$. An intense EPR line has been recorded at high temperatures; it is suggested that the line is associated with oxygen–vanadium clusters (ferromagnetic ordering). The linewidth, resonance field and integrated intensity of the EPR spectra have shown a strong temperature dependence down to 200 K. Additionally, in one sample a very broad EPR line of Fe^{3+} ions appeared at low temperatures while at high temperatures this line was overlapped by the other line. The temperature dependence of the integrated intensity of this broad line has shown the Curie–Weiss behaviour. In the vanadate oxide materials with two strong magnetic ions in the structure (iron(III) and nickel(II)), the spectrum of the Fe^{3+} ions is not observed. Different oxygen deficiency processes could explain the differences in the EPR spectra of both types of $Ni_2FeV_3O_{11-\delta}$ compounds.

Key words: *EPR; vanadate oxide; oxygen deficiency*

1. Introduction

Recently, very strange physical properties have been reported in some insulating vanadates and, in consequence, they have been very intensively studied [1–6]. The disorder of iron and metal atoms revealed in the structural studies of multicomponent

*Corresponding author, e-mail: ngouskos@phys.uoa.gr

vanadates $Me_2FeV_3O_{11-x}$ (Me = Zn and Mg) could be responsible for significant differences observed in their physical properties [5–7]. The temperature dependences of the EPR spectra of the polycrystalline vanadium oxides $Ni_2FeVO_{6-\delta}$ and $Zn_2FeV_3O_{11-\delta}$ have been investigated [8, 9]. For $Ni_2FeVO_{6-\delta}$, an intense EPR line associated with ferromagnetic clusters in the Fe–V layers were observed. Strong temperature dependences of its linewidth, resonance field and intensity have also been found in magnetic susceptibility measurements. For $Zn_2FeV_3O_{11-\delta}$, a very broad and intense EPR line originating from the high-spin iron(III) ions has been recorded and at about 50 K, an influence of the dynamical spin fluctuation on the EPR line has been observed [9].

The polycrystalline nickel–iron–vanadium oxide (Ni–Fe–V–O system) is a very interesting subject of extensive experimental investigations, due to its various magnetic interactions associated with the magnetic frustration induced by three oxidation states of the vanadium ion. $Ni_2FeVO_{6-\delta}$ crystallizes in the rhombohedral $FeTiO_3$-type (ilmenite) structure, comprising alternate metal layers forming a two-dimensional magnetic structure. It was assumed to be a ferrimagnet with a high Neel temperature and feeble magnetocrystalline anisotropy [10]. The hexagonal structural layers of nickel ions with antiferromagnetic ordering are expected not to essentially influence magnetic properties of this system. In the stoichiometric compound ($\delta = 0$) every other site is expected to be occupied by the Fe^{3+} ions separated by diamagnetic V^{5+} ions, with positive superexchange interactions. The magnetic moment obtained from the temperature dependence of the magnetic susceptibility is much smaller than for the ideal magnetic structure. Additionally, observed remarkable singularities suggest that different magnetic interactions operate in this system [1, 3]. Vanadium ions exhibit three main valence states: V^{3+} (spin $S = 1$), V^{4+} ($S = 1/2$) and V^{5+} ($S = 0$) due to oxygen deficiency with main contribution of the V^{5+} ions for $\delta = 0$. Thus modifying the Fe–Fe interactions could lead to the coexistence of various magnetic phases. A qualitative description of the magnetisation curve has been attempted in terms of the Ising model with random-bond quenched disorder reflecting the distorted Fe–Fe bonds by randomly distributed V ions with different valence states [10]. Thus it is suspected that for systems containing more vanadium ions at various oxidation levels the magnetic interactions could be more interesting.

In the present work, the $Ni_2FeV_3O_{11-\delta}$ compound, where every fourth site is expected to be occupied by Fe^{3+} ions separated by diamagnetic V^{5+} for the stoichiometric compound ($\delta = 0$) by two different thermal annealing regimes, has been prepared. EPR experiments have been carried out in order to trace intrinsic magnetic centres with frustration phenomena and to obtain a further insight into its complex magnetic properties resulting from various oxygen deficiency processes the samples were subjected to.

2. Experimental

The polycrystalline $Ni_2FeV_3O_{11-\delta}$ samples used in this study have been obtained by the solid-state reaction method [11]. Two different thermal annealing programmes

have been used for preparation of this compound. The first type of sample (sample A) has been synthesised from vanadates, according to the equation:

$$FeVO_4 + Ni_2V_2O_7 = Ni_2FeV_3O_{11}$$

During the synthesis, the powdered mixture was thermally annealed for 24 h at 913 K and for 24 h at 1073 K. The thermal annealing process was different from that proposed by Melentev et al. [12]. The second type of sample (sample B) was synthesized as follows: the mixture of oxides (NiO, 50.00 mol %, V_2O_5, 37.50 mol %, and Fe_2O_3, 12.50 mol %) was annealed in air atmosphere at 873 K during 24 hours (twice). Then the pellet was thermally annealed at 923 K during 24 hours (twice) and $Ni_2FeV_3O_{11}$ compound was synthesized according to the reaction:

$$4NiO + 3V_2O_5 + Fe_2O_3 = 2Ni_2FeV_3O_{11}$$

The obtained compound has a blackish-brown colour, with the melting point 1208 K (in contrast to 1238 K for the same compound obtained by Melentev et al. [12]) and with $Ni_3V_2O_8$ and $NiFe_2O_4$ stable decomposition products [12].

Sample identification by the X-ray powder diffraction revealed the presence of the phase with triclinic symmetry and with the following unit cell parameters: a = 0.8818(2) nm, b = 0.7582(2) nm, and c = 0.7023(3) nm, α = 117.06(3)°, β = 89.44(4)°, γ = 105.35(2)°, Z = 2 [11]. The experimentally determined density value is d = 4.21(5) g/cm^3, and is in a reasonable agreement with the X-ray density of d_{rtg} = 4.17 g/cm^3.

The EPR spectra were recorded using a conventional X-band spectrometer BRUKER E 500 with the magnetic field modulation of 100 kHz. The magnetic field was scaled with the usual NMR technique. The sample, containing 30 mg of the material in the form of fine powder was placed into a 2 mm diameter quartz tube. The measurements were done in the temperature range from 4.2 K to 300 K using an Oxford Instrument flow cryostat.

3. Results and discussion

Figure 1 presents the temperature dependence of the EPR spectra for the samples A and B. The corresponding EPR spectra at high temperatures consist of a single, slightly asymmetric EPR line, of an almost Lorentzian lineshape, typical of the exchange narrowed systems in the sample A and an additional very wide line in the sample B. In both cases, strong temperature dependences of all EPR parameters (I – integrated intensity, defined as the product of line amplitude and square of linewidth, ΔB – peak-to-peak linewidth and B_r – resonance field) are observed. The EPR line for the sample A has been well fitted with the Lorentzian lineshape in the investigated temperature range (Fig. 2a).

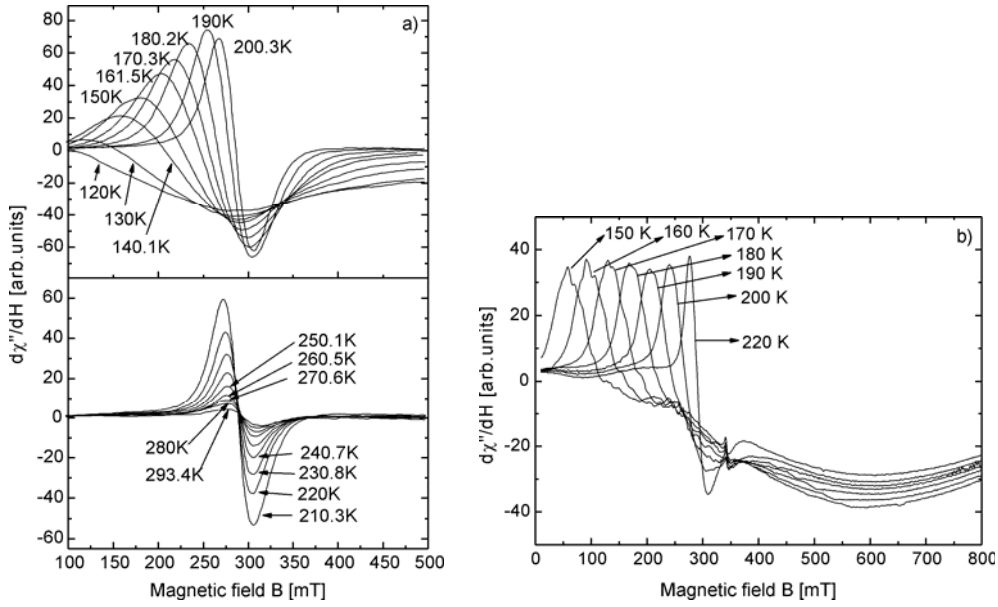

Fig. 1. The EPR spectra for the sample A (a), and B (b), at selected temperatures

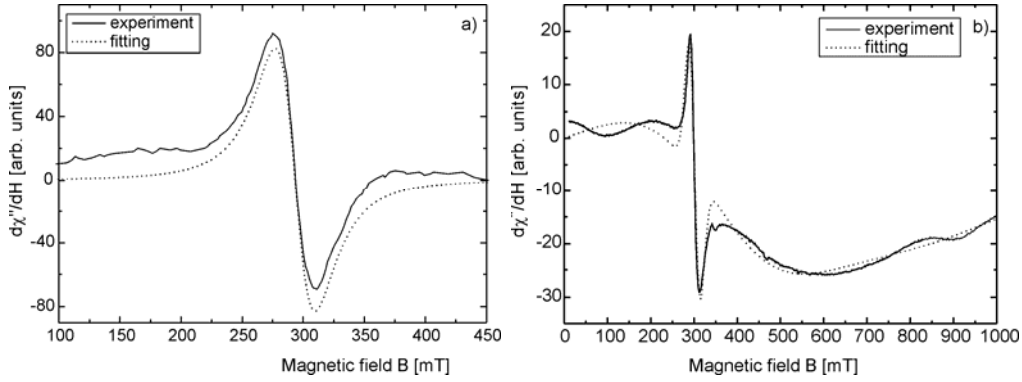

Fig. 2. Comparison of the experimental (solid line) and fitted (dashed line) EPR spectra for the sample A (a) and sample B (b), at 270 K

The EPR line for the sample B has been approximated by two Lorentzian lines, one narrow, similar to the line observed in the sample A and the other very broad, arising probably from the iron(III) ions (Fig. 2b).The resonance field of the broad component is almost constant in the whole investigated temperature range and the line is probably due to the spurious phases present in a very small amount in the samples. At room temperature, a narrow line is centred at 294 mT (corresponding to the effective g-factor $\approx$ 2.24), with the linewidth ΔB = 31.3(3) mT, for the sample A, and at 330 mT ($g \approx 2.00$), with the linewidth ΔB = 30.2(3) mT, for the sample B. A slight

difference was observed between both samples as the EPR intensity and linewidth of this line is concerned. The temperature dependence of the integrated intensity of the EPR narrow line, $I(T)$, which is proportional to the spin susceptibility, is very weak for both samples at higher temperatures ($T > 160$ K). The value of the linewidth ΔB at high temperatures and the temperature dependence of the integrated intensity $I(T)$ down to 195–200 K is similar for both samples. Below this temperature, a strong temperature-dependent shift of the resonance field in the direction of lower magnetic fields is observed (Fig. 3) in both samples and the ratio of the change of magnetic field δB with temperature has the following values: $\delta B/\Delta T \approx 0.0709$ mT/K at high temperatures (above 200 K) and $\delta B/\Delta T \approx 1.69$ mT/K at lower temperatures for the sample A, while for the sample B $\delta B/\Delta T = 3.74$ mT/K at lower temperatures, this value being over twice greater than that for the sample A. This EPR line disappears below 110–130 K in both cases or is overlapped by a very broad EPR line from the Fe^{3+} ions. This may suggest that the dipole–dipole (or exchange) interactions and the dynamical fluctuations of the spins essentially depend on thermal treatment processes.

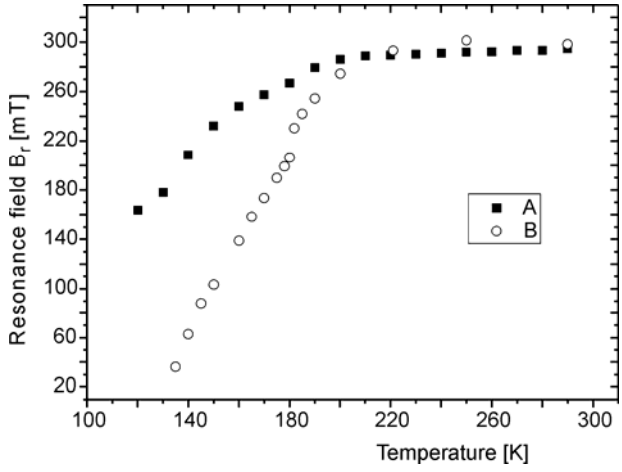

Fig. 3. Temperature dependence of the resonance field $B_r(T)$ of the narrow EPR line in the sample A (full squares) and sample B (empty circles)

The temperature behaviour of the integrated intensity complies with the corresponding temperature variation of the magnetic susceptibility curve at higher temperature, indicating that the observed EPR spectrum probes the bulk magnetic processes. In the sample A, the EPR line is more intense than in the sample B that at higher temperatures coexists with a broad EPR line originating from the Fe^{3+} ions. Above 200 K, the g parameter, the linewidth ΔB and the resonance field are almost constant in both samples. Below 200 K, for both samples the linewidths begin to increase very strongly and the resonance field shifts towards lower magnetic fields (Fig. 3). An excessive broadening of the EPR linewidths for both samples is observed at low temperatures. The amplitude of the resonance line reaches the maximum in the same tem-

perature range (Fig. 4) in which the shift of the resonance line starts to increase strongly with the decreasing temperature.

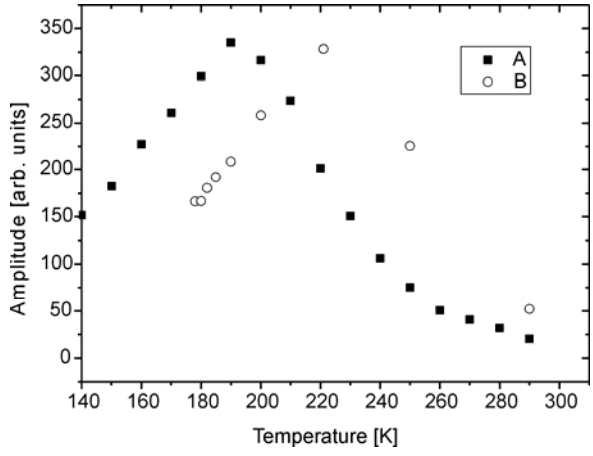

Fig. 4. Temperature dependence of the EPR signal amplitude for the sample A (full squares) and sample B (empty circles)

An interesting behaviour of the temperature dependence of I(T) is observed in the high-temperature region. Below 220 K, a rapid increase of ΔB is observed implying the onset of the critical fluctuations near the corresponding phase transition. The resonance field exhibits a relatively small decrease as temperature decreases down to ca. 200 K. The temperature dependence of the EPR parameters in the sample $Ni_2FeVO_{6-\delta}$ shows an almost same behaviour at higher temperatures [8]. The temperature behaviour of the EPR line of Fe^{3+} ions is in agreement with the results of magnetic measurements that indicate the presence of a certain amount of high-spin iron ions not taking part in the magnetic interaction at high temperatures. In a system containing no vanadium ions, e.g. α-Fe_2WO_6, the EPR spectrum is dominated by a line from iron(III) ions and usually at high temperatures the line is very broad [13] and near the critical temperature it displays a very interesting behaviour. A new vanadate compound, $Fe_8V_{10}W_{16}O_{85}$, has recently been investigated by the EPR method [14] and the origin of its EPR spectrum at high temperatures is still unclear.

The temperature dependence of FMR (ferromagnetic resonance) spectra of magnetic nanoparticles embedded in non-magnetic matrices, recorded with an EPR spectrometer, showed a behaviour similar to that observed for the investigated samples [15, 16]. Thus it is suggested that for the samples A and B the spectra are associated with the fraction of iron(III) ions becoming ferromagnetically ordered in small clusters. The spectrum recorded with an EPR spectrometer is therefore of the ferromagnetic resonance type because it originates not from separate spins but from a group of magnetically coupled ions. The magnetic clusters would produce the FMR absorption. The resonance condition in the presence of ferromagnetic clusters is modified by an internal magnetic field B_{int}:

$$h\nu = g\mu_B(B_0 - B_{\text{int}}) \tag{1}$$

where B_{int} could be connected with the shift of resonance FMR line and thus described by the following relation:

$$B_{\text{int}} = B_0(1 - \alpha\Delta T) \tag{2}$$

where B_0 is an external applied magnetic field, μ_B is the Bohr magneton, and α is the gradient of the change of magnetic field with temperature. The strong increase of $\delta B/\Delta T$ observed below 200 K could be connected with freezing of the magnetic cluster at this critical temperature. Then from Eqs. (1) and (2) one gets:

$$h\nu = g\mu_B B_0 \alpha\Delta T \tag{3}$$

The value of α could depend on the size of magnetic clusters because it describes the value of the internal magnetic field. For the investigated samples, the following values were calculated: $\alpha = 1.1(1)\cdot 10^{-2}$ K^{-1} for the sample A, and $\alpha = 1.3(1)\cdot 10^{-2}$ K^{-1} for the sample B.

For $Me_2FeV_3O_{11-x}$ (Me = Zn or Mg) compounds containing only one magnetic metal ion, the EPR spectra of high-spin iron(III) ion have been recorded [17, 9] while for compounds with a sublattice having two different magnetic ions the EPR spectra from Fe^{3+} ions have not been observed.

4. Conclusions

It has been shown that for the compound $Ni_2FeV_3O_{11-\delta}$ the ferromagnetic resonance spectra dominate the magnetic response and they are associated with the presence of ferromagnetic clusters in the Fe–V layers and the high-spin iron centres. A strong temperature dependence of the FMR spectra is observed with a substantial shift of the resonance lines towards lower magnetic fields. The signal disappears below 110 K in the sample A and 130 K in the sample B. A new coefficient $\delta B/\Delta T$ describing the shift of the resonance lines with temperature was introduced and calculated for both types of samples. The preparation method and thermal annealing processes strongly influence the observed FMR spectra, recorded with the EPR spectrometer.

Acknowledgements

This work has been financed from the means designed for science for years 2005–2008 as a scientific project 1311/T09/2005/29.

References

[1] SCHMIDT S., PALME W., LUTHI B., WEIDEN M., HAUPTMANN R., GEIBEL C., Phys. Rev. B, 57 (1998), 2687.

[2] KOROTIN M.A., ELFIMOV I.S., ANISIMOV V.I., TROYER M., KHOMSKII D.I., Phys. Rev. Lett., 83 (1999), 1387.

[3] LOHMANN M., KRUG VON NIDDA H.A., LOIDL A., MORRE E., DISCHNER M., GEIBEL C., Phys. Rev. B, 61 (2000), 9523.
[4] TRINKL W., LOIDL A., KLEMM M., HORN S., Phys. Rev. B, 62 (2000), 8915.
[5] WANG X., VANDER GRIEND D.A., STERN C.L., POEPPELMEIER K.P., J. Alloys Comp., 298 (2000), 119.
[6] GUSKOS N., WABIA M., KURZAWA M., BEZKROVNYI A., LIKODIMOS V., TYPEK J., RYCHLOWSKA-HIMMEL I., BLONSKA-TABERO A., Radiat. Eff. Defects Solids, 158 (2003), 369.
[7] GUSKOS N., TYPEK J., BEZKROVNYI A., WABIA M., KURZAWA M., ANAGNOSTAKIS E.A., GASIOREK G., J. Alloys Comp., 377 (2004), 47.
[8] GUSKOS N., LIKODIMOS V., LOS S., KEMPINSKI W., STANKOWSKI J., WABIA M., TYPEK J., BLONSKA-TABERO A., TABERO P., RYCHLOWSKA-HIMMEL I., Physica B, 284–288 (2000), 1456.
[9] LIKODIMOS V., GUSKOS N., GLENIS S., SZYMCZAK R., BEZKROVNYI A., WABIA M., TYPEK J., GASIOREK G., KURZAWA M., RYCHLOWSKA-HIMMEL I., BLONSKA-TABERO A., Eur. Phys. J. B, 38 (2004), 13.
[10] KOLPAKOWA L., PIETRZAK J., LATOSInSKA J.N., PAWLICKI P., J. Magn. Magn. Mater., 140 (1995), 1583.
[11] KURZAWA M., BLONSKA-TABERO A., RYCHLOWSKA-HIMMEL I., TABERO P., Mat. Res. Bull., 36 (2001), 1379.
[12] MELENTEV A.B., SURAT L.L., FOTIEV A.A., SUVOROVA G.A., SIRINA T.P., Zh. Neorg. Khim., 33 (1988), 2149.
[13] GUSKOS N., TYPEK J., WABIA M., LIKODIMOS V., FUKS H., RYCHLOWSKA-HIMMEL I., WALCZAK J., Appl. Magn. Res., 14 (1998), 397.
[14] GUSKOS N., LIKODIMOS V., PATAPIS S.K., TYPEK J., WABIA M., FUKS H., GAMARI-SEALE H., WALCZAK J., RYCHLOWSKA-HIMMEL I., BOSACKA M., J. Solid State Chem., 137 (1998), 223.
[15] KOSKAROV YU.A., PANKRATOV D.A., GUBIN S.P., KOSOBUDSKY I.D., BELTRAN M., KHODORKOVSKY Y., TISHIN A.M., J. Appl. Phys., 89 (2001), 2293.
[16] GUSKOS N., ANAGNOSTAKIS E.A., LIKODIMOS V., BODZIONY T., TYPEK J., MARYNIAK M., NARKIEWICZ U., KUCHAREWICZ I., J. Appl. Phys., 97 (2005), 024304.
[17] GUSKOS N., WABIA M., LIKODIMOS V., TYPEK J., KURZAWA M., BLONSKA-TABERO A., RYCHLOWSKA-HIMMEL I., Mol. Phys. Rep., 36 (2002), 27.

Received 9 September 2005
Revised 7 November 2005

Materials Science-Poland, Vol. 24, No. 4, 2006

Influence of conditions of synthesis on superconductivity in $Nd_{2-x}Ce_xCuO_{4-y}$

M. PLEBAŃCZYK[1*], T. KLIMCZUK[1], T, GORTENMULDER[2], P. FIERTEK[1], W. SADOWSKI[1]

[1]Faculty of Applied Physics and Mathematics,
Gdańsk University of Technology, Narutowicza 11/12, 80-952 Gdańsk, Poland

[2] Kamerlingh Onnes Laboratory, Leiden University, PB 9504, 2300 Leiden, The Netherlands

Samples of $Nd_{1.85}Ce_{0.15}CuO_4$ were prepared using two different methods of synthesis (series A and B). The superconductivity was characterized by electrical resistivity and dc magnetic susceptibility measurements. X-ray diffraction (XRD) and energy dispersion X-ray analysis (EDAX) were used to characterize the structure composition and the sample quality. The resistivity measurements show a double transition to the superconducting state. It is proposed that the grains consist of a core with the optimum cerium content (~0.15) and a shell where the cerium content is different. The homogeneity of the samples was estimated through the determination of the slope of resistivity in the superconducting transition region ($d\rho/dT$). Ce content is higher and it is more homogeneously distributed in the samples treated at higher temperatures. EDAX analysis shows that the quantity of Cu on the surface of the samples increases with the temperature of the reduction process.

Key words: *superconductivity; doping; $Nd_{2-x}Ce_xCuO_{4-y}$*

1. Introduction

Superconducting materials with a general formula $Ln_{2-x}Me_xCu\ O_{4-y}$ (Ln = Nd, Pr, Sm, Eu; Me = Ce, Th) are an example of layered copper oxide high-temperature superconductors (HTSC) in which the charge carriers appear to be electrons rather than holes [1, 2]. For the $Nd_{2-x}Ce_xCuO_{4-y}$ system, the crystal structure is tetragonal at all temperatures; it is the so-called *T'* phase with two-dimensional CuO_2 square planes. There is a nominal absence of apical oxygen atoms O(3). Doping with four-valence cerium ($0.13 < x < 0.18$) and additional heat treatment (reduction process) results in the appearence of superconductivity. It is accepted that a small number of oxygen atoms is removed from the *T'* structure ($y \approx 0.01$–0.04) to achieve superconductivity

*Corresponding author, e-mail: monikap@mifgate.mif.pg.gda.pl

[3, 4]. However, the role of heat treatment and of accompanying effects on superconductivity are not fully understood.

The system is characterized by a relatively low critical temperature $T_c \approx$ 19–25 K at the concentration of Ce around $x \approx 0.15$. Different methods and conditions of the synthesis as well as heat treatment could produce samples with different T_c. One of the methods to obtain $Nd_{2-x}Ce_xCuO_{4-y}$ is preparing samples by solid state reactions using oxides as starting materials [1, 5–9]. It is difficult to prepare a homogeneous sample, mainly due to the highly refractory nature of Ce oxide. Some authors [10, 11] used $NdCeO_{3.5}$ as starting material or CeO_2 freshly made from $Ce(CO_3)_2$. They obtained samples with better Ce distribution. Chemical routes such as nitrate decomposition and liquid mix methods make it possible to get homogeneous samples of $Nd_{2-x}Ce_xCuO_{4-y}$ [9].

The aim of this work was to show how the conditions of the synthesis and reduction process influence the quality of samples, transport and superconductivity characteristics.

2. Experimental

Samples of $Nd_{(2-x)}Ce_xCuO_{4-y}$ were prepared by a solid state reaction from a stoichiometric mixture of respective oxides. The starting materials were Nd_2O_3, CeO_2 (Fluka Chemie, 99.95%) and CuO (Fluka Chemie, >99%). The starting powder Nd_2O_3 was calcinated at 900 °C for 2 hours in air before use in order to eliminate impurities.

After a thorough mixing, two samples with $x = 0.15$ (optimal doping) were pressed into pellets. The pellets were placed in a furnace chamber with an Al_2O_3 boat and treated as is shown in Table 1. Samples A and B were cut into plates ($1.2 \times 1.4 \times 8.6$ mm^3) and finally heated in reducing atmosphere (Ar, 99.999%), in the temperature range from 800 °C to 1100 °C (with the step of 50 °C) for 19 hours.

Table 1. The conditions of the synthesis of the samples A and B

Sample A		Sample B	
Temperature of reduction [°C]	Time [h]	Temperature of reduction [°C]	Time [hrs]
950	48	950	17
1000	48	1000	12
1050	24	1050	12
		1100	15
		1140	2

All samples were examined by the resistivity measurements in the temperature range 4.8–300 K, using the standard four-point method [12]. Four Cu wires (50 μm) were glued onto the surface with the silver paste. The contact resistance was smaller

than 0.3 Ω at room temperature. Zero field cooling dc (H_{dc} = 1 and 10 Oe) magnetizations were measured in the range of 1.8–30 K (MPMS Quantum Design).

X-ray diffraction (XRD) and energy dispersion X-ray analysis (EDAX) of $Nd_{1.85}Ce_{0.15}CuO_{4-y}$ were used to characterize the structure composition and the quality of sample (porosity, surface density).

3. Results and discussion

3.1. X-ray diffraction analysis

X-ray diffraction analysis showed that the starting material synthesized at higher temperature (series B) is a pure $Nd_{1.85}Ce_{0.15}CuO_4$ phase, whereas samples of series A contained impurities, characterized by low-intensity reflection at 2Θ = 28.29° corresponding to the (222) reflection of $NdCeO_{3.5}$, and a reflection at 2Θ = 35.59° – (002) reflection of CuO (Fig. 1).

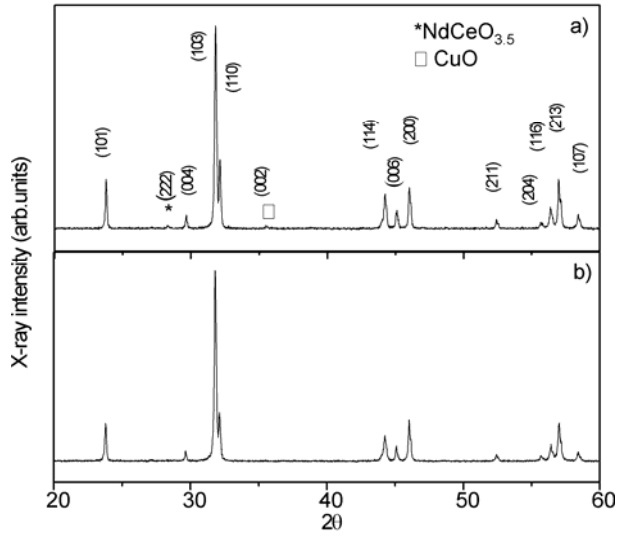

Fig. 1. X-ray diffraction patterns of $Nd_{(2-x)}Ce_xCuO_{4-y}$ after two different processes of synthesis

From the result of the Rietveld refinement, the lattice constants were found: a = 3.9469(1) Å, c = 12.0782(6) Å for series A, and a = 3.9473(1) Å, c = 12.0772(6) Å for series B. It is well known that increasing Ce content in $Nd_{2-x}Ce_xCuO_{4-y}$ unit cell results in a significant decrease of the c/a ratio of the lattice parameters. The displacement between the (110) and (103) reflections is directly proportional to this ratio with smaller displacement indicating a smaller c/a ratio

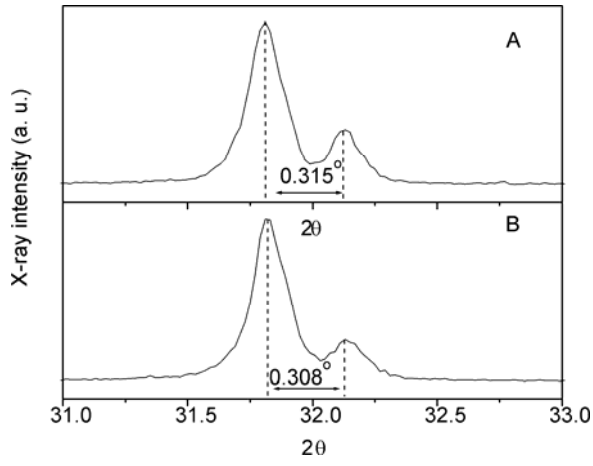

Fig. 2. Displacement between the (110) and (103) peak reflections of $Nd_{(2-x)}Ce_xCuO_{4-y}$ for samples A and B

[7, 10, 11]. The estimated $\Delta(2\Theta)$ values are 0.315(1)° and 0.308(4)° for the sample from series A and B, respectively (Fig. 2). This suggests that the Ce content is higher and possibly more homogenous in the series B.

3.2. Resistivity measurements

Figure 3 shows the temperature dependence of the resistivity $\rho(T)$ for representative samples treated at various temperatures (T_{red}). Semiconducting behaviour ($d\rho/dT < 0$) is observed for samples treated at temperatures below T_{red} = 900 °C for the series

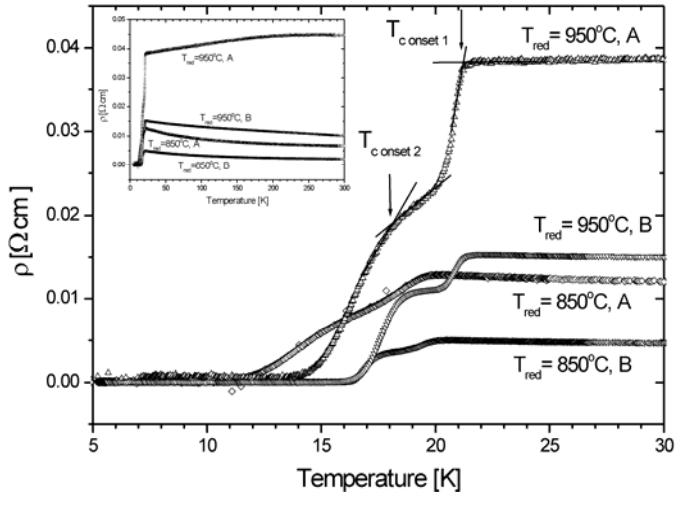

Fig. 3. Resistivity measurements. The curves $\rho(T_{red})$ for sample A and sample B reduced at 850 and 950 °C. In the inset, the whole temperature range (4.2–300 K) is presented

A and below 950 °C for the series B. The resistivity increases with increasing T_{red} and the slope ($d\rho/dT$) becomes positive, which means that metallic behaviour prevails.

The resistivity measurements show a double transition to the superconducting state, as was previously observed by Klamut and Gerber [13, 14]. Mang et al. examined reduced $Nd_{2-x}Ce_xCuO_{4-y}$ crystals and showed that the interior of the sample was less damaged than its exterior [3]. The core piece protected by the shell is less exposed to the reducing atmosphere. Similar topics were also discussed in [15].

It is proposed that grains contain a core with cerium content close to the optimal value (~0.15) and the shell, where the quantity of cerium is different. Consequently $T_{c\,onset\,1}$ corresponds to the temperature at which the grain core becomes a superconductor, and $T_{c\,onset\,2}$ is the critical temperature of the grain shell. Below $T_{c\,onset2}$, percolating chains of the Josephson intergrain couplings are created, and zero resistance is achieved.

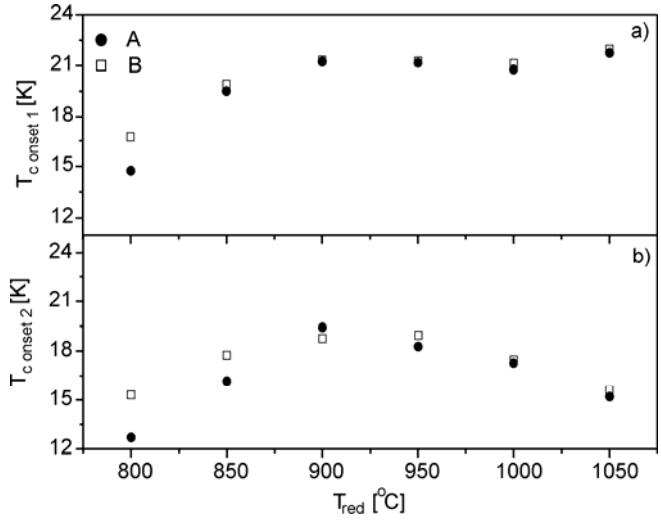

Fig. 4. Dependence of $T_{c\,onset\,1}$ and $T_{c\,onset\,2}$ versus temp. of reduction

Increase of the reduction temperature (T_{red}) causes the increase of $T_{c\,onset\,1}$ (Fig. 4a). Similarly, $T_{c\,onset\,2}$ increases but only for samples treated below 900 °C (series A) and 950 °C (series B). This feature confirms that $T_{c\,onset\,2}$ corresponds to the grain shell because every change in the material, namely decomposition process, starts from the shell.

Both critical temperatures for the series A and B (Fig. 4a and 4b) show the same behaviour, T_c's being slightly higher for the series B. It is caused by higher purity of the samples synthesized at higher temperature. The homogeneity of samples was estimated through calculation of $d\rho/dT|_1$ and $d\rho/dT|_2$ (Fig. 5). The best superconducting properties (the highest T_c and homogeneity) is exhibited by the samples reduced at 950 °C (series A) and at 1000 °C (series B).

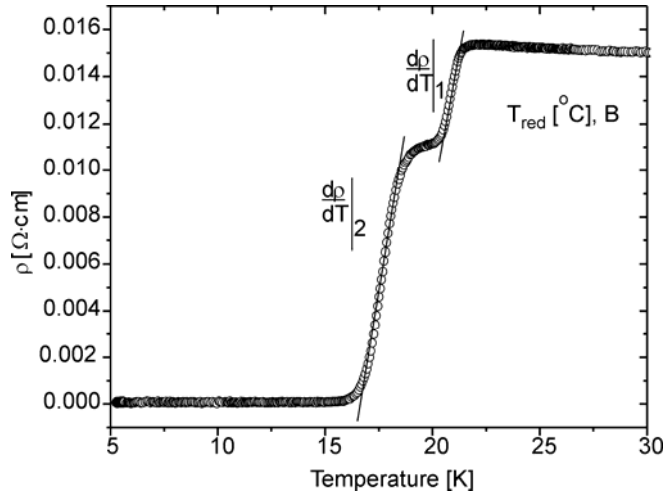

Fig. 5. Example of the determination of homogeneity of a sample

3.3. Magnetic measurements

Figure 6 shows zero-field cooling dc (H_{dc} = 10 Oe) susceptibility $\chi_{dc}(T)$ data for $Nd_{1.85}Ce_{0.15}Cu)_{4-y}$ samples: series A (upper figure) and series B (lower figure). It can

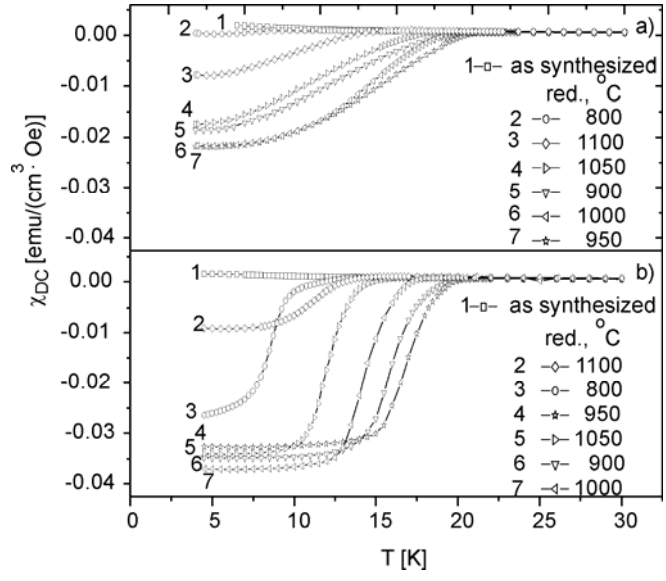

Fig. 6. The dc magnetic measurements, ZFC. The magnetic susceptibility χ_{dc} vs. temperature in the samples: a) A, b) B for various temperatures of annealing in the magnetic field of 10 Oe

be observed that only as-synthesized samples are bulk superconductors. The additional reducing process is necessary to obtain superconductivity. Contrary to the resistivity measurement, the transition is one step-like in character and the highest critical temperature (about 20 K) for both series is observed for samples treated at $T_{red} = 950$ °C.

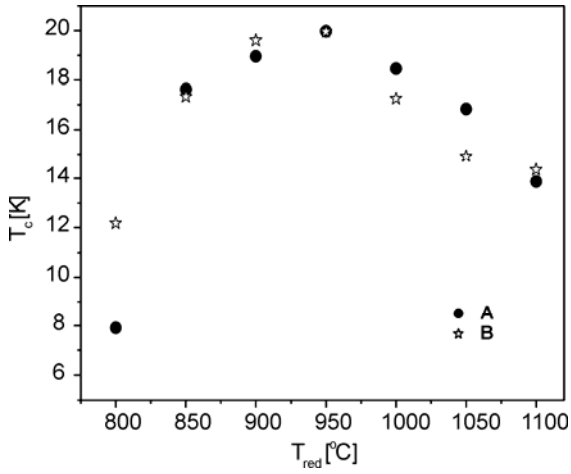

Fig.7. $T_{c\,onset}$ versus temperature of reduction in the field of 10 Oe

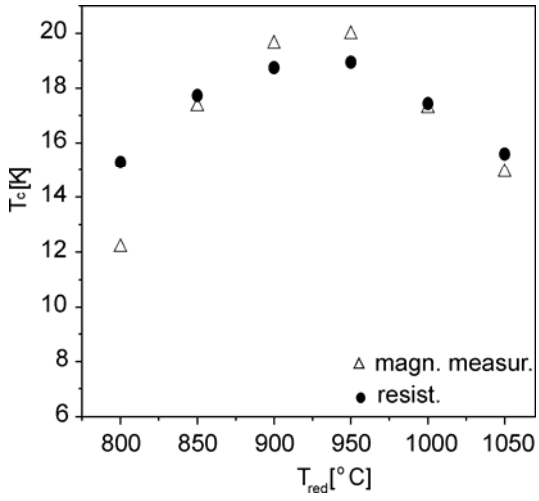

Fig. 8. $T_{c\,onset}$ from magnetic measurement and $T_{c\,onset\,2}$ from resistivity measurement for samples B

Figure 7 presents the dependence of T_c (determined from magnetic measurements) as a function of T_{red}. The dependence is very similar to that observed for $T_{c\,onset\,2}$ taken from resistivity measurements (compare with Fig. 4b). Figure 8 proves that the magnetic T_c corresponds to $T_{c\,onset\,2}$ which confirms our proposed model with an optimal doped core and a shell.

Figure 9 presents field dependence of the magnetization at 5 K for six representative samples.

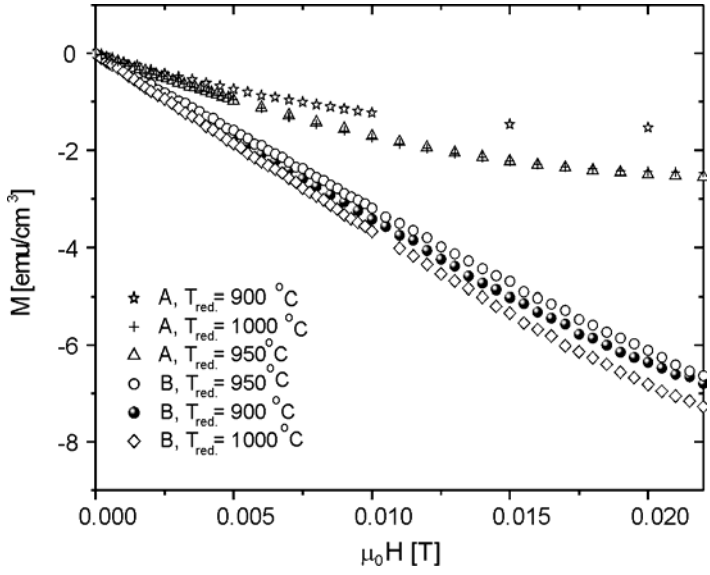

Fig. 9. Magnetic field dependences of the magnetization of the samples A and B treated at various temperatures. The measurements were taken at 5 K

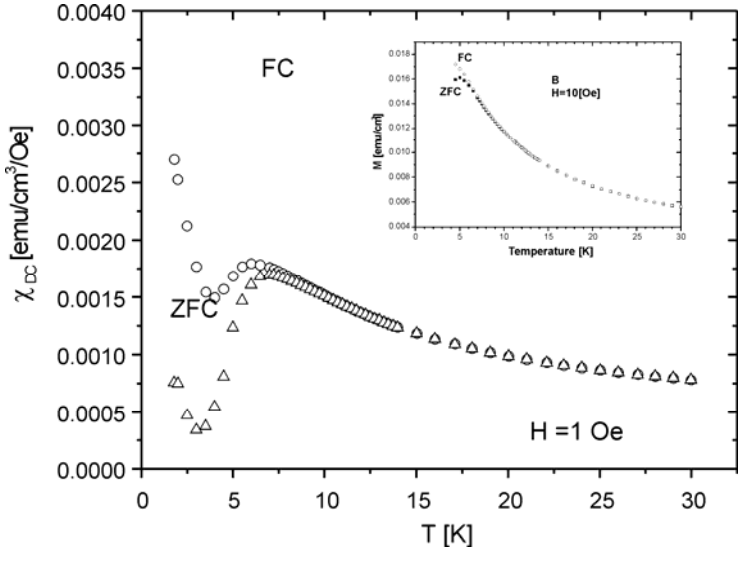

Fig.10. The magnetic susceptibility χ_M versus temperature T for the sample B in the magnetic fields of 1 Oe and 10 Oe (in the inset). The samples were measured immediately after the synthesis

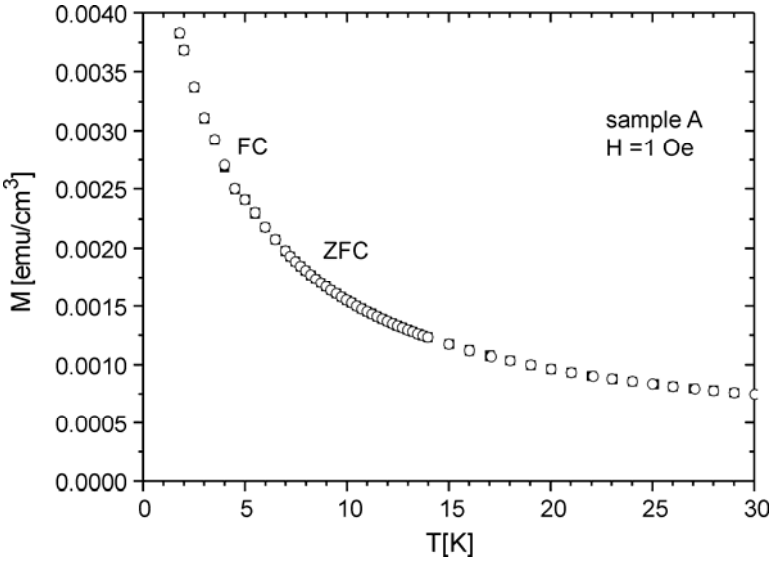

Fig. 11. The magnetization M versus temperature T
for the as-synthesized sample A in the magnetic field of 1 Oe

Both $M(\mu_0 H)$ and $\chi_{dc}(T)$ measurements indicate that samples from the series B contain more superconducting fraction and an optimal sample was obtained after the treatment at T_{red} = 1000 °C.

It is interesting to note that as synthesized samples from the series B show a slight sign of superconductivity (Fig. 10), in contrast to samples from series A (Fig. 11). This suggests that the synthesis conducted in air at a suitably high temperature may yield superconducting samples. However, the observed superconductivity is not bulk in its character and T_c is very low (7 K).

3.4. EDAX and SEM analyses

For each sample ten EDAX measurements were taken in different places and the mean value was calculated. Before measurements, the samples were mechanically polished. The percentage contribution of holes to the total area (Fig. 12) was estimated, which indicates the influence of the synthesis and the reduction conditions on the porosity. Lower number of holes means lower porosity and higher density of samples. Therefore, we can conclude that samples from the series B are of better quality.

Figure 13 presents the SEM image of the surface after treatment at T_{red} = 950 °C. White spots visible in the figure are sites where CuO (the product of decomposition reaction) appears.

Figure 14 presents the ratio of Cu/(Nd + Ce) for samples from series B as a function of T_{red}. With increasing T_{red}, the ratio Cu/(Nd + Ce) increases. Assuming that Nd and Ce content does not change on the surface (Nd + Ce = const.), this means that Cu

diffuses from the bulk to the surface. A rapid drop observed for the sample treated at T_{red} = 1100 °C, which is higher than Cu melting point (1083 °C), might be explained by the Cu evaporation process.

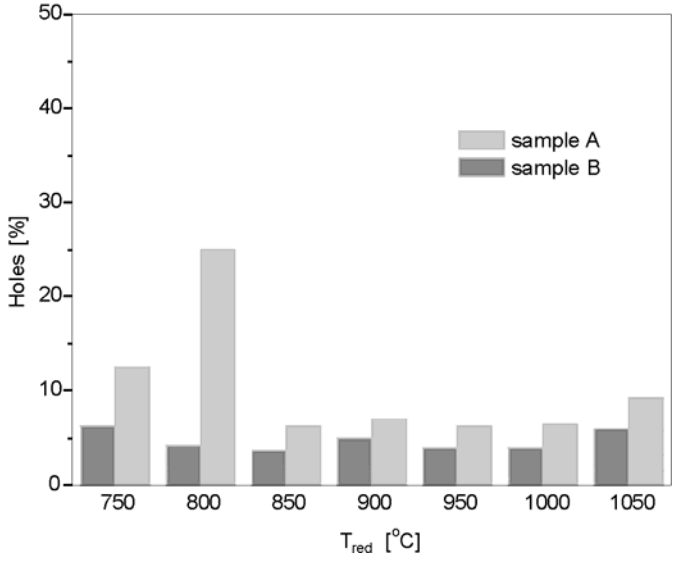

Fig. 12. EDAX analysis of holes on the surface of $Nd_{2-x}Ce_xCuO_{4-y}$ samples in function of temperature of reduction

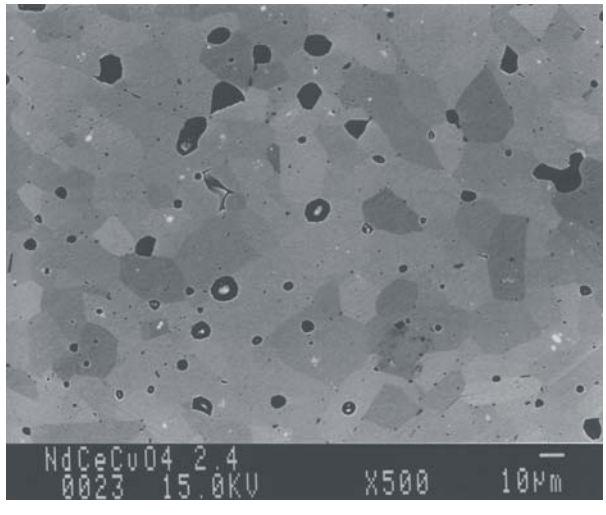

Fig. 13. SEM picture of $Nd_{2-x}Ce_xCuO_{4-y}$ annealed at 950 °C

Mang et al. [3] showed that one of the decomposition products, $(Nd,Ce)_2O_3$, causes the secondary phase to form an oriented quasi-two-dimensional epitaxial structure on $Nd_{2-x}Ce_xCuO_{4-y}$ crystals.

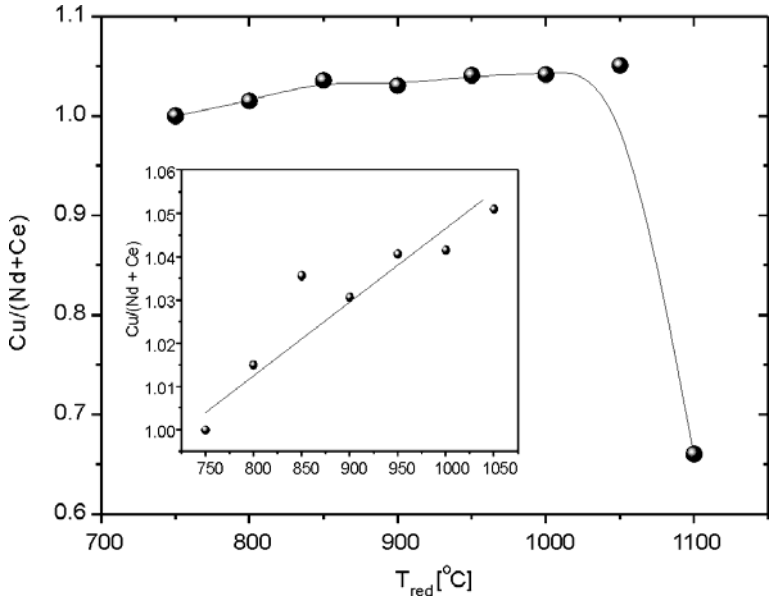

Fig. 14. Analysis of the amount of copper on the surface of sample B versus temperature of reduction. Inset: The temperature range 750–1050 K. Note the expanded vertical scale

For typical reduction conditions the volume fraction of $(Nd,Ce)_2O_3$ is about 1%. The presence of the secondary phase can be the reason of the difference between the interior and exterior of grains.

4. Conclusions

An appropriate choice of conditions of the synthesis allows us to obtain single -phased $Nd_{2-x}Ce_xCuO_4$. We have shown that the conditions of the process (temperature, number of steps) have a considerable influence on the quality of samples and their superconducting characteristics. Optimal temperatures of reduction of our samples are between 950 °C and 1000 °C.

Increasing temperature of reduction causes the increase in the amount of copper on the surface of the samples but at about 1100 °C we have noticed a rapid drop caused by the evaporation of copper from the surface of the sample.

It is proposed that grains contain the core characterized by the optimum content of cerium (~ 0.15) and the shell where its content is different than that in the core. Consequently, two superconducting transition temperatures are observed in resistivity measurements, where $T_{c\,\mathrm{onset}\,1}$ is the temperature in which the core of grain becomes a superconductor. Decreasing of temperature causes that the shell of grain starts to be superconducting ($T_{c\,\mathrm{onset}\,2)}$, the percolating chains of Josephson intergrain couplings are created, and zero resistance is achieved.

Diffusion of copper and degradation of $Nd_{2-x}Ce_xCuO_{4-y}$ result in a deterioration of superconducting properties. This explains a decrease of $T_{c\,onset2}$ above a certain temperature, because every change in the materials, including the decomposition process, is initiated on the surface.

References

[1] MARKET J.T., MAPLE M.B., Solid State Commun., 70 (1989), 145.
[2] TOKURA Y., TAKAGI H., UCHIDA S., Nature, 337 (1989), 345.
[3] MANG P.K., LAROCHELE S., MECHTA A., VAJK O.P., ERICKSON A.S., LU L., BAYERS W.J.L., MARSHELI A.F., PROKES K., GREM M., Phys. Rev. B, 70 (2004), 094507.
[4] KIM J.S., GASKELL D.R., Physica C, 209 (1993), 381.
[5] SERQUIS A., PRADO F., CANEIRO A., Physica C, 313 (1999), 271.
[6] TAKAGI H., UCHIDA S. AND TOKURA Y., Phys. Rev. Lett., 62 (1989), 1197.
[7] CONCEIÇÃO A., COHENCA C.H., JARDIM R.F., Physica C, 333 (2000), 170.
[8] KLAUD M., STROBEL J.P., LIPPERT M., SAEMANN-ISCHENKO G., GERHAUSER W., NEMULLER H.W., Physica C, 165 (1990), 251.
[9] SERQUIS A., PRADO F., CANEIRO A., Physica C, 253 (1995), 339.
[10] LOPEZ-MORALES M.E., SAVOY R.J. AND GRANT P.M., Solid State Commun., 71 (1989), 1079.
[11] LOPEZ-MORALES M.E., SAVOY R.J. AND GRANT P.M., J. Mater. Res., 5 (1990), 2041.
[12] VAN DER PAUW L.J., Philips Res. Rep., 13 (1958), 1.
[13] GERBER A., GRENET T., CYROT M. AND BEILLE J., Phys. Rev. Lett., 65 (1990), 3201.
[14] KLAMUT P.W., Phys. Stat. Sol., 136 (1993), 181.
[15] BRINKMANN M., REX T., BACH H., WESTERHOLT K., Phys. Rev. Lett., 74 (1995), 4927.

Received 9 September 2005
Revised 4 November 2005

Materials Science-Poland, Vol. 24, No. 4, 2006

Defect passivation of multicrystalline silicon solar cells by silicon nitride coatings

M. LIPIŃSKI[1*], P. PANEK[1], S. KLUSKA[2], P. ZIĘBA[1], A. SZYSZKA[3], B. PASZKIEWICZ[3]

[1]Institute of Metallurgy and Materials Science of Polish Academy of Sciences, Reymonta 25, 30-059 Cracow, Poland

[2]AGH University of Science and Technology, Mickiewicza 30, 30-059 Cracow, Poland

[3]Faculty of Microsystem Electronics and Photonics, Wroclaw University of Technology, Wybrzeże Wyspiańskiego 27, 50-370 Wrocław, Poland

The influence of the hydrogenated silicon nitride coatings (SiN_x:H) formed by the plasma enhanced chemical vapour deposition on the electrical activity of interfaces of the grains of mc-Si solar cell was examined. Passivation effects were evaluated by the measurements of light-beam-induced current scan maps. It was found that the SiN_x:H layer obtained under optimized conditions significantly improves local photocurrent at the grain boundaries. The electrical parameters of mc-Si solar cells with and without the SiN_x:H layers were compared.

Key words: *silicon nitride coating; passivation; silicon solar cell*

1. Introduction

Multicrystalline silicon wafers contain a large variety of extended crystallographic defects like grain boundaries or dislocations. These defects reduce effective diffusion lengths of minority carriers. In order to improve the material quality, it is necessary to passivate the defects. It is known that the hydrogenation gives very good results. One of the most promising method is application of the hydrogenated amorphous silicon nitride layers (a-SiN_x:H) deposited by the plasma-enhanced chemical vapour deposition (PECVD). These layers are used as very effective antireflective coatings [1–4], the main interest in these films, however, is attributed to the bulk and surface defect passivation of silicon. It was shown that hydrogen released from the SiN_x:H layer during the thermal treatment of a solar cell can passivate silicon defects [5–13].

*Corresponding author, e-mail: marlipin@wp.pl

This paper describes the results of investigation of the passivation of grain boundaries by the SiN_x:H layer using light-beam induced current (LBIC) mapping of the surfaces in silicon cells.

2. Experimental

The substrates used in this work were 'as-cut', boron doped p-type, 1 Ω·cm multicrystalline (mc-Si) wafers (Baysix). The thickness of wafers was 320 μm and the area was 10×10 cm^2. The manufacturing sequence for the cell fabrication can be presented in the following steps:

- saw damage removing by the KOH chemical etching;
- emitter formation by the $POCl_3$ diffusion with sheet resistance ≈ 40 Ω/sq;
- parasitic junction removal by chemical etching in acid solution;
- phosphorous silica glass etching (PSG) in HF solution;
- PECVD of the SiN_x:H layer or TiO_x/SiO_2 for the reference cell;
- screen-printing front (Ag paste) and back (Al) contacts;
- co-firing front and back contacts in the infrared (IR) furnace.

The first series of Si wafers (with n^+–p junctions) was covered with SiN_x:H layers in a PECVD system produced by the Elettrorava (AGH University of Science Laboratory). The layers were prepared by direct RF (13.56 MHz) plasma chemical vapour deposition using SiH_4 and NH_3 as source gases. It was shown [3] that the refractive index of SiN_x:H layer depends on the $[SiH_4]/[NH_3]$ flow ratio and it can be changed in a wide range from 1.8 to 2.4. In this work, the refractive index of 2.0 was selected for the best match with air. The thickness of the layer was 80 nm in order to receive the minimum reflectance at the wavelength of 650 nm of the solar spectrum. The other deposition parameters were the following: the substrate temperature 225 °C and the deposition time 7 min 40 sec. In the second series, SiN_x:H layers were deposited on silicon wafers in a direct, low frequency (LF) PECVD system, designed specially for solar cells and for a very large number of wafers in one processing step (IMEC).

The n^+–p junctions and metallization of all the cells were made applying the same process in the Photovoltaic Laboratory of the Polish Academy of Sciences. For comparison, a reference cell with TiO_x antireflection coating, thermally oxidized at 800 °C for the surface passivation have been prepared as well.

The metallization of solar cells was made by the screen-printing process which is commonly used in industrial production. A silver paste PV145, manufactured by DuPont, was used for the front contact. The back contact covering the entire rear surface was deposited with a pure Al paste. The two collection back bus bar contacts were printed with a silver paste containing 3 wt. % of aluminium paste. After screen printing, the pastes were dried by heating at 200 °C and subsequently co-fired in an infrared (IR) belt furnace (LA-310). The silver front contacts were fired through the SiN_x:H layer. The temperature profile and the speed of the belt furnace are very criti-

cal parameters. They were optimized in order to receive the optimal values of electrical parameters of the solar cells. The best solar cells were obtained for a very short time of firing (very high speed of the belt) and high temperature in the one zone of the furnace (ca. 900 °C).

3. Measurements

The parameters of the solar cells were measured under standard AM 1.5 (100 mW/cm^2) radiation at 24 °C. The results are presented in Table 1. The measurements of *I–V* characteristics allow one to determine the basic parameters such as: I_{sc} – the short circuit current, V_{oc} – the open circuit voltage, FF – the fill factor and E_{ff} – the efficiency, and others parameters used for the optimization of firing conditions of the metallization, like: r_s – the series resistance and r_{sh} – the shunt resistance.

Table 1. Electrical parameters of mc-Si solar cells with SiN_x and TiO_x/SiO_2 layers

No.	ARC	r_s [Ω·cm^2]	r_{sh} [kΩ·cm^2]	I_{sc} [A]	V_{oc} [V]	FF [%]	E_{ff} [%]
1	SiN_x (IMEC)	0.70	2.2	3.17	0.596	75.2	14.2
2	SiN_x (AGH)	1.15	>10	3.05	0.589	72.5	13.0
3	TiO_x/SiO_2	0.72	10.2	2.79	0.589	76.5	12.6

In order to investigate the effect of the SiN_x:H layers on defect passivation, the technique LBIC was used. The method is based on the excitation of material with a light beam with a specified wavelength and intensity and measuring the current response for this excitation. As a result of focusing the light beam with defined shape, the light spot with a specified diameter on the tested sample is obtained. Based on the assumption of power density distribution on a sample surface and inside the material, the carriers generated in a time unit is determined. All the minority carriers generated by the illumination which do not participate in the recombination process create the induced signal.

The LBIC images of induced photocurrent distribution were obtained using the experimental set-up described in Ref. [14]. The optical systems consisting of a LED light source (650 nm), a diaphragm with 100 μm aperture and a glass objective were used in formation of the light beam. The diameter of light spot obtained with this system was 10 μm. Two computer-controlled translation stages provided the *x–y* scanning capability with 0.25×1.0 μm^2 step size. Steady state current induced in the external circuit was recorded for each position of the light beam spot. The LBIC images were obtained as the maps of values of induced photocurrent in the function of the *x–y* light beam position.

4. Results and discussion

The electrical parameters of solar cells are presented in Table 1. The SiN_x:H layers in cells 1 and 2 have been deposited in the IMEC (Inter-University Microelectronics

Centre in Leuven, Belgium) and the AGH Laboratory, respectively. The parameters of the reference cell with the TiO_x /SiO_2 coating are given for comparison. It is seen in Table 1 that the I_{sc} value of the solar cell with SiN_x:H layer deposited in the AGH Laboratory is improved in comparison with the reference cell but the V_{oc} values are still similar. The solar cell with the SiN_x:H made in the IMEC Laboratory is the best, a considerable improvement of I_{sc}, V_{oc} and efficiency (E_{ff} = 14.2 %) was obtained. One can notice that the fill factor of cell 2 is smaller than for other cells due to its high series resistance.

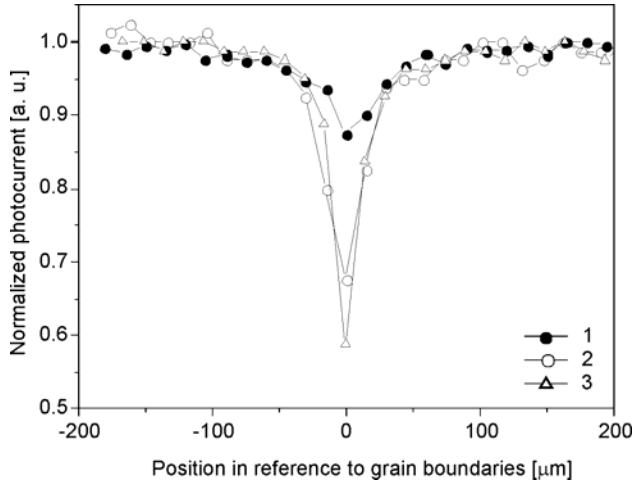

Fig. 1. The cross-section of the current signal across the interface of grains for the cells with SiN_x:H (1 – IMEC, 2 – AGH) and the reference cell with TiO_x/SiO_2 (3)

Figure 1 shows the cross-section current signals across the interface of grains for the cells 1–3 obtained in the LBIC measurements. One can see that the photocurrent of the cell in the grains interface with SiN_x:H deposited in IMEC is the highest. The improvement of photocurrent by the SiN_x:H deposited in the AGH Laboratory is smaller due to non-optimized conditions of PECVD deposition of this layer.

5. Conclusions

Both kinds of the SiN_x:H layers used as the antireflection and passivating coatings improve electrical parameters of the solar cells in comparison with the TiO_x/SiO_2 coating. The best parameters of the solar cells were obtained for the SiN_x:H deposited in the IMEC Laboratory. Investigation using the light beam induced current maps shows that this layer gives a significant increase of the photocurrent in the grains interface. In the case of the SiN_x:H layer deposited in the AGH Laboratory, the improvement in the LBIC signal is very small. Thus, one can conclude that the deposition conditions of the layers should be further optimized in order to improve the

defect passivation. In addition, the firing parameters of metallization should be changed in order to decrease the series resistance and improve the fill factor of cells as well.

Acknowledgements

The research was supported by the Ministry of Science and Informative Technology in Poland in the frame of the national-solicited project PBZ/100/T08/2003 and in the frame of statutory work of the Institute of Metallurgy and Materials Science of the Polish Academy of Sciences.

References

[1] EKAI R., VERBEEK M., NAGEL H., AUER R., ABERLE A., HEZEL R., Proc. 2nd World Conf. on Photovoltaic Solar Energy Conversion, Vienna, 1998, p. 1430.
[2] NAGEL H., ABERLE A.G., HEZEL R., Prog. Photovolt. Res. Appl., 7 (1999), 245.
[3] LIPIŃSKI M., ZIĘBA P., JONAS S., KLUSKA S., SOKOŁOWSKI M., CZTERNASTEK H., Opto-Electr. Rev., 12 (2004) 41.
[4] CHEN Z. AND ROCHATGI A., Proc. 1st World Conf. on Photovoltaic Solar Energy Conversion, Hawaii, 1994, p. 1331.
[5] ABERLE A.G., LAUINGER T., HEZEL R., Proc. 14th European Photovoltaic Solar Energy Conf., Barcelona, 1997, 684.
[6] RUBY D.S., WILBANKS W.L. AND FLEDDERMANN C.B., Proc. 1st World Conf. on Photovoltaic Solar Energy Conversion, Hawaii, 1994, 1335.
[7] DUERINCKX F., SZLUFCIK J., ZIEBAKOWSKI A., NIJS J., MERTENS R., Proc. 14th European Photovoltaic Solar Energy Conf., Barcelona, 1997, 792.
[8] ABERLE A.G. AND HEZEL R., Prog. Photovolt. Res. Appl., 5 (1997), 29.
[9] ROHATGI A., YELUNDUR V., JEONG J., EBONG A., MEIER D., BABOR A. M., ROSENBLUM M.D., Proc. 16th European Photovoltaic Solar Energy Conf., Glasgow, 2000, p. 1120.
[10] LENKEIT B. AND HEZEL R., Proc. 17th European Photovoltaic Solar Energy Conf., Munich, 2001, 342.
[11] DUERINKX F., SZLUFCIK J., Sol. Energy Mat. Sol. Cells, 72 (2002), 231.
[12] WINDERBAUM S., CUEVAS A., CHEN F., TAN J., HANTON K., MACDONALD D., ROTH K., Proc. 19th European Photov. Solar Energy Conf., Paris, 2004, 576.
[13] SCHMIDT J., MOSCHNER J.D, HENZE J., DAUWE S., HEZEL R., Proc. 19th European Photovolt. Solar Energy Conf., Paris, 2004, 391.
[14] PASZKIEWICZ B., SZYSZKA A., PASZKIEWICZ R., WOŚKO M., TŁACZAŁA M., Proc. 5th Inter. Conf. on Advanced Semiconductor Devices and Microsystems, Smolenice Castle, Slowakia, 2004, p. 275.

Received 9 September 2005
Revised 10 November 2005

Materials Science-Poland, Vol. 24, No. 4, 2006

Graded SiO_xN_y layers as antireflection coatings for solar cells application

M. LIPIŃSKI[1*], S. KLUSKA[2], H. CZTERNASTEK[2], P. ZIĘBA[1]

[1]Institute of Metallurgy and Materials Science of the Polish Academy of Sciences, Reymonta 25, 30-059 Cracow, Poland

[2]AGH University of Science and Technology, Mickiewicza 30, 30-059 Cracow, Poland

The results of theoretical optical optimization of the graded index oxynitride antireflection coatings for silicon solar cells are presented. The calculation of reflectance and absorption of layers were carried out using the Bruggeman effective medium approximation with various concentration profiles of SiN_x:H in the SiO_2 matrices. The experimental optical data of SiN_x:H layers deposited by RF (13.56 MHz) plasma enhanced chemical vapour deposition system in various conditions were used for simulation. The highest improvement of the short-circuit current J_{SC} (44.6%) was obtained with an SiO_xN_y graded layer for SiN_x:H with a low refractive index (2.1 at 600 nm) and abrupt concentration profile which is characteristic of a double layer SiO_2–SiN_x:H. The graded index profile can be advantageous for SiN_x:H with higher indices ($n \geq 2.4$). Moreover, the enhancement of J_{SC} obtained by application of the antireflection coating is smaller (42.3% for $n = 2.4$) in this case. The improvement should be higher if the effect of surface passivation is taken into account.

Key words: *graded refractive index; oxynitride; antireflection coating*

1. Introduction

Antireflection coatings are very important parts of solar cells. Presently, application of SiN_x:H layers obtained by plasma enhanced chemical vapour deposition (PECVD) is the crucial step to obtain high-efficiency silicon solar cells. The most important is the possibility to use them for surface and bulk passivation [1]. SiN_x:H layers can be used as excellent antireflection coatings due to a high flexibility of their optical parameters. Refractive indices of such layers can be changed in a wide range (from 1.8 to 2.9 at 600 nm) by adjustment of gas composition (SiH_4:NH_3) [2]. High values of n are advantageous in respect of good surface passivating properties. Moreover, the layer with a high value of n has a considerable absorption due to a high extinction coefficient. Therefore, a compromise has to be reached between reflectance,

*Corresponding author, e-mail: marlipin@wp.pl

absorption and passivation properties. It is supposed that one of the ways to obtain good optical and passivation properties is application of graded index antireflection coatings based on the silicon oxynitride (SiO_xN_y:H) which changes its composition from SiO_2 to SiN_x:H. This kind of coating can be accomplished by PECVD by changing composition of the SiH_4:NH_3:N_2O atmosphere.

In Ref. [3], a theoretical model of graded oxynitride films is presented based on the Bruggeman effective medium approximation. In this model, SiO_xN_y is a SiO_2 matrix with SiN_x:H particles. Although this is not the case in reality, the approximation gives good results in the visible and near-infrared range. In the paper, the results of simulation using the same model are presented together with experimental optical parameters of SiN_x:H layers deposited by PECVD.

2. Simulation

For the simulation of optical parameters of the SiO_xN_y layers the SCOUT software was used [4]. The Bruggeman effective medium approximation (EMA) [6] was chosen [3, 5]. In the EMA, an SiO_xN_y film is considered as a composite of two phases: SiO_2 matrix and SiN_x:H particles. The effective dielectric function ε_{ff} of the composite SiO_xN_y layer can be expressed by the formula:

$$(1-f)\frac{\varepsilon_m - \varepsilon_{ff}}{\varepsilon_m + 2\varepsilon_{ff}} + f\frac{\varepsilon_p - \varepsilon_{ff}}{\varepsilon_p + 2\varepsilon_{ff}} = 0 \tag{1}$$

where ε_m is the dielectric function of SiO_2 matrix, ε_p – the dielectric function of the particle (SiN_x:H) material, f – the volume fraction of the particle material in the matrix material, $f \leq 1$ ($f = 0$ for SiO_2, $f = 1$ for SiN_x:H).

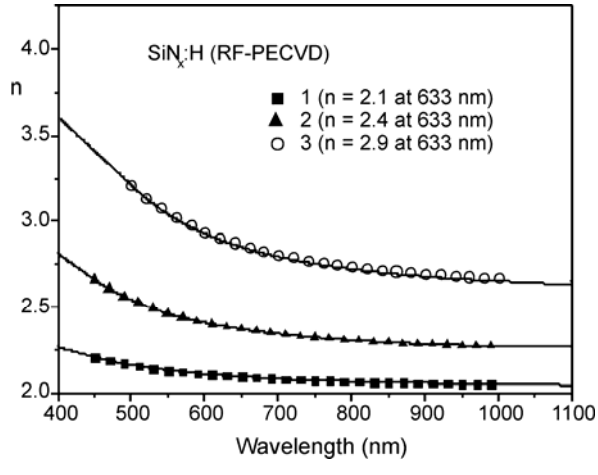

Fig.1. The measured dispersion of the refractive index n for various RFPECVD SiN_x:H films [2]

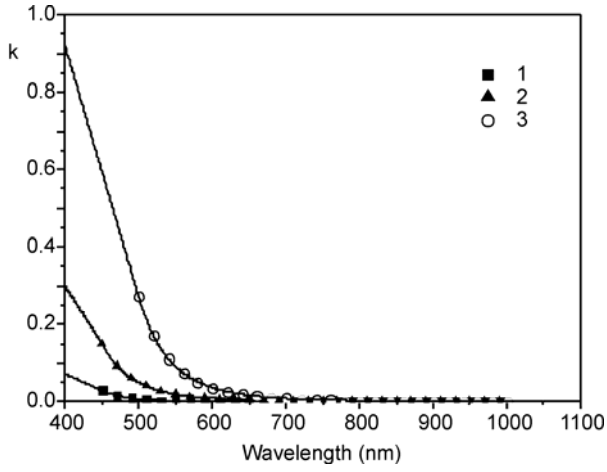

Fig. 2. The measured dispersion of the extinction coefficient k for the RFPECVD SiN_x:H films from Fig. 1

The wavelength-dependent refractive index $n(\lambda)$ and the extinction coefficient $k(\lambda)$ of SiN_x layers deposited by the RF PECVD for various NH_3/SiH_4 ratios [2] were used to calculate optical parameters of the graded SiO_xN_y layers. Figures 1, 2 show the dispersion of the optical constants of these layers. The dielectric function for the SiO_2 layer and Si (polycrystalline) base material was taken from the database of the SCOUT program.

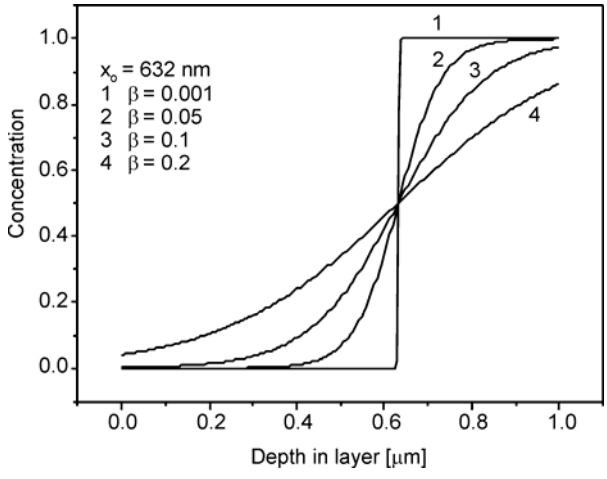

Fig. 3. The profiles of SiN_x:H concentration in the SiN_xO_y material [3]

The optical parameters of graded SiO_xN_y layers were determined for various concentration gradients. The latter was exposed by the volume fraction of silica in the

SiN_x:H material $f(x)$ as a function of the parameter x being the ratio of the layer depth to its thickness. According to Ref. [3], $f(x)$ was taken in the form:

$$f(x) = 1 - \left[1 + \exp\left(\frac{x - x_0}{\beta}\right)\right]^{-1} \tag{2}$$

The examples of concentration profiles for various β values are shown in Fig. 3. The parameter x_0 was fixed to obtain the minimum reflectance $R_{\min} = 0$. The thickness of the antireflection coating (ARC) layer d was chosen to obtain $R_{\min}$ for $\lambda = 700$ nm.

3. Optimization of ARC

The following expressions were applied for the optimization of antireflection coating: the density of the short-circuit current J_{SC} losses due to the reflection J_{ref}, and absorption J_{abs} :

$$J_{SC} = J_{SC\,\max} - J_{\text{ref}} - J_{\text{abs}} \tag{3}$$

$$J_{SC\,\max} = q \int_{\lambda_{\min}}^{\lambda_{\max}} F_{ph}(\lambda) IQE(\lambda) d\lambda \tag{4}$$

$$J_{\text{ref}} = q \int_{\lambda_{\min}}^{\lambda_{\max}} R(\lambda) F_{ph}(\lambda) IQE(\lambda) d\lambda \tag{5}$$

$$J_{abs} = q \int_{\lambda_{\min}}^{\lambda_{\max}} A(\lambda)\, F_{ph}(\lambda) IQE(\lambda) d\lambda \tag{6}$$

where $\lambda_{\min} = 300$ nm, $\lambda_{\max} = 1200$ nm, q is the charge of electron, $F_{ph}(\lambda)$ – the incident photon flux calculated from the AM1.5G solar spectrum (normalized to the power density of 100 mW·cm^{-2}), $R(\lambda)$ – the reflectance, $A(\lambda)$– the absorption of the ARC layer, $IQE(\lambda)$ – the internal quantum efficiency of the solar cell. $J_{SC\max}$ is the maximal J_{SC} value for the reflectance $R(\lambda) = 0$ and absorption of antireflection coating $A(\lambda) = 0$ for the whole λ range.

The $IQE(\lambda)$ was calculated using the PC-1D program [7] for the two sets of parameters given in Table 1. For the simulation of cell 1, the parameters used were typical of the polycrystalline silicon solar cell (efficiency 16%) and for the simulation of cell 2 – the parameters for the single crystalline solar cells characterized by the efficiency of about 20% as in Ref. [8]. The IQEs for these two solar cells are presented in Fig. 4.

Table 1. Parameters used for the calculation of the IQE of two n^+-p silicon solar cells using the simulation programme PC-1D and calculated values of the maximal and minimal (without ARC) values of J_{SC}

Parameter	Cell	
	1	2
Cell thickness [μm]	300	350
Diffusion length within the base [μm]	150	810
Specific resistance of the base [Ω·cm]	1	1.5
Emitter peak doping [cm^{-3}]	2×10^{20}	7×10^{19}
Junction depth [μm]	0.5	0.4
Emitter sheet resistance [Ω/sq.]	40	100
Front surface recombination velocity [cm/s]	10^5	1.5×10^4
Back surface recombination velocity [cm/s]	10^7	60
$J_{SC\max}$ ($R = 0$, $A = 0$) [mA/cm^2]	35.4	40.8
$J_{SC\min}$ (without ARC) [mA/cm^2]	23.0	26.5

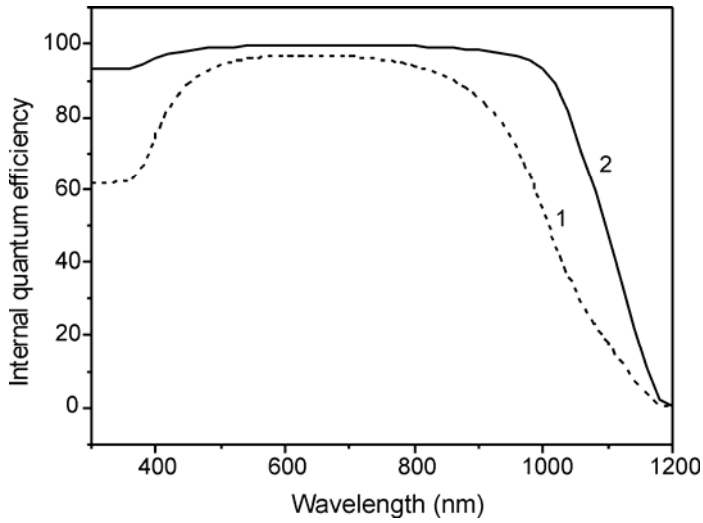

Fig. 4. Internal quantum efficiencies for two solar cells (1 and 2) simulated by the PC-1D program

In order to describe the improvement in J_{SC} due to ARC, the ratio $\Delta J_{SC}/J_{SC}$ was calculated according to the equation:

$$\frac{\Delta J_{SC}}{J_{SC}} = \frac{J_{SC}(\text{with ARC}) - J_{SC}(\text{without ARC})}{J_{SC}(\text{without ARC})} \tag{7}$$

One can see that the maximum values of $\Delta J_{SC}/J_{SC}$ for the cell 1 and cell 2 are close to 54%.

4. Results

Figure 5 presents reflectances for various profiles $f(x)$ of graded SiN_xO_y and single homogenous SiN_x:H layers for comparison (1 and 2). Table 2 shows the results of calculation of the parameters from Eqs. (3)–(6) used for the optimization of antireflection coatings. The results of optical optimization of the SiO_xN_y antireflection coatings for the various gradient profiles depending on β and x_0 parameters are presented in Table 3.

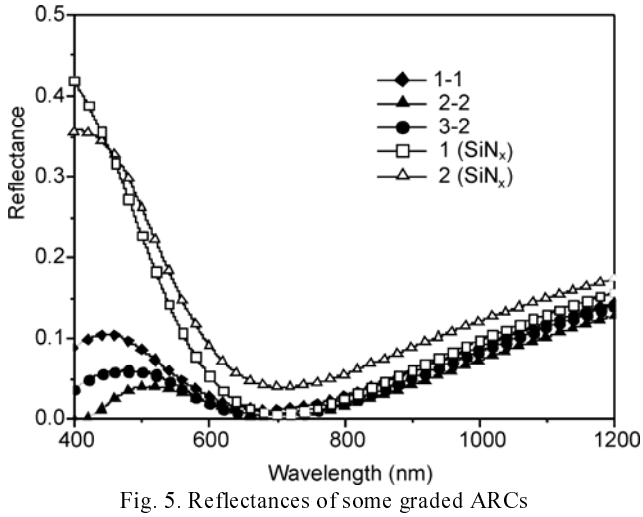

Fig. 5. Reflectances of some graded ARCs and SiN_x:H layers for the comparison

Table 2. Calculated short circuit current densities and losses factors due to the reflectivity and absorption for single homogeneous SiN_x antireflection coatings

Cell	n	D [nm]	J_{ref}	J_{abs}	J_{sc}	$\Delta J_{sc}/J_{sc}$ [%]
			[mA/cm^2]			
1	2.1	85.0	3.42	0.71	31.42	36.6
2	2.4	75.5	4.35	2.79	28.78	25.1

It is seen from Table 3 that the highest J_{SC} value is obtained for the layer 1–1 which can be considered as a double SiO_2–SiN_x:H layer where SiN_x:H has a low index n (2.1). In the case of SiN_xO_y layer composed of SiO_2 and SiN_x:H with a higher index n, the optimal layer is obtained for the graded concentration with the β factor equal to 0.05 and 0.2 for the SiN_x:H with n = 2.4 and 2.9, respectively. The reflectance losses J_{refl} are lower (for SiN_x:H with n = 2.4 and 2.9) than in the case of double SiO_2 –SiN_x:H layer (for n = 2.1) but the values of J_{SC} are lower, too, due to high absorption losses.

Table 3. Results of the optical optimization of graded SiO_xN_y ARCs considered as a the mixture of SiO_2 with SiN_x:H

No.	n	x_o	β	d [nm]	J_{ref}	J_{abs}	$J_{ref}+J_{abs}$	J_{sc}	J_{sc}^*	$\Delta J_{sc}/J_{sc}$ [%]
					[mA/cm^2]					
1–1	2.1	0.63	0.001	128	1.68	0.47	2.15	33.28	38.05	44.6
1–2	2.1	0.63	0.050	126	2.06	0.35	2.41	33.03	37.78	43.5
1–3	2.1	0.46	0.100	119	2.05	0.50	2.55	32.88	37.63	42.9
2–1	2.4	0.63	0.001	136	0.82	1.95	2.77	32.66	37.30	41.9
2–2	2.4	0.63	0.05	136	0.94	1.75	2.69	32.74	37.40	42.3
2–3	2.4	0.63	0.100	132	1.23	1.64	2.87	32.55	37.21	41.5
3–1	2.9	0.64	0.1	142	0.54	4.46	5.00	30.43	34.88	32.2
3–2	2.9	0.72	0.2	121	1.16	3.41	4.57	30.86	35.28	34.1
3–3	2.9	0.72	0.3	109	1.47	3.33	4.80	30.63	35.01	33.1

For n = 2.1, 2.4 and 2.9 (at 633 nm) for the IQE cell 1. Additionally, the results of J_{SC}^* simulated for the IQE cell 2 (see Fig. 4) are given.

For the SiN_x:H layer with n = 2.9, the reflectance losses are the lowest, however, the absorption losses are very high. For the optimal profile with β = 0.2, the J_{sc} is considerably lower in comparison with others layers (1–1 and 2–2).

Comparing the values of the $\Delta J_{SC}/J_{SC}$ parameter and J_{SC} values from Tables 2 and 3 one can conclude that all the graded SiO_xN_y films composed of SiO_2 and SiN_x:H with n = 2.1 or 2.4 are better than simple homogeneous SiN_x:H layers.

5. Conclusion

Optical improvement of graded layers can be obtained due to the reduction of total optical losses in comparison with single layers. The mixture of SiO_2 and SiN_x:H with the large index n (n = 2.4 or n = 2.9) has high absorption losses which can be reduced by the optimal profile concentration. The graded index profile can be profitable for SiN_x:H with the high refractive index n ($n \geq 2.4$). Moreover, the enhancement of J_{SC} obtained by the antireflection coating is smaller (42.3% for n = 2.4) in comparison with the SiO_2–SiN_x:H double layer for n = 2.1. In the presented simulation, the surface passivation effect was not considered. It is supposed that the influence of refractive index on the surface recombination makes the graded profile to be more profitable with higher refractive index.

Acknowledgements

This research was supported by the Ministry of Science and Informative Technology, Poland in the frame of the national-solicited project: PBZ/100/T08/2003.

References

[1] CHEN Z. AND ROCHATGI A., Proc. 1st WCPEC, Hawaii, 1994, p.1331.

[2] LIPIŃSKI M., ZIĘBA P., JONAS S., KLUSKA S., SOKOŁOWSKI M., CZTERNASTEK H., Opto-Electr. Rev., 12 (2004), 41.

[3] MAHDJOUB A., ZIGHED L., Thin Solid Films, 478 (2005), 299.
[4] THEISS W., SCOUT version 2.3, web: www.mtheiss.com.
[5] SNYDER P.G., XIONG Y.-M., WOOLAM J.A., AL-JUMAILY G.A., GAGLIARDI F. J., J. Vac. Sci. Technol., A10 (1992), 1462.
[6] BRUGGEMAN A. G., Ann. Phys. (Leipzig), 24 (1935), 636.
[7] BASORE P.A., CLUGSTON D.A., PC-1D vers.5.4, web: www.pv.unsw.edu.au.
[8] NAGEL H., ABERLE A.G., HEZEL R., Prog. Photovolt.: Res. Appl., 7 (1999), 245.

Received 9 September 2005
Revised 10 November 2005

Materials Science-Poland, Vol. 24, No. 4, 2006

Quasi-periodic microstructuring of iron cylinder surface under its corrosion under combined electric and magnetic fields

O. YU. GOROBETS, D. O. DERECHA*

Institute of Magnetism of NAS of Ukraine, Kiev, 03142, Ukraine

The phenomenon of quasi-periodic microstructuring of the surface of iron cylinder under its corrosion in the nitric acid, under combined electric and homogeneous permanent external magnetic fields has been investigated. Temporary dependences of microstructure parameters on the strength of the magnetic field, voltage and concentration of acid are presented in the paper.

Key words: *microstructuring; self-organization; magnetoelectrolysis; magnetic field*

1. Introduction

Technologies of metal electrodeposition to create surfaces possessing functional properties constitute about 25% of the surface modification market [1]. Magnetoelectrolysis is one of the most prospective directions in this field [2–12]. In particular, magnetic field applied to electrolytic cell allows obtaining "branchy" structure of a fractal surface as well as surfaces with improved smoothness and reflectivity [13, 14]. It is also well known that magnetic field influences the corrosion rate of metals, for example, copper [15] and iron [16]. However, use of magnetic field in structuring metal surface under corrosion has been much less investigated than its application to electrodeposition. Magnetohydrodynamic stirring of electrolytes has a considerable influence on structuring of metal surface under combined magnetic and electric fields. It is explained theoretically on the basis of the magnetohydrodynamic equations and the theory of the convective diffusion [2–16]. Recently multivortex stirring of nitric acid solution was revealed in the vicinity of the surface of a metallic cylinder under its corrosion under constant magnetic field when electric field was not applied [16]. In such conditions, quasi-periodic microstructuring of the surfaces of steel and iron cylinders was found

*Corresponding author, e-mail: dderecha@yandex.ru

[17, 18]. The effect of quasi-periodic microstructuring of a surface corroding under magnetic field is an example of nonlinear self-organization. Thereupon investigation of the influence of magnetic field on the surface structure of a metallic cylinder under its cathode and anode corrosion represents fundamental and applied interest.

2. Experimental

The surfaces of iron cylinders were investigated under corrosion in solutions of nitric acid under external constant magnetic and electric fields. The installation consists of an electromagnet with pole tips and a visualization system [16]. Two iron cylinders 1 are fixed in a container 2, parallel to each other at the distance of 3 cm as is shown in Fig. 1. Brass plates 3 with the gaps are used for fixing the cylinders outside the container and for the contact with the electric circuit which is connected to the plates. The circuit consists of a voltage source, the resistor 4 used to change the voltage between the two cylinders, and the voltmeter 5. The voltmeter is connected with the copper plates 3 and the voltage between the cylinders is measured. The container is fixed between the pole tips of the electromagnet in such a way that magnetic field is parallel to the symmetry axes of the cylinders. Thus, the direction of magnetic field is perpendicular to the direction of the electric field in the vicinity of the surface of each cylinder.

The experiments were carried out in external magnetic field from 80 to 240 kA/m, the concentrations of nitric acid solution ranged between 7 and 21%. The voltage was changed in the range of 0.1–1.5 V.

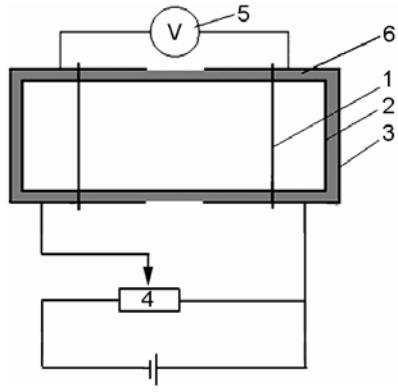

Fig. 1. The functional scheme of the electric circuit connected to the container with iron cylinders. See the text for further discussion

In this work, a comparison of the structures of the surfaces of the iron cylinders was made under the following conditions of corrosion:

a) without electric and without magnetic field; b) under electric field only; c) under magnetic field only; d) under combined electric and magnetic fields.

3. Results and discussion

The microstructure of the surface resulting from corrosion does not depend on the coordinate along the cylinder axis (Fig. 2), i.e., the long-range ordering of the corroded surface is not observed along the cylinder axis.

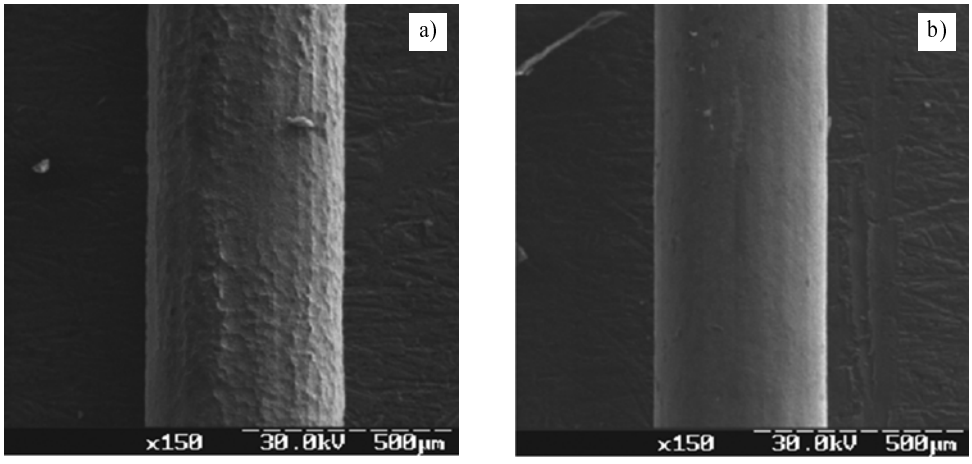

Fig. 2. An iron cylinder after corrosion in 14% solution of nitric acid, the voltage between the cylinders is 1.5 V, the duration of experiment – 10 min: a) cathode corrosion; b) anode corrosion

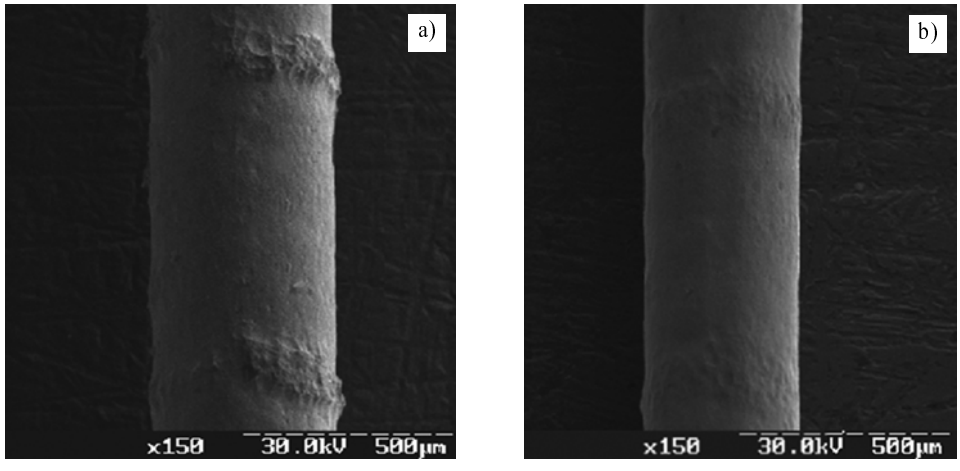

Fig. 3. An iron cylinder after corrosion in 14% solution of nitric acid, the voltage between the cylinders is 1.5 V, the magnetic field strength – 240 kA/m, the duration of experiment – 10 min: a) cathode corrosion; b) anode corrosion

Quasi-periodic structuring of the surface of the cylinder was observed under applied magnetic field only (condition c)). Periodically repeated elevations and cavities

are formed as is reported in [17, 18, 23]. The period of the quasi-periodic surface structure T ($T = L + l$, where L is the elevation length, l is the cavity length) is much greater than the characteristic size of the surface microstructure, i.e. in this case, long-range ordering of the shape of corroded surface is observed along the cylinder axis.

The long-scale quasi-periodic microstructuring of the corroded surface is observed under the combined electric and magnetic fields (condition d)), as well as in the case of application of a magnetic field only (Fig. 3).

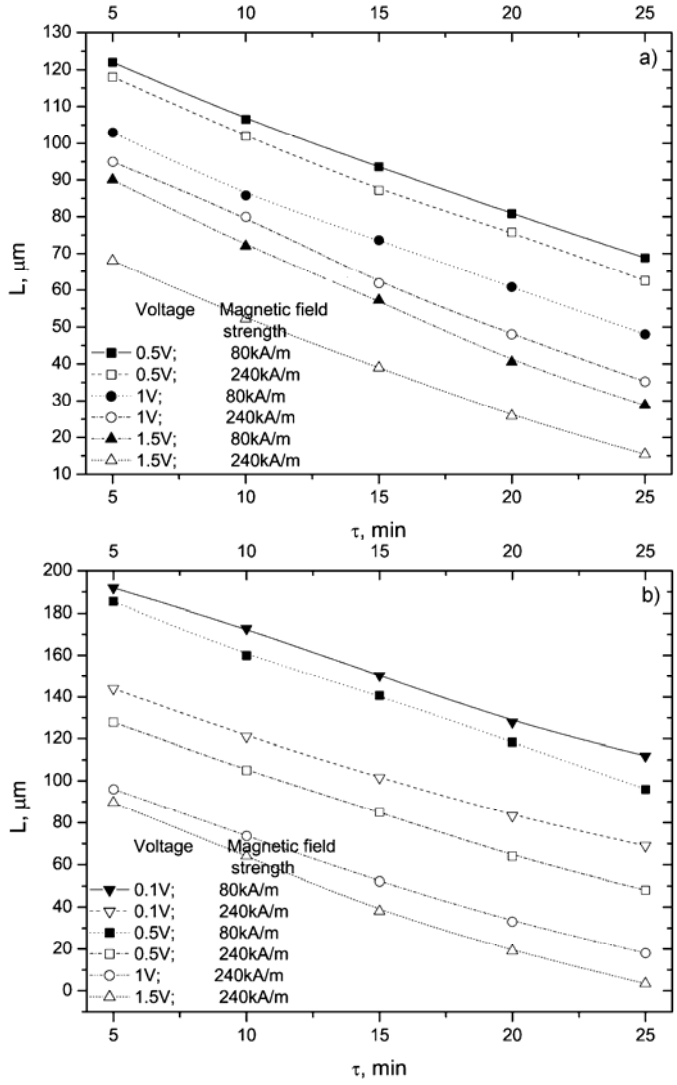

Fig. 4. Time dependences of the elevation length L of the quasi-periodic surface structure of the cylinder: a) under its cathode corrosion in the 7% solution of nitric acid, b) under its anode corrosion. Mean error ~25%

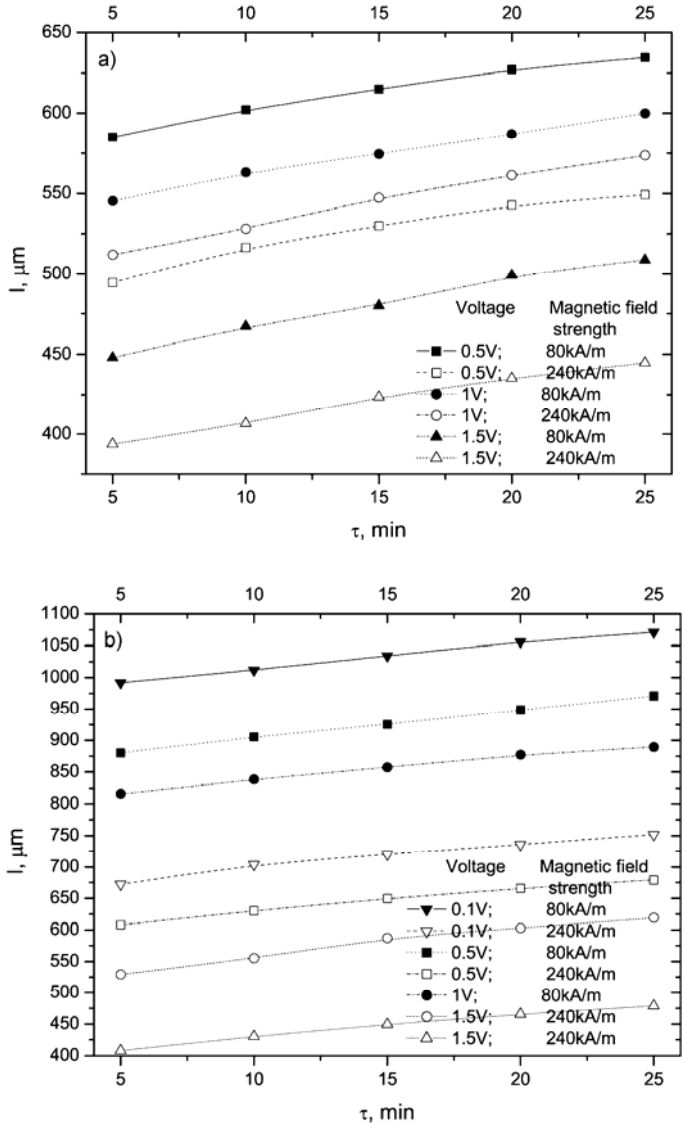

Fig. 5. Time dependences of the cavity length *l* of the quasi-periodic surface structure of the cylinder: a) under its cathode corrosion in 7% solution of nitric acid, b) under its anode corrosion. Mean error ~25%

Characteristic parameters of the structure of quasi-periodic surface of the cylinder (period *T*, elevation length *L*, cavity length *l*, amplitude *A*, being the difference between the cylinder diameters at the elevation and at the cavity, cylinder diameter at the elevation *D* differ in the cases c) and d). In the case d), they also differ for the cathode and anode corrosion. The microstructure period under anode corrosion is longer than under cathode corrosion. The period *T* decreases when the external mag-

netic field strength, the voltage between the cylinders and the concentration of nitric acid increase, i.e. the quasi-periodic surface structure becomes more small-scale. The elevation length L decreases in the course of time while the cavity length increases both for the cathode and anode corrosion (Figs. 4, 5). The higher magnetic and electric field, the smaller are the elevation lengths L.

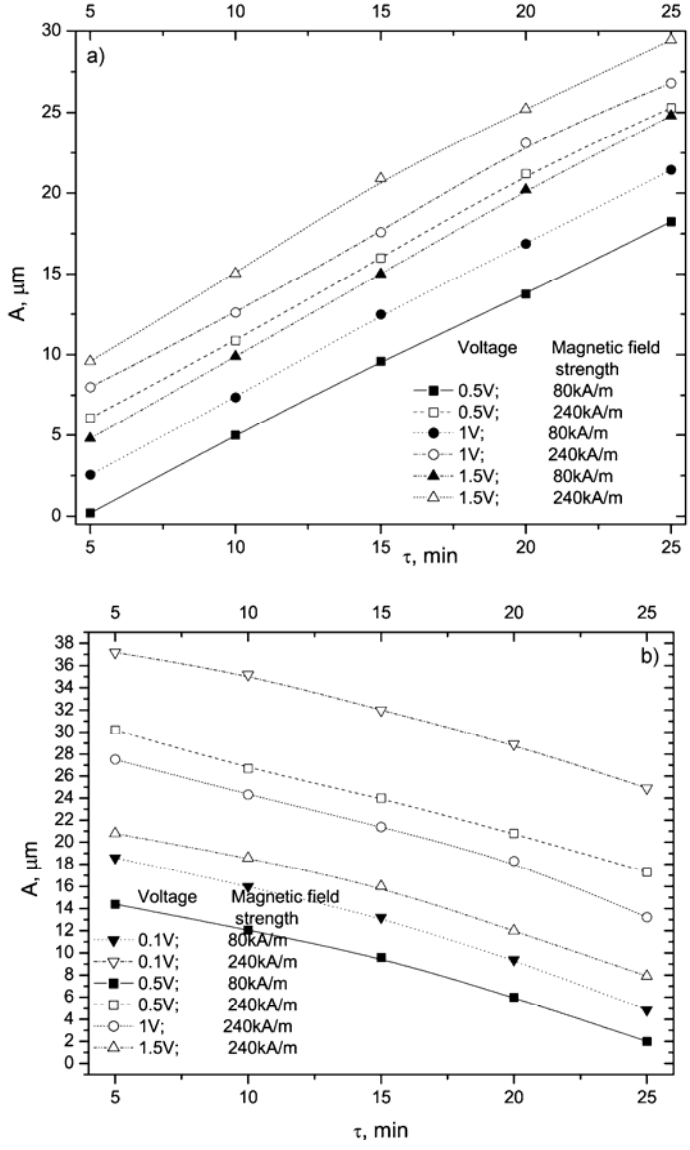

Fig. 6. Time dependences of the amplitude A of the quasi-periodic surface structure of the cylinder: a) under its cathode corrosion in the 7% solution of nitric acid, b) under its anode corrosion. Mean error ~25%

The amplitude of the structure of surface under the anode corrosion decreases when the voltage between the cylinders increases; the amplitude A tends to zero at the voltage higher than 0.5 V, i.e. A becomes smaller than the characteristic size of the surface roughness under corrosion without magnetic field. At the same time, the quasi-periodic structure is formed at the cathode surface at 1±0.5 V and its amplitude increases when the voltage increases. It is shown in Fig. 3: the quasi-periodic structure at the cathode surface is visible, while there is no such structure at the anode

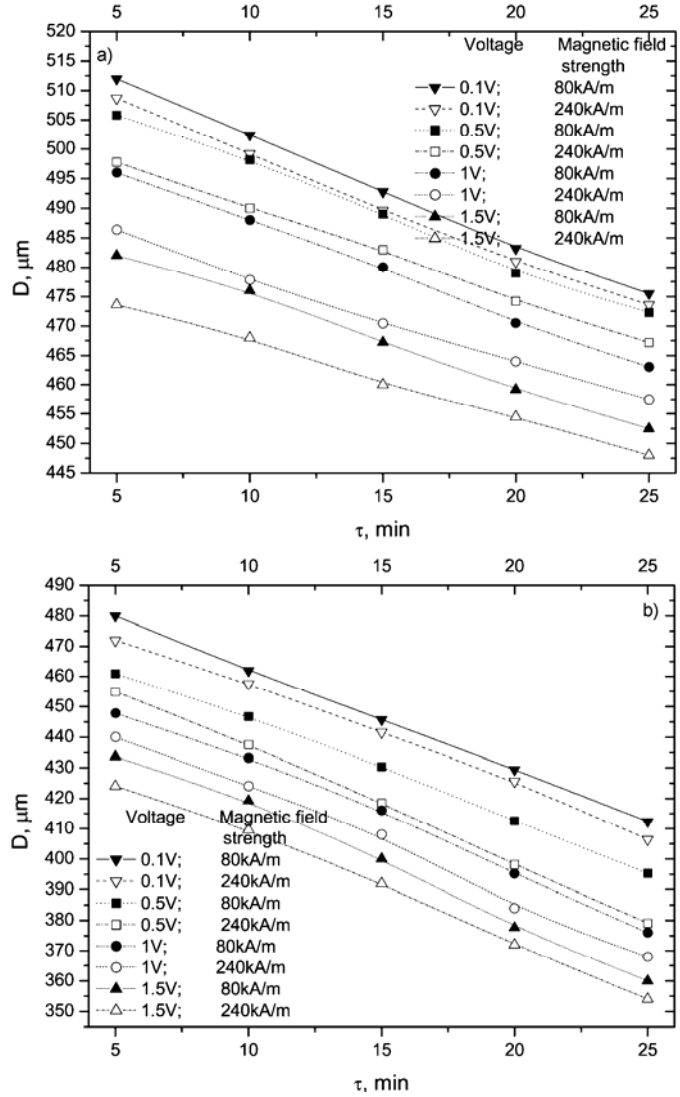

Fig. 7. Time dependences of the cylinder diameter D at the elevation of the quasi-periodic surface structure of the cylinder: a) under its cathode corrosion b) under its anode corrosion in the 7% solution of nitric acid. Mean error ~25%

surface by this time. Besides, the amplitude A decreases under the anode corrosion and it increases under the cathode corrosion with time (Figs. 6a, b).

It is obvious from Figs. 2 and 3 that the cylinder diameter is greater under the cathode corrosion than under the anode one. The diameter D decreases with time both for the cathode and the anode corrosion (Figs. 7a, b).

4. Conclusion

The characteristic parameters of the quasi-periodic structure of surface of an iron cylinder depend on the concentration of the nitric acid solution, the voltage between the cylinders, the value of the external magnetic field and time. The results of the present work can be used to control the structure of the corroded metallic surface under external electric and magnetic fields. It may find application for production of components of microelectronics, micromachinery, microelectromechanical systems [19–21], high gradient ferromagnetic matrices for magnetic filters [22] and in other fields where the controlled corrosion is used.

Acknowledgements

This work was executed owing to funds of the Ministry of Education and Science of Ukraine, rendered as the grant of the President of Ukraine for support of scientific researches of young scientists.

References

[1] CELIS J.P., DE BONTE M., ROOS J.R., Trans. I.M.F., 72 (1994), 89.
[2] FAHIDY T.Z., Prog. Surf. Sci., 68 (2001), 155.
[3] MOFFAT T.P., BONEVICH J.E, HUBER W.H., J. Electrochem. Soc., 147 (2000), 4524.
[4] YANG S.Y., YANG I.J., HORNG H.E., HONG CHIN-YIH, YANG H.C., Magnetohydrodyn., 36 (2000), 16.
[5] BODEA S., VIGNON L., BALLOU R., MOLHO P., Phys. Rev. Lett., 83 (1999), 2612.
[6] FAHIDY T.Z., *The Effect of Magnetic Fields on Electrochemical Processes*, [in:] B.E. Conway, J. O'M. Bockris, R.E. White, *Modern Aspects of Electrochemistry*, Kluwer, New York, 1999, 404.
[7] WASKAAS M., KHARKATS Y.I., J. Phys. Chem., B103 (1999), 4876.
[8] COEY J.M.D., HINDS G., LYONS M.E.G., Europhys. Lett., 47 (1999), 267.
[9] LEVENTIS N., CHEN M., GAO X., CANALAS M., ZHANG P., J. Phys. Chem., B102 (1998), 3512.
[10] ALBOUSSIÈRE T., GARANDET J.P., MOREAU R., Magnetohydrodyn., 32 (1997), 359.
[11] TACKEN R.A., JANSSEN L.J., J. Appl. Electrochem., 25 (1995), 1.
[12] FAHIDY T.Z., J. Appl. Electrochem., 13 (1983), 553.
[13] OLIVAS P., ZAHRAI S., BARK F.H., J. Appl. Electrochem., 27 (1997), 1369.
[14] ALEMANY A., OLIVAS P., J. Appl. Electrochem., 34 (2004), 19.
[15] SHINOHARA K., AOGAKI R., J. Appl. Electrochem., 67 (1999) 35.
[16] GOROBETS S.V., GOROBETS O.YU., RESHETNYAK S.A., J. Magn. Magn. Mater., 272 (2004), 2408.
[17] GOROBETS S.V., GOROBETS O.YU., MAZUR S.P., SLUSAR A.A., Phys. Stat. Sol., 12 (2004), 3686.
[18] GOROBETS YU.I., GOROBETS O.YU., MAZUR S.P., BRUKVA A.N., Phys. Met. Metallogr., 99 (2005), 139.

[19] DATTA M., IBM J. Res. Devel., 42 (1998), 5.
[20] TUMMALA R.R., RYMASZEWSKI E.J., *Microelectronics Packaging Handbook*, Van Nostrand Reinhold, New York, 1989, 905.
[21] DATTA M., *Electrochemical Micromachining* [in:] N. Masuko, T. Osaka (Eds.), *Electrochemical Technology: Innovations and New Developments,* Kodansha Gordon and Breach, Tokyo, 1996, 302.
[22] O'BRIEN N., SANTHANAM K.S.V., J. Appl. Electrochem., 20 (1990), 781.
[23] GOROBETS S.V., GOROBETS O.YU., BRUKVA A.N., Appl. Surf. Sci., 252 (2005), 448.

Received 10 September 2005
Revised 29 November 2005

Materials Science-Poland, Vol. 24, No. 4, 2006

Phase transitions in $Co_{78}Si_9B_{13}$ and $Fe_{78}Si_9B_{13}$ metallic glasses induced by isochronal annealing

E. JAKUBCZYK*

Institute of Physics, Jan Długosz University, al. Armii Krajowej 13/15, 42-201 Częstochowa, Poland

The crystallization process of $Co_{78}Si_9B_{13}$ and $Fe_{78}Si_9B_{13}$ metallic glasses was stimulated by isochronal annealing at various temperatures (573–823 K). By the DSC, X-ray diffraction, Hall and electrical resistivity measurements it was found that the crystallization proceeds through two main stages. At the first stage, α-Co and α-Fe phases are formed and at the second stage Co_2B and Fe_2B phases are crystallized. During the crystallization, the ferromagnetic ordering of both alloys is still conserved. $Fe_{78}Si_9B_{13}$ alloy has a much wider range of structural stability. The activation energy determined from DSC measurements and the total energy of the created phases obtained by quantum chemistry method confirmed the sequence and the type of the created phases. The creation of crystalline phases from the amorphous matrix was related to a distinct decrease of the electrical and Hall resistivities and the spontaneous Hall coefficient.

Key words: *metallic glass; crystallization; phase transition; activation energy; Hall effect*

1. Introduction

Rapid solidification from liquid state leads to the formation of a metastable amorphous structure. Metallic glasses are obtained in this way and they evolve through changes of the chemical and topological short-range ordering (CSRO and TSRO) and then changes of medium range ordering (MRO) to a polycrystalline state [1, 2]. The initiation and the kinetics of the crystallization process depend on their anisotropic microstructure and fluctuations of defect density. The transformation of the amorphous to the crystalline state can occur by the following typical processes: polymorphous, eutectoid, primary and peritectoid crystallization [3]. The type of transformation depends mainly on the alloy composition. The investigation of phase transitions in metallic glasses is important from both scientific and application points of view. This paper concentrates on the analysis of the influence of composition on the struc-

*Corresponding author, e-mail: e.jakubczyk@ajd.czest.pl

ture relaxation caused by isochronal annealing. For comparison, the most distinctive glasses from the $Fe_{78-x}Co_xSi_9B_{13}$ family, i.e. $Co_{78}Si_9B_{13}$ and $Fe_{78}Si_9B_{13}$ were chosen. The structural changes coincide with the changes of physical properties, and the latter ones are especially significant when a phase transition occurs. Standard methods have been applied to study the phase transitions, i.e. the DSC (differential scanning calorimetry), X-ray diffraction, electrical resistivity as well as the investigation of the Hall effect. The combination of methods makes it possible to determine the order of phase transition and also the type scattering of charge carriers [4–6].

2. Experimental

Ribbons of $Co_{78}Si_9B_{13}$ and $Fe_{78}Si_9B_{13}$ metallic glasses were prepared by the roller quenching method. DSC measurements were carried out using a STA-409 NETZSCH apparatus under an argon stream at heating rates of 5, 10, 15 and 20 K/min. Measurements of the electrical and Hall resistivities and X-ray diffraction were done at room temperatures for the as-received as well as isochronally (4 h) annealed samples at various temperatures (573–823 K) in an inert argon atmosphere. The X-ray studies were performed using a DRON-2.0 diffractometer with MoK_α radiation. The Hall voltage was measured by the constant current method at a constant magnetic field [7]. The electrical resistivity was also measured in the dc regime. The quantum -chemical calculations of the total energy of the created phases were done using a semi-empirical method of the HyperChem 6.0 program [8, 9].

3. Results and discussion

The thermal stability and kinetics of non-isothermal crystallization of $Co_{78}Si_9B_{13}$ and $Fe_{78}Si_9B_{13}$ metallic glasses were investigated by the DSC measurements. The measurements of the crystallization process were carried out for alloys at the heating rates of 5, 10, 15 and 20 K/min.

Figures 1a and 2a show the DSC curves of both alloys taken at various heating rates. It is clearly seen that all the DSC curves display two exothermic peaks indicating that the transformation of the amorphous to the polycrystalline state proceeds through two main stages. The temperatures corresponding to both peaks of both alloys increase with the increase of the heating rate. In the case of $Co_{78}Si_9B_{13}$, the exothermic peaks in DSC curves are widely separated, while those of $Fe_{78}Si_9B_{13}$ are closely situated. The temperature for the first peak for $Co_{78}Si_9B_{13}$ alloy is lower than that for the $Fe_{78}Si_9B_{13}$ alloy. Based on the Kissinger equation, the activation energy E_a for crystallization of phases can be estimated as follows [10–12]:

$$\frac{d\left(\ln\frac{v}{T_p^2}\right)}{d\left(\frac{1}{T_p}\right)} = -\frac{E_a}{R} \tag{1}$$

where v denotes the heating rate, T_p – peak temperature and R is the gas constant.

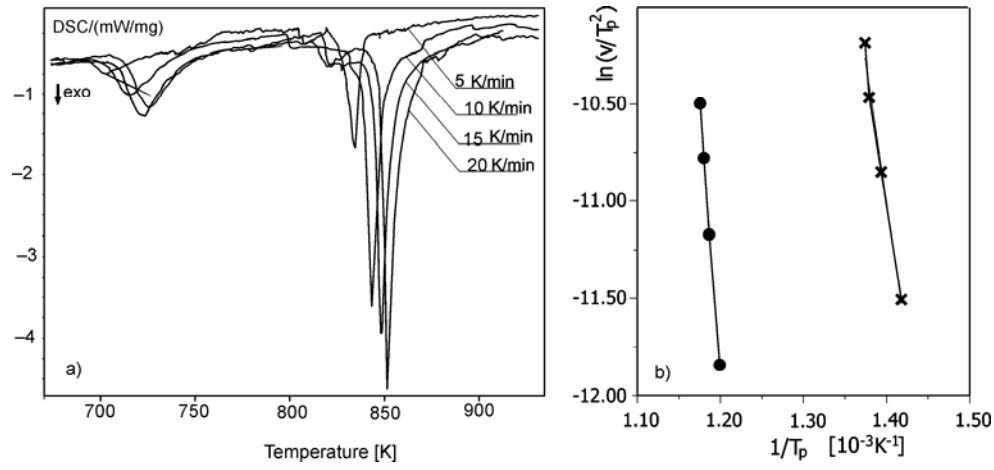

Fig. 1. Dependences for $Co_{78}Si_9B_{13}$ metallic glass: a) DSC curves at various heating rates, b) relationship between $\ln(v/T_p^2)$ and $1/T_p$ for both stages of crystallization (• – first stage, × – second stage)

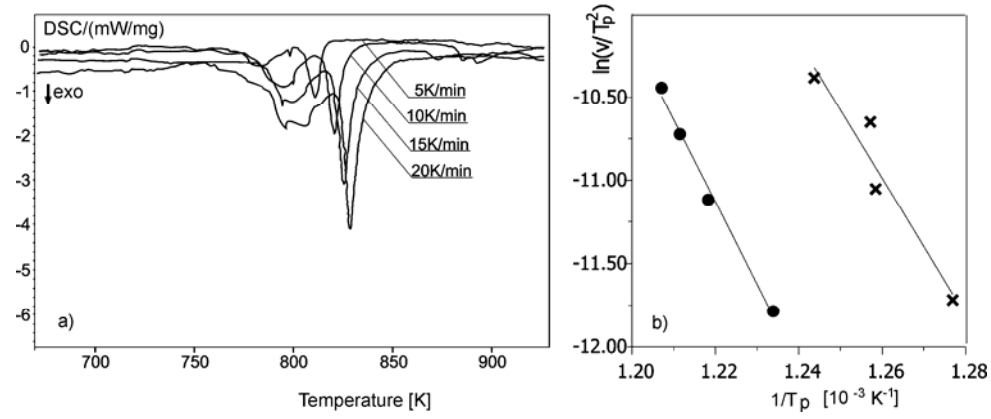

Fig. 2. Dependences for $Fe_{78}Si_9B_{13}$ metallic glass: a) DSC curves at various heating rates; b) relationship between $\ln(v/T_p^2)$ and $1/T_p$ for both stages of crystallization (• – first stage, × – second stage)

The plots of $\ln(v/T_p^2)$ vs. $1/T_p$ for both alloys yield straight lines with the slopes equal to $-E_a/R$ (Figs. 1b, 2b).

The values of the activation energy for the first and the second stage of crystallization for $Co_{78}Si_9B_{13}$ and $Fe_{78}Si_9B_{13}$ metallic glasses are given in Table 1. Thermal stimulation of the crystallization process for the first stage of the crystallization requires higher activation energy for the $Fe_{78}Si_9B_{13}$ alloy in comparison with $Co_{78}Si_9B_{13}$. The other results presented in this paper confirm occurring of the structural changes in the $Fe_{78}Si_9B_{13}$ metallic glass after annealing at higher temperatures.

Table 1. The activation energies [kJ/mol] for the first (E_{a1}) and the second (E_{a2}) stage of crystallization for $Co_{78}Si_9B_{13}$ and $Fe_{78}Si_9B_{13}$ metallic glasses

$Co_{78}Si_9B_{13}$		$Fe_{78}Si_9B_{13}$	
E_{a1}	E_{a2}	E_{a1}	E_{a2}
241	472	341	410

Figures 3 and 4 show the results of the measurement of the Hall resistivity ρ_H as a function of the external magnetic field B_0 in the as-received samples and in the samples annealed isochronally at various temperatures. With the increase of the annealing temperature ρ_H decreases. For the $Co_{78}Si_9B_{13}$ alloy the first decrease of the slope of the initial part of the dependence $\rho_H = f(B_0)$, as well as the decrease of the magnitude of the next part (slowly increasing) of this curve occurs for the samples annealed at 623 K. The next distinct steps are observed for the samples annealed at 673 K and 773 K.

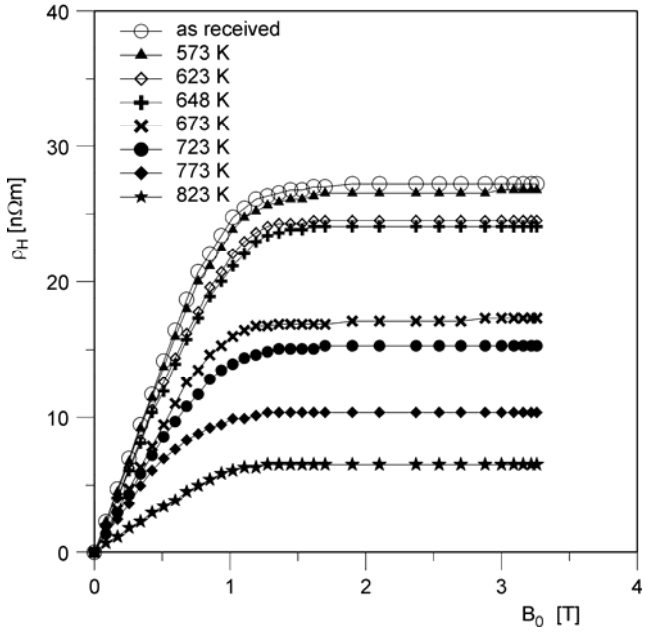

Fig. 3. The Hall resistivity ρ_H as a function of the applied magnetic induction B_0 for the samples of the $Co_{78}Si_9B_{13}$ alloy annealed at various temperatures

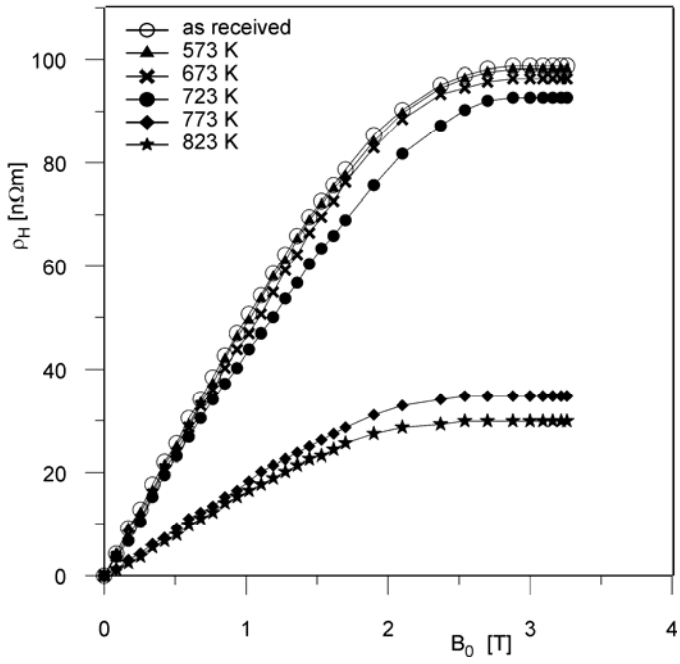

Fig. 4. The Hall resistivity ρ_H as a function of the applied magnetic induction B_0 for the samples of the $Fe_{78}Si_9B_{13}$ alloy annealed at various temperatures

For the $Fe_{78}Si_9B_{13}$ alloy the abrupt decrease of curves $\rho_H = f(B_0)$ occurs for the samples annealed at 723 K and 773 K. The investigated alloys are the ferromagnetic materials and therefore the Hall resistivity is [4–6, 13]:

$$\rho_H = R_0 B_0 + \mu_0 R_S M \tag{2}$$

where R_0 and R_s are the ordinary and spontaneous Hall coefficients, respectively, and M is the magnetization of the sample. Each curve from Figs. 3 and 4 is typical of ferromagnetic substances. This demonstrates that during the crystallization process the macroscopic ferromagnetic ordering of both alloys is conserved. The first term of Eq. (2) is the ordinary Hall resistivity ($\rho_{H0} \propto B_0$). It is related to the Lorentz force acting on the current carriers and corresponds to the slowly growing part of the $\rho_H = f(B_0)$ curve above the magnetization saturation. The second term is the spontaneous Hall effect ($\rho_{Hs} \propto M$) and is represented by the initial part of the $\rho_H = f(B_0)$ curve. The ρ_{Hs} is connected with a ferromagnetic state and determined by the following mechanisms: spin-orbit interaction, skew scattering and side jump [4, 5]. These mechanisms decrease the mean free path of carriers. For the initial part of the $\rho_H = f(B_0)$ curves the spontaneous Hall coefficient R_s was calculated using the linear regression

$$R_S = \left(\frac{\partial \rho_H}{\partial B_0} \right)_{B_0 \to 0}$$

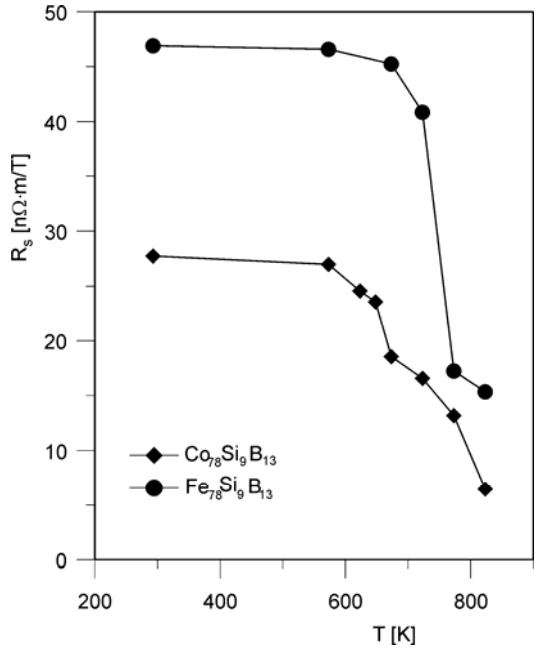

Fig. 5. The spontaneous Hall coefficient R_s, as a function of annealing temperature T for the samples $Co_{78}Si_9B_{13}$ and $Fe_{78}Si_9B_{13}$ alloys

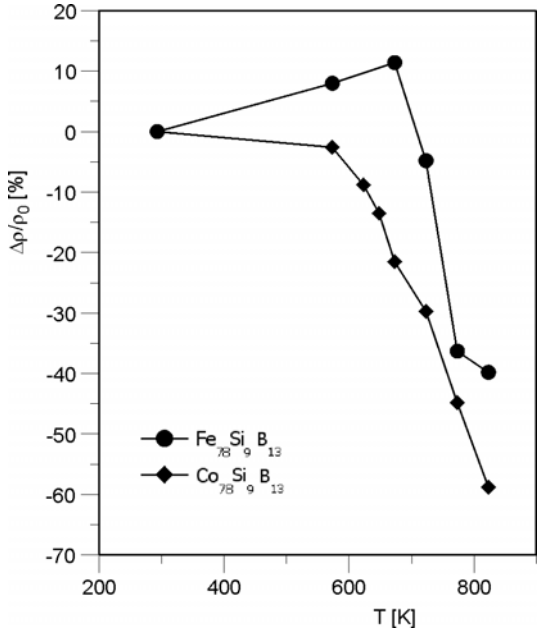

Fig. 6. The relative electrical resistivity $\Delta\rho/\rho_0$ as a function of annealing temperature T for the samples of $Co_{78}Si_9B_{13}$ and $Fe_{78}Si_9B_{13}$ alloys

Figure 5 presents the dependence of R_s on the annealing temperature T for both alloys. Figure 6 shows relative changes of the electrical resistivity ρ (related to the resistivity of the as-received state ρ_0) vs. the annealing temperature. For the $Fe_{78}Si_9B_{13}$ alloy, an increase of $\Delta\rho/\rho_0$ value in the initial step of annealing is observed, connected with the structural changes of TSRO type. The decrease of the electrical resistivity during the crystallization is due to the increase of the free path of the carriers in ordered structure in medium and long range.

According to Berger and Bergmann, the spontaneous Hall coefficient R_s is described by the dependence [4–6]:

$$R_s = a\rho + b\rho^2 \tag{3}$$

where a and b are constants roughly independent of temperature and ρ is the resistivity.

The first term of Eq. (3) is responsible for the classical asymmetric scattering of charge carriers and the second term describes the quantum effect and corresponds to the lateral displacement of the charge carrier trajectory at the point of scattering, i.e. the side jump. The dependence of $\lg R_s$ on $\lg\rho$ gives the exponent n in the relation $R_s \propto \rho^n$ and through its value it can be concluded which type of scattering is dominant for the spontaneous Hall effect. Figure 7 shows these dependences for both alloys. The calculated exponents n for $Co_{78}Si_9B_{13}$ and $Fe_{78}Si_9B_{13}$ are 1.58 and 1.91, respectively. The values n indicate that during the crystallization process the charge carriers are mainly scattered by nonclassical mechanism, i.e. side jump.

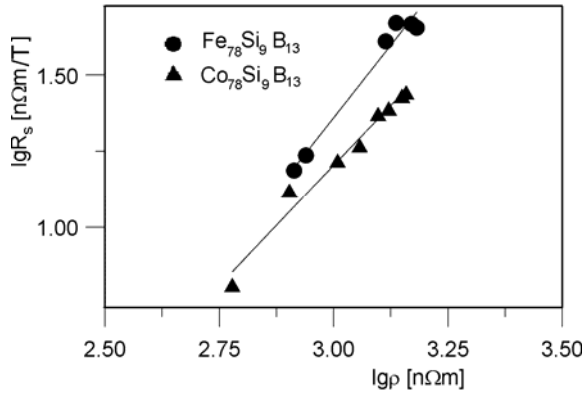

Fig. 7. The dependence of $\lg R_s$ on $\lg\rho$ for $Co_{78}Si_9B_{13}$ and $Fe_{78}Si_9B_{13}$ alloys annealed at various temperatures

To analyse the structural changes and identify the crystalline phases formed from the amorphous matrix, the X-ray diffraction investigations for the as-received as well as annealed samples were performed (Fig. 8.). The results prove that the first stage of the crystallization begins after the annealing of the samples at 648 K and 723 K for the $Co_{78}Si_9B_{13}$ and $Fe_{78}Si_9B_{13}$ alloys, respectively. A qualitative analysis proves that they are the α-Co and α-Fe phases [14]. After annealing at 773 K, the phases Co_2B

and Fe_2B are created. It is possible that the metallic phases include a certain amount of Si [15–17].

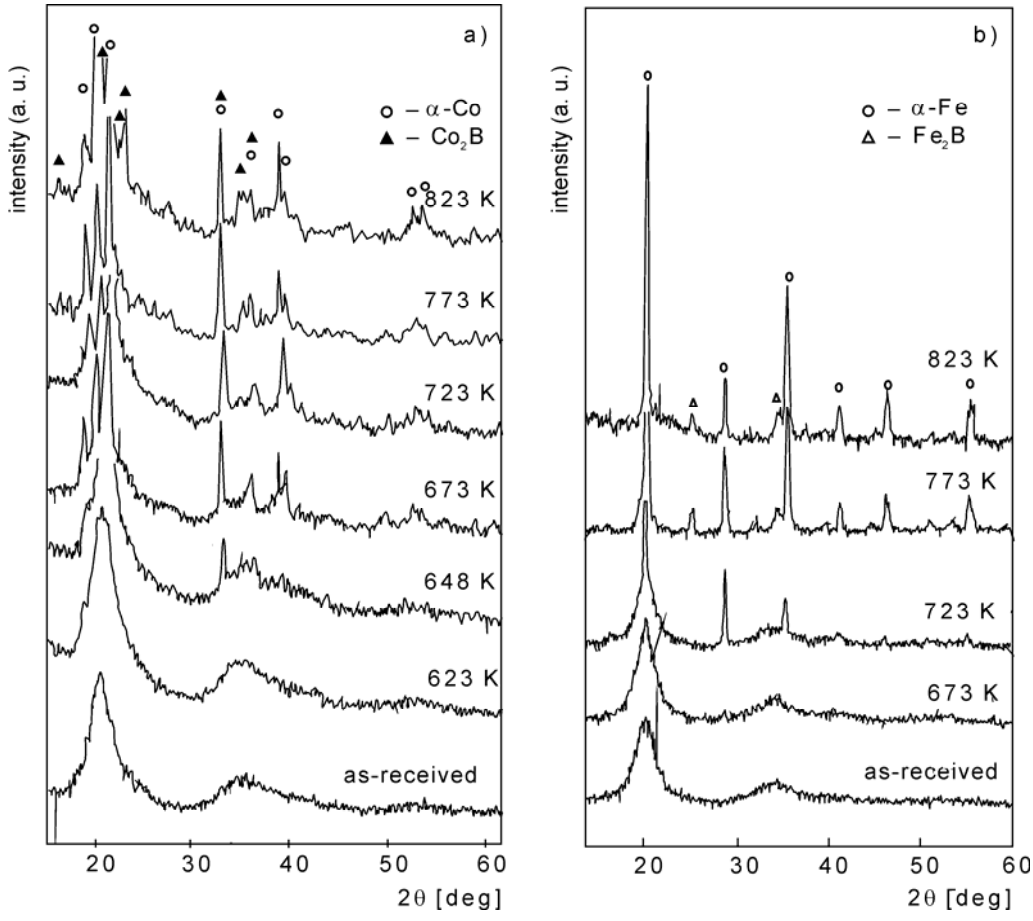

Fig. 8. X-ray diffraction patterns for the samples of alloys: a) $Co_{78}Si_9B_{13}$ and b) $Fe_{78}Si_9B_{13}$

The first stage of crystallization of both alloys occurs as a result of the primary crystallization and the second one as a result of the polymorphous crystallization. The structural changes appear in the measurements of the electrical and Hall resistivities after annealing at temperatures lower than in X-ray diffraction and DSC studies. It demonstrates that the methods involving the electronic transport are more sensitive to structural changes.

To verify the sequence of the created phases determined by the X-ray diffraction, quantum chemical calculations of the total energy of the model clusters were carried out. The value of the total energy of α-Co clusters (–22 8327.7 kcal/mol) is lower than that of Co_2B clusters (–16 1397 kcal/mol). The obtained energies for α-Fe (–16 3806 kcal/mol) and Fe_2B (–11 9125.9 kcal/mol) are in an analogous rela-

tion. These results prove that in both alloys the metallic phases crystallize first from the amorphous matrix during the annealing because they require less energy in comparison with borides which crystallize at higher temperatures.

The differences between the calculated values of the energy of metallic and boride phases are 66 930.7 kcal/mol and 44 680.1 kcal/mol for $Co_{78}Si_9B_{13}$ and $Fe_{78}Si_9B_{13}$, respectively. The difference between the temperature of crystallization of metallic and boride phases in the alloy with Co is higher than that of the alloy with Fe and it confirms the results of the DSC measurements.

4. Conclusions

The crystallization processes of $Co_{78}Si_9B_{13}$ and $Fe_{78}Si_9B_{13}$ metallic glasses proceed in two stages. At the first stage, α-Co and α-Fe phases crystallize and at the second one, Co_2B and Fe_2B phases are formed during annealing. The most sensitive method of examination of structural changes is the Hall effect. With this method, the following temperatures of the phase transitions of the first order for the first and the second stage were found:

- first stage

$$M_{78}Si_9B_{13} \xrightarrow[723\ \text{K for M = Fe}]{623\ \text{K for M = Co}} \alpha\text{-M} + \text{amorphous}$$

- second stage

$$\text{amorphous} \xrightarrow{773\ \text{K}} M_2B$$

The $Fe_{78}Si_9B_{13}$ alloy has a wider thermal range of structural stability.

The substitution of Co with Fe drastically increases the Hall resistivity in the as-received state and it is connected with the increase of scattering of charge carriers by Fe atoms. During the crystallization process, the ferromagnetic order of both alloys is conserved. The dominant type of scattering of charge carriers is the side jump effect. The Hall and electrical resistivities decrease abruptly after the crystallization of a suitable phase. The activation energy for both stages of crystallization as well as the total energy for clusters of created phases obtained from DSC measurements and quantum chemistry method prove that at the first stage the metallic phases are created and at the second one the metal borides are formed.

References

[1] VAN DEN BEUKEL A., RADELAAR S., Acta Metall., 31 (1983), 419.
[2] VAN DEN BEUKEL A., Key Engin. Mater., 81–83 (1993), 3.
[3] KOSTER U., Key Eng. Mater., 81–83 (1993), 647.
[4] BERGER L., BERGMANN G., *The Hall Effect of Ferromagnets*, [in:] C.L. Chien, C.R. Westgate (Eds.), *The Hall Effect and Its Applications*, Plenum Press, New York, 1980, 55.

[5] MCGUIRE T.R., GAMBINO R.J., O'HANDLEY R.C., *Hall Effect In Amorphous Metals*, [in:] C.L. Chien, C.R. Westgate (Eds.), *The Hall Effect and Its Applications*, Plenum Press, New York, 1980, 137.
[6] STOBIECKI T., PRZYBYLSKI M., Phys. Stat. Sol. (b), 134 (1986), 131.
[7] JAKUBCZYK E., Acta Phys. Polon. A, 99 (2001), 673.
[8] *HyperChem™, Release 6.01 for Windows*, *Molecular Modelling System*, Hypercube, Inc., 2000.
[9] JAKUBCZYK E., JAKUBCZYK M., Czech J. Phys., 54 (2004), D165.
[10] KISSINGER H.E., Anal. Chem., 29 (1957), 1702.
[11] WANG H.R., GAO Y.L., HUI X. D., MIN G.H., CHEN Y., YE Y.F., J. Alloys Comp., 349 (2003), 129.
[12] SHAPAAN M., LENDVAY J., VARGA L.K., J. Non-Cryst. Sol., 330 (2003), 150.
[13] HURD C.M., *The Hall Effect in Metals and Alloys*, Plenum Press, New York, 1972.
[14] VILLARS P., *Pearson's Handbook Desk Edition, Crystallographic Data for Intermetallic Phases*, ASM International, Materials Park, OH 44073, USA, 1997.
[15] BANERJI N., JOHRI U.C., KULKARNI V.N., SINGRU R.M., J. Mater. Sci., 30 (1995), 417.
[16] WOLNY J., SMARDZ L., ZAJĄC W., SOŁTYS J., DUBOIS J. M., J. Magn. Magn. Mater., 41 (1984),191.
[17] JAKUBCZYK E., MANDECKI Z., FILIPECKI J., J. Non-Cryst. Solids, 192, 193 (1995), 509.

Received 9 September 2005
Revised 9 November 2005

Materials Science-Poland, Vol. 24, No. 4, 2006

Analysis of the wave packet interference pattern in the Young experiment

K. CIEŚLAK*, J. M. OLCHOWIK

Lublin University of Technology, Institute of Physics, Nadbystrzycka 38, 20-618 Lublin, Poland

At its beginning, the quantum mechanics has been so controversial theory that not all physicist were able to agree with its assumptions. Nowadays, it seems that the problem does not exist any more, although the quantum theory is still incomplete. The main point of the discussion, which has been raised all the time, is the problem of the measurement understood as the influence of an observer or a detector presence on the wave packet describing the state of the observed system. In this paper, the problem of the influence of the detector on the state of the system is reported on the basis of two-slit experiment described in new formalism called projection evolution. This new approach connects two ways of state evolution: unitary evolution and evolution visible during the measurement.

Key words: *quantum measurement; projection evolution; two-slit experiment*

1. Projection evolution

There are two possible ways of evolution of the quantum state of a system, which is completely predictable and reversible, called unitary evolution, as well as the irreversible rapid process connected with measurements [1]. There have been a few attempts of bringing these two possible ways of evolution together but up to now none of them has been fully satisfying.

The projection evolution is considered as a new fundamental law of quantum evolution [2]. The classical formalism of quantum mechanics has been applied for the description of that theory. The only change done in this formalism is that the unitary time evolution and the projection postulate were replaced by the projection evolution. In such an approach, the evolution is simply considered as a sequence of measurements made by Nature occurring with a specified probability determined by the state of the system. The new theory is concise an transforms into a unitary evolution and the theory of quantum projection measurements.

*Corresponding author, e-mail: k.cieslak@pollub.pl

To start with, let us consider that quantum state of a system is described by a density operator ρ, while τ is the evolution parameter responsible for ordering of physical events. For each value of τ, a family of projection operators is defined, which fulfil the following conditions:

$$M(\tau;\nu)M(\tau;\nu') = \delta_{\nu\nu'}M(\tau;\nu)$$
$$\sum_{\nu} M(\tau;\nu) = I \tag{1}$$

In Equation (1), operators $M(\tau,\nu)$ represent the properties of the system responsible for unitary evolution. Contrary to the traditional evolution theory, we postulate that the quantum state of the system is determined by a randomly chosen projection of its previous state by means of one of the $M(\tau,\nu)$ operators, for each value of the evolution parameter τ:

$$\text{Prob}\,(\tau;\nu) = \text{Tr}\,[M(\tau;\nu)\rho(\tau - d\tau)] \tag{2}$$

where $\rho(\tau - d\tau)$ describes a quantum state at the former value of the evolution parameter. In other words, it can be said that the projection postulate is used to obtain a new state of the system.

On the basis of the considerations above, it can be implied that the evolution parameter τ is time. In order to simplify our considerations, let us assume discrete values of time $t_0 < t_1 < t_2 < \ldots t_n \ldots$. In this notation, the projection evolution leads to the recurrent equation describing quantum states of the system:

$$\rho(t_{n+1}) = \frac{M(t_{n+1};\nu_{n+1})\rho(t_n)M(t_{n+1};\nu_{n+1})}{Tr[M(t_{n+1};\nu_{n+1})\rho(t_n)M(t_{n+1};\nu_{n+1})]} \tag{3}$$

In Equation (3), $\rho(t_n)$ stays for the quantum state of the system at the time t_n, while the state of the system in the following moment of time t_{n+1} is chosen randomly with the probability given by Eq. (2), where ν_{n+1} takes the values from the range required by Eq. (1).

Equation (3) leads to the conclusions that the evolution of the quantum system may follow different paths, as the series of projections are chosen randomly in moments of time t_0, t_1, ... using Eqs. (3) and (2), the probability of the fact that the quantum state ρ_0 of the system would be determined in a specific way, can be calculated:

$$\text{Prob}(t = t_0;\nu_0,\nu_1,\nu_2\ldots,\nu_n) = \text{Tr}[M(t_n;\nu_n)M(t_{n-1};\nu_{n-1})\ldots M(t_0;\nu_0)\rho_0$$
$$M(t_0;\nu_0)\ldots M(t_{n-1};\nu_{n-1})M(t_n;\nu_n) \tag{4}$$

The time evolution is defined herein as a measurement made by Nature. However, the measurements made in a laboratory have to be a part of the evolution operator. The major conclusion of the theory presented is that there is no difference between

the evolution and measurement, so the reduction of the quantum states is a natural part of the projection evolution. In particular cases, the projection evolution operators can be given by unitary operators which can be interpreted as traditional evolution operators $U(t)$ generated by Hamiltonian of the system:

$$M(t;\nu) = U(t-t_0)M(t_0;\nu)U^+(t-t_0) \tag{5}$$

When $U(t)$ commutate with $M(t_0;\nu_0)$, projection evolution operators are time independent.

On the other hand, when the operators (5) are applied to Eq. (3), we get unitary evolution of Schrödinger's type:

$$\rho(t) = U(t-t_0)\frac{M(t_0;\nu_0)\rho_0 M(t_0;\nu_0)}{Tr\left[M(t_0;\nu_0)\rho_0 M(t_0;\nu_0)\right]}U^+(t-t_0) \tag{6}$$

which means that the evolution leads to the real known Schrödinger equation. This leads to the conclusion that the unitary evolution and measurements can be independently considered as parts of the projection evolution.

2. Two-slit experiment

The two-slit experiment, known as the Young experiment, is schematically presented in Fig.1. In the most simplified version, the system consists of two slits, particles which are able to go through the slits and a screen.

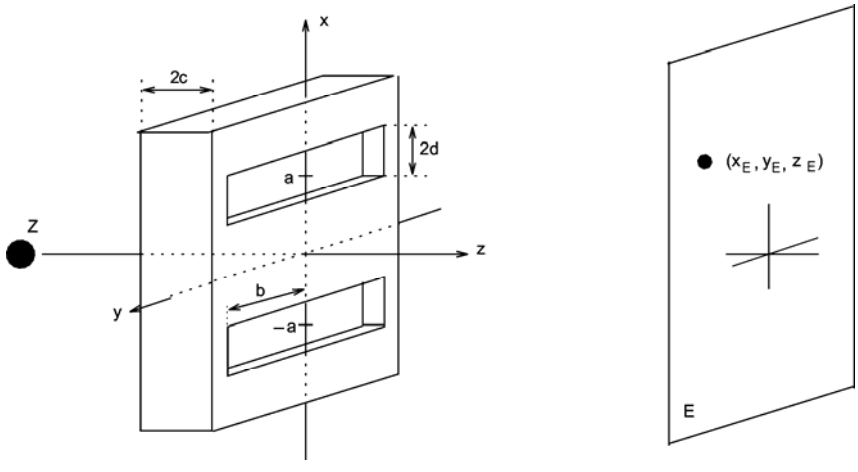

Fig. 1. Two-slit experiment [2]: Z – source, E – screen

The complementary rule is manifested in this experiment, showing the result of interaction between the system and the detector as the disturbance in a characteristic

interference pattern on the screen. According to some attempts of interpretation of this event in the field of quantum physics, this interference pattern is destroyed as a result of the influence of a detector on the quantum state of the system in which the measurement is done. Quantum physicists claim that the act of observation causes significant changes in the quantum state of the system observed. In this paper, the projection evolution will be used in order to explain the influence of the detector on the quantum state of the system observed.

The main assumption in this approach is that the momentum broadening occurs for the particles which can be found between the source and the slits, and the slits and screen as well. This momentum broadening is represented by $\alpha_\nu(k)$ in the formalism describing the projection evolution.

The aim of the latter consideration is to determine the distribution value of probability that the particle would be found on the screen in a defined point $\vec{x}_E$. First of all, the evolution operator describing evolution of a particle which passes through the slits in its way from the source to the screen has to be constructed:

$$M(t;\nu)=\begin{cases} U(t-t_0)M_k(\vec{k})U^+(t-t_0) & \text{when} \quad t_0 \le t < t_1; \nu = \vec{k} \in R^3 \\ M_s(\nu) & \text{when} \quad t_1 \le t < t_2; \nu = 0,1 \\ U(t_E-t_2)M_s(\nu)U^+(t_E-t_2) & \text{when} \quad t_2 \le t < t_E; \nu = \vec{k} \in R^3 \\ M_E(\nu') & \text{when} \quad t \ge t_E; \nu = 0 \,\text{lub} \quad \nu = \vec{x}_E \in X_E \end{cases} \tag{7}$$

where $M_k(\vec{k})=|\nu\rangle\langle\nu|$ projects on the states of the given momentum between the source an the slits:

- $M_s = \int_\Delta d^3x |\vec{x}\rangle\langle\vec{x}|$ projects on a slit state space.
- $M_k(\vec{k}') = |\nu'\rangle\langle\nu'|$ projects on a momentum state space between the slits and the screen.
- $M_E(\nu') = |\vec{x}_E\rangle\langle\vec{x}_E|$ is connected with screen states.
- $|\nu\rangle = |\psi_\nu\rangle = \int_{R^3} d^3\vec{k}\alpha_\nu(\vec{k})|\vec{k}\rangle$ where $\alpha_\nu(\vec{k})$ determines the shape of the wave packet.

The main point of interest is to know the position on the screen of the particle after passing the slits. The probability that the particle would be found on the screen in a point $\vec{x}_E$ is given by:

$$\begin{aligned} \text{Prob}(\vec{x}_E;\nu';\nu) = \text{Tr}[&M_E(\vec{x}_E)U(t_E-t_2)M_s(\nu)M_s(\Delta)U(t_1)M_\nu(\nu)\rho_0 \\ &M_\nu(\nu)U^+(t_1)M_s(\Delta)M_s(\nu)U^+(t_E-t_2)M_E(\vec{x}_E)] \end{aligned} \tag{8}$$

Using Eqs. (7) and (8), the probability can be established by formula:

$$\text{Prob}(\vec{x}_E;\nu';\nu) = |\langle\nu|\psi_0\rangle|^2 \left| \int_\Delta d\vec{x} \langle\vec{x}_E|U(t_E-t_2)|\vec{x}\rangle\langle\vec{x}|U(t_1)|\nu\rangle \right|^2 \tag{9}$$

It is assumed that the wave packet is broadened around given $\vec{k}_0$ in k_x, k_y, k_z axes directions and it has the shape of the Gaussian packet:

$$\alpha_v(k) = \frac{1}{(2\pi)^{3/2}\sqrt{\sigma\eta\mu}} \exp\left\{\frac{-(k_x - k_{0x})^2}{2\sigma}\right\} \exp\left\{\frac{-(k_y - k_{0y})^2}{2\eta}\right\} \exp\left\{\frac{-(k_z - k_{0z})^2}{2\mu}\right\} \quad (10)$$

where σ, η, μ are responsible for the shape of the wave packet in the directions of particular axes.

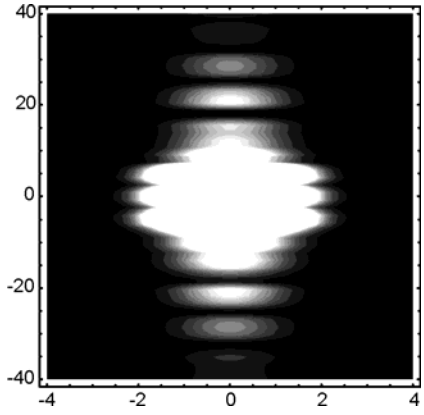

Fig. 2. The distribution value of probability on the screen for symmetric Gauss wave packet

As shown in Fig. 2, a lot of similarities can be found between the distribution value of probability obtained on the basis of theoretical analysis and the interference pattern observed in the experiment.

3. Influence of the detector

Another aspect of the two-slit experiment which needs to be considered is the influence of the detector on the quantum state of the system being under observation. In particular, one question should be answered: what will happen if we put a detector in one of the slits and this way disturb a quantum state of the system. That kind of situation implies the modification of the evolution operator (7) by the detector operator represented by:

$$M_D(\kappa) = \begin{cases} M_D(u) = \int_{\Delta'_u} d^3\vec{x} \left|\vec{x}\right\rangle\left\langle\vec{x}\right| & \text{if particle passes through the upper slit, } \kappa = u \\ M_D(d) = \int_{\Delta'_d} d^3\vec{x} \left|\vec{x}\right\rangle\left\langle\vec{x}\right| & \text{if particle passes through the lower slit, } \kappa = d \\ I - M_D(u) - M_D(d) & \text{if particle hits the wall, } \kappa = w \end{cases} \quad (11)$$

In the result of that modification, the projection evolution operator will be described by the following expressions:

$$M(t;\nu)=\begin{cases} U(t-t_0)M_k(\vec{k})U^+(t-t_0) & \text{when} \quad t_0 \le t < t_1; \nu=\vec{k}\in R^3, \\ M_s(\nu) & \text{when} \quad t_1 \le t < t_2; \nu=0,1, \\ M_D(\kappa) & \text{when} \quad t_2 \le t < t_3; \nu=\kappa=u,d,w, \\ U(t_E-t_2)M_s(\nu)U^+(t_E-t_2) & \text{when} \quad t_2 \le t < t_E; \nu=\vec{k}\in R^3, \\ M_E(\nu') & \text{when} \quad t \ge t_E; \nu=0 \; or \quad \nu=\vec{x}_E\in X_E. \end{cases} \tag{12}$$

Using this form of the projection evolution operator (13) one can calculate the probability of finding a particle on a screen:

$$\text{Prob}(\vec{x}_E,k',k)=\left|\left\langle x_E\left|U(t_E-t_3)\right|\nu'\right\rangle\left\langle\nu'\left|M_s(\Delta)M_D(\kappa)U(t-t_1)\right|\nu\right\rangle\left\langle\nu\left|\psi_0\right\rangle\right|^2 \tag{13}$$

where $\kappa = u$ describes the particle passing through the upper slit and $\kappa = d$ describes the particle passing through the lower slit. In both cases, the distribution of probability on the screen is the same as for the diffraction pattern of one slit.

4. Conclusions

In many theories describing quantum physics the concept of measurement is related to the reduction of the packet wave, which is explained by the influence of an observer or a detector on system observed. It is not necessary to involve the idea of influence of a detector on a quantum state in projection evolution because it comes from the main assumption of the theory: time evolution is defined as a measurement made by Nature in every stage of the experiment. As described above, the influence of an observer on the system is natural, and comes from the theory, not from different assumptions.

Acknowledgement

The authors would like to thank Prof. Andrzej Góźdź (Institute of Physics, Maria Curie-Skłodowska University) for his support and valuable advice.

References

[1] GRABOWSKI M., INGARDEN R.S., *Quantum Mechanics*, Warszawa, PWN, 1989 (in Polish).
[2] GÓŹDŹ A., DĘBICKI M., PIETROW M., Int. J. Mod. Phys., E14 (2005), 477.
[3] PRESKILL J., *Quantum Information and Computation*, Lecture Notes for Physics 229, California Institute of Technology, September, 1998.

Received 9 September 2005
Revised 9 December 2005

Materials Science-Poland, Vol. 24, No. 4, 2006

TMAH texturisation and etching of interdigitated back-contact solar cells

P. PAPET, O. NICHIPORUK, A. FAVE, A. KAMINSKI*, B. BAZER-BACHI, M. LEMITI

Laboratoire de Physique de la Matière, UMR–CNRS 5511, Institut National des Sciences Appliquées de Lyon, Bât. Blaise Pascal, 7 avenue Jean Capelle, 69621 Villeurbanne Cedex, France

In order to decrease reflectivity of silicon solar cells, NaOH or KOH texturisations are usually used leading to a pyramidal structure. However, these solutions are toxic and pollutant. Effectively, K^+ or Na^+ ions contaminate the passivation layer (SiO_2 or SiN) deposited on the surface of the cell after texturisation. An alternative to KOH and NaOH texturisation is tetramethyl ammonium hydroxyde $(CH_3)_4NOH$) (TMAH). TMAH is not pollutant, not toxic and its use leads also to a pyramidal structure. Moreover, the etching rate and surface morphology can be controlled by the concentration of the solution, temperature and the addition of surfactant. Moreover, TMAH is selective with dielectrics and metals. It can therefore be used to produce self-aligned interdigitated back-contact solar cells (IBC). In this work, we have analysed the surface morphology and reflectivity after texturisation in TMAH in various experimental conditions. We have tested the possibility to use selective etching of the emitter of a back-contact solar cell by protecting the surface of the emitter with a metal grid. This new process permits to reduce the number of lithographic steps necessary to produce IBC solar cells.

Key words: *solar cell; texturing; TMAH*

1. Introduction

A key question in fabrication of photovoltaic cells is the cell cost. One of the promising ways of development is the reduction of material cost using thin film technologies [1, 2]. An interdigitated back-contact solar cell (IBC) is a very interesting technology for thin films because all contacts are at the back of the cell, hence the light absorption is increased. This absorption can be further improved by an optimised texturisation. Texturing of monocrystalline silicon is usually done in alkaline solutions. Such solutions are cheap but pollutant for passivation layers. In this paper, we investigate alternative solutions containing tetramethyl ammonium hydroxide $(CH_3)_4NOH$, TMAH) [3]. TMAH solutions are widely used in microelectronic and micro-electro-mechanical systems (MEMS) because they combine high etching rates,

*Corresponding author, e-mail: anne.kaminski@insa-lyon.fr

good-quality anisotropic etching with full compatibility with microelectronic technologies. Moreover, they are clean room compatible, nontoxic and easy to handle [4, 5]. Iencinella [6] reported a recipe for random pyramidal texturing by TMAH solution containing dissolved silicon but this process was not easy to carry out. The first part of this study presents an alternative method to create uniform and reproductible pyramidal textures on silicon wafers with TMAH.

TMAH solutions also exhibit excellent selectivity to silicon oxide, silicon nitride and Al and Ag masks [7, 8]. In the second part of this paper, we present the optimization of the TMAH solution in order to develop a simplified technological process for fabrication of self-aligned interdigitated back-contact solar cells with only one lithographic step.

2. Optimization of the texturisation solution

2.1. Experiment

Texturing solutions were prepared using a 25% commercial TMAH solution, deionized water and standard isopropanol (IPA) used to avoid the formation of big hydrogen bubbles on the surface of silicon. All etching experiments were carried out

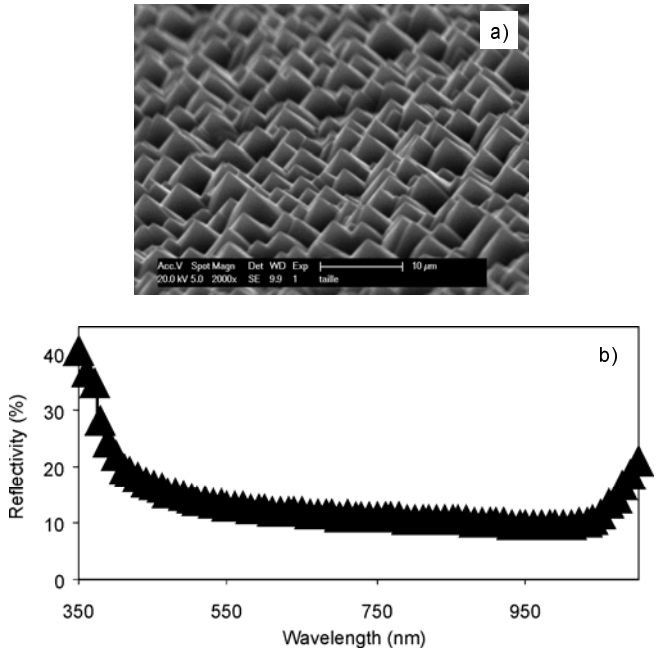

Fig. 1. SEM picture (a) of a TMAH textured wafer after optimized etching (30 min, 2% TMAH, 10% IPA, 80 °C). Hemispherical reflectance (b) of a TMAH textured silicon sample (30 min, 2% TMAH, 9% IPA, 90 °C)

using [100]-oriented, p-doped (1–10 Ω·cm) silicon wafer double-side polished. Before the etching process, the samples were dipped in a 5% HF solution for 10 seconds to remove the native oxide and rinsed in deionized water. The weighted reflectance (WR) is calculated by normalization of the hemispherical reflectance spectrum (350 –1100 nm) with the AM1.5D spectrum [9]. An example of the pyramidal structure and of the reflectivity obtained after the texturisation are presented in Fig. 1.

2.2. Results

First, we varied the TMAH concentration from 0 to 5%. In Table 1, one can see that the weighted reflectance decreases with increasing TMAH concentration to 2%. This result is explained by uniformity improvement. At 5%, the reflectivity is higher because pyramids are smaller but the uniformity is still obtained. TMAH solution is quite expensive, thus the concentration as low as only 2% needed to texture surface makes this method very cost competitive.

Table 1. Influence of temperature, TMAH and IPA concentration on weighted reflectance

[TMAH], % ([IPA]: 10%, 30 min, 80 °C	0	0.5	1	2	5
Weighted reflectance, %	41	18	15	13	20
Temperature, °C ([IPA]: 10%, [TMAH]: 2%, 30 min	60	70	80	90	
Weighted reflectance, %	15.2	14.4	13.5	13.3	
[IPA], % ([TMAH]: 2%, 30 min, 80 °C	0	6	9	14	23
Weighted reflectance, %	35	14.5	13	16	29

Isopropanol (IPA) is used as a surfactant diminishing the adherence of hydrogen bubbles to the etched surface. The dependence between IPA concentration and reflectivity is shown in Table 1. The reflectance decreases with IPA concentration up to 9% due to uniformity improvement. Beyond this concentration, the uniformity was always obtained but the surface reflectance increased. The pyramids were smaller thus we can make the assumption that the wettability was so important that bubbles stuck on silicon surface were too small to obtain high pyramids.

To determine the temperature influence, experiments were carried out at temperatures ranging between 60 °C and 90 °C. In Table 1, one can see that the surface reflectance decreases with temperature increasing. Sundaram [10] reported that on increasing temperature, the etch rate of the (100) and (110) crystallographic planes increased faster than the each rate of the (111) crystallographic plane. When temperature increases, this difference of etch rate results in higher pyramids and leads to a lower reflectance.

In order to analyse the reflectance with an antireflection coating (ARC), we covered the front surface of TMAH textured photovoltaic cells with a silicon nitride layer. The weighted reflectance diminishes from 10.2% (polished surface with an ARC) to 2.7% with TMAH pyramidal texture.

3. Fabrication of self-aligned interdigitated back-contact solar cells

In interdigitated solar cells, all contacts are placed at the back of the cell (Fig. 2), leading to an improved optical confinement and low series resistance compared to conventional p-n junction solar cells. However, this type of solar cells requires from two to six steps of lithography and alignment because their doped regions and contacts are on the same side of the cell.

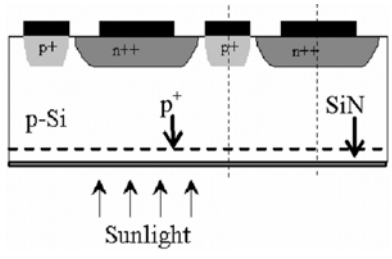

Fig. 2. Structure of an interdigitated back-contact solar cell

In order to reduce the number of technological steps, we tested the possibility of using a selective etching of the emitter by protecting the surface of the emitter with a metal grid. This process is self-aligned because only one lithographic step without alignment is necessary to fabricate the cell [11].

The following steps are used for the solar cell fabrication:

- Deposition of n^+ phosphorous doping glass on the whole surface of the wafer and drive-in.
- Formation of n-contact pattern by deposition of Ti/Pd/Ag followed by lift-off or by evaporation through the shading mask.
- Selective etching in TMAH solution. The Ti/Pd/Ag contacts act as masks during the etching and Ti/Pd/Ag cantilevers are formed. They are used as spacers to separate the metal contacts;
- Al deposition all over the surface of the cell and rapid thermal annealing (RTA) firing. After this step, p and n contacts are not short-circuited because of the particular n-contact profile obtained after the etching (Fig. 3).

One of the most critical steps in the process is the formation of Ti/Pd/Ag cantilevers; they have to be large enough to avoid short-circuit between n and p contacts. The advantage of using TMAH is a possibility to control the anisotropy of the etching (i.e,. the (100)/(111) etch ratio) by adding the surfactant [8]. In the latter part of this paper we present the optimisation of the TMAH solution (TMAH and IPA concentra-

tions, temperature) in order to obtain the best ratio the etch width (under Ti/Pd/Ag contacts) to its depth (Fig. 3).

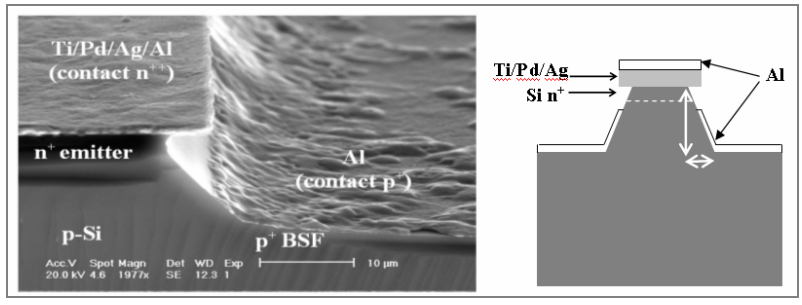

Fig. 3. Scanning electron microscopy picture (left) of a self-aligned interdigitated back-contact solar cell and of the Ti/Pd/Ag cantilever obtained by TMAH etching. Structure (right) of a self-aligned interdigitated back-contact solar cell (only one contact has been shown). The vertical white arrow corresponds to the etch depth ((100) planes) and the horizontal one to the etch width ((111) planes)

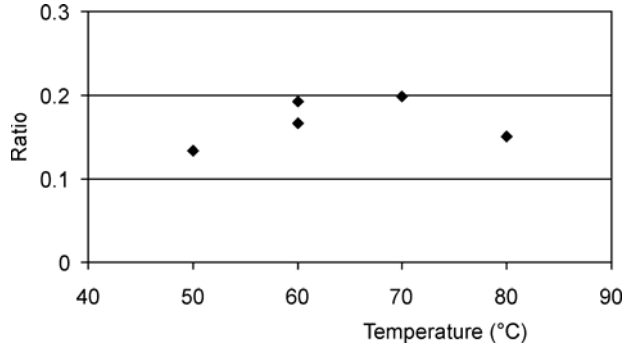

Fig. 4. The ratio of etching rates of (111) and (100) planes vs. temperature of solution: [TMAH] – 0.83%, [IPA] – 83%, duration – 3h

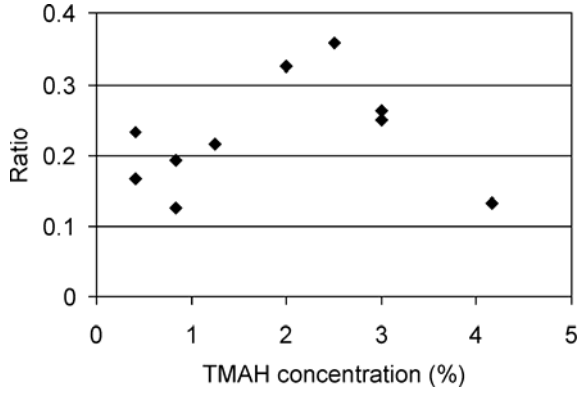

Fig. 5. The ratio of etching rates of (111) and (100) planes vs. TMAH concentration: [IPA] – 83%, 60 °C, 3h

The samples were dipped in TMAH solution during 3 h. The measurements of the etch widths and depths have been performed by the scanning electron microscopy (SEM). When temperature increases (TMAH and IPA concentrations are respectively 0.83% and 83%), the etching rates of both planes (100) and (111) increase, the ratio being almost stable (Fig. 4). When the TMAH concentration increases to about 2.5% (at 60 °C, IPA concentration – 83%), we observe an increase of the etch width and of the ratio of etching rates (Fig. 5). For TMAH concentrations higher than 2.5%, the ratio decreases drastically.

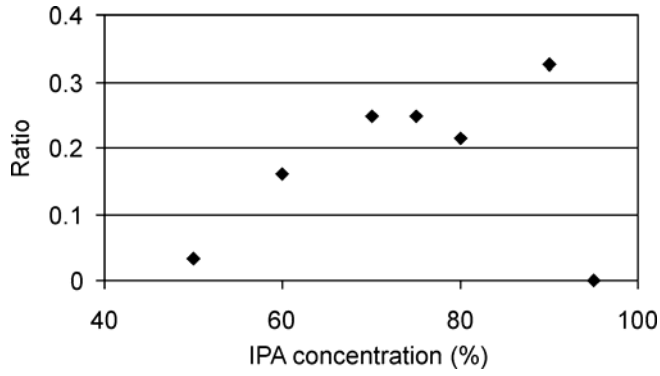

Fig. 6. The ratio of etching rates of (111) and (100) planes vs. [IPA] concentration: [TMAH] – 0.83%, 60 °C, 3h

Finally we have analysed the influence of IPA concentration on the ratio with an etching temperature of 60°C and a TMAH concentration of 1.25%. When the IPA concentration increases (Fig. 6), we observe a decrease of the etch depth and an increase of the etch width and of the ratio. For very high concentrations (95%), we cannot measure precisely the etch depth because the etch rate of the plane (100) is too slow, hence the ratio is difficult to determine. The optimised solution consists of 2.5% TMAH and an IPA in concentration of 85% with the application of a high temperature to have a higher etching rate.

4. Conclusions

In this paper, we have optimized the TMAH solution in order to texture the surface of silicon solar cells and to simplify the elaboration of interdigitated back-contact solar cell. The advantage of TMAH is that it is not pollutant for passivating layer unlike KOH, few toxic and clean room compatible.

Our best texturing solution contains 2% of TMAH and 9% of IPA and allows to realize optimized pyramidal texturing surfaces.

Concerning the use of TMAH in order to realize self-aligned interdigitated back contact solar cells, we have optimized the TMAH solution to obtain a higher ratio of

(111) and (100) planes etching rates. The best ratio corresponds to the solution with the concentration of TMAH of 2.5% and IPA concentration of 85 %.

In conclusion, TMAH is a very good candidate to replace KOH or NAOH solutions for the texturisation and the elaboration of solar cells.

Acknowledgements

This work was supported by ADEME, the French Agency for Environment and Energy Management under the contract No. 99 05 019 and by the Rhône-Alpes Region.

References

[1] BERGMANN R.B., WERNER J.H., Thin Solid Films, 403–404 (2002), 162.
[2] BRENDEL R., Japan J. Appl. Phys., 40 (2001), 4431.
[3] YOU J.S., KIM D., HUH J.Y., PARK H.J., PAK J.J., KANG C.S., Sol. Energy Mater. Sol. Cells, 66 (2001), 37.
[4] THONG J.T.L., CHOI W.K., CHONG C.W., Sens. Actuat. A, 63 (1997), 243.
[5] SHIKADA M., SATO K., TOKORO K., UCHIKAWA D., Sens. Actuat. A, 80 (2000), 179.
[6] IENCINELLA D., CENTURIONI E., RIZZOLI R., ZIGNANI F., Sol. Energy Mater. Sol. Cells, 87 (2005), 725.
[7] MADOU M.J., *Fundamentals of Microfabrication*, New York, McGraw-Hill, 1997.
[8] SARRO P.M., BRIDA D., VLIST W., BRIDA S., Sens. Actuat. A, 85 (2000), 340.
[9] HONSBERG CH., BOWDEN S., *Photovoltaics: Devices, Systems and Applications* (CD), The University of New South Wales, Australia, 1999.
[10] SUNDARAM K.B., VIJAYAKUMAR A., SUBRAMANIAN G., Micro. Eng. 77 (2005), 230.
[11] NICHIPORUK O., KAMINSKI A., LEMITI M., FAVE A., LITVINIENKO S., SKRYSHEVSKY V., 20th EU PVSEC Barcelona (Spain), 2005, p. 1060.

Received 9 September 2005
Revised 27 September 2005

Materials Science-Poland, Vol. 24, No. 4, 2006

Hydrogen interactions in magnetic resonance imaging Histogram-based segmentation of brain tissues

S. GUŁKOWSKI*, J. M. OLCHOWIK

Institute of Physics, Lublin University of Technology, Nadbystrzycka 38, 20-618 Lublin, Poland

Magnetic resonance imaging (MRI) is a very popular, non-invasive medical diagnostic technique providing images of the human body. The method, commonly used in clinics and hospitals all over the world, is based on the magnetic properties of hydrogen atom and its interactions with magnetic field. MR images show differences in water content and distribution in various body tissues. Even different tissues in the same organ, such as the gray and white matter in brain, can easily be distinguished. For a precise analysis of the images obtained in the result of MR examination, special computer applications are used. The paper presents the basis for the magnetic resonance imaging and description of the method of brain segmentation which could be a useful software tool in daily medical diagnosis practice.

Key words: *magnetic resonance imaging; histogram-based segmentation*

1. Introduction

Present diagnostic technologies provide us with various methods of imaging of human body tissues. One of these methods commonly used in clinics and hospitals all over the world is magnetic resonance imaging (MRI). MRI is based on the principles of nuclear magnetic resonance (NMR), a very important method for studying nuclear and atomic systems.

MRI is based on the magnetic properties of hydrogen atom and its interaction with a strong external magnetic fields and radiowaves to produce highly detailed images with excellent soft tissue contrast. Moreover, for more accurate analysis of a tissue or its pathology, special computer applications are created. These methods of image processing are very helpful in daily work of physicians.

* Corresponding author, e-mail: s.gulkowski@pollub.pl

2. Basis for magnetic resonance imaging

Human body is composed primarily of fat and water, thus also of many hydrogen atoms. The nucleus of the hydrogen atom contains a single proton which is chracterized by spin, being a magnetic moment vector. In nuclear magnetic resonance, such unpaired magnetic moments are of great importance. In a static, strong magnetic field $\vec{B}_0$, each of them alings in one of the two possible orientations: parallel (low-energy state) and anti-parallel (high-energy state) to the direction of the field. In addition to aligning with $\vec{B}_0$, protons precess at a frequency given by the Larmor equation:

$$\omega_0 = \gamma B_0 \tag{1}$$

This equation tells us that the frequency depends on the strength of the external magnetic field and on the ratio specific for a given nucleus – gyromagnetic ratio γ, which for hydrogen is 42,58 MHz/T [1].

At room temperature, the number of spins in the low-energy state n^{up} slightly outnumbers the number of spins in the high-energy state n^{down}. The Boltzmann distribution tell us that [2]:

$$\frac{n^{\text{down}}}{n^{\text{up}}} = \mathrm{e}^{E/kT} \tag{2}$$

where: E is the energy difference between the spin states, k is Boltzmann constant, and T is the temperature in kelvins.

The difference between the number of spins (magnetic moments) in the low-energy- and high-energy states creates the net magnetization. In the equilibrium, the net magnetization vector is aligned with the direction of the applied magnetic field $\vec{B}_0$, and does not precess. The z-component of net magnetization is called longitudinal magnetization M_z. There is no transverse magnetization M_{xy} [2], being the xy-plane component of the net magnetization. The higher hydrogen concentration in a specific human tissue, the stronger is magnetization of the tissue. This is the main idea of spin density technique of MRI [3].

It is possible to change net magnetization. If we apply a specific resonance frequency pulse, called 90° pulse of $\vec{B}_1$ magnetic field with energy equal to the energy difference between the spin states, the net magnetization spirals down around the z-axis to the xy plane. The $\vec{B}_1$ field should be orthogonal to the main field $\vec{B}_0$.

After the $\vec{B}_1$ magnetic field is applied, some "lower energy" spins move to the "higher energy" level, hence the longitudinal magnetization disappears. Simultaneously, individual spins are precessing in phase, so transversal magnetization appears. This transversal magnetization rotates about the z-axis and induces in the receiver a signal called free induction decay (FID). After RF pulse, the magnetization $\vec{M}$ re-

turns to its equilibrium state during the relaxation process. The z-component of the net magnetization M_z gets longer in T_1 relaxation time and the xy-component gets shorter in T_2 relaxation time. This signal contains information about the density of the matter and the relaxation times in the examined object.

3. Method of imaging

The FID signal that we get for a given $\vec{B}_0$ field after the application of a 90° pulse is the signal from every hydrogen magnetic moment (spin) all over the body. The aim is to distinguish the signal from each (x,y,z) point and to obtain a 3D image.

3.1. Gradient of magnetic field – slice selection

Slice seletion in MRI is achived by applying a one-dimensional, linear magnetic field gradient during the period the RF pulse is applied. A 90° pulse applied in conjunction with a magnetic field gradient will rotate magnetization vectors which are located in a slice or plane through the object [2]. It is possible because magnetic moments from different planes (along z axis) experience different value of the static field ($\vec{B}_z$), so they have unique resonance frequency ω_z. Applying the RF pulse with resonance frequency, we select the spins from the one plane. Spins located above and below this plane are not affected by RF pulse.

3.2. Gradient of phase and frequency encoding

To distinguish information from a chosen slice of the scanning object, phase and frequency encoding gradients are applied. Every spin from the selected slice precesses at the same Larmor frequency given by the applied magnetic field. If we apply the phase encoding gradient $\vec{G}_x$ along the x-axis, the net magnetizations at different locations begin to precess with different frequencies. When the phase encoding gradient is turned off, all net magnetization vectors precess at the same frequency but at different phase along the x-axis. After the phase encoding gradient, the frequency encoding gradient is applied. As a result, the spin packets precess at rates dependent on their y-location [2]. This sequence results in each of the net magnetization vectors of a chosen slice which is characterized by unique phase and precessional frequencies. Performing the Fourier transform, we can obtain these information from the FID signal.

In order to visualise the information about hydrogen density or relaxation times obtained from the FID signal, special computer programs are employed which can convert these data into images. Many medical applications give the display of images in three planes of imaging.

For a more accurate analysis of the tissues of interest or their pathology, the medical software tools have implemented special image processing methods, such as level-window or pseudocolouring, which improve quality of images. Many applications use more advanced techniques to select interesting information from images. The next section shows an example of the histogram based on segmentation technique, which uses the Levenberg–Marquardt optimization function.

4. Computer analysis of anatomical structures in medical image

A very important task in computer analysis of an MR image is the segmentation of white and gray matter from the human brain image. Segmentation means classifying each voxel of the image (voxel is defined as a volume element of a slice corresponding to the appriopriate pixel of image) as belonging to a specific type of tissue [4].

As shown in the histogram of MR slice of healthy head (Fig. 1), it contains three distinct peaks. These peaks correspond to different kinds of tissues. First represent the cerebrospinal fluid (CSF), second – gray matter and third – white matter of brain. In order to segmentate these structures, we have to found the boundaries between the adjacent peaks.

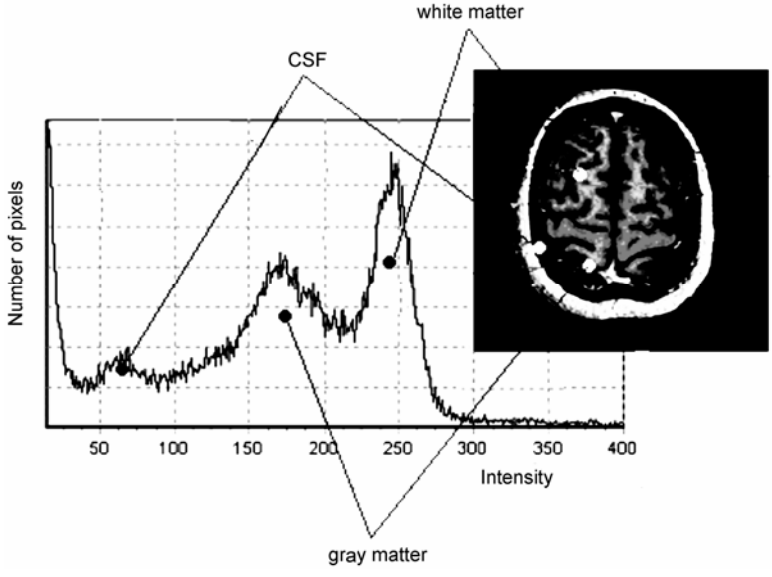

Fig. 1. Histogram of MR T1-weighted slice with peaks corresponding to various tissues. Image of brain taken from [5]

Because of the overlapping, the choice of the intensity levels and the threshold values is very subjective and depends on the kind of the slice. It is necessary to use an algorithm that could follow the shape of the histogram. A good solution is the

Levenberg–Marquardt (L–M) algorithm which allows one to fit precisely a model function $f(a,x_i)$ into a histogram. The model function is a sum of Gaussian distributions:

$$f\left(a,x_i\right)=f\left(A_k,\mu_k,\sigma_k,x_i\right)=\sum_{k=1}^{Q}A_k\exp\left[-\frac{(x_i-\mu_k)^2}{\sigma_k^2}\right] \tag{3}$$

where Q is the number of Gaussians and A_k, μ_k, σ_k are characteristic parameters of each Gaussian.

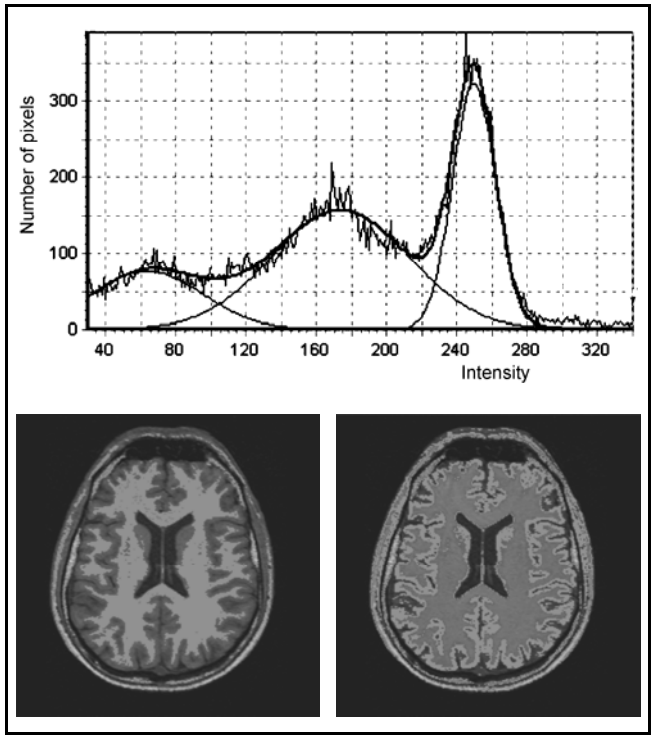

Fig. 2. A histogram of MR image after L-M optimization; white and gray matter that have been segmented from the image

On the basis of these parameters, it is possible to find threshold values between peaks corresponding to a given tissue and the segmentation of these tissues from the image. The results of the white and gray matter segmentation are shown in Fig. 2.

5. Conclusions

Magnetic resonance imaging (MRI) is a powerful, non-invasive medical technique that providing highly-detailed images with excellent soft tissue contrast. With its ad-

vanced software applications, it allows accurate and high-precision medical diagnosis. The gray and white matter segmentation results obtained by L–M optimization of the image histogram brought us to the conclusion that the presented segmentation technique could be very useful for medical imaging. This solution allows one to analyse MR images quickly and precisely, hence it should be useful in a variety of medical applications, additionally to such simple and widely used methods as window/level or pseudocolours. Although MRI is very popular in clinics and hospitals all over the world, it is still quite a young and progressing technique in the diagnostics of human body.

References

[1] GONET B., *Magnetic Resonance Imaging*, PZWL, Warszawa, Poland, 1997.

[2] HORNAK J.P., *The Basics of MRI*, 1996–2005, available on-line: http://www.cis.rit.edu/htbooks/mri/inside.htm.

[3] FAULKNER W., *MRI: Basic Physics, Instrumentation, and Quality Control*, Blackwell Science, Williston, USA, 2002.

[4] BAUKMANN I., *Handbook of Medical Imaging Processing and Analysis*, Academic Press, London, 2000.

[5] MANGIN J., COULON O., FROUIN V., *Robust brain segmentation using histogram scale-space analysis and mathematical morphology*, [in:] W.M. Wells, A. Colchester, S. Delp (Eds.), *Medical Image Computing and Computer-Assisted Intervention*, Springer-Verlag, Berlin, 1998.

Received 9 September 2005
Revised 9 December 2005

Materials Science-Poland, Vol. 24, No. 4, 2006

Epitaxial films of GaInPAsSb quinary solid solutions

V. V. KUZNETSOV[1*], E. R. RUBTSOV[1], E. A. KOGNOVITSKAYA[2]

[1]St. Petersburg State Electrotechnical University, 197376, St. Petersburg, Prof. Popova 5, Russia

[2]Ioffe Physico-Technical Institute, 197376, St. Petersburg, Prof. Popova 5, Russia

The method of the obtaining quinary solid solutions on the basis of $A^{III}B^{V}$ compounds (GaInPAsSb) with specified properties was developed. New GaInPAsSb/GaSb, GaInPAsSb/InAs heterostructures were obtained to create optoelectronic devices for the 2–5 μm spectral range. The broken-gap type II heterojunction was formed at the InAs/$Ga_{0.92}In_{0.08}P_{0.05}As_{0.08}Sb_{0.87}$ heterostructure, and a light-emitting diode was fabricated with the emission intensity maximum at 1.9 μm.

Key words: *solid solution; liquid-phase epitaxy; antimonide; semiconducting III–V materials; light emitting diode*

1. Introduction

The development of the fibre optical links of third generation based on the fluoride optical fibres with minimal dispersion and minimal optical losses requires operating on the middle infrared range (2–5 μm). Prospective materials for the optoelectronic circuit technology for this spectral range are narrow-band solid solutions based on $A^{III}B^{V}$ compounds (GaInPAsSb quinary solid solutions (QSS), in particular). Their advantage is the possibility of independent variation of three parameters: band gap, the lattice parameter and thermal expansion coefficient which become determinative when selecting the heteropair materials to form an ideal heterojunction.

The research was aimed to obtain quinary solid solutions on the basis of $A^{III}B^{V}$ compounds with specified properties and to obtain the new GaInPAsSb/GaSb, GaInPAsSb/InAs heterostructures for the fabrication of an optoelectronic device sensitive for the radiation in the 2–5 μm spectral range.

*Corresponding author, e-mail: vvkuznetsov@mail.eltech.ru

2. Technology and research

The development of the heteroepitaxial technological process to obtain multicomponent solid solutions (MSS) from liquid phase was based on a comprehensive approach which can be divided into the following steps: providing conditions for the isoperiodic substitution; selection and justification of the thermodynamic model; determination of the miscibility gap for solid solutions with specified compositions within a specified temperature range; analysis of the liquid–solid interphase equilibrium; fabrication of the solid solution with the selected composition; analysis of the elastic strains at the heteroboundary; modelling of relaxation processes of interphase interaction at the heteroboundary. These steps are the basis for the development of multi-parametric technological process of the liquid phase heteroepitaxy of MSS of the specified properties.

Composition of the GaInPAsSb QSS was determined by the method of linear interpolation of the binary components using data from [1]. The band gap of the GaIn PAsSb QSS was interpolated as a combination of the band gaps of two quaternary systems (GaPAsSb and InPAsSb) with substitution of the metallic sublattice components and taking into account a non-linear contribution from the mixing effects [2]. Technological parameters of the liquid phase epitaxy (LPE) for fabrication the GaInPAsSb solid solution lattice-matched to InAs and GaSb were determined on the basis of the liquid–solid interphase equilibrium by a simple solution model [3–5]. The method of analysis and the main data for the calculation are given in [1, 2, 6–8]. Correction of the unreliable parameters of the interatomic interaction in the liquid phase between the elements P–As, P–Sb, As–Sb and the components of the solid phase GaP–GaSb and InP–InSb was carried out experimentally (the composition range of the solid phase was $Ga_{0.06}In_{0.94}P_{0.12}As_{0.8}Sb_{0.08}$ (InAs substrate) and $Ga_{0.05}In_{0.95}P_{0.10}As_{0.74}Sb_{0.16}$ (GaSb substrate)). The corrected interaction parameters allowed us to perform the reliable calculation of the liquidus and solidus compositions within the epitaxial process temperature range along the InAs and GaSb isoperiods on the both sides of the binodal space.

In the case of lattice mismatch between the layer and the substrate, elastic strains arise at the heteroboundary [2]. The coherent phase diagrams were used to take into account the contribution of the elastic strains into the liquid–solid heterophase equilibrium of the quinary systems. The equations for the coherent phase diagram of the $A^{III}B^{V}$-based $A_xB_{1-x}C_yD_zE_{1-y-z}$ quinary systems were derived using a simple solution model. The equations for the activity coefficients of the components in the elastically strained solid phase of the QSS were also obtained. The detailed derivation is given in [9]. The general equation of the coherent phase diagram of the quinary system has the following form:

$$\Delta S_{ij}^{F}\left(T_{ij}^{F}-T\right)+RT\ln\frac{4x_i^l x_j^l \gamma_i^l \gamma_j^l}{\gamma_i^{sl}\gamma_j^{sl}}=RT\ln x_i^s x_j^s+RT\ln\gamma_{ij}^{s,ex}+RT\ln\gamma_{ij}^{s,el} \qquad (1)$$

where ΔS_{ij}^{F}, T_{ij}^{F} are the entropy and the melting temperature of the components, respectively; γ_{ij}^{s}, γ_{i}^{l}, γ_{j}^{l} are the activity coefficients of the components in the liquid and solid phases; $x_{i,j}^{l}$ is the atomic fraction of the component in the melt.

To estimate the contribution from the elastic strains, the calculation of the contact supercooling ΔT_K was carried out using the interaction parameters from [2]. The calculation of the contact supercooling was carried out for the $Ga_xIn_{1-x}P_yAs_zSb_{1-y-z}$ quinary systems lattice matched to InAs and GaSb substrates at 773 K with lattice mismatch $f = -1\%$. It was shown that the negative values of the contact supercooling indicate the position of the thermodynamic instability boundaries of the QSS. Figure 1 shows the results of the calculations of the ΔT_K for the $Ga_xIn_{1-x}P_yAs_zSb_{1-y-z}$/InAs system at $T = 773$ K ($f = -1\%$, <111>).

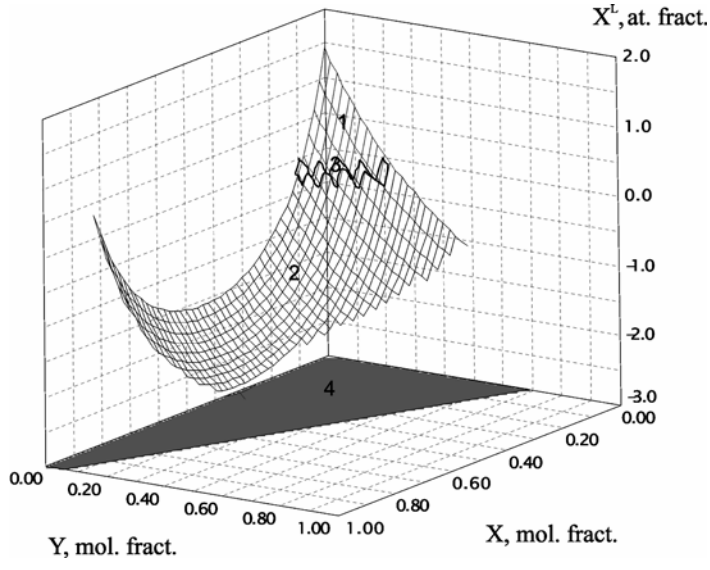

Fig. 1. Contact supercooling in $Ga_xIn_{1-x}P_yAs_zSb_{1-y-z}$/InAs system at 773 K, $f = -1\%$ ⟨111⟩: 1 – positive values, 2 – negative values, 3 – the range of circumzero values, 4 – a projection of the isoperiodic section

The analysis of the results shows that the areas of the negative contact supercooling, which coincide with the areas of the thermodynamic instability of the QSS, take a significant part of the phase space. It should be emphasized that this is connected with variation of the curvature of the dependence of the solid solution free energy on composition in these areas.

In the case of the layer–substrate lattice parameters mismatch, the elastic strains at the heteroboundary arise. This causes the stabilizing effect of the lattice parameter: the solid solution lattice parameter approaches that of the substrate. Elastic contribution to the total energy balance caused shift of the phase equilibrium and, hence, a modification of the solid solution composition. Quantitatively, this effect is de-

scribed by a stabilizing factor q [10, 11]. The equation to calculate the stabilization factor of the $A_xB_{1-x}C_yD_zE_{1-y-z}$ type quinary solid solutions was obtained in the following form:

$$q = 1 + 2\sigma[k_x^2(\delta_2\delta_3 - \beta_3^2) + k_y^2(\delta_1\delta_3 - \beta_2^2) + k_z^2(\delta_1\delta_2 - \beta_1^2) + 2k_xk_y(\beta_2\beta_3 - \delta_3\beta_1) + \frac{2k_xk_z(\beta_1\beta_3 - \delta_2\beta_2) + 2k_yk_z(\beta_1\beta_2 - \delta_1\beta_3)]}{\delta_3(\delta_1\delta_2 - \beta_1^2) + \beta_3(\beta_1\beta_2 - \delta_1\beta_3) + \beta_2(\beta_1\beta_3 - \delta_2\beta_2)} \quad (2)$$

where $\sigma = V\lambda/a_s^2$, λ is the reduced modulus of elasticity, a_s is the substrate lattice period, V is the molar volume, $k_x = \partial a/\partial x$, $k_y = \partial a/\partial y$, $k_z = \partial a/\partial z$, $\frac{\partial^2 G}{\partial y^2} = \delta_2$; $\frac{\partial^2 G}{\partial x^2} = \delta_1$; $\frac{\partial^2 G}{\partial z^2} = \delta_3$; $\frac{\partial^2 G}{\partial x \partial y} = \beta_1$; $\frac{\partial^2 G}{\partial x \partial z} = \beta_2$; $\frac{\partial^2 G}{\partial y \partial z} = \beta_3$; where G is the free energy of one mol of QSS without elastic deformations.

The equation for the stabilization factor corresponds to the left-hand side part of the coherent spinodal equation [12] in which the denominator of the fraction corresponds to the chemical spinodal equation. This results in the stabilization factor approachings infinity at the boundary of the spinodal decomposition region. Therefore, the stabilizing influence of the substrate increases sharply near the composition areas confined by the chemical spinodal.

The calculation of the stabilization factor was carried out for the $Ga_xIn_{1-x}P_yAs_zSb_{1-y-z}$ solid solutions lattice-matched to GaSb and InAs at 773 K ($f = -1\%$). Figure 2 represents the results of the calculations of q for $Ga_xIn_{1-x}P_yAs_zSb_{1-y-z}$/InAs.

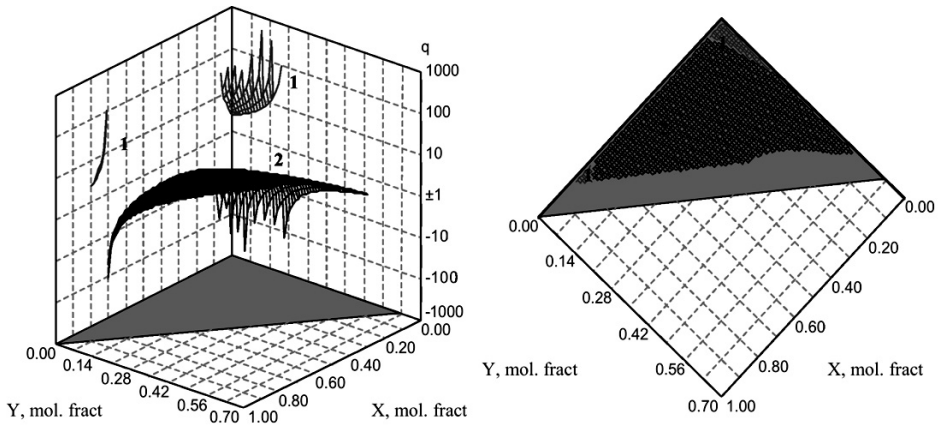

Fig. 2. Stabilization factor of $Ga_xIn_{1-x}P_yAs_zSb_{1-y-z}$/InAs system at 773 K, $f = -1\%$. ⟨111⟩: 1 – positive values, 2 – negative values

Analysis of the results shows that within the area of the spinodal decomposition, the stabilization factor becomes negative. Similar to the case of the contact supercool-

ing, this happens due to the variation of the curvature of the dependence of the solid solution free energy on composition which leads to the change of the sign of Δa.

Fabrication of the semiconducting isomorphic QSS becomes more complicated due to the thermodynamic restrictions that arise not only because of the spinodal decomposition area, but also due to the fusibility restriction. The essence of the fusibility restriction is that at any temperature above the melting point of the most fusible component of the solid solution, a solid phase composition range exists for which the equilibrium liquid phase can not be found [13]. In the systems containing Sb this composition range shows itself at $T \sim 800$ K (since $T^{F}_{\mathrm{InSb}} = 798$ K). This restriction can arise also below the melting temperature of the most fusible component. This can be proven by the solidus isotherm that was calculated at $T = 793$ K for the AlGaInAsSb/GaSb system (Fig. 3). The analysis shows that the fusibility restriction arises reducing the amount of indium (as the solvent) and increasing the amount of antimony in the liquid phase up to ~ 0.5 atomic fraction (the amount of other component fracting is significantly smaller).

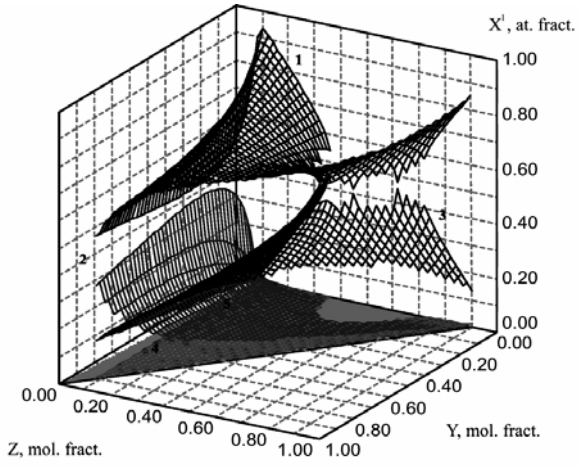

Fig. 3. Solidus isoterms of $Al_xGa_yIn_{1-x-y}As_zSb_{1-z}$/GaSb system at $T = 793$ K: 1 – In, 2 – Ga, 3 – Sb, 4 – As, 5 – Al

The calculation of the area of the fusibility restriction was carried out for the $Ga_xIn_{1-x}P_yAs_zSb_{1-y-z}$ system lattice-matched to GaSb and InAs. It was shown that the area of the fusibility restriction increases with temperature, while the thermodynamic instability area decreases. Therefore, the mutual effect of the fusibility restriction and thermodynamic instability leads to a decrease of the areas of the compositions of solid solutions that can be fabricated in these systems by LPE.

It should be noted that the elastic strains also influence the area of the fusibility restriction. This depends on the sign of the heteropair lattice mismatch (f). Analysis of the results of calculation of the liquidus isotherms (that was carried out for the $Ga_xIn_{1-x}P_yAs_zSb_{1-y-z}$/InAs system at 773 K shows that the area of the fusibility restriction decreases when $f < 0$, and increases when $f > 0$.

Based on the preliminary thermodynamic analysis, the interdependence between the thermodynamic parameters of the solid solution components, phase boundaries and the growth conditions of the GaInPAsSb QSS were obtained. In other words, the areas of restrictions should be taken into consideration for determination of the technological parameters of the heterostructure fabrication.

3. Experimental

LPE "step-cooling" method was used to grow the GaInPAsSb solid solutions on GaSb substrates from the Sb-rich melts in order to prevent the substrate subsolution and to reduce the concentration of the stoichiometric defects (V_{Ga} + Ga_{Sb}). GaSb (100) monocrystalline plates (n-type, Te-doped up to the concentration of $n = (1–5)\times10^{17}$ cm^{-3}) were used as the substrates. Epitaxial growth was preceded by homogenization of the melt at 923 K during 1–1.5 hour. The liquidus temperature (T^l) and the critical supercooling (ΔT_{cr}) were determined by the "in situ" method. Temperature range of the epitaxy process was 843–878 K, of the supercooling ΔT = 8–17 K. The thicknesses of the obtained layers were 1–4 μm.

The GaInPAsSb QSS on the InAs substrates were grown from In-rich melts (to prevent the substrate subsolution process). Monocrystalline InAs <111> plates (400 μm thick) were used as the substrates. Homogenization of the melt was carried out at 993 K during 1.5 hour. The temperature range was 920–925 K, ΔT = 5–9 K, the growth duration was 1–3 min, the thickness of the layers was 2–10 μm [14].

Compositions of the solid solutions were determined using the X-ray microanalyzer JXA–5 "Camebax", while the components distribution in the layer was measured by the secondary ion mass spectroscopy (SIMS) method. Estimation of the lattice parameters mismatch (LPM) between the layer and the substrate, and evaluation of the heterostructure crystal imperfection were done by the double crystal X-ray diffraction method. GaAs laser diode was used for the photoluminescence (PL) excitation and PL emission was recorded by a cooled (T = 77 K) InSb photodiode.

Solid solution was doped by Zn (acceptor) or Te (donor) to form the p-n heterojunction. Tellurium (in the composition of the Te-In hanging alloy) was placed into the melt just before the epitaxy process. Doping with Zn was done from the gas phase (by placing the In–Zn alloy into the specific temperature zone of the reactor). Zn concentration in the melt was determined by the vapour partial pressure of Zn, which was set by zone source temperature. Concentration of charged particles in the fabricated layers was 5×10^{17} cm^{-3}. Compositions of the fabricated $Ga_{1-x}In_xP_yAs_zSb_{1-y-z}$ epitaxial layers lattice-matched to GaSb were within the following ranges: $0.90 < x < 0.97$, $0.04 < y < 0.1$, $0.80 < z < 0.90$ [15]. Compositions of the grown $Ga_{1-x}In_xP_yAs_zSb_{1-y-z}$ epitaxial layers lattice-matched to InAs were within the ranges: $0.91 < x < 0.92$, $0.01 < y < 0.05$, $0.08 < z < 0.16$ and $0.07 < x < 0.1$, $0.07 < y < 0.13$, $0.77 < z < 0.81$. Table 1 shows the data for $Ga_xIn_{1-x}As_yP_zSb_{1-y-z}$/InAs solid solutions obtained from the experiment and from calculations.

Table 1. The experimental and calculations data for $Ga_xIn_{1-x}P_yAs_zSb_{1-y-z}$/InAs solid solutions

T, K	Composition of liquid phase (atomic fraction)				Composition of solid phase (mole fraction); 1 – calculation, 2 – experiment			
	$x^l_{Ga}\times10$	$x^l_P\times10$	$x^l_{As}\times10$	$x^l_{Sb}\times10$		x	y	z
925	0.0303	1.63	3.24	3.77	1	0.060	0.120	0.768
					2	0.08	0.08	0.81
					2	0.072	0.09	0.78
920	2.925	0.0862	0.24151	4.11	1	0.907	0.011	0.165
					2	0.92	0.012	0.165
					2	0.91	0.011	0.160

4. Results and discussion

Photoluminescence (PL) and electroluminescence (EL) methods were used to investigate the epitaxial layers. The investigations were carried out at 77 K (PL and EL) and 296 K (EL). 0.5×0.5 mm^2 chips with a point contact to the epitaxial layer and a uniform contact to the InAs substrate were used to measure EL.

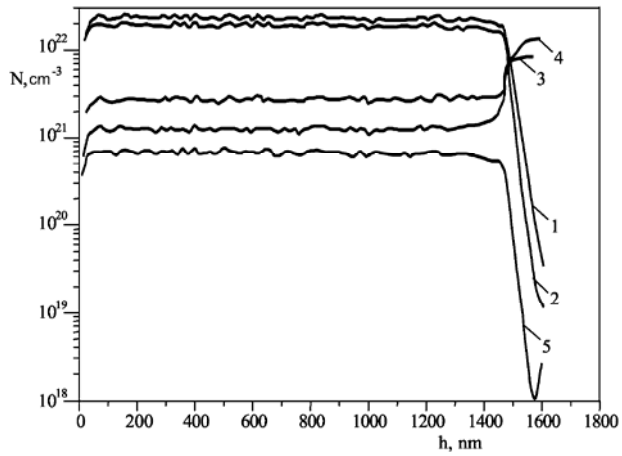

Fig. 4. Composition profiles of GaInPAsSb composition: 1 – In, 2 – As, 3 – Sb, 4 – Ga, 5 – P. h is the linear coordinate along the layer thickness

The structural perfection of the epitaxial layers of the $Ga_{1-x}InxAs_yP_zSb_{1-y-z}$/GaSb solid solutions (SS) with compositions ranges: $0.90 < x < 0.97$, $0.80 < y < 0.90$, $0.04 < z < 0.1$ was evaluated from the results of the X-ray diffraction. Epitaxial layers had a mirror-like surface, lattice parameters mismatch was $1.5\times10^{-3} \le f \le 1.8\times10^{-3}$. Heterostructures had a good crystal perfection and for the best samples the X-ray rocking curves halfwidth was 30–40 arcsec. The existence of the abrupt heterojunc-

tions can be proven by the results of SIMS (Fig. 4). A sharp change of the concentration of components can be seen clearly on the layer–substrate boundary with the boundary region width of about 50–70 nm). The PL wavelengths of the epitaxial layers were within 3.2–3.9 μm (T = 77 K), the radiation intensity of the QSS significantly (3–7 times) exceeded the radiation intensity of the obtained quaternary GaInAsSb solid solutions [15] with the same band gaps.

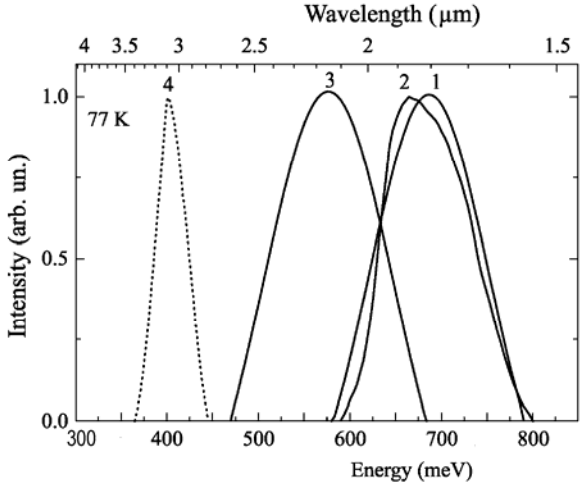

Fig. 5. PL spectra of $Ga_{0.92}In_{0.08}P_{0.05}As_{0.08}Sb_{0.87}$/InAs heterostructure: 1 – undoped, 2 – Zn-doped, 3 – Te-doped, 4 – InAs substrate

The PL spectra of the $Ga_{0.92}In_{0.08}P_{0.05}As_{0.08}Sb_{0.87}$/InAs structure are shown in Fig. 5. The maximum of the n-InAs substrate PL spectrum is at $h\nu$=400 meV, the maximum of the SS PL spectrum is at $h\nu$ = 580–685 meV. PL maximum of the purposely undoped GaInPAsSb solid solution ($h\nu$ = 690 meV) is conditioned by the transitions between the conduction band and the double-ionized acceptor levels. This explains a significant FWHM of the PL spectrum ($\Delta h\nu$ = 100 meV). Doping the solid solution with Zn (as an acceptor) leads to the recombination to the deeper acceptor level and produces a spectrum shift (~20 meV) to the lower energies with the same spectrum halfwidth. Doping with donor (Te) leads to the compensation of the p-type conductivity, hence the SS layers demonstrate a slight n-type conductivity. The PL maximum of the Te-doped SS shifts by 110 meV to lower energies ($h\nu$ = 580 meV) in comparison to undoped SS. The band gap of the $Ga_{0.92}In_{0.08}P_{0.05}As_{0.08}Sb_{0.87}$ SS measured at 77 K is 695 meV [14].

Studies of EL of the InAs/GaInPAsSb heterostructures were carried out. The interpretation of the experimental results was done in the framework of the broken gap type II heterostructure luminescence model [16].

Both the substrate–layer heterostructures and the homo p–n junction structures in the bulk n-InAs/P-GaInPAsSb/N-GaInPAsSb SS were used for the EL investigation.

The current–voltage characteristics of the p-P, p-N, n-N and n-P structures changed insignificantly within the 77–300 K temperature range, indicating the tunnelling current flow. The isotype p-P and N-n structures demonstrated rectifying characteristics and produced EL in the 77–300 K temperature range, whereas the P-n structure showed no rectification nor EL. This fact confirms that in the grown InAs/GaInPAsSb structure the type II heterojunction was formed.

Analysis of the EL spectra (Fig. 6) of the n-N-p (at 77 K) and n-P-N (at 77 and 300 K) structures showed that in the both cases the spectra consist of two bands: the short-wave band (685–695 meV, 77 K), produced by the recombination emission in the SS, and the long-wave band (400 meV, 77 K) due to the recombination emission in the substrate. At 300 K the emission maxima are at 640 and 360 meV.

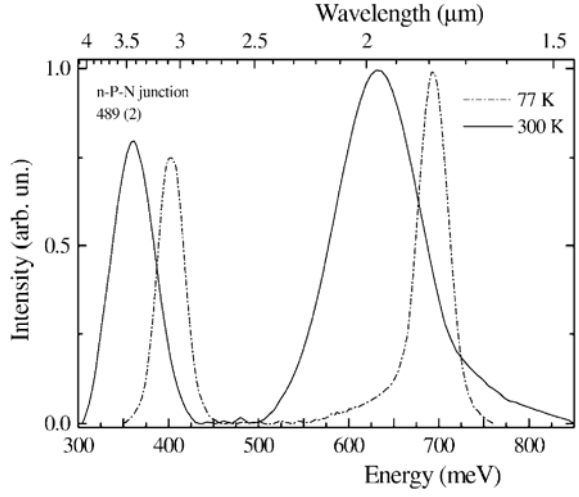

Fig. 6. EL spectra of the n-InAs/P-GaInPAsSb/N-GaInPAsSb structure

The temperature shift of the maxima correspond to the temperature dependence of the InAs band gap (3×10^{-4} eV/K) which speaks for a good crystal perfection of the epitaxial layer. It is assumed that in the homo-p-n heterojunction of the SS, similarly as in InAs, the p-region becomes the emitting region, since the electron diffusion length exceeds that of holes. This is supported by the close matching of the PL spectra of the p-type material of the SS and the EL spectra of the P-N junction.

On the basis of the homo-p-n junction in the bulk SS the LEDs were fabricated with the radiation maximum at 1.9 μm and FWHM of the spectrum amounting to 0.3 μm.

5. Conclusion

A comprehensive thermodynamic analysis of the quinary Ga–In–P–As–Sb system was carried out. The epitaxial layers of the $Ga_xIn_{1-x}P_yAs_zSb_{1-y-z}$ QSS on the (100)

GaSb substrates within the composition range $0.9 \le x \le 0.97$, $0.04 \le y \le 0.1$, $0.80 < z < 0.90$ and on the (111) InAs substrates ($0.91 < x < 0.92$, $0.08 < y < 0.16$, $0.01 < z < 0.05$) were formed. It was shown that in the $Ga_{0.92}In_{0.08}P_{0.05}As_{0.08}Sb_{0.87}$/InAs heterostructure, the broken gap type II heterojunction is formed which became a basis for the development of the light-emitting diode and photodiode with the emission intensity and photosensitivity maximum at the 1.9 μm range.

Acknowledgement

The authors gratefully acknowledge the help of Dr. B.A. Matveev in the preparation of the paper.

References

[1] RUBTSOV E.R., SOROKIN V.S., KUZNETSOV V.V., Russian J. Phys. Chem., 71 (1997), 415.
[2] KUZNETSOV V.V., MOSKVIN P.P., SOROKIN V.S., *Nonequilibrium Effects in Liquid-Phase Heteroepitaxy of Semiconductor Solid Solutions*, Moscow, Metallurgiya, 1991 (in Russian).
[3] GUGGENHEIM E.A., *Thermodynamics*, 3rd Ed., North-Holland, Amsterdam, 1957.
[4] GIL'DENBRANT G., *Nonelectrolytes Solubility*, Moscow, 1938.
[5] OLCHOWIK J.M., Phys. Stat. Sol. A, 142 (1994), 415.
[6] OLCHOWIK J.M., Phys. Stat. Sol. A, 146 (1994), K19.
[7] RUBTSOV E.R., KUZNETSOV V.V., LEBEDEV O.A., Inorg. Mater., 34 (1998), 525.
[8] KUZNETSOV V.V., STUS N.M., TALALAKIN G.N., RUBTSOV E.R., Crystall. Rep., 37 (1992), 998.
[9] KUZNETSOV V.V., RUBTSOV E.R., RATUSHNYI V.I., KOGNOVITSKAYA E.A., Crystall. Rep., 49 (2004), 193.
[10] OLCHOWIK J.M., SADOWSKI W., SZYMCZUK D., J. Cryst. Growth, 158 (1996), 241.
[11] SOROKIN V.S., Crystall. Rep., 31 (1986), 844.
[12] KUZNETSOV V.V., RUBTSOV E.R., Russian Tsvetn. Metallurgiya, 3 (1997), 57.
[13] OLCHOWIK, J.M. SADOWSKI W., SZYMCZUK D., J. Cryst. Growth, 153 (1995), 11.
[14] AIDARALIEV M., ZOTOVA N.V., KARANDASHOV S.A., MATVEEV B.A., REMENNYI M.A., STUS N.M., TALALAKIN G.N., SHUSTOV V.V., KUZNETSOV V.V., KOGNOVITSKAYA E.A., Semiconductors, 36 (2002), 944.
[15] KUCHINSKII V.I., VASIL'EV V.I., GAGIS G.S., DERYAGIN A.G., DUDELEV V.V., Proc. of LFNM 2003, 5th International Workshop on Laser and Fibre-Optical Networks Modelling, Kharkov (Ukraine) 19–20 Sept. 2003, p. 76.
[16] MIKHAILOVA M.P., TITKOV A.N., Semicond. Sci. Technol., 9 (1994), 1279.

Received 9 September 2005
Revised 9 November 2005

Materials Science-Poland, Vol. 24, No. 4, 2006

FMR study of nanocarbon materials obtained by carburisation of nanocrystalline iron

U. NARKIEWICZ[1*], W. ARABCZYK[1], I. PEŁECH[1], N. GUSKOS[2, 3], J. TYPEK[3], M. MARYNIAK[3], M. J. WOŹNIAK[4], H. MATYSIAK[4], K. J.KURZYDŁOWSKI[4]

[1]Institute of Chemical and Environment Engineering, Szczecin University of Technology, Pułaskiego 10, 70-322 Szczecin, Poland

[2]Solid State Section, Department of Physics, University of Athens, Panepistimiopolis, 157 84 Zografos, Greece

[3] Institute of Physics, Szczecin University of Technology, al. Piastów 17, 70-310 Szczecin, Poland

[4]Faculty of Materials Science and Engineering, Warsaw University of Technology, Wołoska 141, 02-507 Warsaw, Poland

Samples of nanocrystalline iron were carburised with ethylene and next reduced with hydrogen. Both carburisation and reduction were monitored by the thermogravimetry. The obtained samples were characterised using X-ray diffraction, high-resolution transmission electron microscopy and ferromagnetic resonance. The samples after carburisation contained cementite (Fe_3C) and carbon deposit (nanofibres and nanotubes). As the result of reduction with hydrogen at 450 or 500 °C cementite was reduced to iron. A major part of carbon was also hydrogenated, only thin carbon nanotubes remained. The FMR spectra of the prepared samples were recorded at room temperature. The sample after carburisation has shown a wide FMR line with weak intensity while the resonance field has been shifted to lower magnetic field. This spectrum has been attributed to the presence of cementite. The FMR lines corresponding to samples after reduction are more intense and are connected with the presence of α-Fe nanoparticle conglomerates.

Key words: *carburisation; reduction; iron carbide; FMR; HRTEM*

1. Introduction

Iron carbide-based nanoparticles are of growing interest due to their improved magnetic properties as well as potential application in catalysis, sensors and reduction of the cost required to produce bulk quantities [1–5]. In particular, nanocomposites

*Corresponding author, e-mail: urszula.narkiewicz@ps.pl

containing iron carbide (Fe_3C) are suited to diverse technological applications due to their enhanced mechanical properties [6] and importance in ferrous metallurgy [7]. Fe_3C nanoparticles were found to be more resistant to oxidation than α-Fe nanoparticles due to formation of carbonaceous layers on the particle surfaces [1, 2]. Many preparative methods to obtain iron carbide and carbon materials are known, among them the effective one is chemical vapour deposition (CVD) with application of transition metal catalysts [8–11]. Usually, the CVD method generates different forms of carbon, like, e.g., amorphous carbon, carbon fibres or nanotubes. To remove amorphous carbon many methods have been used [12–14] and among them the hydrogenation process carried out at 900 °C [15]. The ferromagnetic resonance (FMR) method can be very useful for investigation of the magnetic interaction and concentration of magnetic nanoparticles (especially iron carbide and α-Fe) and their magnetic interaction [16–19]. In this work, nanoparticles (iron carbide, α-Fe and nanocarbons) formed during carburisation of nanocrystalline iron with ethylene were studied using X-ray diffraction (XRD) high-resolution transmission electron microscopy (HRTEM) and FMR methods.

2. Experimental

Nanocrystalline iron was obtained by fusion of magnetite with small amounts of promoter oxides (Al_2O_3 and CaO), followed by reduction with hydrogen. The material obtained after the fusion was crushed and sieved to obtain a fraction in the range 1.2–1.5 mm and then reduced with hydrogen according to a procedure described previously [20]. After reduction, nanocrystalline iron was obtained and the promoters remained in the oxidised state. To avoid rapid oxidation on contact with air, the samples were passivated under nitrogen containing traces of oxygen. The chemical composition of the obtained samples was characterised by the AES-ICP method (Yvon –Jobin). Besides iron, the samples contained 2.9% of Al_2O_3 and 3.0% of CaO. The role of two promoter oxides was to stabilize the nanocrystalline iron structure against sintering. The phase composition of the samples was determined by XRD method (Philips X'Pert); the mean crystal size of iron particles calculated using Scherrer's equation was 17 nm.

The carburisation processes were carried out in the spring thermobalance equipped with a cathetometer. The mass changes were registered with the accuracy of 10^{-4} g. A platinum basket hung in the thermobalance was used to place a single layer of grains.

Before each carburisation, the thin passivation layer of the sample was removed by reducing polythermally under hydrogen (40 dm^3/h) at the temperature rising from 20 °C to 500 °C. The carburisation processes were carried out under pure ethylene (40 dm^3/h) under atmospheric pressure at 550 °C. After carburisation, the samples were cooled to room temperature under nitrogen flow. Some carburised samples were treated with hydrogen at the temperatures of 450 °C and 500 °C. The phase composi-

tions of the samples after carburisation, and after carburisation followed by reduction was determined by XRD and their morphology was investigated by HRTEM (Jeol JEM 3010) and atomic force spectroscopy (AFM, Digital Instruments) methods.

Magnetic resonance absorption measurements were carried out with a conventional X-band (ν = 9.43 GHz) Bruker E 500 spectrometer with 100 kHz magnetic field modulation. The samples, each containing around 20 mg of the material, were placed into 4 mm-in-diameter quartz tubes. Prior to the measurements, the samples were magnetized with a steady magnetic field of 1.6 T to saturate any domain structure. The measurements were performed at room temperature.

3. Results and discussion

The sample of nanocrystalline iron was carburised under ethylene at 550 °C until the mass increase of 1.2 g C/g Fe (Sample III). The thermogravimetric (TG) line of the carburisation process is shown in the left part of Fig. 1. According to XRD analysis (upper pattern in Fig. 2), the sample contains two phases: cementite and graphite. In the HRTEM image of the same sample (Fig. 3a), dark agglomerates of iron carbide can be seen, dispersed in carbon. Some carbon fibres are visible and at the end of these oblong carbon forms the crystallites of Fe_3C are located. Besides thick carbon fibres, agglomerates of iron carbides encapsulated with carbon are also visible in the left top corner of the picture. At higher magnification (Fig. 3b), it is seen that the particles of cementite are encapsulated in the shell of 15 nm in thickness, formed by sheets of graphite. Thin multiwall carbon nanotubes can also be observed, about 10 nm in diameter (Fig. 3c).

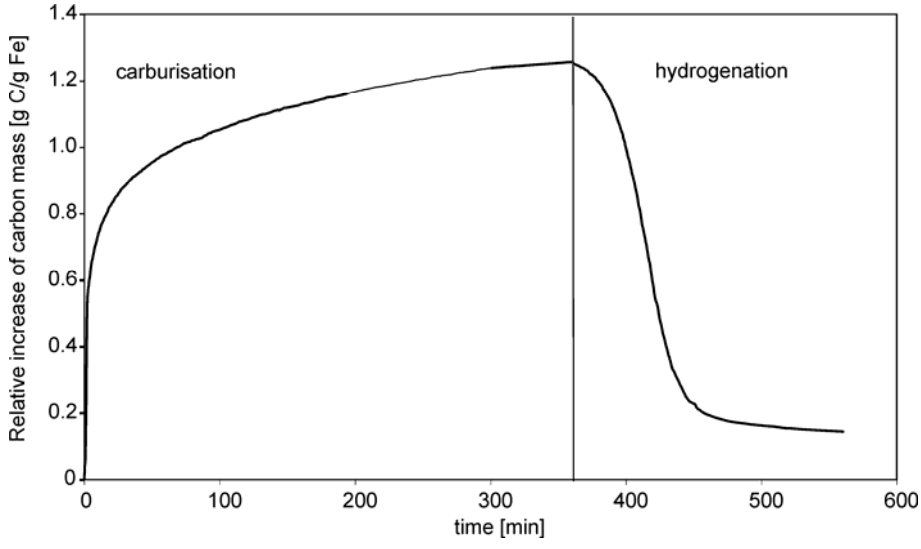

Fig. 1. TG curves of carburisation at 550 °C and reduction at 500 °C

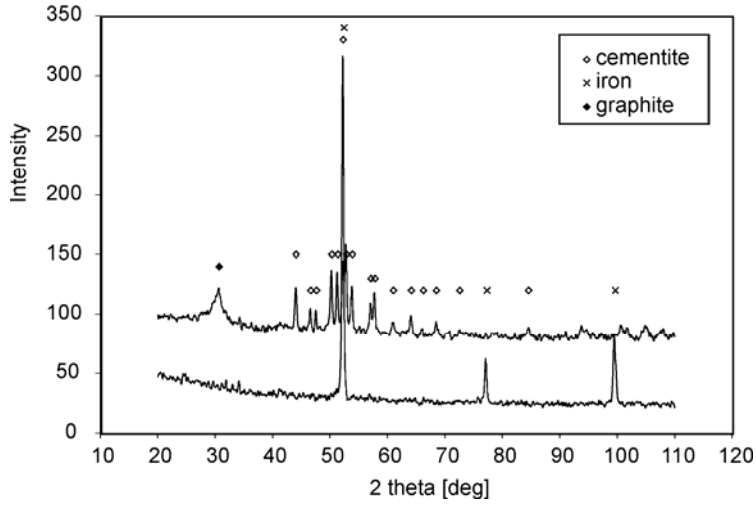

Fig. 2. XRD patterns of the samples: after carburisation at 550 °C (upper spectrum) and after reduction at 450 °C (lower spectrum)

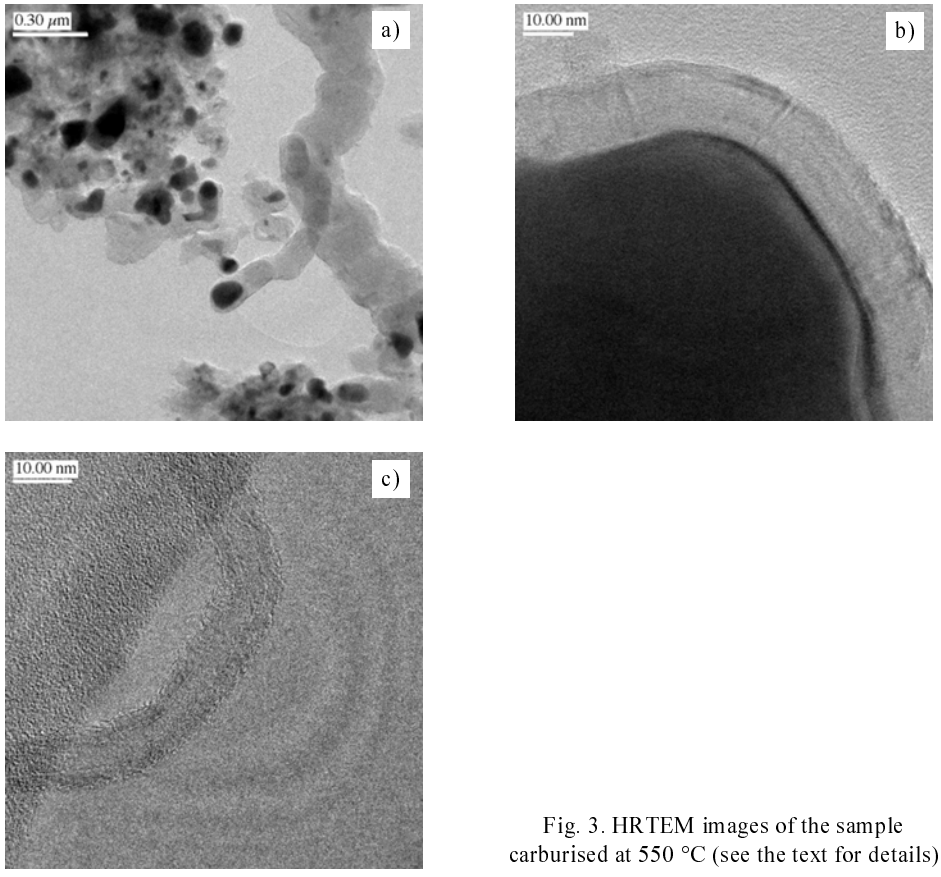

Fig. 3. HRTEM images of the sample carburised at 550 °C (see the text for details)

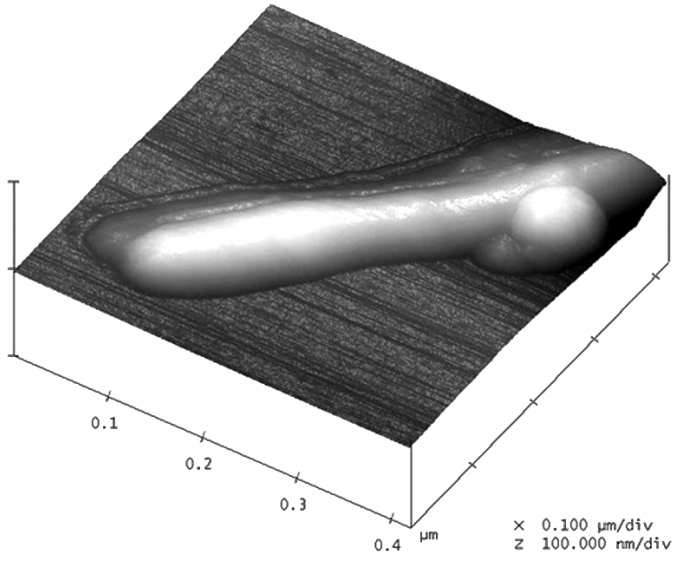

Fig. 4. AFM picture of the carburised sample at 550 °C

In the AFM picture of this sample, some oblong carbon forms can be observed (Fig. 4), below 100 nm in diameter.

The carburised sample was next subject to hydrogenation at 450 °C (sample II). As a result of this process, the carbon content in the sample decreased from 1.2 to 0.4 g C/g Fe. In the XRD pattern of this sample, only the peaks corresponding to α-Fe are observed (lower pattern in Fig. 2). In the HRTEM picture of the sample thick carbon fibres are no more found (Fig. 5a), they should have been removed as a result of hydrogenation. In Figure 5b a multiwall bamboo-shaped nanotube is shown.

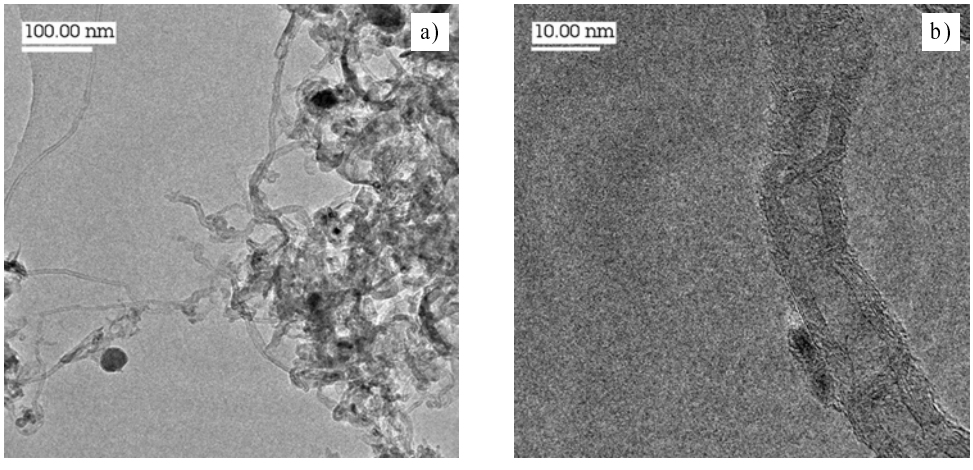

Fig. 5. HRTEM images of the sample carburised at 550 °C
and then reduced at 450 °C (see the text for details)

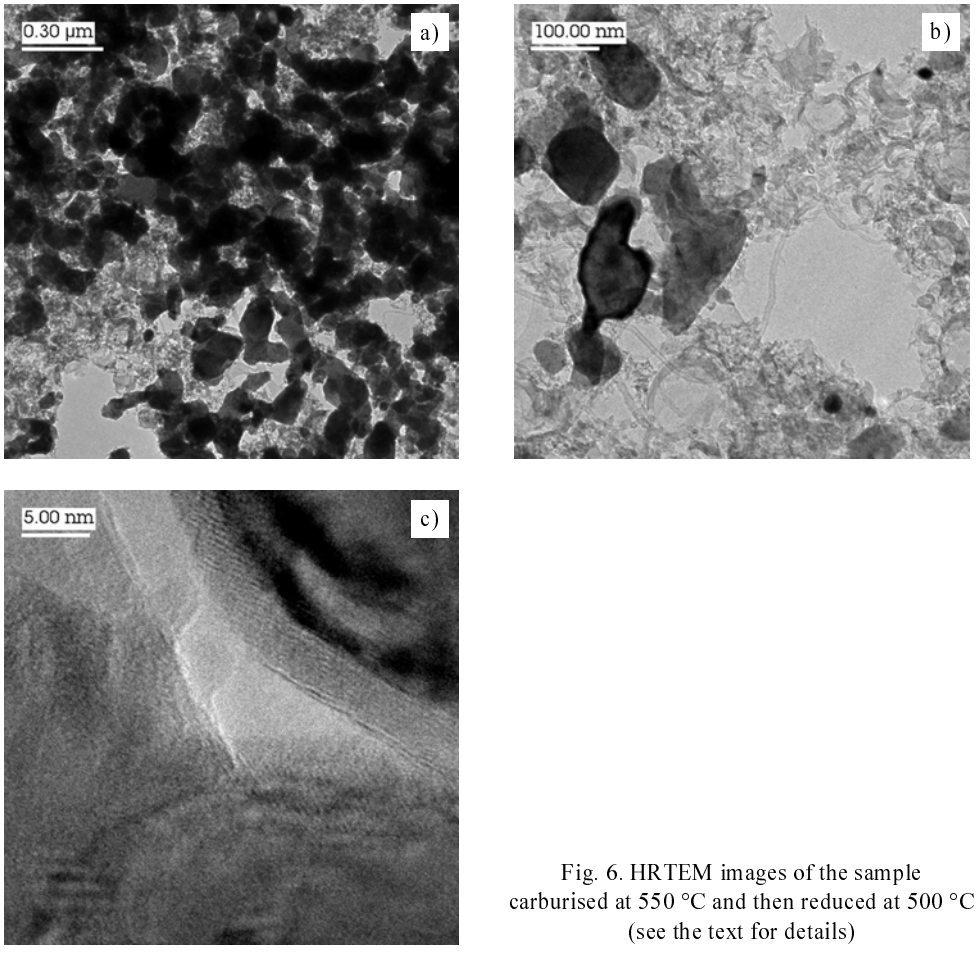

Fig. 6. HRTEM images of the sample carburised at 550 °C and then reduced at 500 °C (see the text for details)

After the hydrogenation of the same carburised sample at a higher temperature (500 °C), a further mass decrease was observed, until 0.2 g C/g Fe (sample I). The TG line corresponding to this hydrogenation process is shown in Fig. 1. As in the case of sample II, only the phase of α-Fe was detected by XRD analysis; then all iron carbide was reduced to iron. The increase of the iron concentration in carbon matrix is clearly visible in Fig. 6a (compared with Fig. 3a). The particles of iron are well dispersed, contrary to the pristine iron sample (an alloy) before carburisation. Thin carbonaceous forms can be seen in Fig. 6b. Simultaneously, as can be seen in Fig. 6c, the thickness of the graphitic layer after hydrogenation is lower (below 5 nm) than that after carburisation (about 15 nm, Fig. 3b).

Figure 7a presents the FMR spectra of all three samples, recorded at room temperature. In all spectra, a strong shift of the resonance lines in the direction of low magnetic field is observed. Intense FMR lines are broader than weaker ones. The obtained FMR spectra have shown a similarity to the FMR spectra of iron carbide and α-

iron [16-18]. The spectra of samples I and II are dominated by a line produced by α-iron, while the spectrum of the sample III is dominated by carbide iron. The fitting

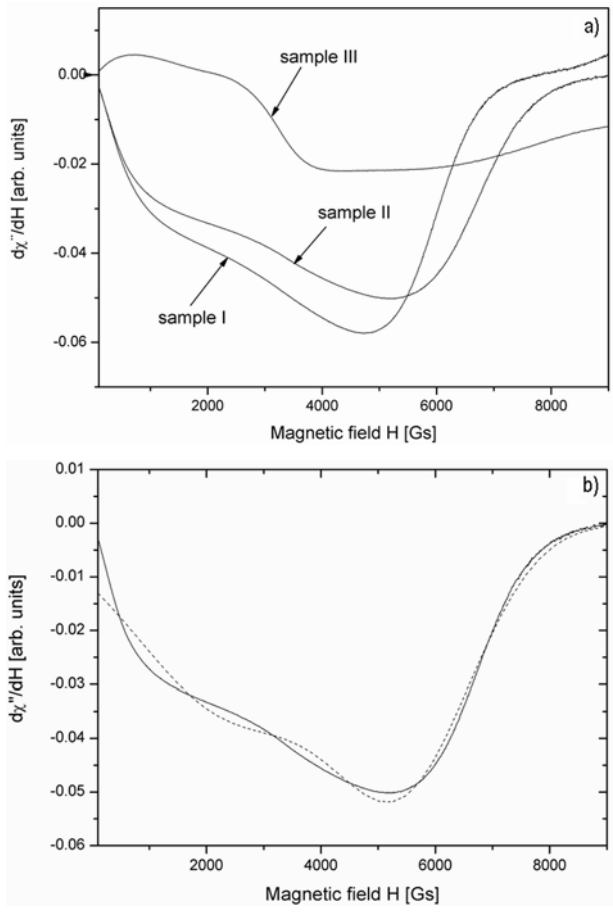

Fig. 7. FMR spectra of the samples: I – carburised at 550 °C followed by reduction at 500 °C; II – carburised at 550 °C followed by reduction at 450 °C; III – carburised at 550 °C (a); and the fitted FMR spectrum (dotted line) for sample II (b)

of the extended resonance absorption signals has been performed using Lorentzian -type curves taking into account absorption at both H_r and $-H_r$, induced by two oppositely rotating components of the linearly polarized radio-frequency incoming experimental field. The resonance absorption lines for samples I and II were fitted with two Lorentzian curves, one centred on the magnetic field near zero and the other at a higher field (Fig. 7b). Table 1 gives the values of FMR spectral parameters. Despite of this crude approximation, the results of the fitting could give a satisfactory explanation of the experimental results [18]. The results of the FMR measurements of the carburised and reduced samples are summarised in Table 1.

Table. 1. FMR parameters of the carburised and hydrogenated samples.

Sample	Composition	I_1 [a. u.]	ΔH_1 [mT]	H_{r1} [mT]	I_2 [a. u.]	ΔH_2 [mT]	H_{r2} [mT]
I, reduced at 500 °C	Fe+C, 0.2 g C/g Fe	5.8	410(1)	190(1)	2.7	184(30)	62(20)
II, reduced at 450 °C	Fe+C, 0.4 g C/g Fe	5.0	310(1)	210(1)	1.5	180(10)	~0
III, carburised	Fe_3C+C, 1.2 g C/g Fe	0.5	140(4)	250(3)	3	789(10)	35(10)

The FMR lines could originate mainly from ferromagnetic iron ions with their individual spins coupled by the exchange interaction within each nanoscale metallic grain. The iron ion with localised spins forming non-separated ferromagnetic nanoparticles is subject to magnetic field produced by the following interaction processes:

$$H_{tot} = H_{dem} + H_{dip} + H_{ex} \tag{1}$$

which could change the resonance condition:

$$h\nu = g\mu_B(H_{ex} \pm H_{in}) \tag{2}$$

where h is the Planck constant, μ_B is the Bohr magneton, H_{ex} is the applied external magnetic field, H_{in} is the internal magnetic field, H_{dip} is the magnetic dipole field from the neighbouring nanoparticles or agglomerates, H_{dem} is the so-called demagnetising field.

FMR spectra of the samples I and II are dominated by the signal arising from α-iron. The spectrum of the sample I is more intense in comparison to the sample II and the resonance field is more shifted to lower magnetic field. Despite of carburization of the sample III, iron carbide is a dominating phase while in the sample II produced at a lower hydrogenation temperature, the α-iron content is increased so that iron carbide is not observed by XRD measurements (Fig. 2). Essential changes in magnetic interaction are observed among the investigated samples influencing the values of the linewidth and intensity of the FMR spectrum (Fig. 7a). Increasing temperature of the hydrogenation process (about 50 K) decreases the carbon mass or increase the concentration of α-iron. The FMR spectrum of the sample III is dominated by iron carbide (Fig. 7a) which produces a characteristic very wide FMR line. Nanocrystalline α-iron forming conglomerates could create stronger magnetic field and magnetic interactions essentially influence the values of the FMR parameters, especially the linewidth and position of the resonance field.

4. Conclusions

Three samples of nanocrystalline iron were obtained, carburised with ethylene and subsequently reduced with hydrogen. After the treatment of the sample with hydrogen at 450 °C iron carbide is reduced to α-iron, which is reflected in FMR spectra. The

amount of carbon is reduced from 1.2 to 0.4 g C/g Fe which corresponds to the elimination of amorphous carbon and thick carbon nanofibres. After the reduction under hydrogen at 500 °C, the remaining mass of carbon of 0.2 g C/g Fe corresponds to thin multiwall carbon nanotubes. The FMR spectrum of this sample corresponds to an increased amount of iron. Changes of concentration of magnetic nanocrystallites strongly influences the FMR spectra. The position of the resonance line depends strongly on the concentration of magnetic nanocrystalline agglomerates suggesting that the dipole–dipole interaction could play an essential role in the magnetic interactions.

Acknowledgements

This work was partially supported by the grant PBZ-KBN-095/TO8/2003.

References

[1] BI X-X., GANGULY B., HUFFMAN G.P., HUGGINS F.E., ENDO M., EKLUND P.C., J. Mater. Res., 8 (1993), 1666.
[2] ZHAO X.Q., LIANG Y., HU Z.Q., LIU B.X., J. Appl. Phys., 80 (1996), 5857.
[3] GRIMES C.A., HORN J.L., BUSH G.G., ALLEN J.L., EKLUND P.C., IEEE Trans. Magn., 33 (1997), 3736.
[4] GRIMES C.A., QIAN D., DICKEY E.C., ALLEN J.L., EKLUND P.C., J. Appl. Phys., 87 (2000), 5642.
[5] DENES F.S., MANOLACHE S., MA Y.C., SHAMAMIAN V., RAVEL B., PROKES S., J. Appl. Phys., 94 (2003), 3498.
[6] GOODWIN T.J., YOO S.H., MATTEAZZI P., GROZA J.R., Nanostruct. Mater., 8 (1997), 559.
[7] YUMOTO H., NAGAMINE Y., NAGAHAMA J., SHIMOTOMAI M., Vacuum, 65 (2002), 527.
[8] VENEGONI D., SERP P., FEURER R., KIHN Y., VAHLAS C., KALCK P., Carbon, 40 (2002), 1799.
[9] QIAN W., LIU T., WANG Z., YU H., LI Z., WIE F., LUO G., Carbon, 41 (2003), 2487.
[10] QIAN W., LIU T., WEI F., WANG Z., LI Z., App. Catal. A: General, 258 (2004), 121.
[11] GULINO G., VIEIRA R., AMADOU J., NGUYEN P., LEDOUX M.J., GALVAGNO S., CENTI G., PHAM-HUU C., App. Catal. A: General, 279 (2005), 89.
[12] BOUGRINE A., NAJI A., GHANBAJA J., BILLAUD D., Synth. Met., 103 (1999), 2480.
[13] SHI Z., LIAN Y., ZHOU X., GU Z., AHANG Y., IIJIMA S., Solid State Comm., 112 (1999), 35.
[14] ZHANG Y., SHI Z., GU Z., IIJIMA S., Carbon, 38 (2000), 2055.
[15] IVANOV V., FONSECA A., NAGY J.B., LUCAS A., LAMBIN P., BERNAERTS D., ZHANG X.B., CARBON, 33 (1995), 1727.
[16] NARKIEWICZ U., GUSKOS N., ARABCZYK W., TYPEK J., BODZIONY T., KONICKI W., GASIOREK G., KUCHAREWICZ I., ANAGNOSTAKIS E.A., Carbon, 42 (2004), 1127.
[17] GUSKOS N., ANAGNOSTAKIS E.A., TYPEK J., GASIOREK G., BODZIONY T., NARKIEWICZ U., ARABCZYK W., KONICKI W., Mol. Phys. Rep., 39 (2004), 58.
[18] GUSKOS N., TYPEK J., NARKIEWICZ U., MARYNIAK M., AIDINIS K., Rev. Adv. Mat. Sci., 8 (2004), 10.
[19] GUSKOS N., ANAGNOSTAKIS E.A., LIKODIMOS V., BODZIONY T., TYPEK J., MARYNIAK M., NARKIEWICZ U., KUCHAREWICZ I., J. Appl. Phys., 97 (2005), 024304.
[20] NARKIEWICZ U., ARABCZYK W., KONICKI W., PATTEK-JAŃCZYK A., J. Mater. Res., 20 (2005), 386.

Received 9 September 2005
Revised 25 November 2005

Materials Science-Poland, Vol. 24, No. 4, 2006

Electron spin resonance study of copper(II) hydrogenmalonate dihydrate complex

S. MARCZYŃSKI[1], J. TYPEK[1*], N. GUSKOS[1, 2], E. GRECH[3], B. KOŁODZIEJ[3]

[1]Institute of Physics, Szczecin University of Technology, al. Piastów 17, 70-310 Szczecin, Poland

[2]Solid State Physics, Department of Physics, University of Athens, Panepistimiopolis, 15 784 Zografos, Athens, Greece

[3]Department of Inorganic and Analytical Chemistry, Szczecin University of Technology, al. Piastów 17, 70-310 Szczecin, Poland

Copper(II) hydrogenmalonate dihydrate complex has been studied by using the electron spin resonance (ESR) method. Numerically deconvoluted ESR spectra of Cu(II) ions have been investigated at 4.2–295 K temperature range. The powder ESR spectrum has been described by three *g*-factors and additionally 1.5% of the existing spurious phases of a copper(II) complex has been revealed. The temperature dependence of the integrated ESR intensity has shown a Curie–Weiss type behaviour, consisting of two terms with different Curie–Weiss temperatures. The observed ferromagnetic interactions suggest the presence of two different paramagnetic species. It is proposed that the $[Cu(H_2O)_4][Cu(mal)_2(H_2O)_2]$ copper(II) dimer complex is responsible for the low-temperature ($T < 50$ K) behaviour of the investigated sample.

Key words: *copper complex; ESR; malonate complex*

1. Introduction

Synthesis of ferro- and ferrimagnetic systems with a tunable T_c and three-dimensional (3D) ordering from molecular precursors including transition metal ions is one of the active branches of molecular inorganic chemistry [1–3]. The nature of interactions between transition metal ions (or transition metal ions and radicals) is rather complicated because it involves electrostatic (orbital) and magnetic (mainly dipolar) interactions. Therefore, the systems fulfilling necessary requirements to exhibit expected magnetic properties are not easy to design. There is a continued interest in the structural chemistry of copper(II) malonate, $Cu(O_2CCH_2CO_2)$ because of extensive use of malonate ions in the crystal engineering [4–6]. Malonate is a flexible and

*Corresponding author, e-mail: Janusz.Typek@ps.pl

versatile ligand. The structural complexity of malonate complexes is due to the ability of this dicarboxylate ligand, different from other dicarboxylic ligands, to adopt several chelating bidentate and/or different carboxylato-bridging coordination modes. The ability of the carboxylate bridge to mediate significant ferro- or antiferromagnetic coupling between paramagnetic centres is used to design materials with extended magnetic interactions [7–9]. Additionally, the group provides an efficient pathway coupling magnetic centres depending on structural aspects of metal environment [10–12].

Copper(II) malonate complexes with the formula $Cu(C_3H_2O_4)\times nH_2O$, where n = 0, 1, 2, 2.5, 3, 4 have been reported previously [13–17]. The number of water molecules influences the structural function of the malonate ions, which are bidentate in n = 4 complex and reveal tridetadte-bridging function in n = 3 and n = 2 complexes. The type of structure changes from isolated complexes for n = 4 to a one-dimensional polymer for n = 2 complexes [5]. The reason for the variety of products from reaction between copper(II) salts and malonic acid is attributed to the conditions of the synthesis, pH value, stoichiometry and temperature. Also important is the a symmetry of the melanate dianion which cannot, for example, pack across the centre of inversion in solids.

The aim of this temperature ESR study of copper(II) hydrogenmalonate dihydrate ($Cu(mal)_2(H_2O)_2$, henceforth abbreviated as CuHM), is to reveal its magnetic properties. The ESR spectrum of powder samples of this compound will be analysed and fitted with an appropriate combination of single ESR lines. The obtained thermal dependence of the ESR parameters will be used to draw conclusion on the magnetic content of the studied sample.

2. Experimental

Crystals of CuHM were grown by a slow evaporation of aqueous solutions prepared by dissolving stoichiometric amounts of malonic acid and copper carbonate in water. The obtained deep-blue small single crystals were in the form of prisms. Powder samples were prepared by grinding a large number of small crystallites.

ESR measurements were carried out in a standard X band Bruker E 500 spectrometer. The spectrometer was equipped with TE_{102} cavity with 100 kHz field modulation. The investigated samples were in the form of powder and were placed in 4 mm diameter quartz tubes. ESR detected the power P absorbed by the sample from the transverse magnetic microwave field as a function of the static magnetic field H. The signal-to-noise ratio was improved by recording the derivative dP/dH using the lock-in technique with field modulation. An Oxford flow cryostat was used for temperature -dependent measurements in the 4–300 K temperature range.

3. Results and discussion

The CuHM compound, with the chemical formula $Cu(C_3H_2O_4)\times 2H_2O$, crystallizes in the monoclinic $P2_1/n$ space group [4]. Figure 1 presents a schematic representation

of the CuHM complex. In the structure of the title compound, the hydrogen malonate ions are almost planar. In the Cu complex, the metal coordination clearly shows the geometrical pattern typical of the Jahn–Teller effect [4].

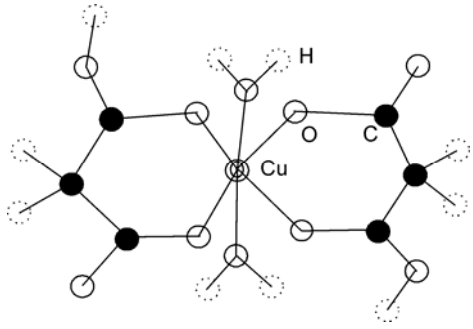

Fig. 1. Schematic representation of the formula of the CuHM complex

The ESR spectrum of a single crystal of CuHM at room temperature consists of an intense, single line without a hyperfine structure; its position strongly varies with the orientation of the sample in an external magnetic field. The lack of the hyperfine structure could indicate that the signal does not originate from isolated paramagnetic copper(II) ions. It is thus possible that the ions are strongly coupled by the exchange interaction (ferromagnetic or antiferromagnetic). Large exchange narrowing effects could suppress the hyperfine splitting. To examine the lineshape of that line, the derivative absorption signal was analysed and the result is shown in Fig. 2.

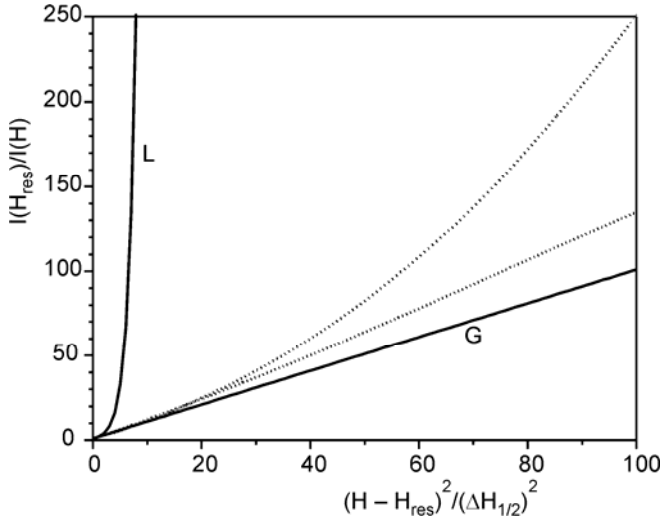

Fig. 2. ESR lineshape analysis of the CuHM single crystal at room temperature. The left- and right-hand side of the experimental CuHM line is represented by the dotted lines. Lorentzian (L) and Gaussian (G) type lines (solid lines) are presented for reference

The figure with an ordinate and an abscissa given as that in Fig. 2 is convenient, because the Lorentzian lineshape is reproduced as a straight line, as first introduced in [18]. In this figure, $I(H)$ is the height of the derivative line, $\Delta H_{1/2}$ is the halfwidth of the absorption curve, and H_{res} is the resonance field. For reference, the line which arises from Gaussian lineshape, which falls off much faster in the wings, is also given in Fig. 2. The recorded spectrum of CuHM is slightly asymmetric and its lineshape is close to Lorentzian.

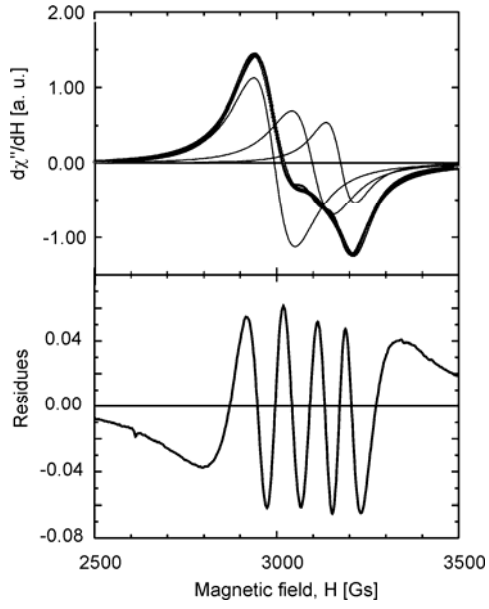

Fig. 3. ESR spectrum of the CuHM powder sample recorded at 50 K. Top panel – deconvolution of the experimental spectrum (circles) into three Lorentzian components (thin solid lines) and the sum of the three components (thick solid line). Lower panel – the difference between the experimental and fitted spectra

To simplify the procedure of the interpretation of the results, only the ESR measurements taken on the powder sample of CuHM will be further discussed. Figure 3 presents a typical recorded ESR spectrum of The CuHM complex at 50 K. The signal has been analysed in terms of being composed of three single Lorentzian lines (Fig. 3, top panel). The result of fitting of the observed ESR signal has been quite satisfactory. The effective g-factors of the components at room temperature are $g_1 = 2.254$, $g_2 = 2.184$, and $g_3 = 2.131$, and their peak-to-peak linewidths amount to 190 Gs, 195 Gs, and 140 Gs, respectively. The existence of these three different components reflects a low symmetry of the copper paramagnetic centre. Moreover, in the residue spectrum (Fig. 3, lower panel), calculated as the difference between the experimental spectrum and the fitted one, two additional signals could be discerned: one broad ($\Delta H = 200$ Gs), single line and other four-line spectrum superimposed on the former one, both centred at effective g-factor 2.20. The four-line spectrum resembles a typical Cu(II) ESR signal with the hyperfine structure arising from isolated paramagnetic centres. The integral intensity of those two spurious phases, and thus the number of paramagnetic impurities, constituted 1,5% of the total observed ESR signal.

The temperature evolution of the ESR spectra of CuHM powder sample is shown in Fig. 4. As the temperature is decreased from room temperature, the intensity of the ESR signal increases, but the overall shape of the spectrum remains roughly the same. To gain more insight into the nature of the paramagnetic centres producing the ESR signal, the temperature variation of the integrated intensity I has been studied. The integrated intensity is the area under the ESR absorption curve and can be calculated by double integration of the derivative ESR spectrum. This quantity is proportional to the susceptibility of the spins participating in the resonance.

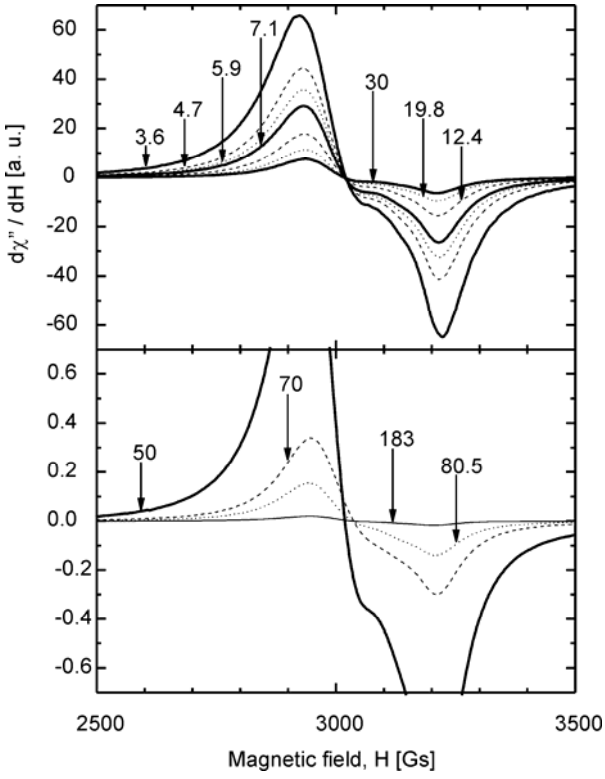

Fig. 4. Temperature evolution of the ESR spectra of the CuHM powder sample. Top panel – low temperatures ($T < 50$ K), lower panel – high temperatures ($T \geq 50$ K)

Figure 5 presents the temperature dependence of the integrated intensity (top panel), the temperature dependence of the reciprocal integral intensity (middle panel), and the product of temperature and the integrated intensity (bottom panel). The experimental data could not be satisfactory fitted by the single Curie–Weiss law, but are fairly well represented by a sum of two Curie–Weiss terms:

$$I = C_1/(T - \Theta_1) + C_2/(T - \Theta_2) \tag{1}$$

The best fit of this function to experimental data (Fig. 5, lower panel) gave the following values of the Curie–Weiss temperatures: $\Theta_1 = 60(14)$ K, $\Theta_2 = 6.8(4.8)$ K. The positive sign of the Curie–Weiss temperature evidences for the ferromagnetic interactions between the copper paramagnetic centres. Another indication of the ferromagnetic interactions is the temperature behaviour of the product of temperature and integrated intensity. This quantity is proportional to the effective magnetic moment of the CuHM complex. On decreasing the temperature, the effective magnetic moment increases (Fig. 5, lower panel).

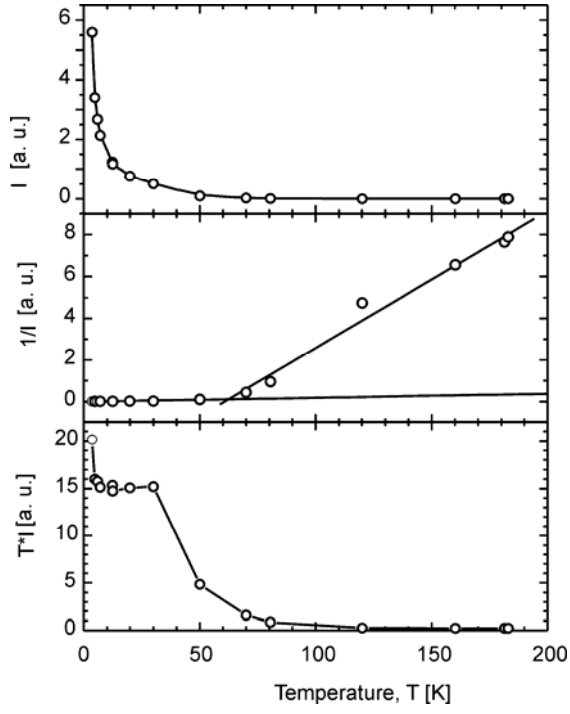

Fig. 5. Temperature dependence of the integrated ESR intensity of the CuHM complex (top panel), the reciprocal integrated intensity (middle panel), and the product of temperature and the integrated intensity (lower panel)

The experimental ESR spectrum of the CuHM complex taken at each temperature was decomposed into three Lorentzian components, and the ESR parameters of each component (the resonance field H_{res} and the peak-to-peak linewidth ΔH_{pp}) have been determined by the least-square fitting. The temperature variation of these parameters is presented in Fig. 6. A closer inspection of Fig. 6 allows to divide the temperature behaviour of magnetic properties of the CuHM complex into two ranges: a high temperature range ($T > 50$ K) and the low-temperature range ($T < 50$ K). In the high temperature range, the changes of resonance fields and linewidths of all three components are very small, if any, and in the low temperature range these parameters are subject

to significant variations. In general, the resonance fields of the components decrease as the temperature is decreased but their linewidths show a more complicated behaviour. The linewidth of the high-field component displays a rapid increase as the temperature is decreased (from 140 Gs at 50 K to 200 Gs at 10 K). It is interesting to note that the behaviour of linewidths of the middle- and low-field components is the same in the high-temperature range, while in the low-temperature range the lines behave oppositely. Shifting of the resonance fields to lower magnetic fields with decreasing temperature indicates on build-up of an internal magnetic field.

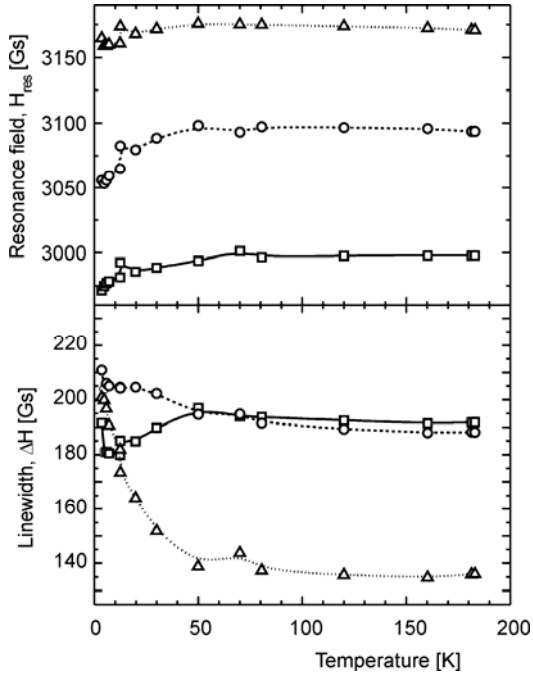

Fig. 6. Temperature dependence of the ESR parameters (resonance field H_{res} – upper panel, peak-to-peak linewidth ΔH – lower panel) of the three components constituting the resonance signal of the CuHM complex

The ESR linewidth in magnetic insulators is usually decomposed into noncritical and critical parts:

$$\Delta H = \Delta H(\infty) + \Delta H_{crit}(T) \tag{2}$$

The first term describes the spin–spin interactions in the high-temperature paramagnetic regime, where spins are uncorrelated. In concentrated paramagnetic systems, a constant contribution to the ESR linewidth is determined mainly by the isotropic exchange narrowing effect, magnetic and structural in homogeneities, and anisotropic spin–spin interactions like, e.g., dipole–dipole interactions and anisotropic exchange [19].

The second term defines an additional contribution to ΔH appearing at low temperatures, when the long-range magnetic order is approached. It is caused by fluctuations of the staggered magnetization in the short-range ordered state. These enhance the spin–spin relaxation rate $1/T_2$ and, consequently, additionally broaden the ESR line [20].

All the above presented results of the ESR study indicate the existence of two types of bulk paramagnetic centres in the investigated sample. There is a ferromagnetic interaction operating in both centres, but with different strengths, which is reflected in different values of the Curie–Weiss temperatures. Although the presence of ferromagnetic interaction has been established, no long-range ferromagnetic order has been observed in the investigated temperature range $T > 4$ K. The behaviour of the high-field component in the low-temperature range points to approaching the long-range ferromagnetic order at $T < 4$ K. A comparison of the published magnetic properties of malonato-bridges copper complexes with recorded ESR behaviour (Fig. 6) suggests that a copper(II) dimer complex may be present in our sample. The coexistence of the monomer and dimer copper(II) complexes would also explain the observed temperature change of the integrated ESR intensity. The low-temperature behaviour of the investigated sample would thus be determined by the copper dimer phase.

The literature data shows that 95% of copper(II) dimers exhibit an antiferromagnetic coupling, but in malonato-bridged metallic complexes, the ferromagnetic coupling is more frequent [8]. The simplest compound with dinuclear copper(II) of this type is $[Cu(H_2O)_4][Cu(mal)_2(H_2O)_2]$. The neutral dinuclear entity consists of a diaquabis(malonato)-cuprate(II) anion and a tetraaquacopper(II) cation connected through a carboxylato group. The environment of the chelated copper(II) ion is octahedral, whereas the coordination of the other is square pyramidal [1]. In square, pyramidal and octahedral environments, the magnetic orbital at each copper(II) atom is defined by short equatorial (or basal) bonds, and it is of the $d_{x^2-y^2}$ type with possible admixture of the d_{z^2} orbital in the axial position. In $[Cu(H_2O)_4][Cu(mal)_2(H_2O)_2]$ dimer, the carboxylate couples a $d_{x^2-y^2}$ magnetic orbital of Cu(1) with a d_{z^2} nonmagnetic orbital of Cu(II), the latter being orthogonal to the former. This kind of coupling (basal-apical or equatorial-axial) is found in many compounds and is always ferromagnetic. The intradimer coupling constant for the $[Cu(H_2O)_4][Cu(mal)_2(H_2O)_2]$ dimer is $J = 1.8$ cm^{-1} and the thermal dependence of its magnetic moment shows a significant increase below 50 K [1]. The presence of copper dimers in the sample is very probable the more so as this phase crystallizes in the same chemical and physical conditions as the monomer phase.

4. Conclusions

In conclusion, it has been shown that the investigated sample is magnetically inhomogeneous and consists mostly of a mixture of the $Cu(mal)_2(H_2O)_2$ monomer and

$[Cu(H_2O)_4][Cu(mal)_2(H_2O)_2]$ dimer copper(II) complexes. Moreover, there is about 1.5% of other spurious phases. Both dominating constituents showed strong ferromagnetic interactions, but no long-range order above 4 K.

References

[1] PASAN J., DELGADO F.S., RODRIGUEZ-MARTIN Y., HERNANDEZ-MOLINA M., RUIZ-PEREZ C., SANCHIZ J., LLORET F., JULVE M., Polyhedron, 22 (2003), 2143.

[2] RODRIGUEZ-MARTIN Y., RUIZ-PEREZ C., SANCHIZ J., LLORET F., JULVE M., Inorg. Chim. Acta, 318 (2001), 159.

[3] RODRIGUEZ-MARTIN Y., HERNANDEZ-MOLINA M., DELGADO F.S., PASAN J., RUIZ-PEREZ C., SANCHIZ J., LLORET F., JULVE M., Cryst. Eng. Comm., 4 (2002), 522.

[4] LENSTRA A.T.H., KATAEVA O.N., Acta Cryst. B, 57 (2001), 497

[5] FILIPPOVA I.G., Moldavian J. Phys. Sci., 1 (2002), 87

[6] NAUMOV P., RISTOVA M., SOPTRAJANOV B., DREW M.G.B., NG S.W., Croatica Chem. Acta, 75 (2002), 701.

[7] TOWLE D.K., HOFFMANN S.K., HATFIELD W.E., SING P., CHAUDHURI P., Inorg. Chem, 27 (1988), 394.

[8] RUIZ-PEREZ C., RODRIGUZ-MARTIN Y., HERNANDEZ-MOLINA M., GELGADO F.S., PASAN J., SANCHIZ J., LLORET F., JULVE M., Polyhedron, 22 (2003), 2111.

[9] CHAWLA S.K., ARORA M., NATTINEN K., RISSANEN K., YAKHMI J.V., Polyhedron, 23 (2004), 3007.

[10] OLDHAM C., [in:] *Comprehensive Coordination Chemistry*, G. Wilkinson, R.D. Gillard, J.A. Mcclevarty (Eds.), Vol. 2, Pergamon Press, Oxford, 1987, p. 435.

[11] LEVSTEIN P.R., CALVO R., Inorg. Chem., 29 (1990), 1581.

[12] RUIZ E., Inorg. Chem., 212 (1993), 115.

[13] PLOQUIN J., Bull. Soc. Chim. France, 18 (1951), 757.

[14] DUBICKI L., HARRIS C.M., KOKOT E., MARTIN R.L., Inorg. Chem., 5 (1966), 93.

[15] SIERON L., Acta Cryst., 60 (2004), 297.

[16] ASAI O., KISHITA M., KUBO M., J. Phys. Chem., 63 (1959), 96.

[17] RAJAN R., J. Chem. Phys., 37 (1962), 460.

[18] DIETZ R.E., MERRITT F.R., DINGLE R., HONE D., SILBERNAGEL B.G., RICHARDS P.M., Phys. Rev. Lett., 26 (1971), 1186.

[19] ABRAGAM A., BLEANEY B., *Electron Paramagnetic Resonance of Transition Ions*, Oxford University Press, Oxford, 1970.

[20] HUBER D.L, Phys. Rev. B, 6 (1972), 3180.

Received 9 September 2005
Revised 23 November 2005

Materials Science-Poland, Vol. 24, No. 4, 2006

Analysis of the process of ozone generation and micro-channel intensity distribution by the discharge analysis method

T. CIEPLAK[1*], C. YAMABE[2], J. M. OLCHOWIK[1], J. OZONEK[1]

[1]Lublin University of Technology, Nadbystrzycka 38, 20-618 Lublin, Poland

[2]Saga University, Saga 840, Japan

Growing range of ozone application followed by the increase of its production makes the problem of optimization of the process of ozone synthesis very significant from the viewpoint of energy consumption. Ozone, using silent discharge method, is mostly generated in the micro-discharge, however the other micro-channel also decomposes it. In order to take advantage of the whole discharge area, the micro-discharges should be distributed as uniformly as possible. Conventional energy sources use coal or oil as fuel. In some cases, it is not possible to reach power lines. From the other point of view, application of traditional power sources causes pollution of environment. To get the ozone generation process as clean as possible and also effective, a plate ozonizer with PV modules was used.

Key words: *ozone generation; silent discharge; solar energy*

1. Introduction

Ozone generators are chemical reactors identified mainly as heat exchangers. The efficiencies for the generation process alone do not exceed 20% at optimal conditions with oxygen as feed gas. Ozone formation is a two-step reaction, which starts with the dissociation of O_2 molecules by the electrons in a micro-discharge:

$$e + O_2 \xrightarrow{k_1} 2O + e \tag{1}$$

The second step describes a three-body reaction:

$$O + O_2 + M \xrightarrow{k_2} O_3 + M \tag{2}$$

where M is a third collision partner which could be atoms of O, molecules of O_2 or O_3.

*Corresponding author, e-mail: t.cieplak@pollub.pl

It seems that one of possible ways to increase the efficiency of synthesis of ozone is to apply an electrode rotation system to the ozonizer. It is known that such a system has a positive effect on the ozone generation process [1–3].

The main feature of silent discharge is that the presence of dielectrics leads to the formation of a large number of micro-discharges. Ozone is mostly generated in the micro-discharge, however the other micro-channel also decomposes it. After O_3 formation, the region of ozone concentration has the same geometrical distribution as the atomic oxygen concentration that is the micro-discharge volume of about r = 100 μm radius. From that region, ozone diffuses to the background with the time $\tau \approx 1.6$ ms.

$$\tau \approx \frac{\pi r^2}{D} \tag{3}$$

The diffusion coefficient of O_3 in O_2 equals $D \approx 0.2$ cm^2·s^{-1}. Applying electrode rotation we can speed up the slowest (see Eq. (3)), third phase of the ozone generation process – ozone diffusion into background. In order to take advantage of the whole discharge area, the micro-discharges should be as far as possible uniformly distributed [4]. We presume that with the electrode rotation we can influence the discharge, bringing it into a more homogeneous form. Described later research employing the method of discharge analysis shows that with higher electrode rotational speed the discharge does become more uniform.

2. Experimental

2.1. Construction of the ozonizer

The main ozonizer system (Fig. 1) consists of an enclosed chamber (later referred to as housing), electrodes, dielectrics and connecting elements. In the presented setup, electrode cooling systems as well as gas cooling systems were not used. Each of the above-mentioned systems was enclosed using the polyacrylate housing. The housing can be separated into two parts, each one with a diameter of 150 mm and the thickness of about 50 mm. The parts of the housing were connected by eight holding down bolts. The electrode system was placed inside the ozonizer body. This system can be partitioned into two electrodes and one dielectrics layer. In the presented part of the research, a glass plate with the thickness of 0.75 mm and the diameter of 80 mm covers the grounded electrode. The upper, high voltage electrode was also used as a part of the gas supply subsystem. In this electrodes configuration, the discharge activity area equals to 1.94×10^3 mm^2. The synthesis gas was brought into the ozonizer centrally through the electrode and four pipes located outside the electrode carried out the product. The research into the parameters of the ozonizer with the rotating electrode required variable discharge gap spacing. The construction of the high voltage electrode made this possible. The variation in gap spacing ranges from 0.5 mm to 3 mm.

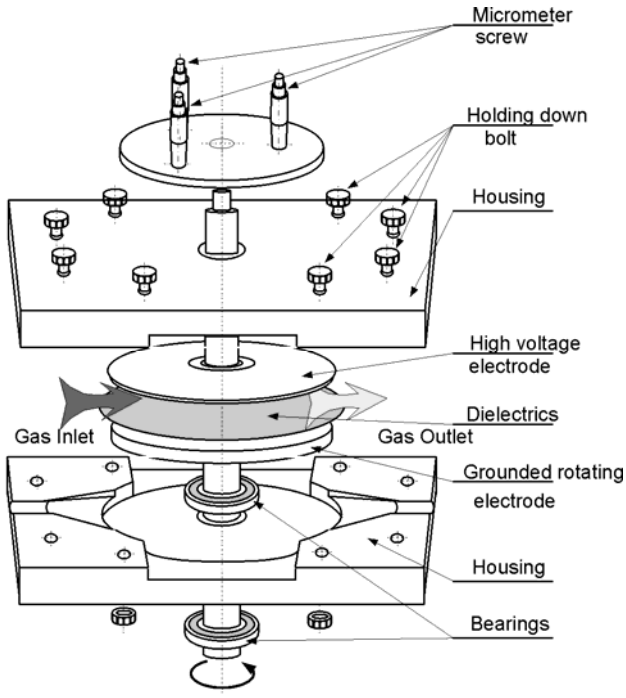

Fig. 1. The main ozonizer diagram

A solar system was used as a power supplying subsystem. The hybrid solar-thermal system (Fig. 2) consisting of 20 photocollectors of "Hevalex" KS 2000 S type and 16 photomodules of "Solara" SM 400 S type was installed on the roof of the Department of Management and Fundamentals of Technology (Lublin University of Technology, Lublin, Poland). A general purpose of the operating system was to provide the thermal system of the department buildings with the electricity generated in PV modules, as well as to ensure the regressive circulation of working liquid in photocollectors, which results in the stabilization of the operating conditions of the solar cell.

Fig. 2. Solar system installed on the roof of the assembly hall of Lublin University of Technology

PV modules can capture more light if they are adapted to rotate around either North-South (NS) or East-West (EW) axes. Rotation around the EW axis allows the

module to compensate the changes of the seasonal sun altitude, while rotation around the NS direction makes it possible to align the module with the daily sun movement. That capability of rotation of the PV modules was achieved by a solar tracking system administered by the PC and powered also by the electricity from the PV modules. This "following-the-sun" system ensures that the flat solar module is faced to the sun for all the time and, consequently, the amount of solar irradiation reaching its surface is increased in comparison with the stationary module.

2.3. Discharge photography method

The setup shown in Figure 3 was assembled in order to get more information about discharges during ozone generation in the rotating electrode ozonizer system. This system was based on the Lichtenberg discharge photographic method. In our setup, a photographic plate was replaced by a photographic paper.

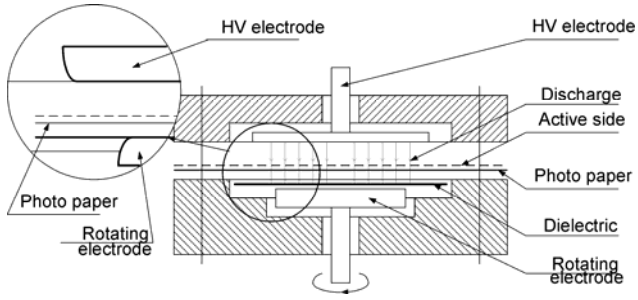

Fig. 3. Scheme of the discharge photography method

Figure 3 shows how the paper was connected to the ozonizer body. Such a placement allowed investigating the influence of the electrode rotation on the discharge conditions. In the other case, when the paper was placed directly on the dielectric, the conditions of gas flow were examined. The paper was sensitive to white light, which enabled recording the light emitted by excited molecules of gas. As a matter of fact, the sensitivity of the paper was lower than that of the photographic plate. The time of the paper exposition was longer and ranged from 2 s to 0.5 s. The time of exposition mainly depended on the kind of gas. The clearest photos were obtained when the exposition times were 2 and 0.5 sec in oxygen and air, respectively. It results from the exposition times that the light emitted by nitrogen was several times more intensive than that emitted by oxygen.

3. Results and discussion

Because of a large number of analyzed photographs, the traditional methods of their evaluation hardly permitted distinguishing the areas with similar light intensities,

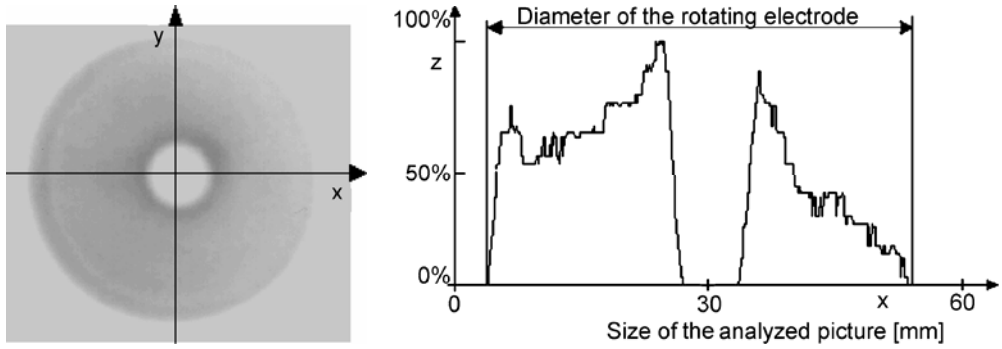

Fig. 4. Discharge picture with the analysis of discharge intensity

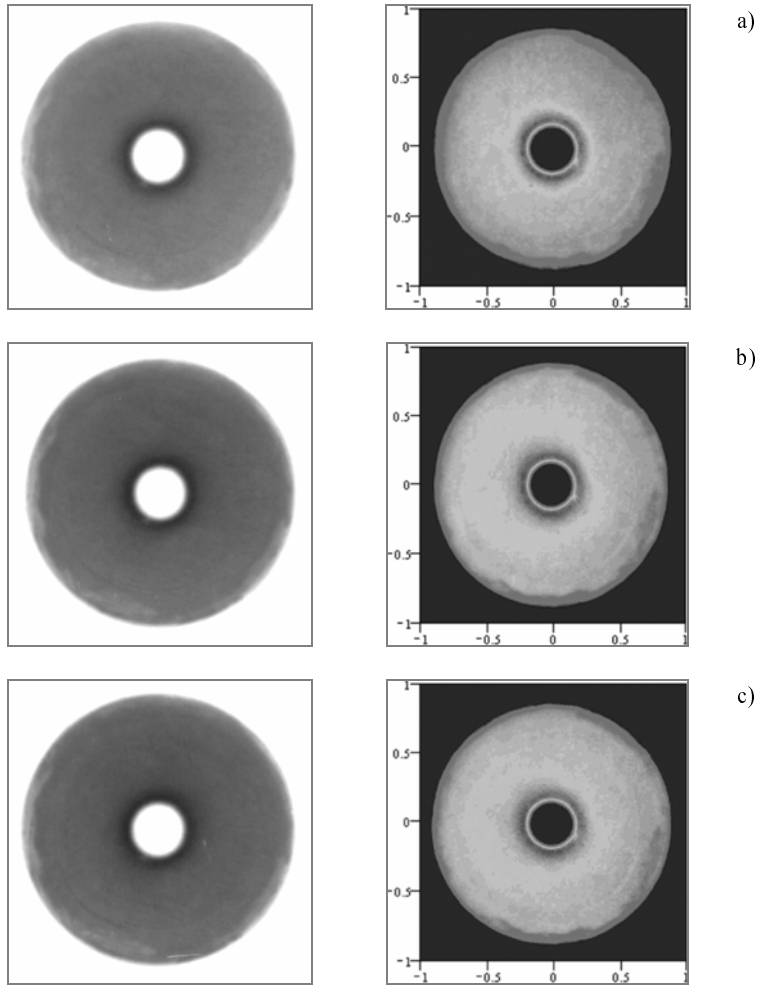

Fig. 5. Discharge photo- and computer analysis. Gas gap – 0.5 mm; gas – oxygen, flow – 1.5 dm^3/min, voltage – 9.0 kV, dielectric – glass (0.75 mm), rotational speed: a) 0 rpm, b) 1200 rpm; c) 1600 rpm

therefore, the developed pictures were exposed to a computer scanning (Fig. 4). As a result, a number of colour graphs (presented here as black-white prints) of scanned pictures were obtained, examples of which are shown in Fig. 5. In Figure 5, a collection of black points represents the areas with no discharge. Gray scale changes from gray to white, corresponding to areas containing from a low (gray) to a very high (white) intensity of discharge. Comparing the images of discharge obtained under similar conditions (the electrode rotational speed was the only variable) some differences between them could be observed. In the case of the rotating electrode, almost the whole electrode area (the electrode outer edge shown as a light circle) was covered by discharge. In some areas discharge was weak or even not observed. The filling of electrode area by discharges was closely related to rotational speed. The homogeneity of the discharges increased with the rotational speed. In the case of a non-rotating electrode, the area of discharge was smaller than that of the electrode. Comparing these cases (rotating and non-rotating) it can be said that the discharge volume was utilized more effectively when the rotating electrode was used.

4. Conclusions

The efficiency of ozone generation in the rotating-electrode ozonizer with rotation 1200 rpm was about 20% higher than that without rotation at oxygen gas flow of 3.0 dm^3/min (Fig. 6).

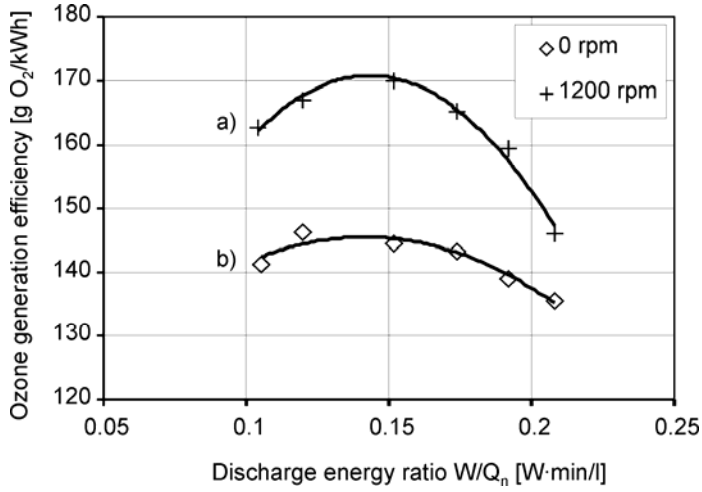

Fig. 6. Ozone generation efficiency for various electrode rotational speeds vs. discharge energy ratio: a) setup 1, gas gap: 1.5 mm, flow: 1.5 dm^3/min b) setup 2, gas gap: 3.0 mm, gas flow rate: 3.0 dm^3/min

No effect of electrode rotation on average discharge power was observed. Average discharge current was not significantly affected by the electrode rotation. Ozone gen-

eration efficiency significantly depends on the discharge gap spacing and increases in the narrow gap distance.

Acknowledgements

This work is supported by a Polish Ministry of Science and Information, Society Technologies project no. 3T09D05228, as well as a part of this work was supported by a Grant-in-Aid of the Ministry of Education, Science, Sports and Culture, Japan.

References

[1] NOMOTO Y., OHKUBO T., ADACHI T., 2nd International Symposium on High Pressure, Low Temperature Plasma Chemistry (Hakone II), Kazimierz, Poland, 1989, p. 45.
[2] HORINOUCHI T., HAYASHI T., JYO S., 7th Annual Conference Ozone Science and Technology, Okayama, Japan, 1998, p. 57.
[3] CIEPLAK T., YAMABE C., Appl. Plasma Sci., 5 (1997), 57.
[4] PIETSCH G.J., Regional Conference on Ozone Generation and Application to Water and Wastewater Treatment, Moscow, Russia, 1998, p. 13.

Received 9 September 2005
Revised 9 November 2005

Materials Science-Poland, Vol. 24, No. 4, 2006

Effect of calcination and structural additives on the EPR spectra of nanocrystalline cobalt oxides

N. GUSKOS[1,2*], J. TYPEK[2], M. MARYNIAK[2], G. ŻOŁNIERKIEWICZ[2], M. PODSIADŁY[3], W. ARABCZYK[3], Z. LENDZION-BIELUŃ[3], U. NARKIEWICZ[3]

[1]Solid State Physics, Department of Physics, University of Athens, Panepistimiopolis, 157 84 Zografos, Greece

[2]Institute of Physics, Szczecin University of Technology, al. Piastów 17, 70-310 Szczecin, Poland

[3]Institute of Chemical and Environment Engineering, Szczecin University of Technology, Pułaskiego 10, 70-322 Szczecin, Poland

Samples of nanocrystalline Co_3O_4 were prepared at various calcination temperatures and with various amounts of structural additives (CaO and Al_2O_3). The samples were characterized by X-ray diffraction. The average size and size distribution of nanoparticles have been calculated. Electron paramagnetic resonance (EPR) spectra of the samples were recorded at room temperature. The spectra have been attributed to divalent cobalt ions. Samples calcinated at higher temperatures showed an almost symmetrical, intensive EPR line. Temperature of calcination determined the character of the EPR spectra. The intensities of EPR spectra depended on the presence of CaO and Al_2O_3 additives.

Key words: *EPR; cobalt oxide*

1. Introduction

Preparation, characterization and application of some transition metal oxides, such as cobalt oxide, have attracted an increasing interest due to their physical properties as well as rich technological applications. Cobalt oxides, due to their magnetic and catalytic properties, are used in a wide range of applications in various fields of industry, including catalyst, pH sensors, gas sensors and magnetic materials [1–6]. Many methods have been used in recent years to prepare Co_3O_4: sol-gel route [7, 8], reduction-oxidation route [9], cobalt salt decomposition [10–13], chemical vapour deposition [14], electrochemical and sonochemical synthesis [15] and pulsed laser deposition [16]. In particular, methods of obtaining nanocrystaline Co_3O_4 are very important, because the properties of Co_3O_4 are highly sensitive to the particle sizes as well as to

*Corresponding author, e-mail: ngouskos@phys.uoa.gr

the concentrations of defects or other phases. Crystals of the above compound with a normal spinel structure (similar as Fe_3O_4) form two sublattices with different valences of cobalt ions, one with cobalt(II) ions in the ground state $^4A_2$ (high spin, $S = 3/2$) in tetrahedral A sites and the other with cobalt(III) ions in the ground state $^1A_{1g}$ (low spin, non-magnetic, $S = 0$) occupying octahedral local lattice [17, 18]. The high-spin state could be stabilised by cation vacancies in the B sublattice. The concentration of oxygen on the surface of Co_3O_4 could be different from that in the bulk [19, 20]. In transition metal compounds, in particular those containing iron(II) and cobalt(III), spin-state transitions between the low-spin- and the high-spin states occur. Electron paramagnetic resonance (EPR) is one of the most effective methods to study the influence of defects on the physical properties of Co_3O_4 [21, 22]. The conditions of preparation have a strong influence on the transition to disorder and magnetic ordered state [23].

The aim of this report is the EPR study of nanocrystalline Co_3O_4 obtained at various calcination temperatures and with various concentrations of structural additives (CaO and Al_2O_3). The differences in the EPR spectra have been correlated with the presence of additives and calcination temperatures.

2. Experimental

The starting materials were $Co(NO_3)_2 \cdot 6H_2O$, $Ca(NO_3)_2 \cdot 4H_2O$, $Al(NO_3)_3 \cdot 9H_2O$ and 25% solution of NH_4OH. The nitrate salts of cobalt, calcium and aluminium were dissolved in distilled water and NH_4OH was added. Two kinds of cobalt hydroxides were precipitated: one with lower concentrations of promoters (samples P) and other with higher concentration of promoters (samples P′). The precipitated cobalt hydroxides were washed with distilled water and dried at 70 °C to obtain the precursor. The precursor P was calcined at 500 °C for 1 h and at 900 °C for 3 h to prepare Co_3O_4 nanoparticles used to obtain samples P1 and P3, respectively. The precursor P′ was calcined at 900 °C for 3 h and was used to prepare samples P2. Co_3O_4 was characterized by X-ray diffraction (XRD, Philips, X'Pert Pro equipment, $Cu_{K\alpha}$ radiation).

The average crystal size of the nanoparticles was calculated from diffraction peak half-widths using the Scherrer formula. Grain size distribution has been calculated by FW(1/5)/(4/5) method. The concentration of CaO and Al_2O_3 in Co_3O_4 was determined using an inductively coupled plasma-atomic emission spectroscopy (ICP-AES, JY 238 Ultrace equipment from Jobin Yvon). The concentration of structural additives in samples P1 and P3 was the same, while sample P2 contained a greater amount of promoters (Table 1).

The EPR measurements were carried out with a conventional X-band ($\nu = 9.43$ GHz) Bruker E 500 spectrometer with 100 kHz magnetic field modulation. The samples in the form of loose powders, each containing around 30 mg of the substance, were placed into 4 mm diameter quartz tubes.

3. Results and discussion

The concentrations of structural additives (CaO and Al_2O_3) in the samples, as well as mean crystallite sizes determined from the Scherrer formula and from the size distributions (Fig.1), are given in Table 1. As could be expected, the calcination temperature has a crucial influence on the mean crystallite size. Sample P1 calcined at 500 °C consists of crystallites with the mean crystallite size of about 56 nm, while in samples P2 and P3, calcined at 900 °C, the crystallite sizes are twice larger.

Table 1. The concentrations of structural additives and the crystallite diameters (*d* and *D*). The parameter σ is the dispersion of crystallite sizes

Sample	Calcination	Promotor concentration		Scherrer analysis	FW(1/5)/(4/5) analysis	
		CaO [wt. %]	Al_2O_3 [wt. %]	*d* [nm]	*D* [nm]	σ [nm]
P1	500 °C (1h)	1.2	2.1	56	48	16
P2	900 °C (3 h)	1.7	2.3	>100	–	–
P3	900 °C (3 h)	1.2	2.1	>100	–	–

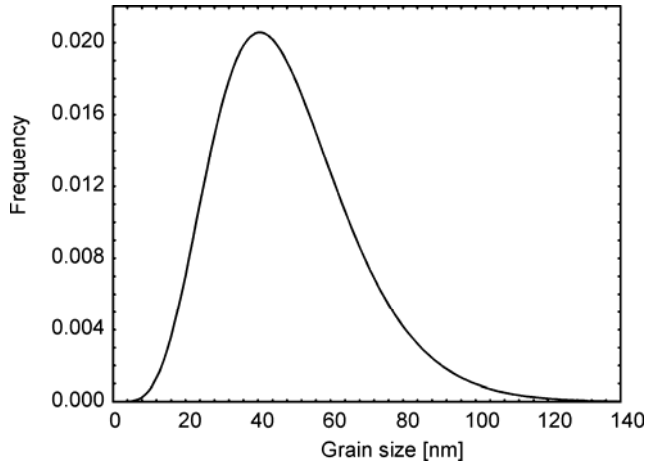

Fig. 1. Grain size distribution of Co_3O_4 (sample P1)

It was also possible to calculate the grain size distribution in sample P1 by the FW(1/5)/(4/5) method. The detailed mathematical procedure is presented elsewhere [24, 25]. The average grain size calculated by this method is 48 nm and is smaller than the value calculated by the Sherrer's method (56 nm). The dispersion of crystallite sizes σ is 19 nm. The grain size distribution is presented in Fig. 1. It could be seen that the majority of the Co_3O_4 crystallites have grain sizes in the range of 15–90 nm. The maximum of the distribution is observed at 40 nm.

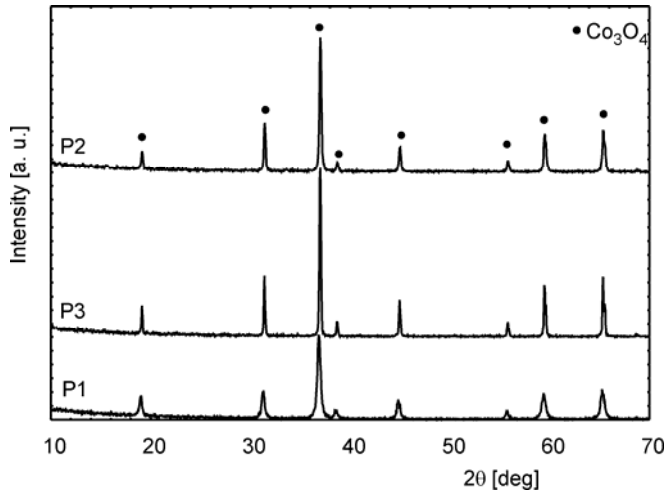

Fig. 2. XRD patterns for the three investigated samples of Co_3O_4 particles

The XRD patterns of Co_3O_4 particles after calcination at various temperatures for the studied samples are shown in Fig. 2. In all the samples the lines from the Co_3O_4 phase dominate the diffraction patterns. Co_3O_4 crystallises in the cubic system, space group $Fd\bar{3}m$, with the lattice parameter $a = 8.084$ Å.

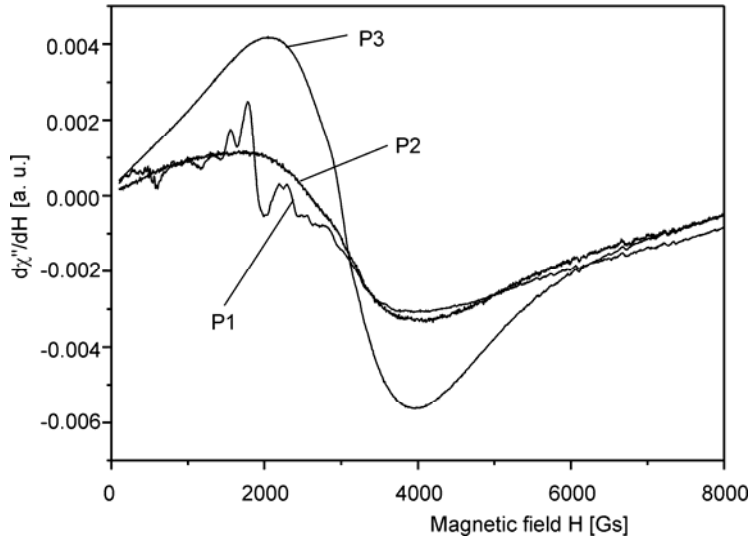

Fig. 3. EPR spectra of the investigated samples at room temperature

Figure 3 presents the EPR spectra of all investigated samples recorded at room temperature. Significant differences in the spectra have been observed between three samples. For the precursor P no EPR signal was recorded while the precursor P′ has shown the EPR spectrum of cobalt(II) ions with a hyperfine structure. The EPR spec-

trum of sample P1 is a superposition of contributions from two paramagnetic centres, one displaying the hyperfine structure and the other producing a very broad line. The amount of structural additives is greater for sample P2 than for sample P3 (Table 1) but the EPR spectrum is more intense for sample P3. An intense, slightly asymmetric line is recorded for both samples P2 and P3 and the resonance line could be fitted by the Lorentzian function including the tail of the resonance absorption at negative fields due to the linearly polarized radio frequency field.

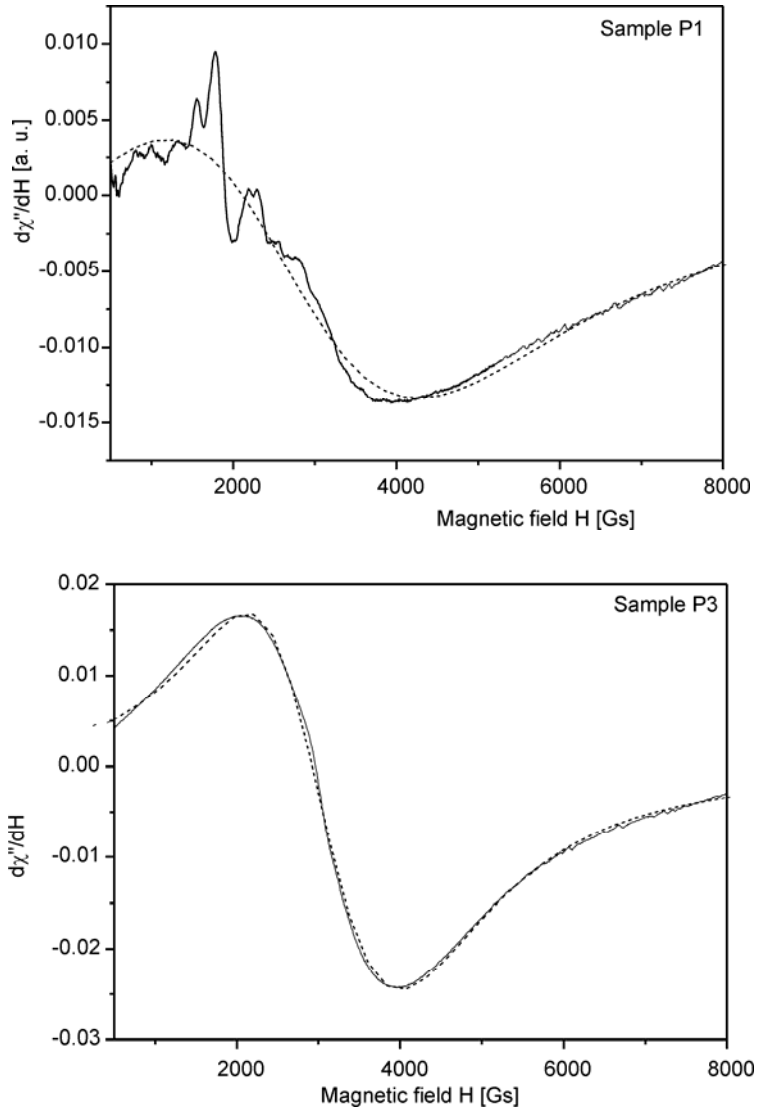

Fig. 4. The fitted (dotted lines) and experimental (solid lines) EPR spectra of sample P1 and sample P3

The results of fitting the EPR spectra of samples P1 and P3 are shown in Fig. 4. In both cases, only the Lorentzian function for the EPR line centred at higher magnetic field has been used. A reasonable fit is obtained for samples P3 and P2 with the resonance line centred at $g = 2.22(1)$ and $g = 2.71(1)$, having the linewidth $\Delta H = 1630(9)$ Gs and $\Delta H = 2070(9)$ Gs, respectively. The EPR line at higher magnetic field for sample P1 is centred at $g = 2.52(1)$ with the linewidth $\Delta H = 1810(10)$ Gs. An additional EPR spectrum with a hyperfine structure appeared in sample P1 at $g_{\text{eff}} = 3.5(1)$.

While cobalt(II) ions at the tetragonal sites in the spinel lattice should produce a single EPR line with the Lorentzian lineshape and with the g-factor of about 2.25 [22], often strongly asymmetric lines with effective g-values $4 > g_{\perp} > 3.5$ and $g_{\parallel} \approx 2$ are observed. The linewidth depends very strongly on the sample thermal preparation processes and increases with decreasing calcination temperature [22]. In this system, the quenching conditions are very important for the very existence of the cobalt(II) EPR signal. A slow cooling of the sample results in the disappearance of the EPR spectrum while doping by other ions could essentially change the intensity of the EPR signal [21].

Low annealing temperature of the sample results in the EPR spectrum that is a superposition of signals from two different paramagnetic centres (sample P1 – Fig. 3) while high annealing temperature of the sample produces the EPR spectrum consisting of one very broad line. In all three cases, the EPR spectra could be regarded as originating from two kinds of paramagnetic entities, suggesting that during the synthesis two kinds of paramagnetic centres were formed. The structural additives could give two different additional phases (Table 1) and they contribute to the EPR spectra of cobalt(II) ions. For low concentration of additives and low annealing temperature (sample P1), the EPR spectrum is composed of two much different paramagnetic centres of cobalt(II) ions (Fig. 4a), while for high annealing temperature mainly one very broad line is observed. At higher concentration of structural additives (sample P3), the EPR spectrum is dominated by a very intense line which probably conceals the other weaker line (Fig. 4b). It could be considered that the EPR linewidth is determined by the cobalt(II) ions spin relaxation time rather than the presence of, e.g., dipolar and isotropic exchange interactions that could produce an exchange narrowed line with the Lorentzian lineshape in the centre of the line [26, 27]. The peak-to-peak width of the resonance line would be approximately given by:

$$\Delta H_{pp} = \frac{2}{\sqrt{3}} \frac{M_2}{H_{ex}} \tag{1}$$

where H_{ex} is the exchange field and M_2 is the second moment of the line, with M_{2d} being the dipole-dipole interaction, M_{2hf} – the hyperfine structure interaction and M_{2f} – the fine structure interaction. These interactions, for a sample in a powder form, could be related by the following formulas:

$$M_{2d} = \frac{3}{4} S(S+1) g^2 \mu_B^2 \sum_j r_{jk}^{-6} \tag{2a}$$

$$M_{2hf} = \frac{1}{3} A_{hf}^2 I(I+1) \tag{2b}$$

$$M_{2f} = \frac{1}{5} \left(4S(S+1) - 3\right) D^2 \tag{2c}$$

The dipole-dipole interactions between magnetic moments of cobalt ions was estimated to have the value of $M_{2d} = 2.6 \times 10^6$ Gs^2 and the hyperfine interaction $M_{2hf} \approx 5.25 \times 10^4$ Gs^2 with $H_{ex} \approx 3 \times 10^5$ Gs [22]. These two interactions (Eqs. (2a) and (2b)) could not explain the observed values of the linewidths in our spectra.

For cobalt(II) ions placed in a near tetrahedral surrounding, the main contribution to the linewidth arises from the splitting of the ground spin quartet due to the deviation of the local crystal fields from the cubic symmetry. Such a deviation should lead to the appearance of term $H_f = D\Sigma_i (S_{iz})^2$ in the spin Hamiltonian and the contribution to the second moment given by Eq. (2c). By the procedure described in Ref. [22], the following values of M_{2f} have been obtained: 4.15×10^8 Gs^2 for sample P3, 5.27×10^8 Gs^2 for sample P2 and 4.61×10^8 Gs^2 for sample P1. The EPR spectrum of tetrahedral cobalt(II) ions in Co_3O_4 is extremely sensitive to the disorder created in the bulk of the crystallites both by the bulk defects and the grain boundary layers, containing the part of the oxygen prevailing in excess of the stoichiometric amount [22]. As is well known, the integrated intensity of the EPR spectrum, proportional to the product of linewidth ΔH and line amplitude I, is directly related to the number of paramagnetic centres. Thus comparison of integrated intensities of the investigated samples could give information on relative influence of the annealing temperature and the structural additives on the amount of paramagnetic centres. The values of the relative ratio of the EPR integrated intensities

$$\frac{\left(\Delta H_{P3}\right)^2 I_{P3}}{\left(\Delta H_{P1}\right)^2 I_{P1}} = 1.78 \quad \text{and} \quad \frac{\left(\Delta H_{P3}\right)^2 I_{P3}}{\left(\Delta H_{P2}\right)^2 I_{P2}} = 1.24$$

suggest an essential increase of the concentration of cobalt(II) ions in a deformed crystal field in sample P3.

4. Conclusions

The EPR spectra of Co_3O_4 samples strongly depend on the calcination temperature and on the concentration of structural additives. For the precursor P the EPR spectrum of cobalt(II) ions was not observed while for the precursor P′ an intense EPR spec-

trum of cobalt(II) with the hyperfine structure was recorded. An increase of concentration of structural additives (30% increase for CaO and 9% for Al_2O_3) increases the EPR integrated intensity of 1.24 times while higher annealing temperature increase by 1.78 the concentration of paramagnetic cobalt(II) in low symmetry of the crystal field. Two kinds of EPR spectra of cobalt(II) ions were observed: one without a hyperfine structure and the second one with a very broad line for sample P1.

References

[1] JANSSON J., PALMQVIST A.E.C., FRIDELL E., SKOGLUNDH M., OSTERLUND L., THORMAHLEN P., LANGER V., J. Catal., 211 (2002), 387.
[2] QINGWEN L., GUOAN L., YOUQIN S., Anal. Chim. Acta, 409 (2000), 137.
[3] YANG H., HU Y., ZHANG X., QIU G., Mater. Lett., 58 (2004), 387.
[4] HAYASHI E., IWAMATSU E., BISWAS M.E., SANADA Y., AHMED S., HAMID H., YONEDA T., Appl. Catal. A, 179 (1999), 203.
[5] MORALES U., CAMPERO A., SOLORZA-FERIA O., J. New Mat. Electr. Systems, 2 (1999), 89.
[6] MAKHLOUF S.A., J. Magn. Magn. Mater., 246 (2002), 184.
[7] SVEGL F., OREL B., GRABEC-SVEGL I., KAUCIC V., Electrochim. Acta, 45 (2000), 4359.
[8] BARRERA E.C., VIVEROS T.G., MORALES U., Renew. Energy, 9 (1996), 736.
[9] NI Y., GE X., ZHANG Z., LIU H., ZHU Z., YE Q., Mat. Res. Bull., 36 (2001), 2383.
[10] ARDIZZONE S., SPINOLO G., TRASATTI S., Electrochim. Acta, 40 (1995), 2683.
[11] FURLANETTO G., FORMARO L., J. Colloid Interface Sci., 170 (1995), 169.
[12] SATO M., HARA H., KURITANI H., NISHIDE T., Sol. Energy Mater. Sol. Cells, 45 (1997), 43.
[13] VERELST M., ELY T.O., AMIENS C., SNOECK E.,. LECANTE E., MOSSET A., RESPAUD M., BROTO J.M., CHAUDRET B., Chem. Mater., 11 (1999), 2702.
[14] GAUTIER J.L., RIOS E., GRACIA M., MARCO J.F., GANCEDO J.R., Thin Solid Films, 311 (1997), 51.
[15] VIJAYA KUMAR R., DIAMANT Y., GEDANKEN A., Chem. Mater., 12 (2000), 2301.
[16] KOSHIZAKI N., NARAZAKI A., SASAKI T., Scripta Mater., 44 (2001), 1925.
[17] WILL G., MASCIONANI N., PARRISH W., HART M., J. Appl. Cryst., 20 (1987), 394.
[18] SMITH W.L., HOBSON A.D., Acta Cryst. B, 29 (1973), 362.
[19] MARCUS-SAUBAT B., BEAUFILS J.P., BARBAUX Y., J. Chim. Phys., 83 (1986), 317.
[20] BELOVA J.D., ZAV'YALOV S.A., ROGINSKAYA Y.E., Russian J. Phys. Chem., 60 (1986), 140.
[21] STOYANOVA R., ZHECHEVA E., ANGELOV S., Mat. Chem. Phys., 26 (1990), 239.
[22] ANGELOV S., ZHECHEVA E., STOYANOVA R., ATANASOV M., J. Phys. Chem., Solids, 51 (1990), 1157.
[23] BRABERS V.A.M., BROEMME A.D.D, J. Magn. Magn. Mater., 104–107 (1992), 405.
[24] PIELASZEK R., J. Alloys Comp., 382 (2004), 128.
[25] PIELASZEK R., Ph. D. thesis, Faculty of Physics, Warsaw University, 2003.
[26] VAN VLECK J.H., Phys. Rev., 74 (1948), 1168.
[27] ANDERSON P.W., WEISS P.R., Rev. Mod. Phys., 25 (1953), 269.

Received 9 September 2005
Revised 24 November 2005

Materials Science-Poland, Vol. 24, No. 4, 2006

Processing of porous structures of $YBa_2Cu_3O_{7-\delta}$ High-temperature superconductor

P. FIERTEK*, W. SADOWSKI

Gdańsk University of Technology, Faculty of Applied Physics and Mathematics,
ul. Narutowicza 11/12, 80-952 Gdańsk, Poland

Technological aspects of fabrication of the $YBa_2Cu_3O_{7-\delta}$ ceramics with preparation of open pores are presented. The highest porosity of the sample with open pores and suitable mechanical properties was performed using $C_{12}H_{22}O_{11}$ (sugar sucrose) as the supplementary phase.

Key words: *$YBa_2Cu_3O_{7-\delta}$; open porous structure*

1. Introduction

The search for applications of superconductive ceramics is mainly focused on two groups of materials: thin films and bulk ceramics. The main aim of this research to assure their proper use and to optimize parameters such as: critical current, critical magnetic field and critical temperature [1–4]. Superconductive ceramics can also be interesting material for other practical applications. Materials with porous structure can be used, for example, as gas filters [5] or as composites with superconductive matrices.

Despite many papers concerning the syntheses of $YBa_2Cu_3O_{7-\delta}$ [3, 4, 6–8], fabrication of open-pore superconductive ceramics is not well known yet [9, 10]. Therefore, various technological aspects of fabrication of $YBa_2Cu_3O_{7-\delta}$ open-pore ceramics have been studied. The basic problem is using an adequate supplementary filler in order to obtain a homogeneous localization of free spaces. Filling should not destroy the superconductive properties. It should also enable fabrication of samples with good mechanical properties. Various materials being used as supplementary phases, for example: wax, graphite or polyurethane foams, the best results were obtained using the crystalline sucrose as a filler.

* Corresponding author, e-mail: pafiertek@wp.pl

2. Experimental

2.1. Sintering granules of $YBa_2Cu_3O_{7-\delta}$

During the initial stage of this research, in order to obtain an open-pore structure, granules of $YBa_2Cu_3O_{7-\delta}$ were sintered so as to preserve pores that had been formed between not pressed granules. Superconductive $YBa_2Cu_3O_{7-\delta}$ material was prepared using the standard method of powders sintering. It was then ground and separated into three fractions: 0.2–0.4 mm; 0.4–0.63 mm and 0.63–0.8 mm. The sintering proceeded in the temperature range from 940 to 1100 °C and the time of sintering changed from 10 min to 3 h. The best results were obtained after sintering at 940 °C for 3 h (Fig. 1)

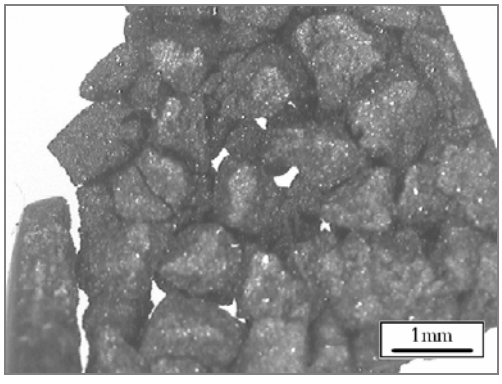

Fig. 1. Sample obtained by mixing $YBa_2Cu_3O_{7-\delta}$ granules of the size of 0.63– 0.8 mm, not pressed and sintered at 950 °C by 3h

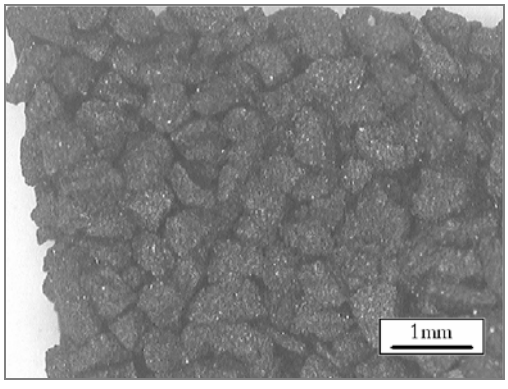

Fig. 2. Sample obtained by sintering $YBa_2Cu_3O_{7-\delta}$ granules filled with wax and slightly pressed

Generally, the obtained samples were either mechanically weak or containing a molten matrix. Therefore, the method was not reproducible. In order to improve the mechanical properties of the samples, it was modified by filling free spaces between granules in the matrix with liquid wax. After solidification of the filler, the sample was pressed and sintered to obtain intergranular bindings. The wax filler made possible a tight pressing of the granules without losing empty spaces between them. This resulted in fluidisation of the wax under high pressure and its outflow from the matrix. Nevertheless, weak pressing of the granules allowed one to obtain samples with open pores (Fig. 2). Unfortunately, they were not mechanically stable.

2.2. Fabrication of the $YBa_2Cu_3O_{7-\delta}$ porous ceramics by using poly(pyrrole imide) foams

Another way to obtain porous structure of the $YBa_2Cu_3O_{7-\delta}$ ceramics was described in [9,10]. Poly(pyrrolone imide) (PPI) foams were used as porous structure replicas. The authors presented two methods of preparing the porous structure. The first method consisted in a complete filling of the PPI foams, then they obtained negatives of the foams. The other method consisted in covering the structure of the PPI foams with $YBa_2Cu_3O_{7-\delta}$, then they obtained replica of PPI foams. Both methods required mixing of very finely ground superconductive with a liquid in order to obtain a suspension of an optimum viscosity. The next stage for both methods is burning out PPI and sintering $YBa_2Cu_3O_{7-\delta}$. In the present work, this stage (a slow heating) was carried out to ca. 400 °C. It should inhibit burning of PPI foam. Then the sample was sintered at 935 °C for 24 h. The difference between the methods described above consists in choosing a proper viscosity of the suspension and the method of filling with the foam. In the case of fabricating replica, a moderate viscosity of the suspension should be chosen in order to provide open pores in the soaked foam samples (Fig. 3). In the case of applying the foam as the supplementary filler, use of a thick suspension of $YBa_2Cu_3O_{7-\delta}$ was required to fill all free spaces within the foam.

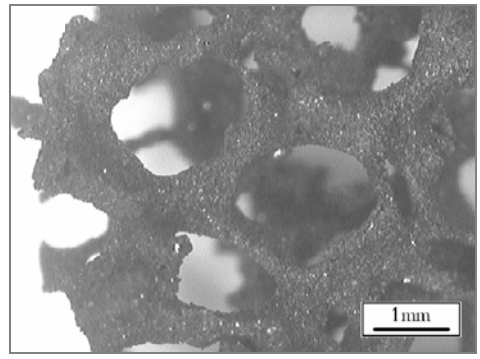

Fig. 3. A porous sample obtained by burning out PPI foams covered with $YBa_2Cu_3O_{7-\delta}$ suspension

The critical point of such technique of fabrication of open-pore ceramics was the preparation of the $YBa_2Cu_3O_{7-\delta}$ suspension of appropriate viscosity and also depositing a small amount of the suspension on the foam by soaking it. In order to obtain the required viscosity, the following liquids were applied: methanol, water, glycerine or their mixtures. Despite many attempts, the obtained samples were neither reproducible enough nor mechanically resistant, mainly due to the lack of pressing the $YBa_2Cu_3O_{7-\delta}$ ceramic before sintering them. Therefore the obtained samples were not suitable for a further material research.

2.3. Mixture of the $YBa_2Cu_3O_{7-\delta}$ granules and crystalline sucrose

The basic disadvantage of the previously described methods of preparation of open-pore structures was insufficient pressing of the samples or not pressing them

before the sintering stage. Because of this, the samples exhibited poor mechanical properties. In order to avoid such problems, a method consisting in mixing granules of the filler with granules of $YBa_2Cu_3O_{7-\delta}$ was elaborated. Such material was produced by the first method and additionally very strongly pressed before sintering the samples. The best results were obtained when applying the crystalline sucrose as a filler.

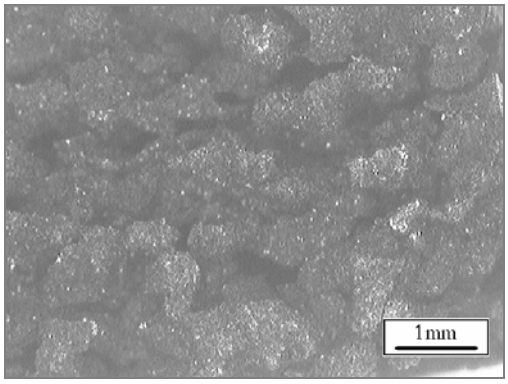

Fig. 4. The outer side of the porous sample $YBa_2Cu_3O_{7-\delta}$ and sucrose granules pressed at 700 MPa sintered at 935 °C by 36 h and oxidized at 475 °C by 36 h

In order to open pores, the filler was added in the amount necessary to obtain 50% and 60% volume fraction. Using such an amount of the filler assured the connection between granules of the filler and existence of open-pore system after sintering the mixture. The granules with the same size range were mixed. The mixtures were pressed up to 700MPa, slowly heated to 400 °C and sintered at 935 °C for 36 h. The method turned out to be well reproducible and gave the samples of good quality (Fig. 4).

2.4. XRD and $R(T)$ measurements

X-ray diffraction (XRD) patterns were recorded with an X'Pert MRD (Philips) difractometer using CuKα radiation (2θ range of 20–65°). Finally, electrical characterization $R(T)$ were carried out using a standard four probe geometry (Ag paste to Ag electrodes deposited onto the samples).

3. Results and discussion

The best results were obtained with the method using mixed granules of $YBa_2Cu_3O_{7-\delta}$ and a filler. It allowed to press the mixture very tight and thereby to obtain suitable connections between granules of $YBa_2Cu_3O_{7-\delta}$. The crystalline sucrose turned out to be the best filler, which allowed us to obtain the material having good mechanical resistance, containing 60 vol. % of the pores. It, was characterized by the average density of about 2.76 g/cm^3 and the size of pores dependent on the size of the used granules. In order to analyse the quality of the samples, XRD and $R(T)$ measurements were performed.

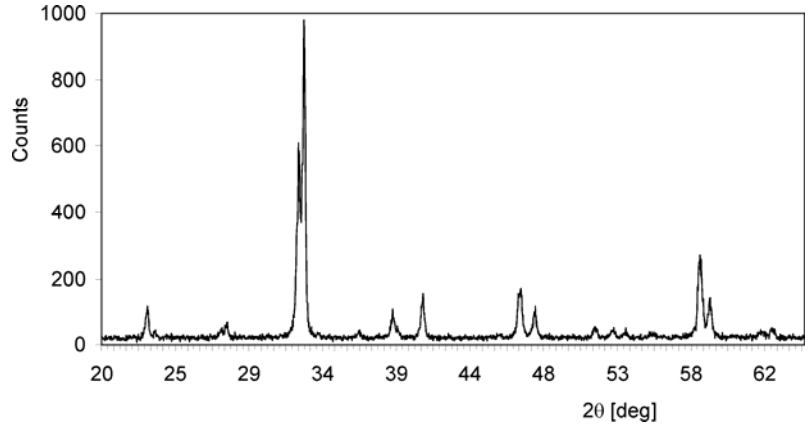

Fig. 5. XRD pattern for standard $YBa_2Cu_3O_{7-\delta}$

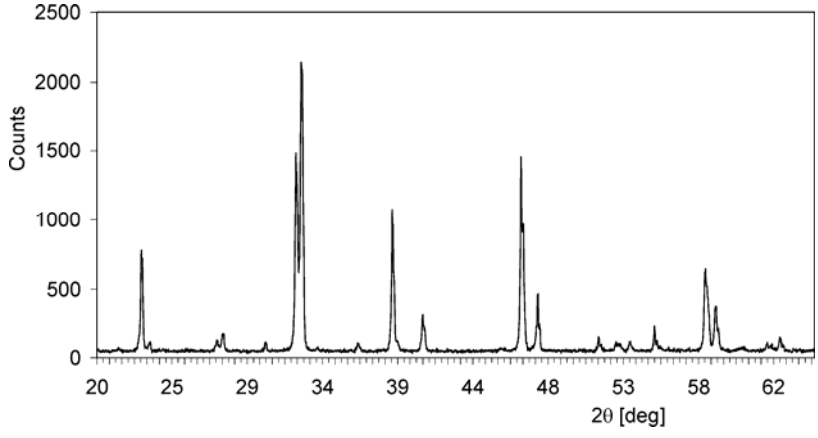

Fig. 6. XRD pattern for the $YBa_2Cu_3O_{7-\delta}$ after sintering with sugar

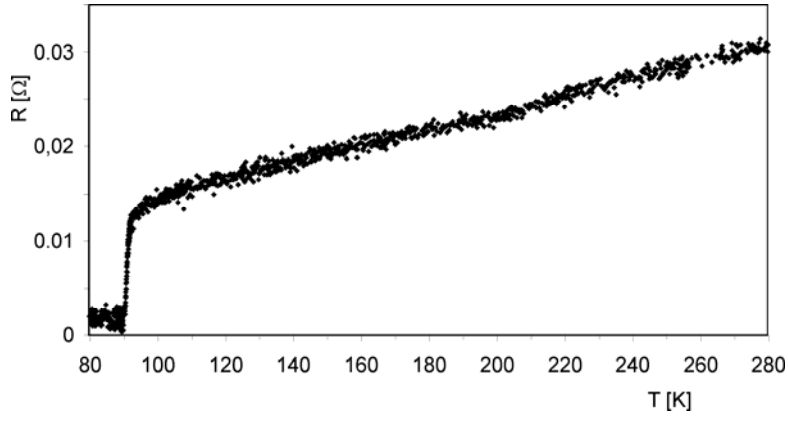

Fig. 7. *R–T* plot for a superconductive sample having open pores filled with Iron and fixed with wax

Figures 5 and 6 present the XRD patterns for a reference sample and the sample after sintering with sucrose and oxidation at 475 ºC for 36 h. The X-ray analysis revealed absence of remaining sucrose filler: the samples were burned out completely. Moreover, the $R(T)$ dependence points to the metallic nature of the material above the transition temperature and a narrow (2–3 K) transition to superconductivity at 91 K (Fig. 7).

4. Conclusion

The method of producing the porous $YBa_2Cu_3O_{7-\delta}$ ceramics consisting in using granules of supplementary materials as fillers, gave the best results in the case of crystalline sucrose. The obtained materials have good superconductive and mechanical properties. Therefore such a technique is suitable for obtaining materials applicable in a material research.

Acknowledgements

Authors thank B. Kusz, M. Gazda, W. Lizak and other researchers in the Department of Physics of Solids at Gdańsk University of Technology for the support during the experiments.

References

[1] KITAMURA T., YOKOYAMA M., J. Appl. Phys., 69 (1991), 821.
[1] SHLYK L., KRABBES G., FUCHS G., Phys. C, 390 (2003), 325.
[2] JIAO Y.L., XIAO L., REN H.T., ZHENG M.H., AND CHEN Y.X., Phys. C, 386 (2003), 266.
[3] MURALIDHAR M., JIRSA M., SAKAI N., MURAKAMI M., Supercond. Sci. Technol., 16 (2003), R1.
[4] XIAO L., REN H.T., CIAO Y.L., ZHENG M.H., CHEN Y.X., Phys. C, 386 (2003), 262.
[5] HORIE K., OHYAGI M., NAPOLI C., ISHIZAKI K., Scripta mater., 44 (2001), 1683.
[6] KNIZHNIK A., SHTER G.E., GRADER G.S., REISNER G.M., ECKSTEIN Y., Phys. C, 400 (2003), 25.
[7] OTTAVIANI G., NOBILI C., NAVA F., AFFRONTE M., MANFREDINI T., MATACOTTA F.C., GALLI E., J. Less-Common Met., 150 (1989), 177.
[8] FERRERI A., BERENOV A., BUGOSLAVSKY Y., PERKINS G., MACMANUS-DRISCOLL J.L., Phys. C, 372 (2002), 873.
[9] REDDY E.S., HERWEG M., SCHMITZ G.J., Supercond. Sci. Technol., 16 (2003), 608.
[10] NOUDEM J.G., REDDY E.S., SCHMITZ G.J., Phys. C, 390 (2003), 286.

Received 8 September 2005
Revised 10 November 2005

Materials Science-Poland, Vol. 24, No. 4, 2006

Dependence of GaAs and Si surface energy on the misorientation angle of crystal planes

A. ZDYB[1*], J. M. OLCHOWIK[1], M. MUCHA[2]

[1]Institute of Physics, Technical University of Lublin, ul. Nadbystrzycka 38, 20-618 Lublin, Poland

[2]Department of Mathematics, Informatics and Mechanics, Warsaw University, ul. Banacha 2, 80-952 Warsaw, Poland

The paper reports on the dependence of Si and GaAs surface energies on the misorientation angle of Si and GaAs crystal planes in a broad angle range. The energetic balance between GaAs and Si is unfavourable for growth of GaAs on Si substrate. Minima of the surface energy correspond to GaAs/Si heterostructure interface energy minima which indicate preferable crystal orientations for obtaining GaAs layers on Si.

Key words: *III–V semiconductors; interface*

1. Introduction

The growth of GaAs epitaxial layers on Si substrate has been the focus of extensive research in recent years because of their applications for electronic devices. Among many growth methods used to obtain GaAs/Si heterostructure [1–4], liquid phase epitaxy (LPE) seems to be one of the best [5].

Heteroepitaxial growth, like GaAs on Si, is in general more complicated than homoepitaxial growth because of the misfit between the substrate and the layer. Relations between surface energies of the substrate and the layer are crucial for the growth process. The surface energy varies with the orientation of the crystal plane because of variation of atom arrangement on the surface. In consequence, the value of heterostructure interfacial energy depends on the orientation of the substrate plane showing some orientations more preferable for epitaxial growth. This paper presents the dependence of Si and GaAs surface energy on the misorientation angle over a broad range of angles, discussing also the importance of the balance of surface energies.

*Corresponding author, e-mail: a.zdyb@pollub.pl

2. Theory

It is well known that four primary growth modes of an epitaxial film on a substrate are distinghished [6, 7]: layer-by-layer growth mode, island growth mode, the growth mode where islands grow on the top of an initial smooth layer and the columnar growth mode. The particular growth mode that results depends on a balance between the surface energy of the substrate and epitaxial layer and the lattice mismatch between the layers. In order to obtain the most ideal layer-by-layer growth mode, the following formula has to be fulfilled:

$$\gamma_l + \gamma_{in} - \gamma_s \leq 0 \tag{1}$$

where γ_l – surface energy of the layer, γ_{in} – interface energy, γ_s – surface energy of substrate.

The calculations of surface energy are based on the parametrizable model for a tetravalent semiconductor, proposed by Ackland [8]. The model consists of a sum over all atoms of a pair potential and a sum over all valence electrons bond energy:

$$E = \frac{1}{2}\sum_{i=1}^{N}\sum_{j=1}^{N} A\mathrm{e}^{-\alpha r_{ij}} - \frac{1}{2}\sum_{i=1}^{N}\sum_{n=1}^{4} Br_{ik_n}\mathrm{e}^{-\beta r_{ik_n}} \tag{2}$$

where the n sum runs over four electron pairs which have atom i as one of their foci and k_n as the other, and r_{ik} is the separation between the two ions on which the electron orbital is centred. Pairwise repulsion is represented by an exponent. The strength of the covalent bond is represented by the radial part of the hydrogenic p wave function. A, B, α, β are fitting parameters. In the Ackland model these paremeters have been determined for Si. In our recent study, the values of A, B, α, β parameters were determined for GaAs [9], thus the model can now be used in calculations for both Si and GaAs.

The energy described by Eq. (2) can be used in calculations of the surface energy. We have performed numerical calculations by using a computer program [10]. The energy described by Eq. (2) was divided by the number of atoms taken into account, the result being referred to as E_w. The following formula for the surface energy [11] was used:

$$\gamma_{(hkl)} = E_w \rho_{(hkl)} z_{(hkl)} \tag{3}$$

where $\rho_{(hkl)}$ is the density of atoms on the crystal plane, $z_{(hkl)}$ – number of broken bonds for one atom in this plane.

3. Results

First, the analysis of surface energy was performed for typical low-index Si planes: (001), (011), (111) and (113). The density of atoms and number of broken

bonds for one atom for each plane were determined by taking into account the geometry of Si crystal [10]. The results are presented and compared with literature data in Table 1.

Table 1. Surface energies [mJ/m^2] of Si planes γ_1 found in this work compared to the values γ_2 and γ_3 obtained by other authors

Si plane	γ_1	γ_2	γ_3
(001)	2512	2537[1]	2310[1], 1488[2]
(011)	1776	1794[1]	1601[1], 1721[2]
(111)	1467	1465[1]	1225[1], 1405[2]
(113)	2272	2240[1]	1380[2]

1 – [7], 2 – [12].

In Table 1, our calculations of Si surface energies $\gamma_{1\,\mathrm{have}}$ been compared with the surface energies based on the nearest neighbour broken-bond model γ_2 [7] and other literature data γ_3 [12]. There is a very good agreement between our results γ_1 and the literature data γ_2. In our study, we considered unrelaxed and unreconstructed surfaces and that is why the values of the surface energies obtained by us are higher than the values for reconstructed surfaces γ_3. In semiconductors, bond directionality is of great importance, thus reconstruction and relaxation decrease the value of surface energy, even by1000 mJ/m^2 [12,13].

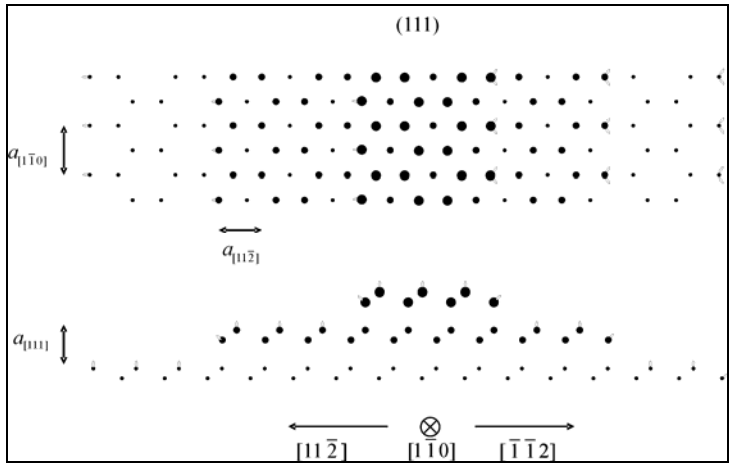

Fig. 1. Atomic model of the (111) plane tilted in $[11\bar{2}]$ and $[[\bar{1}\bar{1}2]$ direction. The small elliptic features indicate broken bonds

The dependence of Si and GaAs surface energy on the angle of misorientation of crystal planes (θ) was studied. The values of surface energy were calculated according to Eq. 3 in which the density of broken bonds was a function of misorientation angle. In order to find the dependence between the density of broken bonds and

misorientation angle we have performed the analysis of atom arrangement on vicinal planes. First, we considered the (111) plane (Fig.1) tilted in $[\bar{1}\,\bar{1}2]$ and $[11\bar{2}]$ directions and we have found the expression for broken bonds density l as a function of the misorientation angle θ:

$$l = \frac{\left(3a_{[111]} + ua_{[11\bar{2}]}\tan\theta\right)\cos\theta}{3a_{[111]}a_{[1\bar{1}0]}a_{[11\bar{2}]}} \tag{4}$$

where $a_{[111]}$, $a_{[11\bar{2}]}$, $a_{[1\bar{1}0]}$ are the lattice constants of the surface unit cell (Fig. 1), $u = 4$ when θ goes in the $[\bar{1}\,\bar{1}2]$ direction and $u = 2$ when θ goes in the $[11\bar{2}]$ direction.

We also performed the analysis for other crystal planes. The relation between broken bonds density and misorientation angle was found for (011) plane tilted in [001] direction, (001) plane tilted in [011] and (001) plane tilted in [010] direction.

Our model assumes that vicinal surfaces consist of regular steps with a well defined height. In fact, clean vicinal Si surfaces usually consist of irregularly distributed steps, there are some cases, however, when it is possible to obtain their regular distribution [14–16]. The model can be applied to surfaces with irregularly distributed steps if we consider the obtained broken bond density the as average value for the whole surface. Figures 2–5 show the results of the calculations of the surface energy versus the surface plane misorientation angle for all the mentioned planes.

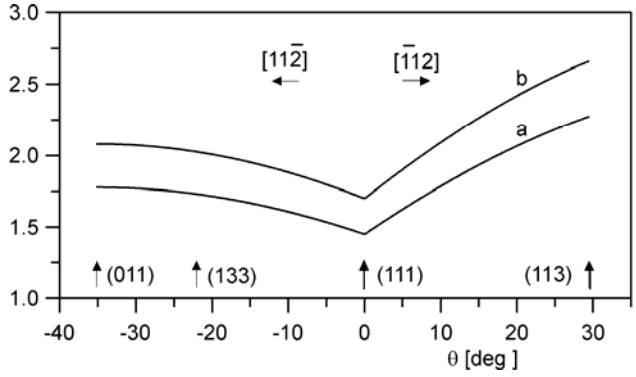

Fig. 2. The dependences of surface energies of Si (a) and GaAs (b) on the misorientation angle θ of (111) plane to $[11\bar{2}]$ direction

According to the presented model, the (111) plane has the lowest value of surface energy and (001) plane has the highest value. The results of this study agree with our analysis [9] of GaAs/Si heterostructure interface energy showing the importance of the balance between the surface energy of the substrate and the layer. The interface energy depends on the surface energy of the substrate and the layer and its minima indicate crystallographic planes that can be favourable for the growth of the layer.

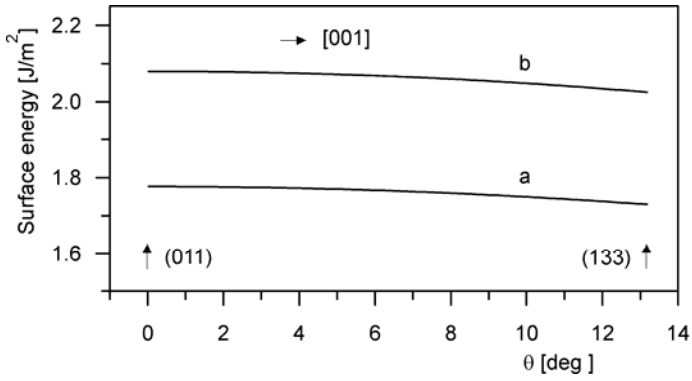

Fig. 3. The dependences of surface energies of Si (a) and GaAs (b) on the misorientation angle θ to (011) plane in [001] direction

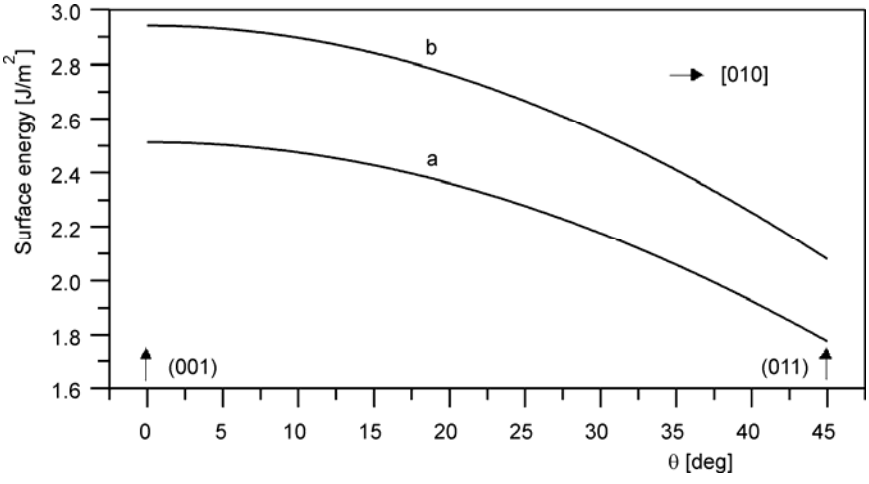

Fig. 4. The dependences of surface energies of Si (a) and GaAs (b) on the misorientation angle θ from (001) plane to (011) plane in [010] direction

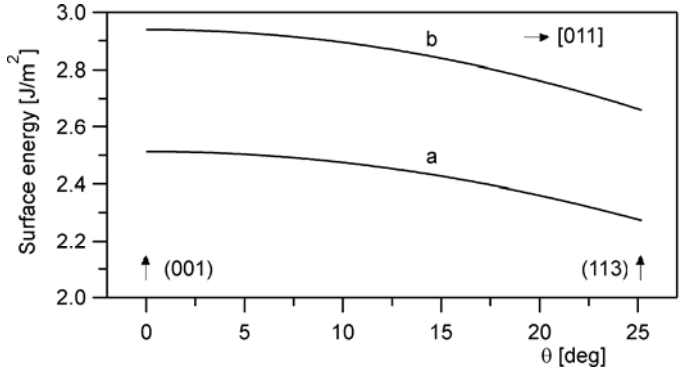

Fig. 5. The dependences of surface energies of Si (a) and GaAs (b) on misorientation angle θ to (001) plane in [011] direction

4. Conclusions

GaAs surface energy is higher than that of Si surface energy hence the energetic balance is unfavourable for the growth of GaAs on Si substrate. However, for some crystallographic planes Si and GaAs surface energies have minima and GaAs/Si heterostructure interface energy has corresponding minima that indicate planes of better growth conditions.

References

[1] MATSUNAGA Y., NARITSUKA S., NISHINAGA T., J. Cryst. Growth, 174 (1997), 635.
[2] CHANG Y.S., NARITSUKA S., NISHINAGA T., J. Cryst. Growth, 192 (1998), 18.
[3] TACHIKAWA M., MORI H., SUGO M., ITOH Y., Jpn. J. Appl. Phys., 32 (1993), L1252.
[4] MAUK M.G., FEYOCK B.W., COTTER J.E., J. Cryst. Growth, 225 (2001), 528.
[5] SMALL M.B., GIESS E.A., GHEZ R., [in:] D.T.J. Hurle (Ed.), *Handbook of Crystal Growth*, Vol. 3, Elsevier, Amsterdam, 1994, p.225.
[6] BAUER E., VAN DER MERWE J.H., Phys. Rev. B, 33 (1986), 3657.
[7] HOWE J.M., *Interfaces in Materials*, Wiley, New York, 1997.
[8] ACKLAND G., [in:] R.M. Nieminen, M.J. Puska, M.J. Maninen (Eds.), *Many-Atom Interactions in Solids*, Proceedings in Physics, Springer-Verlag, Berlin, 1990, p. 249.
[9] ZDYB A., OLCHOWIK J.M., SZYMCZUK D., MUCHA J., ZABIELSKI K., MUCHA M., SADOWSKI W., Cryst. Res. Technol., 37 (2002), 875.
[10] ZDYB A., Ph.D. Thesis, TU Gdansk (2002).
[11] DĄBROWSKI J., MUSSIG H.J., *Silicon Surfaces and Formation of Interfaces*, World Scientific Publ., Singapore, 2000.
[12] EAGLESHAM D.J., WHITE A.E., FELDMAN L.C., MORIYA N., JACOBSON D.C., Phys. Rev. Lett., 70 (1993), 1643.
[13] BARTELT N.C., WILLIAMS E.D., PHANEUF R.J., YANG Y., DAS SARMA S., J. Vac. Sci. Technol., A7 3 (1989), 1898.
[14] PHANEUF R.J., WILLIAMS E.D., Phys. Rev. B, 41 (1990), 2991.
[15] CHABAL Y.J., ROWE J.E., CHRISTMAN S.B., Phys. Rev. B, 24 (1981), 3303.
[16] SHIBATA M., SUMITA I., NAKAJIMA M., Phys. Rev. B, 57 (1998), 1626.

Received 10 September 2005
Revised 9 November 2005

Materials Science-Poland, Vol. 24, No. 4, 2006

Intermolecular interactions in plant cells reflected by ultraweak luminescence phenomenon

A. JAŚKOWSKA*, A. DUDZIAK, M. GOSPODAREK, E. ŚPIEWLA

Institute of Physics, Lublin University of Technology, Nadbystrzycka 38, 20-618 Lublin, Poland

It is commonly known that photons necessarily participate in atomic and molecular interactions. On the other hand, plant, animal and human cells spontaneously emit electromagnetic radiation. The universality of ultraweak cell luminescence is inherently associated with fundamental processes in living organisms. The majority of researchers think that this very weak radiation (10–10^5 photons/(cm^2·s)) results from such radical reactions as, for instance, lipid peroxidation. Having at our disposal the spectra of ultraweak luminescence (UL) from intact *Characeae* cells and their particular cellular structures and fractions, we could confirm that the electron carriers of the mitochondrial respiration chain were active in cytoplasm and in the intact cells but not in the cell walls. We obtained a band of chlorophyll emission in UL spectra. The dark chlorophyll should not emit fluorescence, which we observed under illumination. Nevertheless in our experiments, in which plants were kept in darkness for ca. 12 hours prior to measurement, this emission was observed. The only way to account for this phenomenon is that the energy of excitation is transferred to chlorophyll by other molecules. In this ultraweak sensibilized luminescence, the excited carbonyl molecules $^{1,3}(=C=O^*)$ transfer their energy to chlorophyll molecules with a high quantum efficiency. As we found in the spectral analysis of UL, the intensity at the wavelength of 634 nm – corresponding to dimoles of singlet oxygen – markedly decreased when the cells were exposed to the action of ascorbic acid (AsA) and lignocaine, which are singlet oxygen quenchers.

Key words: *ultraweak luminescence; singlet oxygen; ascorbic acid; lignocaine; Characeae cells*

1. Introduction

Intermolecular interactions generate excited states in metabolic processes of living cells of animal and plant organisms. A reflection of such interactions is the phenomenon of electromagnetic radiation (along a broad scale of the spectra), well known as bioluminescence, photoluminescence, delayed luminescence and ultraweak luminescence (UL).

Detection and identification of excited states in well-defined chemical solutions or in model systems (biologically determined) are fairly easy to be accomplished. They

* Corresponding author, e-mail: a.jaskowska@pollub.pl

are a spectacular example of the investigation of intermolecular interactions via the analysis of luminescence spectra.

This task becomes much more difficult, although not impossible in living systems. The essence of the phenomenon of chemiluminescence consists in the transformation of the energy of chemical reaction into the energy of electronic excitation of the product of reaction which then emits photon of energy $h\nu$. Effective electronic excitation in a condensed state, proper to biological systems, require that the energy of 100–640 kJ/mol (i.e., 1–6.6 eV/molecule) be supplied within a time period shorter than the mean time of oscillation or than the time of keeping the products in solvate surrounding (10^{-11} s). This corresponds to UL in the visible and ultraviolet range of wavelength (200–700 nm). Such high energies are triggered most often in free radical and chain reactions, and also those in redox reactions that run the course of radical mechanism (i.e., dismutation of peroxyradical, disintegration of the peroxides of the dioxyethan type, adiabatic transfer of electrons from donor to acceptor, chemical exchange of electrons).

Some authors ascribe a special meaning to this radiation, i.e. that it conveys some information [1–7]. The transfer of information from cell to cell, i.e. outside the organisation unit, as well as inside it, by means of photons, seems to be a very attractive and promising idea. In the self-steering and self-regulating living organisms, photons arise as a result of sublimated intermolecular interactions connected with a special group of processes in the definite phase of cell metabolism. These photons should initiate other processes as a result of the interactions triggered by photon absorption in the other parts of the structural cell. Today, because of understandable difficulties, there is no sufficient experimental evidence of the above mentioned thesis. Therefore, it is necessary to be satisfied with the study of electromagnetic radiation emitted from the cell into the external media. Growth [8, 9], cell division [10], differentiation [11, 12], the cell response to the environmental stressors [13–15], especially such that initiates protective mechanisms [16, 17], injury [18, 19] and death [20, 21] are manifested by changes in spontaneous UL intensity (most often by its increase). However, we can administer some specific substances and thereby obtain the back reaction (with photon emission) which reagents initiate in the cell. In this case, it is UL induced by the added reagent.

In this study we have applied such reagents of active biological group as radical scavengers and singlet oxygen quenchers. Then by means of spectral analysis we sought to obtain information which particles, strategically important in the cell, are in the terminal phase the most probable emitters of extra weak radiation.

2. Materials and methods

The objects of this research were plant cells from Characeae family, *Nitellopsis obtusa (Desv. In Lois J. Gr.)* taken from Zaglebocze Lake near Lublin in Poland. They were cultured in an air-conditioned laboratory in natural pond water in day/night re-

gime at room temperature. Before measurements they were kept in complete darkness for few hours in artificial pond water (APW) in the following composition (mmol/dm^3): KCl 0.1; NaCl 0.1; $CaCl_2$ 0.1and 20 mmol/dm^3 Hepes buffer. pH of APW was 7.5, achieved by adding 10% NaOH.

The cell walls were obtained by cutting one of the two cell nodes and gently squeezing out cytoplasm from the interior of the cell. Cytoplasm isolated from cells was obtained by the method described by Jaśkowska and Śpiewla [22]. In the isolated cytoplasm, one could observe rotating chloroplasts inside the drops and record action potentials generated on the membrane. The latter was formed as a new reconstruction on the cytoplasm surface. Microsomal fraction was obtained from the homogenate of cells (5 g fresh weight was homogenized in a cold buffer of 0.1 mol/dm^3 Tris–HCl, pH = 7.5 containing 1 mmol/dm^3 EDTA Na_2). After centrifugation at 14 000*g* for 15 min at 4 °C, the supernatant was again centrifuged at 68 000*g* for 2 h at 4 °C. The pellet obtained after the second centrifugation was treated as a fraction enriched in cell membranes. In order to obtain the microsomal fraction enriched in ribosomal components, the supernatant was once again centrifuged at 105 000*g* at 4 °C for 3 h [23].

Measurements of UL were performed by means of Single Photon Counting method (SPC) with the use of a very sensitive photomultiplier (EMI 9558). For spectral analysis we used a set of 20 Russian glass cut-off filters, marked as BC6, BC7, BC8, ZC10, ZC12, ZC16, ZC17, ZC18, OC11, OC12, OC13, OC14, KC10, KC11, KC13, KC14, KC15, KC17, KC18 and KC19 which transmitted electromagnetic radiation above required wavelengths. The scheme of the apparatus is shown in Fig. 1.

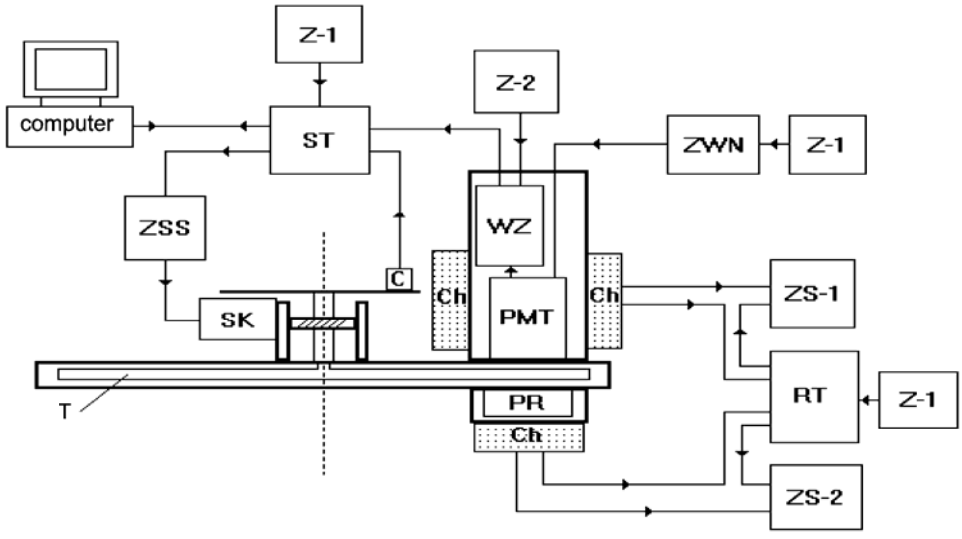

Fig. 1. Scheme of the filter spectrometer: PR – sample, T – turning round shield with cut-off filters, SK – stepping motor, C – controller of start position, PMT – photomultiplier, Ch – thermoelectric cooler, WZ – pulse amplifier, Z, ZS, ZWN, ZSS – voltage supplies, ST – interface, RT – temperature controller

The spectral distribution of UL was calculated and corrected for the total intensity changes with time, transmittance of filters, spectral sensitivity of the photomutiplier and long-lasting phosphorescence of some filters, as described elsewhere [24, 25]. Measurements of the spectral distribution were conducted following 0.5 h exposure to 1 mmol/dm^3 of ascorbic acid (AsA) and 2 mmol/dm^3 of lignocaine because the UL intensity was rather stable then. More details about the apparatus are enclosed in the previous article [26].

3. Results and discussion

The first step of our investigation was to decide whether the UL spectral analysis allows us to distinguish individual bands in the spectra related to the metabolic processes in the plant cells. For this purpose, UL spectra of intact cells and their walls as well as of isolated cytoplasm from the cells have been recorded. The results are presented in Fig. 2 and one can see the difference in the spectral range 450–610 nm when comparing UL spectra from living samples, i. e. intact cells and cytoplasm, with the ones from the cell walls.

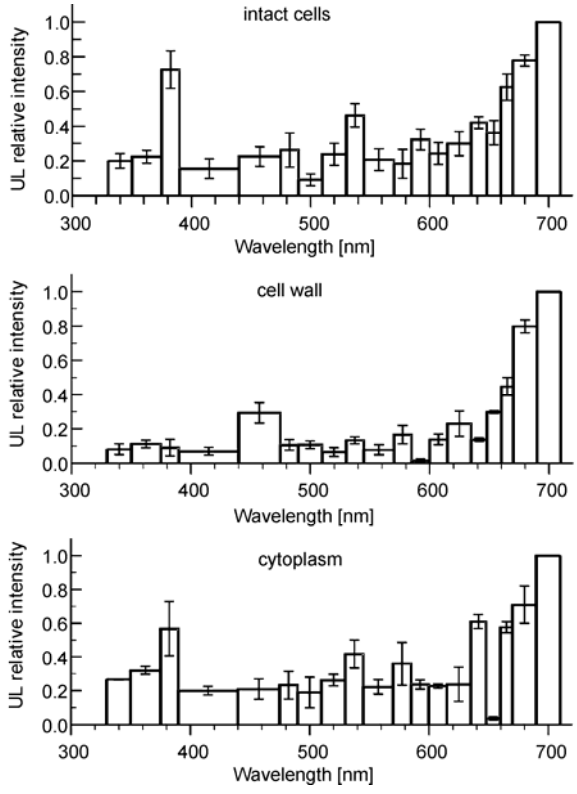

Fig. 2. Spectral distribution of UL from intact *Nitellopsis obtusa* cells and from cell walls and cytoplasm isolated outside the cells (averages of three series of measurements; vertical bars indicate standard errors)

Within the region of wavelengths mentioned above, the electron transfers of mitochondrial respiration chain emit electromagnetic radiation and probably they are responsible for UL within that spectral range. The essential elements of respiration chain are NAD and its reduced form – NADH, FMN and ubiquinone. For this reason, it was worth to compare fluorescent spectra of the mentioned compounds (Fig. 3) with the spectra of the objects under investigation. We would like to remark that the spectra of NADH and FMN are taken from literature [27, 28], whereas the spectrum of ubiquinone was obtained in our own measurements and published earlier [29].

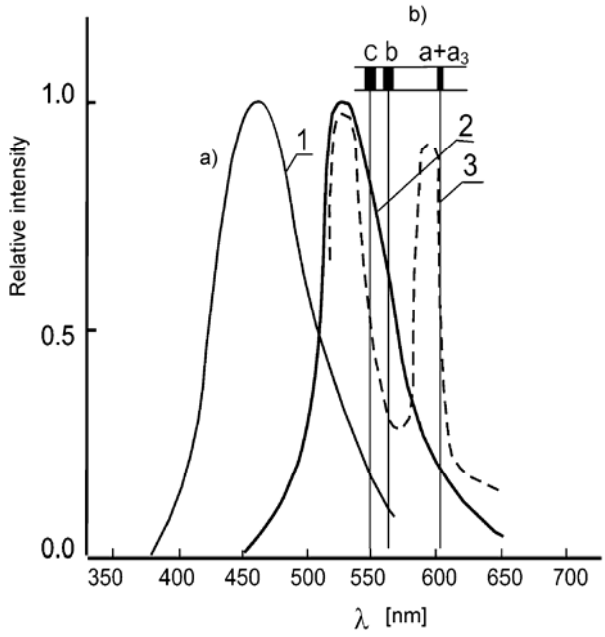

Fig. 3. Normalized fluorescence spectra (a): 1) NADH in 0.05 mol/dm^3 sodium phosphate, excitation at 351 nm [27], 2) FMN in neutral aqueous solution, excitation at 450 nm [28], 3) ubiquinone in benzene, excitation at 505 nm [29]. Light absorption by cytochromes (b): c – 550 nm, b – 563 nm, a + a_3 – 605 nm

Taking into consideration the emission at 450 nm, which may be caused by NADH, we did not record any essential changes between different cell structures. However, the emission at this wavelength from cell walls is a little stronger than that from intact cells and cytoplasm, but differences are not statistically essential. The ultraweak radiation from the cell walls at 530 nm and 590 nm, which can be associated with FMN and ubiquinone fluorescence, is markedly lower. It is justified because mitochonria are absent in the wall structure, which means that the respiration processes does not take place here. However, a relatively higher emission at 450 nm can reflect a large amount of reduced form of NAD, i.e. the first compound of the electron transfer in the respiration chain. This may be caused by the presence of damaged mi-

tochondria from cytoplasm retained in the cell walls. Electron transfer processes related to mitochondrial respiration however, do not occur in the walls, as in intact cells and cytoplasm, which is confirmed by relic emission from the other electron carriers of respiratory chain (FMN, ubiquinone).

It is puzzling that a large intensity of UL of living samples is observed at 380 nm, whereas this peak does not occur for cell walls which are not a living part of the cell. The radiation emitters at 380 nm, pointed out in literature, are oxygen dimoles $2[^1\Sigma_g^+]$ (with a very low emission probability) and carbonyl compounds which most often transfer their energy into chlorophyll. That is why a big intensity of radiation emission at 680 nm (chlorophyll band) is observed in all cases in Fig. 2.

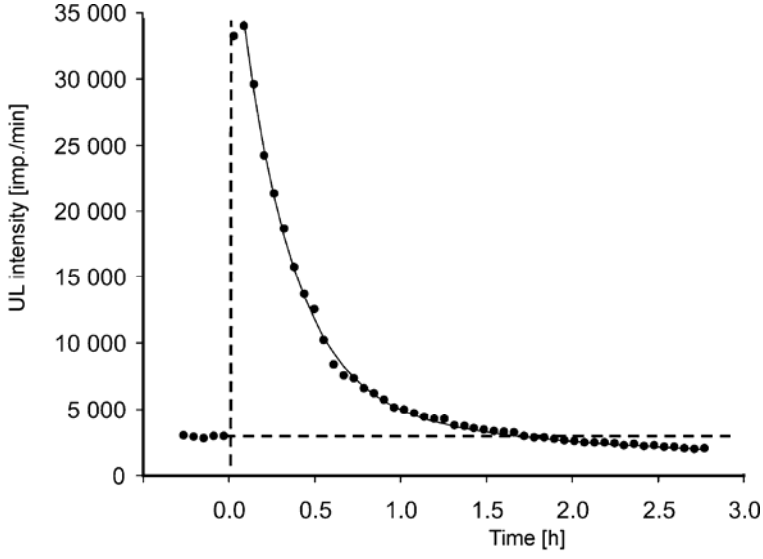

Fig. 4. Decay of the UL from isolated cytoplasm exposed to 1 mmol AsA. The horizontal dashed line shows the level of UL intensity from cytoplasm before AsA treatment. The standard errors for the points before and after AsA action are not more than 4% and 8.5% respectively. The continuous line shows the best fit of UL decay to the double-exponential curve: $y = 39181\exp(-3.32x) + 4760\exp(-0.39x)$; $T_{(1/2)1} = 12.5$ min, $T_{(1/2)2} = 106.3$ min, $R^2 = 0.999$

Ascorbic acid (AsA) is well-known as hydrophilic antioxidant and free radical scavenger (Vit C). When *Nitellopsis obtusa* cells were exposed to its action, first we observed a considerable increase of UL intensity, and then its decrease, but never below the starting level [26]. If UL intensity had fallen below the beginning level, it would have confirmed the antioxidant properties of AsA [30], something that we would like to obtain. Following that, we studied particular subcellular structures and fractions. The kinetics of UL intensity for cytoplasm isolated from cells treated by 1 mmol/dm^3 of AsA (Fig. 4) is almost the same as for the intact cells, but after about 1.7 h UL intensity begins to fall below its starting level. Among the fractions under investigation, i.e. membrane, lipid and microsomal enriched in ribosomes, only in the

last case UL intensity fell below the starting level when ribosomal fraction was treated by 5 mmol/dm^3 of AsA. When these samples were exposed to 1 mmol/dm^3 AsA, there was no change at all (Fig. 5). The period of time after which a decrease of UL intensity is observed (for 5 mmol/dm^3 of AsA), equals about 0.5 h. This decrease is deeper than that for the cytoplasm isolated from the cells.

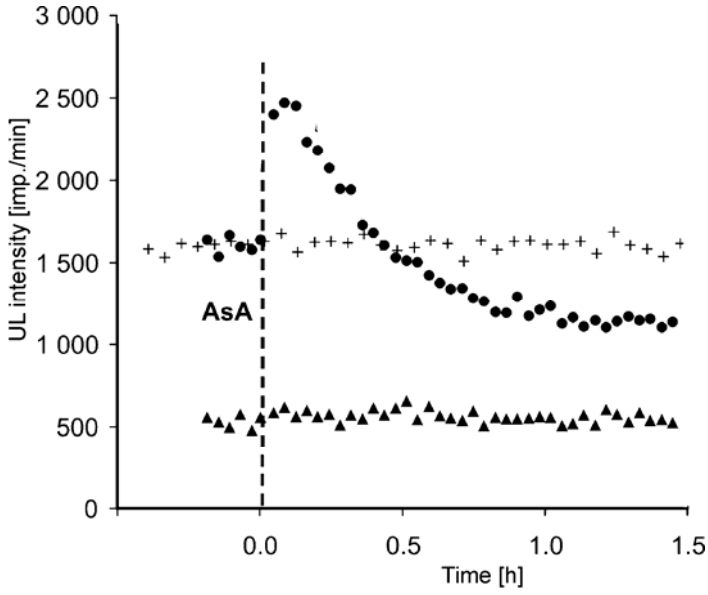

Fig. 5. Time dependence of UL of the ribosomal fraction obtained from *Nitellopsis obtusa* cells exposed to AsA: 5 mmol (black circles) and 1 mmol – (crosses). The standard errors for the points before and after AsA treatment are not more than 5% and 10%, respectively. Triangles show the levels of UL from APW solution before and after exposure to the action of 5 mmol/dm^3 AsA as a function of time (no changes are clearly seen)

Antioxidant action of AsA is represented by the following reaction (Eq.1):

$$AAH^- + O_2^{-\bullet} + H^+ \rightarrow AAH^{-\bullet} + H_2O_2 \quad (1)$$

while the prooxidant action by Eq. (2):

$$AAH^- + O_2 \rightarrow AAH^{-\bullet} + O_2^{-\bullet} \quad (2)$$

where: AAH^- – ascorbate, $AAH^{-\bullet}$ – free radical of ascorbic acid.

In spite of the increase in total UL intensity from the cells exposed to AsA action, we observed in the spectra (Fig. 6) a decrease of radiation at λ = 634 nm, a fact that can be related to photon emission from the dimoles of singlet oxygen represented by the following equation:

$$2O_2(^1\Delta_g) \rightarrow 2O_2(\,^3\Sigma_g^-) + hc/\lambda \quad (3)$$

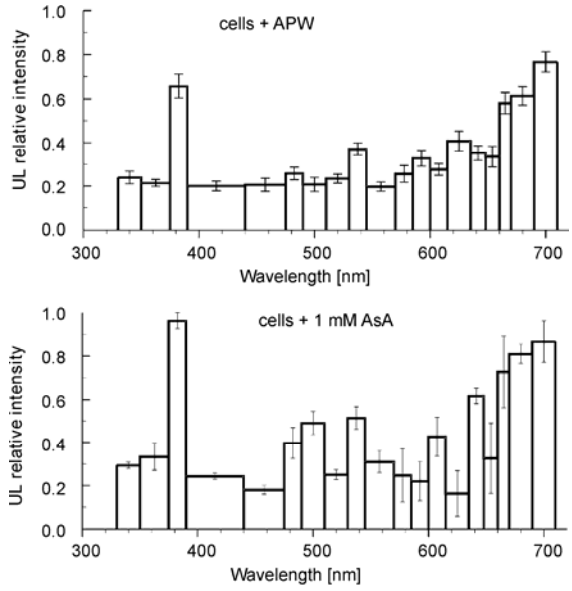

Fig. 6. Spectral distribution of UL from intact *Nitellopsis obtusa* cells before and after exposure to 1 mM AsA action (average of three series of measurements)

AsA is a quencher of singlet oxygen $^1\Delta_g$ at λ = 1270 nm [31]. In our measurements we have shown that AsA is also the quencher for the dimoles of singlet oxygen. In Fig. 7, the scheme of electronic transitions for singlet oxygen molecules and their dimoles is shown.

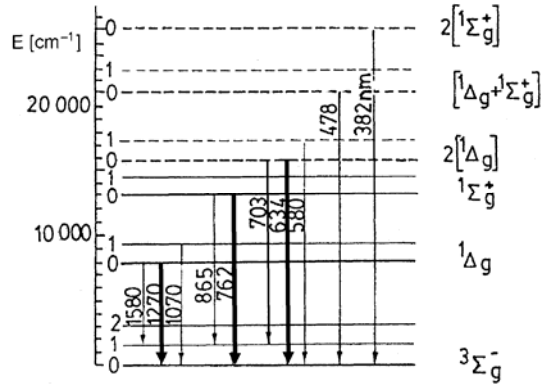

Fig. 7. Scheme of energetic levels and electronic transitions in singlet oxygen molecules [32]

The increase of UL intensity at 450–610 nm, induced by AsA, can suggest that redox processes in mitochondrial respiratory chain appear when the electronic transmitters are excited. The increase at λ = 680 nm (chlorophyll emission) may suggest scav-

enging of a certain pool of free radicals in chloroplasts by AsA. This can intensify the electron reverse transport, which results in generating excited chlorophyll molecules and eventually light emission.

Another reagent being a biologically active substance, i.e. lignocaine from local anaesthetics group, is also a quencher of singlet oxygen – physical and chemical as well. Zanocco [33] found that the main path for the interaction of lignocaine with singlet oxygen corresponds to physical quenching and can be explained in terms of a reversible formation of an exciplex via charge–transfer interactions due to the electrophilic attack of the excited oxygen on the amino group.

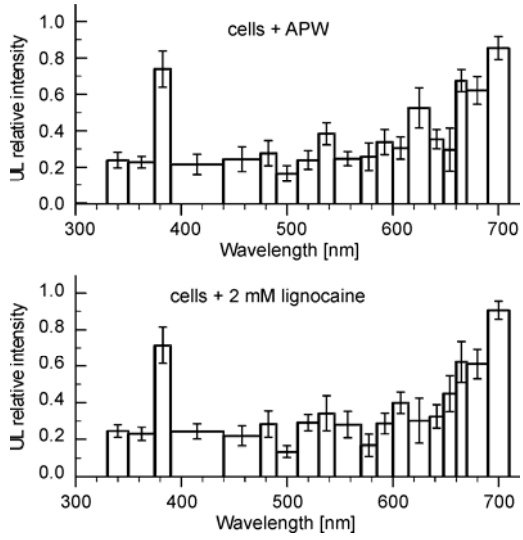

Fig. 8. Spectral distribution of UL from intact *Nitellopsis obtusa* cells before and after exposure to 2 mM lignocaine (average of three series of measurements)

In the spectra obtained in this study, when the reagent influenced the intact cells, we observed UL intensity decrease at $\lambda = 634$ nm (Fig. 8). This means that lignocaine is also a quencher of singlet oxygen dimoles ($2O_2$ $^1\Delta_g$). However, light intensity at the wavelengths related to luminescence of NADH, FMN, ubiquinone, chlorophyll and oxygen dimoles did not change essentially. It is worth to notice that in this case the measurements of UL spectra were performed in the course of 1.5 hours after anaestethic addition when total UL intensity did not change, what we described in our previous paper [34].

5. Conclusions

One of the main and ubiquitous emitters of ultraweak luminescence from plant cells of *Characeae* is chlorophyll with fluorescence at 680 nm. Even a small amount

of it (e.g., in isolated cytoplasm) is visible in spectra of samples which were kept for several hours in darkness. Excitation of chlorophyll, visible in all investigated samples spectra of UL, is also enhanced by the action of ascorbic acid.

NADH, FMN and ubiquinone are other essential cell emitters, which is an evidence that there are interactions in mitochondrial respiration chain. But the intensity of their radiation in the UL spectra of the cell walls is relic. It can prove that UL spectra reflect metabolic processes undergoing in living organisms.

The biologically active substances used in our research (ascorbic acid and lignocaine – known as singlet oxygen quenchers) caused decrease of UL intensity from Characeae cells at 634 nm. This may be interpreted as the quenching of singlet oxygen dimoles.

The existence of peak in UL spectra at 380 nm may be connected with the excitation of singlet oxygen dimoles $2[^1\Sigma_g^+]$, but because of extremely low probability of it this concept requires further investigations.

Single Photon Counting method equipped with a set of cut-off filters is helpful in the identification of intermolecular interactions existing under the influence of exogenous reagent, as we had pointed it out for *Characeae* plants.

References

[1] FRÖHLICH H., Int. J. Quantum Chem., 23 (1983), 1589.
[2] GU Q., Physics (China), 18 (1989), 235.
[3] DEL GUIDICE L., DOGLIA S., MILANI M., VITELLO G., *Structures, correlations and electromagnetic interactions in living matter: theory and applications*, [in:] H. Froelich (Ed.), *Biological Coherence and Response to External Stimuli*, Springer-Verlag, Berlin, 1988.
[4] POPP F.A, NAGL W., LI K.H., SCHOLZ W., WEINGARTNER O., WOLF R., Cell. Biophys., 6 (1984), 33.
[5] VAN VIJK R., J. Sci. Explor., 15 (2001), 183.
[6] KUZIN A.M., Radiats. Biol. Radioecol., 34 (1994), 398 (in Russian).
[7] KUZIN A.M., Biofizika, 45 (2000), 144 (in Russian).
[8] KOBAYASHI M., DEVARAJ B., USA M., TANNO Y., TAKEDA M., INABA H., Photochem. Photobiol., 65 (1997), 535.
[9] KAI S., OHYA T., MORITA K., FUJIMOTO T., Phys. A, 210 (1994), 391.
[10] MEI W.P., *Ultraweak photon emission from synchronized yeast (Saccharomyces cerevisiae) as a function of the cell division cycle* [in:]: F.A. Popp, K.H. Li, Q. Gu, (Eds.), *Recent Advances in Biophoton Research and Its Applications,* World Scientific, Singapore, 1992, p. 243.
[11] KAI S., OHYA T., MORITA K., FUJIMOTO T., Jpn. J. Appl. Phys., 1 (1995), 6530.
[12] NAGL W., POPP F.A., Cytobios., 37 (1983), 45.
[13] SŁAWIŃSKA D., POLEWSKI K., SŁAWIŃSKI J., Bioelectrochem. Bioenerg., 343 (1992), 483.
[14] BOVERIS A., VARSAVSKY A.I., GONÇALVES J., SÁNCHEZ R.A., Photochem. Photobiol., 38 (1983), 99.
[15] VAN WIJK R., TILBURY R.N., SLAWINSKI J., EZZAHIR A., GODLEWSKI M., KWIECINSKA T., RAJFUR Z., SITKO D., WIERZUCHOWSKA D., KOCHEL B., QU Q, POPP F.A., LILIUS E.M., MARNILA P., AKEN J.M., Experientia, 48 (1992), 1092.
[16] NASCIMENTO A.L.T.O., CILENTO G., Photochem. Photobiol., 53 (1991), 379.
[17] MAKINO T., KATO K., IYOZUMI H., HONZAWA H., TACHIIRI Y., HIRAMATSU M., Photochem. Photobiol., 64 (1996), 953.
[18] SALIN M.L., QUINCE K.L., HUNTER D.J., Photobiochem. Photobiophys., 9 (1985), 271.

[19] SUZUKI S., USA M., NAGOSHI T., KOBAYASHI M., WATANABE N., WATANABE H., INABA H., J. Photochem. Photobiol. B: Biol., 9 (1991), 211.
[20] SŁAWIŃSKI J., Indian J. Experimen. Biol., 41 (2003a), 483.
[21] SŁAWIŃSKI J. *Photon emission from perturbed and dying organisms – the concept of photon cycling in biological systems,* [in:] A.F. Popp, L. Beloussov (Eds.), *Integrative Biophysics,* Kluwer Academic Publishers, Dordrecht, 2003, p. 307.
[22] JAŚKOWSKA A., ŚPIEWLA E., Problems Modern Biophys., 4 (1979), 65 (in Polish).
[23] KINNE-SAFRAN E., KINNE R.K.H., Meth. Enzymol., 172 (1989), 3.
[24] INABA H., Experientia, 44 (1988), 550.
[25] TRYKA S., Comput. Chem. 22 (1998), 113.
[26] JAŚKOWSKA A., BORC R., MILCZAREK I., DUDZIAK A., ŚPIEWLA E., Luminescence, 16 (2001), 51.
[27] WISSER A.J.W.G., VAN HOEK A., Photochem. Photobiol., 33 (1981), 35.
[28] NISHIMURA Y., TSUBOI M., Chem. Phys. Lett., 59 (1978), 210.
[29] MILCZAREK I., JAŚKOWSKA A., GOŁĘBIOWSKA D., *Effect of humic acid and polyphenols on ultraweak luminescence from Characeae cells*, [in:]N. Senesi, T.M. Miano (Eds.), *Humic Substances in the Global Environment and Implications for Human Health*, Elsevier, Amsterdam, 1994, p. 323.
[30] RADOTIĆ K., REDENOWIĆ Č., JEREMIĆ M., VUČINIĆ Ž., J. Biolumin. Chemilumin., 5 (1990), 221.
[31] KHAN A.U., J. Biolumin. Chemilumin., 4 (1989), 200.
[32] SŁAWIŃSKI J., *Research method of weak photon emission from biological systems*, [in:] J. Twardowski (Ed.), *Biospectroscopy* 3, PWN, Warszawa, 1989, 107 (in Polish).
[33] ZANOCCO A.L., LEMP E.M., PIZARRO N., DE LA FUENTE J.R., GÜNTHER G., J. Photochem. Photobiol. A: Chem., 140 (2001), 109.
[34] JAŚKOWSKA A., GÓRSKI Z., DUDZIAK A. Proc. SPIE, 5566 (2003), 15.

Received 9 September 2005
Revised 4 November 2005

Materials Science-Poland, Vol. 24, No. 4, 2006

Influence of temperature on the efficiency of monocrystalline silicon solar cells in the South-eastern Poland conditions

J. M. OLCHOWIK[1*], S. GULKOWSKI[1], K. J. CIEŚLAK[1], J. BANAŚ[1], I. JÓŹWIK[1], D. SZYMCZUK[1], K. ZABIELSKI[1], J. MUCHA[1], M. ZDROJEWSKA[1], J. ADAMCZYK[1], R. TOMASZEWSKI[2]

[1]Lublin University of Technology, Nadbystrzycka 38, 20-618 Lublin, Poland

[2]State Higher Vocational School in Biała Podlaska, Sidorska 95/97, 21-500 Biała Podlaska, Poland

Recently, solar energy conversion has become a very actual item, especially when the world faces problems of petroleum supply and there has been a growing demand for using renewable energy sources. In this situation an important question araises how to use solar energy optimally. The quantum efficiency of solar cells depends on many factors: temperature, insolation, spectral characteristics of sunlight, etc. Some of these factors may be changed during exploitation of solar systems in order to increase their efficiency. The paper reports on the influence of temperature on the work efficiency of monocrystaline photovoltaic modules in hybrid solar systems in the conditions of south–eastern Poland.

Key words: *solar energy; solar cell; photovoltaic module*

1. Introduction

The world faces a big problem of depletion of conventional sources of energy which have to be replaced by new ones. The choice of a renewable source of energy depends, however. A very important issue is to know which kind of energy source will suit best the particular region. South-eastern Poland, where the investigation has been carried out, seems to be the best choice for the use of solar energy, as it has the best insolation conditions all over the country. The solar energy may by used to produce electricity in photovoltaic (PV) modules and heat in photocollectors (PT) by a photovoltaic and photothermal conversion. The photovoltaic effect, which is based on a direct conversion of sunlight into electricity, was observed for the first time by

*Corresponding author, e-mail: j.olchowik@pollub.pl

the French physicist, A.C. Becquerel in XIX century. From the exploitation point of view, the most important factor influencing efficiency of PV modules is temperature inside the p-n junctions of semiconducting solar cells. The solar cells may be produced from various materials but silicon still remains the most popular material and crystal silicon modules are most often used. The generation efficiency of the electron-hole pairs inside Si p-n junction depends not only on the quality of crystal structure but also on the insolation conditions as well as on temperature of the cell work. Usually, temperature negatively affects the efficiency of PV conversion, hence various types of cooling systems have been commonly used [1]. However, imperfections of semiconductor structures as well as the quality of atmosphere may give anomalous results. Therefore, to exploit the PV systems optimally, it seems reasonable to analyze their work in various situations.

2. Experimental

The aim of the investigation was to determine the response of PV modules of a hybrid solar system to changes of temperature as well as conditions of insolation. The system was installed on the roof of the Department of the Management and Fundamentals of Technology building of Lublin University of Technology, localized in the south-eastern region of Poland and its charcteristics have been described elsewhere [1]. The system created to investigate the influence of the temperature and the insolation on the efficiency of Si solar cells consists of two monocrystaline photomodules Sunset SM10L type, attached to an aluminum radiator. To stabilize precisely the temperature of one of the modules, it is cooled by the Peltier modules. The measured values of the parameters of PV modules were continuously recorded by a computer system supplied with an advanced software [2–4].

3. Results and discussion

Figures 1–4 present typical images of power obtained in PV modules during the 2005summer in the south-eastern region of Poland. Some fluctuations of the curves, presented in the figures, were caused by fluctuation of the sunlight spectrum reaching the surface of the analyzed modules. The experimental data were statistically calibrated due to a possible asymmetry of the static characteristic of the PV modules.

As can be seen in Figs. 1b and 2b, the cooled PV module gives more power obtained by PV conversion than the one that was not cooled. The other graphs (Figs. 1a, 2a, 3, 4) presenting the response of the modules to the sunlight in the morning hours of the sunny days and on the cloudy days show that there are anomalous differences between cooled and not cooled modules.

The photovoltaic conversion is the most effective in the area near the p-n junction of semiconductors, located close to the solar cell surface and it depends on several

factors: sunlight spectrum, cell spectral sensitivity, reflectivity of a cell surface, semiconductor type, distance of a p-n junction from a surface and the temperature of the cell [5]. The increase of the solar cell temperature caused by the inductive load or by an increase of the environment temperature is usually the reason for a decrease of its efficiency. In particular environmental conditions, however, higher temperature can have a positive effect, as was mentioned in our previous paper [1].

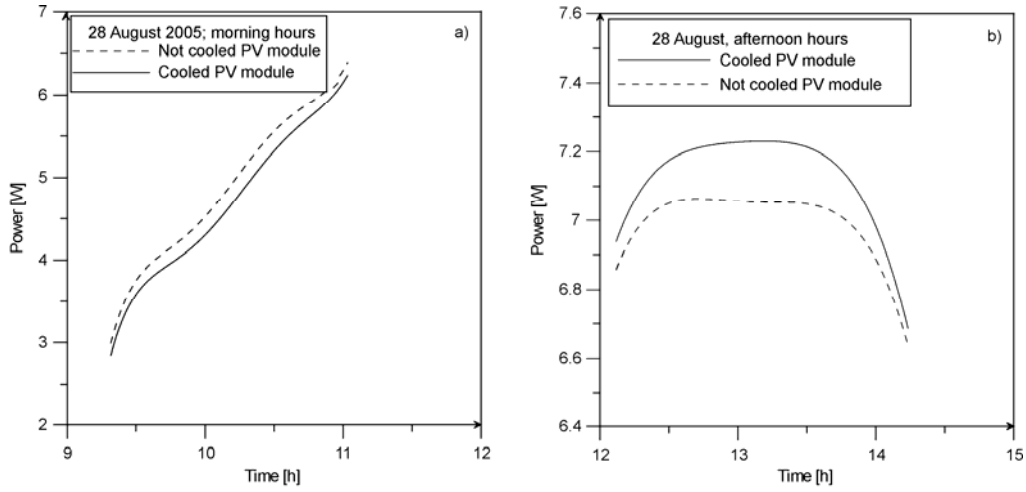

Fig. 1. Power generated in PV modules in a sunny day, in the morning (a) and afternoon (b)

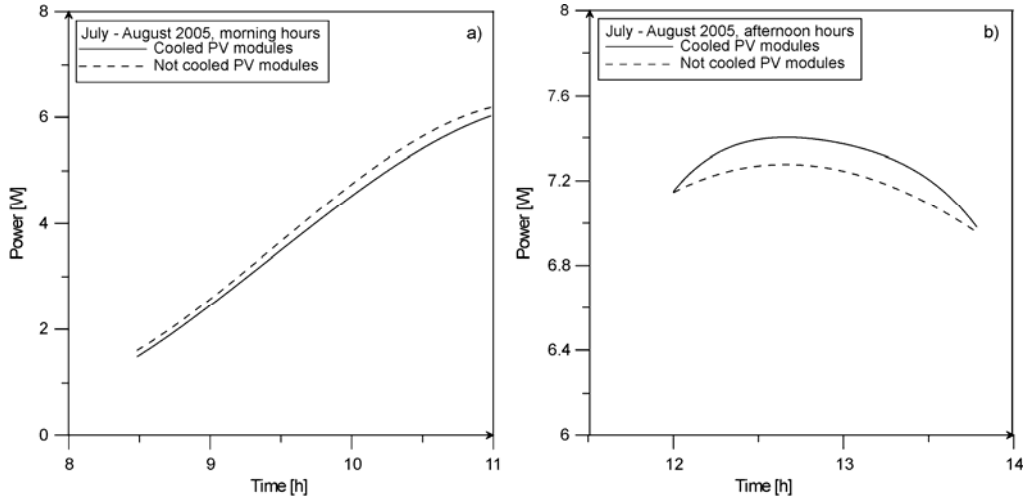

Fig. 2. Average power generated in PV modules in sunny days of July and August 2005, in the morning (a) and afternoon (b)

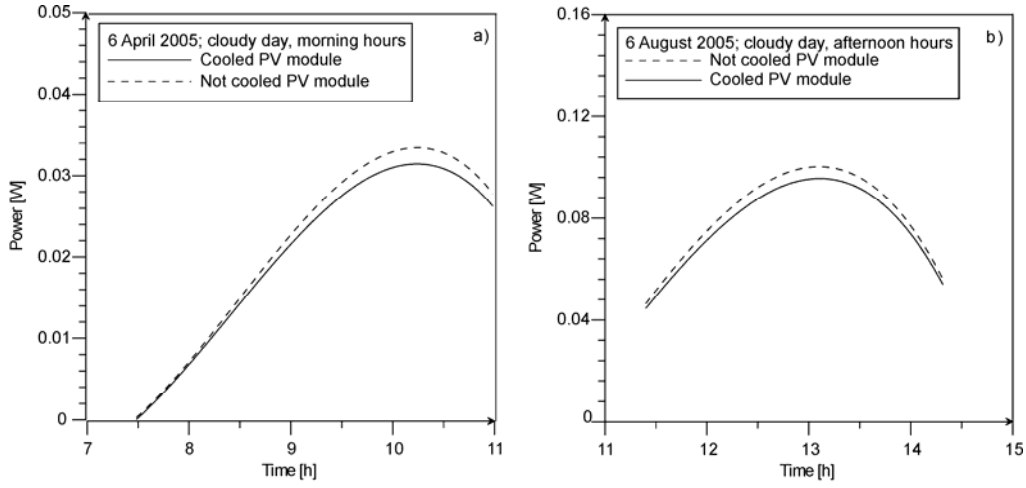

Fig. 3. Power generated in PV modules at a cloudy day in: a) morning and b) afternoon hours

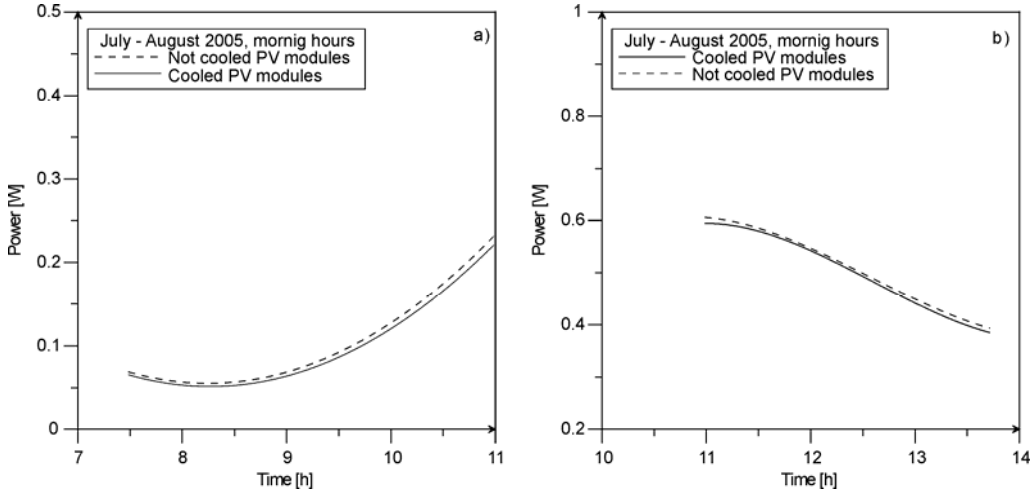

Fig. 4. Average power generated in PV modules in cloudy days of July and August 2005, in the morning (a) and afternoon (b)

According to the theory, the increase of temperature results in a decrease of the semiconductor band gap:

$$E_g(T) = E_g(0) - \frac{\beta T^2}{T + \gamma} \tag{1}$$

where $E_g(0)$ is the energy band gap at $T = 0$, γ and β are the coefficients for a specific semiconductor. The decrease of the energy band gap results in a decrease of the density of short-circuit current. The temperature dependence of the open circuit voltage U_{oc} is as follows:

$$U_{oc}(T) = U_{oc}(300) - \left(\frac{E_g(0)}{q} - U_{oc}(T) \right) \left(\frac{T}{300} - 1 \right) - \frac{3kT}{q} \ln \frac{T}{300} \tag{2}$$

where q is the unit charge.

The differentiation of Eq. (2) gives:

$$\frac{\partial U_{oc}}{\partial T} = \frac{\frac{E_g(0)}{q} + \frac{3kT}{q} - U_{oc}(300)}{T} \tag{3}$$

What follows is that $\frac{\partial U_{oc}}{\partial T}$ diminishes when the open-circuit voltage increases. With the increase of temperature, the fill factor (FF) should also decrease:

$$\frac{\partial FF}{\partial T} = \frac{q}{kT} \left(\frac{\partial U_{oc}}{\partial T} - \frac{U_{oc}}{T} \right) \frac{\partial FF}{\partial U} = \frac{E_g(0) + 3kT}{kT^2} \frac{\partial FF}{\partial U} \tag{4}$$

where:

$$U = \frac{qU_{oc}}{kT} \tag{5}$$

The increase of temperature should always result in a decrease of the efficiency of the photovoltaic conversion. In order to improve the conversion efficiency it is necessary to apply additionally cooling devices. The question is: what are the reasons for the anomalies observed in South-eastern Poland?

Anomalous differences between cooled and not cooled modules were observed in morning hours of the sunny days and cloudy days, and were probably due to a specific solar spectrum which reaches the photomodule surfaces. In this part of a day the solar spectrum consists mainly of the scattered radiation, in which the relative intensity of longer wavelengths is higher. Additionally, the shape of the spectrum is modulated by the composition of the atmosphere including pollution of the air. The energy of the scattered radiation is not sufficient to generate the majority of intrinsic carriers, hence a higher contribution of carriers from impurity levels is observed. In this case, the energy of thermal oscillations of the crystal lattice could be sufficient to activate carriers and in this way to increase the efficiency of not cooled photomodules. It seems that using special cooling system is not always necessary.

4. Conclusions

The efficiency of a Si monocrystalline PVphotomodule depends on the sun insolation reaching its surface. Essentially, in order to increase the photoconversion power

of Si photomodules, advantageous method is to use additional cooling systems. Such a cooling system may insure the hybrid bonding of PV and PT conversions [6]. However, it should be emphasized that in the region of South-eastern Poland, the cooling of solar cells during cloudy days as well as in the morning hours not only is unnecessary, but causes a decrease of their efficiency.

Acknowledgement

This work was supported by the grant of Polish Ministry of Science and Information Society Technologies under the project nr 3T09D 05228.

References

[1] OLCHOWIK J.M., JÓŹWIK I., TOMASZEWSKI R., SZYMCZUK D., ADAMCZYK J., CIEPLAK T., ZABIELSKI K., MUCHA J., *Technical Digest of the International PVSEC-14*, Bangkok, Thailand, 26–30 January 2004, Vol. I, p. 495.

[2] CIEŚLAK K., GUŁKOWSKI S., JÓŹWIK I., MUCHA J., ZDROJEWSKA M., SZYMCZUK D., OLCHOWIK J.M., *PC software for the current–voltage characteristics of solar cells* [in:] J.M. Olchowik (Ed.), *The Global Calculation and the Future of Informatics*, Scientific Publishing of PWSZ in Biała Podlaska, Biała Podlaska, 2004, p. 173 (in Polish).

[3] BANAŚ J., TOMASZEWSKI R., OLCHOWIK J.M., *Computer control of the tracking system „follow the sun" of PV modules*, [in:] J.M. Olchowik (Ed.), *The Global Calculation and the Future of Informatics*, Scientific Publishing of PWSZ in Biała Podlaska, Biała Podlaska, 2004, p. 188 (in Polish).

[4] OLCHOWIK S., OLCHOWIK J.M., *DELPHI as the environment of the monitoring of solar cells*, [in:] J.M. Olchowik (Ed.), The Global Calculation and the Future of Informatics, Scientific Publishing of PWSZ in Biała Podlaska, Biała Podlaska, 2004, p. 180 (in Polish).

[5] OLCHOWIK J.M., JÓŹWIK I., SZYMCZUK D., ZABIELSKI K., MUCHA J., TOMASZEWSKI R., BANAŚ J., OLCHOWIK S., ADAMCZYK J., CIEPLAK T., ZDYB A., Proceedings of the 19th European Photovoltaic Solar Energy Conference and Exhibition, Paris, France, 7–11 June 2004 vol. III, p. 3294.

[6] OLCHOWIK J.M., Polish Patent, *The method and the system of enhancing the hybrid solar system efficiency*, Patent Bulletin, No. 13 (822) (2005) 77 (in Polish).

Received 9 September 2005
Revised 4 November 2005

Materials Science-Poland, Vol. 24, No. 4, 2006

Stirring of electrolytes in the vicinity of metallic matrix in a permanent magnetic field

S. V. GOROBETS[1], O. YU. GOROBETS[2*], I. YU. GOYKO[3], S. P. MAZUR[1]

[1]National Technical University of Ukraine KPI, Kiev, 03056, Ukraine

[3]National University of Food Technologies, Kiev, 01033, Ukraine

[2]Institute of Magnetism of NAS of Ukraine, Kiev, 03142, Ukraine

Magnetohydrodynamic stirring of electrolytes in the vicinity of metallic surface in combined magnetic and electric fields is a phenomenon well known and widely used in modern technology. In the paper the phenomenon of magnetohydrodynamic stirring in the vicinity of metallic surface in the electrolytes was observed only in a magnetic field. The influences of main parameters, such as magnetic field strength and pH of electrolyte solution, on stirring process were investigated.

Key words: *magnetohydrodynamic stirring; multivortex dynamic structure; magnetic field*

1. Introduction

Stirring (mass transfer) in combined electric and magnetic fields is one of the most extensively investigated phenomena [1–4]. It is well known that mixing usually accelerates or changes the character of chemical and electrochemical processes occurring in electrolytes [5–9]. Stirring, widely used for intensification of heat transfer, mass transfer and chemical and biochemical processes, requires additional power sources and complex device construction. It is therefore timely to develop new inexpensive mixing methods and devices. The phenomenon of magnetohydrodynamic electrolyte mixing has served as a basis for development of improved methods of magnetoelectrochemical codeposition of several metals and inert particles, obtaining high quality of deposits, creation of chaotic magnetohydrodynamic mixing of electrolytes (such as Lagrange chaos) at very small Reynolds numbers [10]. Recently, the effect of multivortex electrolyte stirring was found in the vicinity of a solitary electrode in a magnetic field without application of external electrical field [11, 12].

*Corresponding author, e-mail: gor@usuft.kiev.ua

In particular, emergence of a multivortex dynamic structure of electrolyte was revealed in the vicinity of a long metallic cylinder under the influence of a magnetic field [13]. The directions of rotation in the adjacent vortexes are mutually opposite (Fig. 1). In details, hydrodynamics of multivortex dynamic structure of aqueous solution of nitric acid in the vicinity of a steel cylinder was investigated in the work [13].

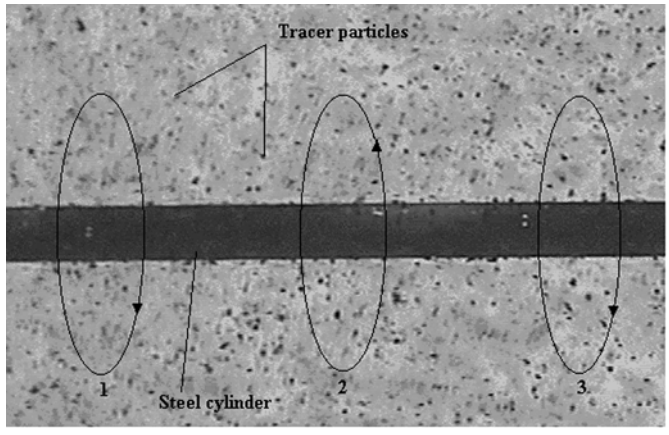

Fig. 1. Schematic drawing of the multivortex structure in the vicinity of a steel cylinder in a steady magnetic field (1, 2, 3 – electrolyte vortexes)

The purpose of the present paper was investigation of the dependence of magnetohydrodynamic mixing of nitric acid solution on magnetic field and pH. The dependence of vortex quantity on cylinder diameter was also investigated. The purpose of the study was determined by practical application requirements. One of the most important parameters characterizing an electrolyte solution is pH value. Therefore, the investigation of electrolyte velocity dependence on pH value is an interesting and necessary task. It is worth noting that pH value can be changed in industrial processes [14, 15] and can be optimized. Modern technologies allow us to use strong magnetic fields, for example, by using permanent magnets. The advantages of permanent magnets are absence of power supply expenditure and a simple construction. Thus, the investigation of electrolyte velocity dependence on magnetic field strength is also an important task. The study of the dependence of number of vortexes on the cylinder length is of interest because it characterizes the problem of uniformity and quality of mixing.

2. Experimental

The experiments were carried out in an installation, consisting of an electromagnet, an optical microscope, a videocamera and a computer similar to the one described in [16]. The vortex velocity dependencies on magnetic field magnitude and solution pH were investigated. The model liquid represented 7% nitric acid solution with addition of non-magnetic tracer particles for a visualisation of electrolyte movement. The

free volume of the microcontainer was filled with 7% nitric acid solution with the tracer particles. The microcontainer with the steel cylinder was fixed between polar tips of an electromagnet. A slow motion of the tracer particles towards the steel cylinder surface was observed without a magnetic field application. Upon switching on the magnetic field electrolyte velocity increases significantly.

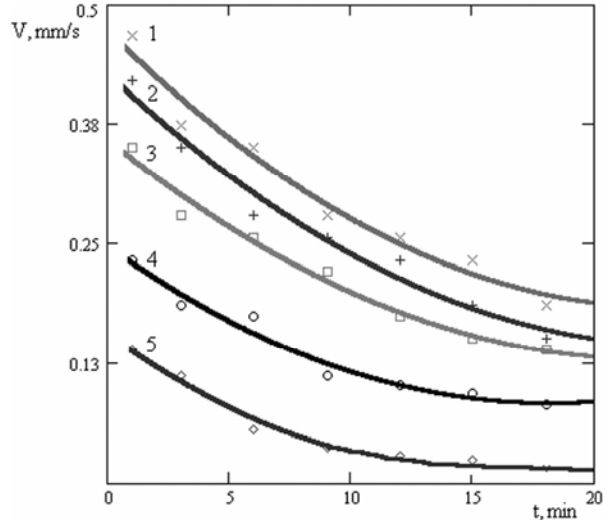

Fig. 2. Vortex velocity dependence on magnetic field magnitude in the vicinity of the steel cylinder surface. The magnetic field *H*: 1 – 1000 Oe, 2 – 2000 Oe, 3 – 3000 Oe, 4 – 4000 Oe; 5 – 500 Oe

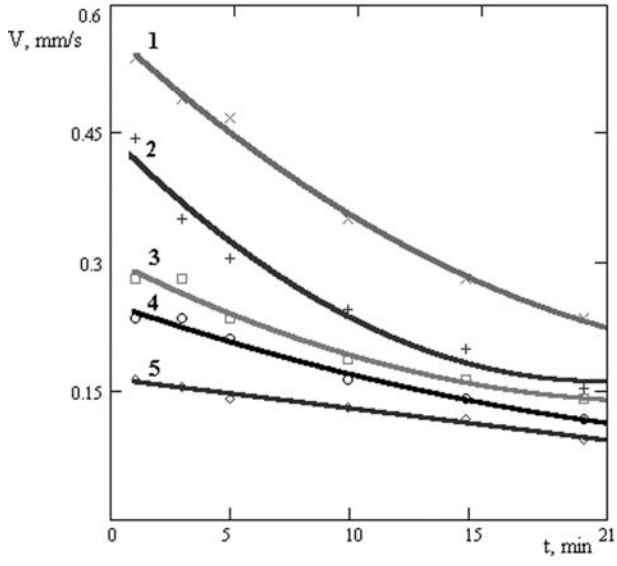

Fig. 3. Dependence of vortex velocity in the vicinity of the steel cylinder surface on solution pH in the magnetic field of 4000 Oe: 1 – pH = 1; 2 – pH = 1,5; 3 – pH = 2; 4 – pH = 3; 5 – pH = 5

The dependence of the vortex velocity on the magnetic field magnitude in the vicinity of the steel cylinder surface is shown in Fig. 2. The electrolyte velocity increases with increasing magnetic field and decreases with experiment time.

The electrolyte velocity is higher at higher acidity of solution and it decreases with experiment time. As is shown in Figs. 4, 5, the number of vortexes depends on the cylinder length L. The number of vortexes is different for different cylinder diameters.

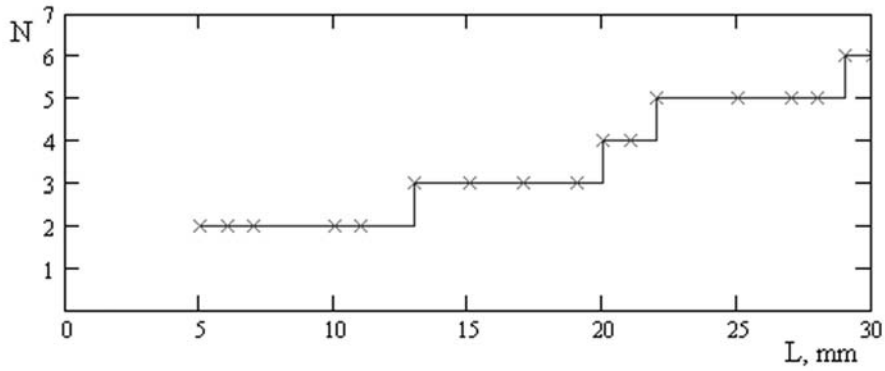

Fig. 4. Dependence of the number of vortexes on the cylinder length L. Cylinder diameter is equal to 0.725 mm (the experimental points are marked with ×)

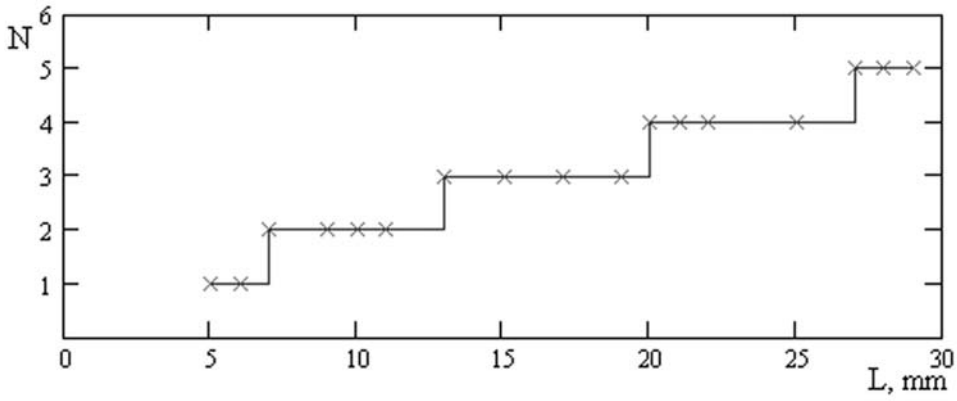

Fig. 5. Dependence of the number of vortexes on the cylinder length L. Cylinder diameter is equal to 0.250 mm (the experimental points are marked with ×)

4. Conclusion

The magnetohydrodynamic stirring is a phenomenon possibly to create new mixing devices that can be used for various applications, for example, mixing of microvolumes. The advantages of the proposed method are electric power economy and

simplified device construction. The dependences obtained in this work allow one to get qualitative estimates in order to optimize the magnetohydrodynamic stirring process without any external electric field applied. A proper choice of pH of solution, an external magnetic field magnitude and diameter of steel wires (independently of their length) can be made based on the present investigation.

References

[1] TACKEN R.A., JANSSEN L.J.J., J. Appl. Electrochem., 25 (1995), 1.
[2] FAHIDY T.Z., J. Appl. Electrochem., 13 (1983), 553.
[3] WASKAAS M., KHARKATS Y.I., J. Phys. Chem., B103 (1999), 4876.
[4] COEY J.M.D., HINDS G., LYONS M.E.G., Europhys. Lett., 47 (1999), 267.
[5] DASH J., US Patent. No. 4 666 568, 1987.
[6] Matsushita Electric Works Ltd., Japanese Patent No. 59 31 894, 1984.
[7] O'BRIEN N., SANTHANAM K.S.V., J. Appl. Electrochem., 20 (1990), 781.
[8] ZHANG H., ZHANG G., Chem. Abstr., 115 (1991), 217159.
[9] YU XIANG, BAU H.H., Phys. Rev., E 68 (2003), 016312.
[10] LEVENTIS N., GAO X., J. Phys. Chem., B. 103 (1999), 5832.
[11] GOROBETS S.V., GOROBETS O.YU., RESHETNYAK S.A., J. Magn. Magn. Mater., 272–276 (2004), 2408.
[12] SHINOHARA K., AOGAKI R., Electrochem., 67 (1999).
[13] GOROBETS YU.I., GOROBETS O.YU., MAZUR S.P., Magnetohydrodynamics, 40 (2004), 1.
[14] STABNIKOV V.N., *Design of processes and devices of food industry*, Vischa shola, Kiev, 1982 (in Russian).
[15] ROMANKOV P.G., KUROCHKINA M.I., *Hydromechanical processes in chemical technology*, Khimiya, Leningrad, 1982 (in Russian)..
[16] GOROBETS S.V., GOROBETS O.YU., Magnetohydrodynamics., 36 (2000), 65.
[17] GOROBETS O.YU., RESHETNYAK S.A., Magnetohydrodynamics., 39 (2003), 211.

Received 9 September 2005
Revised 24 November 2005

Materials Science-Poland, Vol. 24, No. 4, 2006

Magnetic ordering processes in manganese(II) di(hydrogen malonate) monohydrate complex studied by ESR spectroscopy

S. MARCZYŃSKI[1], N. GUSKOS[1,2*], J. TYPEK[1], E. GRECH[3], B. KOŁODZIEJ[3]

[1]Institute of Physics, Szczecin University of Technology, al. Piastów 17, 70-310 Szczecin, Poland

[2]Solid State Physics, Department of Physics, University of Athens, Panepistimiopolis, 15 784 Zografos, Athens, Greece

[3]Department of Inorganic and Analytical Chemistry, Szczecin University of Technology, al. Piastów 17, 70-310 Szczecin, Poland

A new manganese complex of malonic acid $CH_2(COOH)_2 \cdot MnCO_3 \cdot H_2O$ was synthesized. Temperature dependence of the electron spin resonance (ESR) spectrum of Mn(II) was investigated in the 4.2– 295 K temperature range. The obtained ESR spectra were successfully fitted by using a Lorentzian-shape function. The fitting revealed existence of about 2% of a spurious phase of the manganese(II) complex. Strong magnetic interactions have been observed in the investigated temperature range with expected magnetic phase transition at $T_N \approx 2.5$ K. The integrated intensity, linewidth and resonance field of the ESR spectrum have shown that the spin dynamical fluctuations essentially influence the magnetic system. An anomalous behaviour of the ESR resonance field parameter has been observed below 100 K and with decreasing temperature the resonance field shifted to higher magnetic fields.

Key words: *manganese complex; ESR*

1. Introduction

Coordination compounds containing malonic acid as a ligand have been recently intensively studied due to their potential application as materials in molecular electronics, catalysts, biologically active compounds, molecular-based magnetic materials, etc. [1, 2]. Malonic acid, $HOOC–CH_2–COOH$, acts as a ligand with various dentate abilities. As the coordination modes depend on the nature of the metal and on synthesis conditions, the crystal structures of malonate complexes are very diverse – from ionic

*Corresponding author, e-mail address: ngouskos@phys.uoa.gr

to three-dimensional polymers [3]. The malonate ligand occupies one or two coordination positions and neutralizes two positive charges of the metallic ion, allowing the inclusion of other ligands in the coordination sphere of the metal. An important feature of the malonic bridge is the fact that the magnitude of the exchange interaction depends on the possible bridging modes that it can adopt. Thus the ferro- or antiferromagnetic interactions may appear in malonate complexes, governed by the dimensionality of the structure.

Organic complexes of manganese(II) are interesting due to a variety of physical properties. In particular, their magnetic interactions have been studied in view of possible applications [4, 5]. Organic complexes of metal ions could form self-assemblies of molecular rods and tubes where long distance phenomena, such as the electron-energy transfer or magnetic coupling in transition ions, are complicated and can be changed by structural modifications [6, 7]. The manganese(II) ions in the organometallic compounds can be easily ordered into short or long order magnetic states [4, 5].

The aim of this report is to describe the results of investigations of temperature dependence of the electron spin resonance (ESR) spectra of the $CH_2(COOH)_2 \cdot MnCO_3 \cdot H_2O$ complex. Especially the magnetic interactions with possible magnetic ordering processes will be presented and discussed.

2. Experimental

The $CH_2(COOH)_2 \cdot MnCO_3 \cdot H_2O$ manganese complex of malonic acid was obtained in the form of pink powder by a slow evaporation of an aqueous solution prepared by dissolving stoichiometric amounts of malonic acid and manganese carbonate in water [7, 8].

ESR measurements were carried out with a conventional X-band ($\nu = 9.43$ GHz) Bruker E 500 spectrometer with 100 kHz magnetic field modulation. The samples containing around 20 mg of the material were placed into 4 mm diameter quartz tubes. The measurements were performed in the temperature range from room down to liquid helium temperature with $\Delta T = \pm 1.0$ K stability using an Oxford cryogenic system.

3. Results and discussion

Figure 1 presents the temperature dependence of the ESR spectra of the $CH_2(COOH)_2 \cdot MnCO_3 \cdot H_2O$ complex. A very intense, broad and almost symmetrical line is observed in the investigated temperature range. The intensity, linewidth and resonance field of the line strongly depends on temperature. The obtained ESR spectra has been fitted successfully by using the Lorentzian function. The fitting revealed also the existence of about 2% of spurious phase of manganese(II) complex (Fig. 2). This was calculated from the area below the absorption ESR spectra which is proportional to the number of paramagnetic species participating in the resonance.

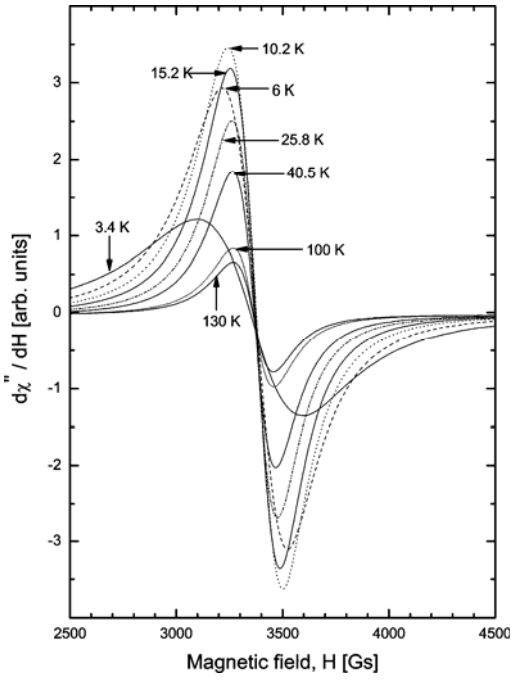

Fig. 1. Temperature dependence of the ESR spectra of the $CH_2(COOH)_2 \cdot MnCO_3 \cdot H_2O$ complex

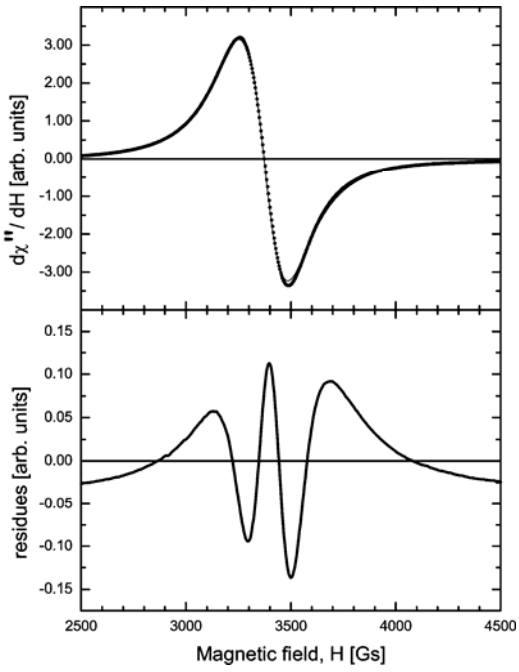

Fig. 2. The experimental (circles) and fitted (solid line) ESR spectra at room temperature. The lower panel presents the difference between the experimental and fitted spectra

At room temperature the ESR line is centered at $g_{\mathrm{eff}} = 2.0135(5)$, with the linewidth $\Delta H = 325(4)$ Gs. The value of about 2 for the g-factor is commonly expected for an S state ion like manganese(II) or iron(III) ($S = 5/2$). The ESR spectra arising from divalent manganese usually show splitting into 6 hyperfine components separated by about 70 to 100 Gs. If the intrinsic linewidth is larger than the splitting, the six hyperfine components overlap giving a single broad (over 600 Gs) ESR line. In the present case, at high temperatures, the linewidth is twice smaller than that value. This could indicate that the observed signal does not originate from isolated paramagnetic manganese(II) ions. It is thus possible that the ions are strongly coupled by the exchange interaction (ferromagnetic or antiferromagnetic). Large exchange narrowing effects could suppress the hyperfine splitting. Figure 3 gives the temperature dependence of the linewidth (ΔH), resonance field (H_r) and integrated intensity (I_{integ}). The integrated intensity, calculated as the area below the absorption line or the product of line amplitude and the square of the linewidth, is proportional to the number of spins participating in the resonance. The temperature dependence of the integrated intensity at higher temperatures could be described well by the Curie–Weiss law, $I_{\mathrm{integ}} = C/(T - \Theta)$, with the Curie–Weiss temperature $\Theta = -6.2(5)$ K. The product $I_{\mathrm{integ}}T$, which is proportional to the effective magnetic moment, is almost constant in the temperature range

from room down to 30 K. Below that temperature a slow decrease of the effective magnetic moment with decreasing temperature is observed.

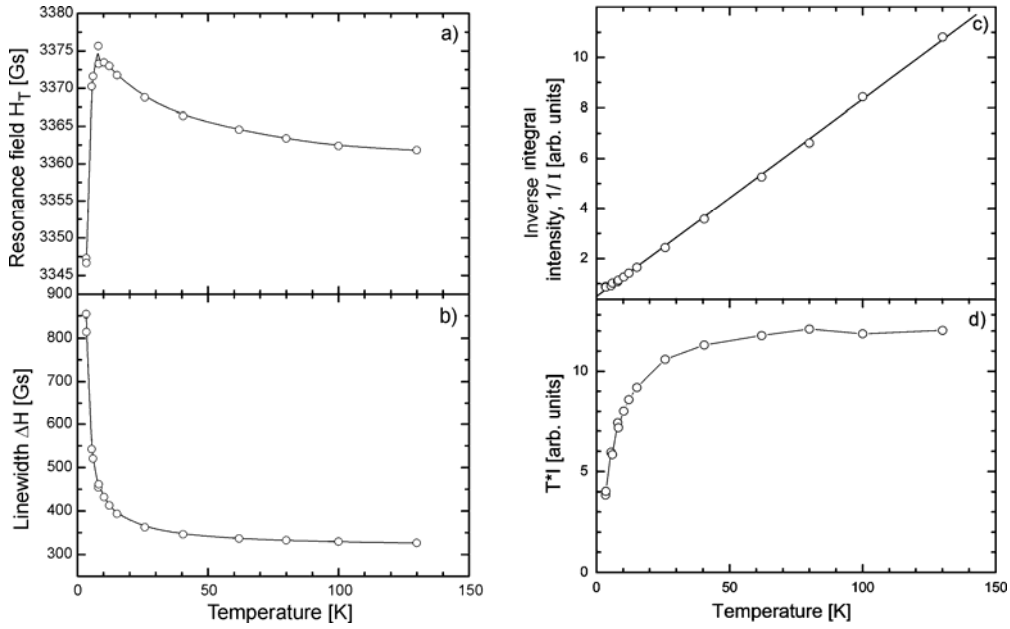

Fig. 3. Temperature dependence of the ESR resonance field (a), linewidth (b), inverse integral intensity (c) and the product of the integral intensity and temperature (d)

This indicates the existence of antiferromagnetic ordering processes involving manganese(II) ions inside the lattice (Fig. 3d). The ESR linewidth exhibits an increase as temperature decreases, most pronounced below 10 K and a rapid increase at lower temperatures where the antiferromagnetic phase transition is expected to occur (Fig. 3b). Broadening of the ESR line is usually observed in anisotropic antiferromagnets due to the slowing down of spin fluctuations as the critical temperature is approached from above [9–11]. This results in a divergence of the spin-correlation length, which, in turn, affects the spin-spin relaxation time of the exchange narrowed ESR lines resulting in the critical broadening of the ESR linewidth in the vicinity of T_N (T_N being the Neel temperature). The temperature dependence of the linewidth in this case can be described by the following relation [11]:

$$\Delta H = \Delta H_{00} + A\left(\frac{T - T_N}{T_N}\right)^{-\gamma} \tag{1}$$

where the first term describes the high temperature exchange narrowed linewidth, which is temperature independent, while the second term reflects the critical behaviour and γ is the critical exponent. Using the best fit procedure to the experimental

results, the following values were obtained: $\Delta H_{00} = 308(3)$ Gs, $A = 266(11)$ Gs, $\gamma = 0.70(3)$ and $T_N = 2.5(1)$ K.

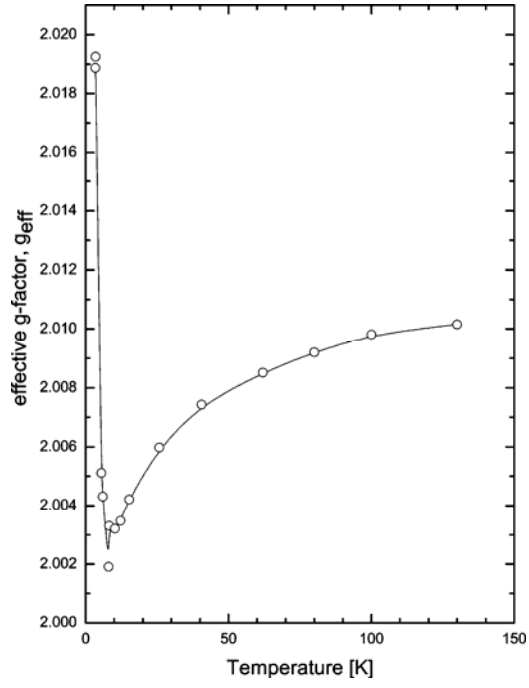

Fig. 4. Temperature dependence of the g_{eff} parameter

The magnetic resonance field increases with decreasing temperature but below 8 K a strongly opposite behaviour is observed (Fig. 3a). From room temperature down to 8 K the increase of the magnetic resonance field is about $\Delta H_r \approx 15$ Gs but from 8 K to 4.2 K the decrease is twice larger. The resonance condition for the spins is:

$$h\nu = g\mu_B(H_0 \pm H_{\text{int}}) \tag{2}$$

where μ_B is the Bohr magneton, H_0 is the applied external magnetic field, and H_{int} is the internal magnetic field. The antiferromagnetic ordering process is responsible for the observed temperature shift of the magnetic resonance field H_r. The shift is positive (toward higher magnetic fields) for temperatures higher than 8 K and is negative for temperatures lower than 8 K. Figure 4 presents the temperature dependence of the g_{eff} parameter. At temperature $T = 8$ K, the minimum value of that parameter is reached with $g_{\text{eff}} = 2.0019(4)$ which is very close to the g-value of a free electron ($g_e = 2.0023$).

4. Conclusions

The manganese(II) complex of malonic acid $CH_2(COOH)_2 \cdot MnCO_3 \cdot H_2O$ shows a strong antiferromagnetic interaction between the manganese(II) ions. At higher temperatures ($T > 50$ K), exchange coupling processes dominate, while at lower tempera-

tures (T < 10 K) the magnetic ordering processes have been observed. The magnetic resonance field increases with the decreasing temperature in the high-temperature range, while below 8 K a sharply opposite behaviour is observed leading to the g-value very close to that of a free electron. Temperature analysis of the linewidth has shown that the temperature of antiferromagnetic phase transition is T_N = 2.5 K.

References

[1] RUIZ-PEREZ C., RODRIGUEZ-MARTIN Y., HERNANDEZ-MOLINA M., DELGADO F.S., PASAN J., SANCHIZ J., LLORET F., JULVE M., Polyhedron, 22 (2003), 2111.
[2] PASAN J., DELGADO F.S., RODRIGUEZ-MARTIN Y., HERNANDEZ-MOLINA M., RUIZ-PEREZ C., SANCHIZ J., LLORET F., JULVE M., Polyhedron, 22 (2003), 2143.
[3] NAUMOV P., RISTOVA M., SOPTRAJANOV B., DREW M.G.B., NG S.W., Croatica Chem. Acta, 75 (2002), 701.
[4] PAPADOPOULOS A.N., Inorg. Chem., 35 (1996), 559.
[5] TANGOULIS V., MALAMATARI D.A., SOULTI K., STERGIOU V., RAPTOPOULOS C.P., TERZIS A., KABANOS T.A. KESSISSOGLOU D.P., Inorg. Chem., 35 (1996), 4974.
[6] LI H., DAVIS C.E., GROY T.L., KELLEY D.G., YAGHI O.M., J. Am. Chem. Soc., 120 (1998), 2186.
[7] CHAWLA S.K., ARORA A., NATTINEN K., RISSANEN K., YAKHMI J.V., Polyhedron, 23 (2004), 3007.
[8] LI J., ZENG H., CHEN J., WANG Q., Chem. Commun., 1213 (1997).
[9] KAWASAKI K., Prog. Theor. Phys., 39 (1968), 285.
[10] KAWASAKI K., Phys. Lett., 26A (1968), 543.
[11] HUBER D.L., Phys. Rev. B, 6 (1972), 3180.

Received 9 September 2005
Revised 24 November 2005